

RENSIT: RadioElectronics. NanoSystems. Information Technologies

Journal "Radioelectronics. Nanosystems. Information Technologies" (abbr. RENSIT) publishes original articles, reviews and brief reports, not previously published, on topical problems in **radioelectronics (including biomedical) and fundamentals of information, nano- and biotechnologies and adjacent areas of physics and mathematics.**

Designed for **researchers, graduate students, physics students of senior courses and teachers.** It turns out **2 times a year** (that includes 2 issues)

Authors of journal are academicians, corresponding members and foreign members of Russian Academy of Natural Sciences (RANS) and their colleagues, as well as other russian and foreign authors on presentation of their manuscripts by the members of RANS, which can be obtained by authors before sending articles to editors. And also after its receiving - on recommendation of a member of editorial board of journal, or another member of Academy of Natural Sciences, that gave her opinion on article at request of editor. The editors will accept articles in both **Russian and English** languages.

Articles are internally peer reviewed (**double-blind peer review**) by members of the Editorial Board. Some articles undergo external review, if necessary.

Journal RENSIT is included in the **DB SCOPUS, EBSCO Publishing**, in the international abstracts database - **Ulrich's International Periodicals Directory**, (USA, New York, <http://www.ulrichsweb.com>), in the **AJ and DB VINITI RAS** (<http://www.viniti.ru>), and DB **Russian Science Citation Index (RSCI)** (http://elibrary.ru/project_risc.asp).

Full-text content is posted in the DB of the **Russian Scientific Electronic Library** - information resource on the Internet <http://elibrary.ru> and is available for registered users. And also - in Open Access **CyberLeninka NEB** of Russian Federation <http://cyberleninka.ru>.

On journal's website <http://www.rensit.ru> posted metadata publications and **RENSIT: Radioelectronics. Nanosystems. Information Technologies - english version** (cover-to-cover translation) of journal, which is a party to **CrossRef**.

The founder - the **Russian Academy of Natural Sciences**
Publisher - Publishing Center of the Russian Academy of Natural Sciences
Publisher Address: 29/16, Sivtsev Vrazhek lane, Moscow 119002, Russian Federation

CONTENTS

MULTIDIMENSIONAL THEORIES OF PHYSICAL FIELDS

BUBBLE STRUCTURES IN MICROPHYSICAL OBJECTS IN 5-D EXTENDED SPACE MODEL

Dmitry Yu. Tsipenyuk, Vladimir B. Belayev 249

NUCLEAR PHYSICS

RESONANT INTERFERENCE EXCHANGE INTERACTION

Gennady V. Myshinsky 261

FRACTALS IN PHYSICS

NUMERICAL MODEL OF FRACTALS IN THE PHYSICAL CHEMISTRY OF MATERIALS SCIENCE

Alexander D. Izotov, Feodor I. Mavrikidi 279

RADIOELECTRONICS

IMPROVING THE ACCURACY OF MEASUREMENT TIME INTERVALS OF RADIO RECEPTION IN THE FRAMEWORK OF RECURSIVE MULTI-STAGE BAYESIAN ESTIMATES

Yuri N. Gorbunov 291

ABOUT AlGaAs-HETEROSTRUCTURES CVC KINETICS SIMULATION

Natalia F. Vetrova, Evgeny V. Kuimov, Sergey A. Meshkov, Vasily D. Shashurin ... 299

NANOSYSTEMS

REDUCTION OF GRAPHENE OXIDE BY SUPERCRITICAL ISOPROPANOL: DEFINITION OF ACETONE IN THE COMPOSITION OF THE MULTICOMPONENT MIXTURE BY GC-MS METHOD

Elena V. Fatyushina, Elena Yu. Buslaeva 307

CONDUCTION MECHANISM OF NANOGRAPHITE FORMED BY METHANE PLASMA DEPOSITION AND SUBSEQUENTLY HEAT TREATMENT

Efim P. Neustroev, Aisen R. Prokopiev 315

BINDING OF SHORT DNA OLIGONUCLEIDES TO THE SURFACE OF REDUCED GRAPHENE OXIDE TO CREATE BIOLOGICAL SENSORS

Ivan A. Komarov, Olga M. Antipova, Nikolay S. Struchkov, Alexander N. Kalinnikov, Sergey N. Scherbin, Vyacheslav A. Seleznev 321

SPECTRAL AND CONDUCTIVE PROPERTIES OF FILM HETEROSTRUCTURES BASED ON FULLERENE-CONTAINING MATERIAL AND 4-METHYLPHENYLHYDRAZONE N-ISOAMYLISATINE

Alexey N. Gusev, Alim S. Mazinov, Andrey S. Tyutyunik, Vladimir S. Gurchenko . 331

INFORMATION TECHNOLOGIES

SOURCE DETECTION IN DISPERSING MEDIA

Venedikt M. Kuz'kin, Sergey A. Pereselkov, Yuri V. Matvienko, Sergey A. Tkachenko 337

CALCULATION OF SEISMIC RESISTANCE OF VARIOUS STRUCTURES USING THE GRID-CHARACTERISTIC METHOD

Alena V. Favorskaya, Igor B. Petrov 345

MODELING VERTICAL FRACTURES USING THE SCHOENBERG MODEL ON STRUCTURED GRIDS BY GRID-CHARACTERISTIC METHOD

Polina V. Stognii, Nikolay I. Khokhlov, Igor B. Petrov 351

ELIMINATING UNAUTHORIZED ACCESS TO THE FREQUENCY RESOURCE OF THE GEOSTATIONARY SATELLITE REPEATER

Andrey V. Sukhov, Anton L. Tovbin, Vladislav V. Osipov 357

MEDICAL PHYSICS

NEW ADDITIVE TECHNOLOGIES FOR FORMING COMPLEX BONE STRUCTURES FOR MEDICAL AND BIOLOGICAL APPLICATIONS

Vladimir N. Gorshenev, Mayya Yu. Ziangirova, Vladimir V. Kolesov, Larisa M. Krasnopolskaya, Alexander A. Prosvirin, Andrey T. Teleshev 369



RUSSIAN ACADEMY
OF NATURAL SCIENCES

DEPARTMENT OF
RADIOELECTRONICS,
NANOPHYSICS AND
INFORMATION
TECHNOLOGIES PROBLEMS

RENSIT:

RADIOELECTRONICS,
NANOSYSTEMS,
INFORMATION
TECHNOLOGIES.

2019, VOL. 11, № 3

FOUNDED IN 2009
3 ISSUES PER YEAR
MOSCOW

Editor-in-Chief

VLADIMIR I. GRACHEV
grachev@cplire.ru

Deputy Chief

ALEXANDER S. ILUSHIN

Deputy Chief

SERGEY P. GUBIN

Executive Secretary

ROSTISLAV V. BELYAEV
belyaev@cplire.ru

EDITORIAL BOARD

Anatoly V. Andreev
Vladimir A. Bushuev
Vladimir A. Cherepenin
Alexander S. Dmitriev
Yuri K. Fetisov
Yuri V. Gulyaev
Yaroslav A. Ilushin
Anatoly V. Kozar
Vladimir V. Kolesov
Albina A. Kornilova
Vladimir A. Makarov
Aleksy P. Oreshko
Andrey I. Panas
Igor B. Petrov
Alexander A. Potapov
Vyacheslav S. Rusakov
Alexander S. Sigov
Valentine M. Silonov
Eugeny S. Soldatov
Arkady B. Tsepelev
Lkhamsuren Enkhtur (Mongolia)
Yoshiyuki Kawazoe (Japan)
Kairat K. Kadyrzhanov (Kazakhstan)
Peter Paul Mac Ken (USA)
Andre Skirtach (Belgium)
Enrico Verona (Italy)

ISSN 2414-1267 online

The journal is registered by the Ministry of Telecom and Mass Communications of the Russian Federation. Certificate El. no. FS77-60275 on 19.12.2014

All rights reserved. No part of this publication may be reproduced in any form or by any means without permission in writing from the publisher.

©RANS 2019

EDITORIAL BOARD ADDRESS
218-219 of, 7 b., 11, Mokhovaya str.,
125009 MOSCOW, RUSSIAN FEDERATION
TEL. +7 495 629 3368
FAX +7 495 629 3678 FOR VLADIMIR I. GRACHEV

DOI: 10.17725/rensit.2019.11.249

Bubble structures in microphysical objects in 5-D extended space model

Dmitry Yu. Tsipenyuk

Prokhorov General Physics Institute of RAS, <http://gpi.ras.ru/>
Moscow 119991, Russian Federation

OPCID: 0000-0001-8367-0883, e-mail: tsip@kapella.gpi.ru

Vladimir B. Belyaev

Center for Relativity and Astrophysics, Efremov Research Institute of Electrophysical Equipment, <http://www.niiefa.spb.su/>
Saint-Petersburg 196641, Russian Federation

E-mail: wbelyaev@yandex.ru

Abstract. It is considered (1+4)-dimensional Extended Space Model (ESM) as a generalization of the special theory of relativity at a 5-dimensional space. Rotations in extended space correspond to the motion of a particle in gravity field in the embedded four-dimensional space-time. Within the framework of ESM the photons have a nonzero mass in a gravitational field. We study how a rotation in ESM agrees with photon dynamics in the Schwarzschild field. Equations of the critical curve are obtained by the nonzero energy integral variation in accordance with principles of the calculus of variations in mechanics. This method is compared with the Fermat's principle and geodesics principle. Energy and momentum of the particle transferred to the gravity field is defined. The force vector acting on the photon in Schwarzschild space-time is found for the weak gravity and corresponds to photon's gravitational mass equal to the twice mass of a material particle of the same energy. Compliance with the law of conservation of energy as a source of gravity leads to the presence of particles with negative gravitational mass and zero kinematic momentum in the results of the annihilation reaction. Bubble gravitational structures of a type gravastar are considered. Accretion of matter onto compact stars results in their absorption of positive energy from the vacuum and the release negative energy in a free deep space. The particles with negative gravitational mass create there antigravitating vacuum with negative pressure. In the present work a non-conservation of energy in gravitational systems is interpreted by the ESM as the rotation of the energy-momentum vector in 5-dimensional space. The comparison bubble cosmic structures with similar possible bubble structures in microphysical objects is made.

Keywords: 5-dimensional space, electromagnetic field, gravity, Maxwell's equations, photon, mass, localization

PACS 04.20.Fy, 04.20.Jb, 11.10.Kk, 13.66.Hk, 97.10.Gz, 98.62.Dm

Bibliography - 46 references

Received 23.07.2019, *peer reviewed* 20.09.2019, *accepted* 23.09.2019

For citation: Dmitry Yu. Tsipenyuk, Vladimir B. Belyaev. Bubble structures in microphysical objects in 5-D extended space model. *RENSIT*, 2019, 11(3):249-260; DOI: 10.17725/rensit.2019.11.249.

CONTENTS

- | | |
|--|---|
| <ol style="list-style-type: none"> 1. INTRODUCTION (250) 2. (TS)-ROTATION IN EXTENDED SPACE MODEL (251) 3. PRINCIPLE OF THE STATIONARY ENERGY INTEGRAL OF PHOTON (252) 4. ENERGY AND MOMENTUM OF PARTICLE TRANSFERRED TO GRAVITY FIELD (253) 5. COMPARISON OF NULL GEODESICS, ENERGY INTEGRAL VARIATION AND FERMAT PRINCIPLES (253) | <ol style="list-style-type: none"> 6. PHOTON'S DYNAMICS IN SCHWARZSCHILD SPACE-TIME (254) <ol style="list-style-type: none"> 6.1. SPHERICAL COORDINATES (254) 6.2. RECTANGULAR COORDINATES (254) 6.3. FORCES AND GRAVITY MASS OF PHOTON (255) 7. GRAVASTAR STRUCTURE (256) 8. ENERGY DENSITY IN SPHERICAL GRAVITATIONAL SYSTEMS (257) 9. CONCLUSION (258) REFERENCES (258) |
|--|---|

1. INTRODUCTION

It is known, that between the mechanical and optical phenomena there is a certain likeness, which historically was exhibited that a set of the optical phenomena managed uniformly well to be described both within the framework of wave, and within the framework of the corpuscular theories. In particular, motion of a beam of light in an inhomogeneous medium in many respects similar to motion of a material particle in a potential field [1]. In the given activity, we shall take advantage of this connection to describe the gravitational phenomena.

The Fermat principle is the basis of geometric optics in media. It is also formulated for Riemannian space-time [2, 3]. In [4, 5] it is proposed a variational principle of the stationary energy integral of a light-like particle, which does not lead to violation of the isotropy of light path and agrees with Fermat's principle for static gravitational fields. It is also applicable to non-stationary gravitational fields in which the particle motion is free. This approach is the choice of Lagrangian of the particle and the definition of canonical momenta and forces as its partial derivatives with respect to the velocities and coordinates in accordance with Lagrange's mechanics. A correspondence is established between the physical energy and momentum of the particle, determined from non-gravitational interactions, and the contravariant canonical momentum vector.

In [6-8] it is investigated a generalization of special theory of relativity in a 5-dimensional space $G(1,4)$ with a metric (+ - - -) having an additional coordinate s . In ESM, in addition to the rotations in plane (TX) relating to the Lorentz transformations, the rotations in planes (TS) and (XS) are considered. In this model the approach is used, where the 5-th coordinate is the interval in $(1+3)$ -dimensions [9]. Movement along additional 5-th coordinate corresponds to the presence of particles rest-mass in $(1+3)D$. This is the case when a photon, get into an exterior field, gains a nonzero mass.

At the same time, it is being localized [10], while in the Minkowski space it is compared to the an infinite plane wave. In this paper we study how

(TS) -rotation agrees with photon dynamics in the Schwarzschild field, which is analyzed using the principle of extreme energy of a light-like particle based on Lagrangian mechanics [11].

Assuming that the standard model of cosmology and gravity theory are correct, astronomers have identified phenomena, whose essence is reduced to following statements [12-17]:

1. The main part of the Universe mass (more than 0.9) is made of dark matter and dark energy, which is associated with physical vacuum.
2. These dark substances do not emit electromagnetic radiation and do not interact with him, or exhibit such properties very weakly but have gravity.
3. The space vacuum has negative pressure, or, in other words, shows properties of an antigravitation, which determines dynamics of Universe extension.

In present work we develop an approach to explanation of above-mentioned phenomena. Accretion of matter onto compact stars results in the birth electron-positron pair with the appearance of additional particles from the vacuum having positive gravitational energy. Subsequent annihilation of e^+e^- pair release particles with negative gravitational mass [11], which are thrown in free deep space and create there antigravitating vacuum with negative pressure. The possibility of existence of body with a negative mass was considered and in general relativity [18]. The particles with positive energy form halo of compact stars and their possible contribution to dark matter is considered.

The photons according to ESM having positive rest-mass in a gravity field are concentrated around massive stars and black holes. Various modes that proposes existing nonzero mass to a photon are discussed in review [19]. In quantum nonlinear medium photons interact with each other so strongly that they begin to act as though they have mass, and they bind together to form molecules [20].

A gravitational model gravastar, or gravitational condensed star [21, 22] was offered as alternative to black holes. Such object corresponds to the

solution of the Einstein equation, which outside of area occupied by masses, coincides with Schwarzschild solution. Inside of gravastar there is other, nonsingular solution, so that metric is as a whole received nonsingular. Gravastar has a structure similar to a structure of a bubble. This bubble has a dense rigid envelope, which is under tension because of liquid substance, pressed apart it from within. The general thin-wall formalism is developed and applied to the investigation of the motion of various bubbles arising in the course of phase transitions in the very early Universe [23, 24]. Regular superconducting solution for interior of the Kerr-Newman spinning particle for parameters of electron represents a highly oblated rotating bubble formed by Higgs field which expels the electromagnetic field and currents from interior to domain wall boundary of the bubble [25]. The external fields correspond exactly to Kerr-Newman solution, while interior of the bubble is flat. Along with this, the bubble configuration of atomic nuclei has been discussed [26]. In the present work we will show, that it is possible result for gravastar when transfer of energy, as a source of gravitational field, to the vacuum coincides with properties of microworld.

2. (TS)-ROTATION IN EXTENDED SPACE MODEL

In Minkowski space $M(1,3)$ a 4-vector of energy and momentum

$$\tilde{p} = \left(\frac{E}{c}, p_x, p_y, p_z \right)$$

is associated to each particle [2]. In the extended space $G(1,4)$ [6-8] it is completed to 5-vector

$$\bar{p} = \left(\frac{E}{c}, p_x, p_y, p_z, mc \right),$$

where m is a rest mass of the particle. In blank space in a fixed reference system there are two types of various objects with zero and nonzero masses. In space $G(1,4)$ to them there corresponds 5-vectors

$$\bar{p}_f = \left(\frac{\hbar\omega}{c}, \frac{\hbar\omega}{c}, 0 \right)$$

and

$$\bar{p}_m = (mc, 0, mc). \tag{1}$$

For simplicity we have recorded these vectors in $(1 + 2)$ -dimensional space. The vector \bar{p}_f describes a photon with energy $\hbar\omega$ and with speed c . The vector \bar{p}_m describes a fixed particle. Next we will consider the motion of a photon.

At hyperbolic rotations on an angle ϕ_{TS} in the plane (TS)

$$\begin{aligned} \frac{E'}{c} &= \frac{E}{c} \cosh\phi_{TS} + p_s \sinh\phi_{TS}, \quad P' = P, \\ p'_s &= p_s \cosh\phi_{TS} + \frac{E}{c} \sinh\phi_{TS} \end{aligned} \tag{2}$$

the photon vector (1) will be transformed as follows:

$$\begin{aligned} \left(\frac{\hbar\omega}{c}, \frac{\hbar\omega}{c}, 0 \right) &\rightarrow \left(\frac{\hbar\omega}{c} \cosh\phi, \frac{\hbar\omega}{c}, \frac{\hbar\omega}{c} \sinh\phi \right) = \\ &\left(\frac{\hbar\omega}{c} n, \frac{\hbar\omega}{c}, \frac{\hbar\omega}{c} \sqrt{n^2 - 1} \right). \end{aligned} \tag{3}$$

In ESM this rotation is associated with the photon's motion in a medium in enclosed three-dimension space with refraction index $n > 1$. In such areas the speed of light is reduced. The parameter n relates the speed of light in vacuum with the speed of light in a medium v as

$$n = c/v. \tag{4}$$

According to the concept that the 5-th coordinate is interval in $(1+3)$ -dimensions the photon gains a rest mass

$$M = \frac{\hbar\omega}{c^2} \sinh\phi = \frac{\hbar\omega \sqrt{n^2 - 1}}{c^2}$$

in gravity field of embedded space-time.

In addition to the (TS) -rotation of 5-momenta (2) in ESM there is (XS) -rotation

$$M = \frac{\hbar\omega}{c^2} \sinh\phi = \frac{\hbar\omega \sqrt{n^2 - 1}}{c^2}$$

$$p'_s = p_s \cosh\phi_{XS} + P \sinh\phi_{XS}.$$

With the help of these transformations from the components of photon 5-momentum \bar{p}_f in a flat extended space, one can pass to the components of its 4-momentum in an arbitrary 4-dimensional space [11]:

$$\begin{aligned} \left(\frac{\hbar\omega}{c}, \frac{\hbar\omega}{c}, 0 \right) &\rightarrow \\ &\rightarrow \left(\frac{\hbar\omega}{c} F^T(x_i), \frac{\hbar\omega}{c} F^P(x_i), \frac{\hbar\omega}{c} F^S(x_i) \right), \end{aligned}$$

where $F^T(x_i)$, $F^P(x_i)$, $F^S(x_i)$ are functions of coordinates. Transformations are not communicative at specified angles of rotation ϕ_{TS} and ϕ_{XS} :

$$(TS) - (XS) \neq (XS) - (TS).$$

In the case of a material particle, a transformation (TX) is added to them.

3. PRINCIPLE OF THE STATIONARY ENERGY INTEGRAL OF PHOTON

In [4, 6] it is proposed a variational principle of the stationary energy integral of photon without violation of Lorentz-invariance. In it the interval in pseudo-Riemann space-time with metrical coefficients \tilde{g}_{11} :

$$ds^2 = \tilde{g}_{ij} dx^i dx^j$$

after substitutions

$$\tilde{g}_{11} = \rho^2 g_{11}, \quad \tilde{g}_{1k} = \rho g_{1k}, \quad \tilde{g}_{kq} = g_{kq}$$

is rewritten in form

$$ds^2 = \rho^2 g_{11} dx^{12} + 2\rho g_{1k} dx^1 dx^k + g_{kq} dx^k dx^q.$$

Here ρ is some quantity, which is assumed to be equal 1. Putting down x^1 as time, coordinates with indexes $k, q = 2, 3, 4$ as space coordinates and considering ρ as energy of light-like particle with $ds = 0$ we present it as

$$\rho = \left(g_{11} \frac{dx^1}{d\mu} \right)^{-1} \left\{ -g_{1k} \frac{dx^k}{d\mu} + \sigma \left[\left(g_{1k} g_{1q} - g_{11} g_{kq} \right) \frac{dx^k}{d\mu} \frac{dx^q}{d\mu} \right]^{1/2} \right\}, \tag{5}$$

where σ is ± 1 and μ is affine parameter.

The partial derivatives with respect to coordinates are written as

$$\frac{\partial \rho}{\partial x^\lambda} = -\frac{1}{2u_1 u^1} \frac{\partial g_{ij}}{\partial x^\lambda} u^i u^j, \tag{6}$$

where $u^i = dx^i/d\mu$ is four-velocity vector. The partial derivatives with respect to components u^i are

$$\frac{\partial \rho}{\partial u^\lambda} = -\frac{u_\lambda}{u_1 u^1}. \tag{7}$$

With $g_{11} = 0$ and $g_{1k} \neq 0$ even if for one k the energy takes form

$$\rho = \frac{g_{kq} u^k u^q}{2u_1 u^1}.$$

In this case the partial derivatives of ρ coincide with (6) and (7).

For the free moving a particle Lagrangian is taken in form

$$L = -\rho \tag{8}$$

and conforms to relation [27]:

$$\rho = u^\lambda \frac{\partial L}{\partial u^\lambda} - L.$$

Partial derivatives of Lagrangian give the canonical momenta

$$p_\lambda = \frac{\partial L}{\partial u^\lambda} = \frac{u_\lambda}{u^1 u_1} \tag{9}$$

and forces

$$F_\lambda = \frac{\partial L}{\partial x^\lambda} = \frac{1}{2u^1 u_1} \frac{\partial g_{ij}}{\partial x^\lambda} u^i u^j. \tag{10}$$

Components of the associated vector of the canonical momenta are

$$p^\lambda = \frac{u^\lambda}{u^1 u_1}. \tag{11}$$

Physical energy and momenta of photon with frequency ω in Minkowski space-time with affine parameter $\mu = ct$ form contravariant 4-vector of momenta $\pi^i = (\hbar\omega/c)u^i$. For arbitrary affine parameter it is rewritten as

$$\pi^i = \frac{\hbar\omega}{c} \frac{u^i}{u^1}. \tag{12}$$

And in pseudo-Riemannian space-time similar energy and momenta of the photon will be put in line with the components of the contravariant vector of momenta. A certain fixed value of the photon's frequency ω_0 is given by the corresponding equality $\omega = \omega_0/u_1$. Comparing expressions (11) and (12), we obtain

$$\pi^i = \frac{\hbar\omega_0}{c} p^i. \tag{13}$$

This one provides Lagrangian of the photon $L_{ph} = \hbar\omega_0 L$. The components of vector

$$F^{ik} = g^{kj} F_\lambda^i \tag{14}$$

associated to (10), with this approach, are proportional to gravity forces:

$$Q^i = \hbar\omega_0 F^i, \tag{15}$$

which acts on the photon. That is, although the non-straight motion of a particle in space-time according to General relativity is due to its curvature, identified with the gravitational field, we, studying the motion in the coordinate frame of reference, consider the analogy with the action of forces on the particle. That is, although the indirect motion of a particle in

space-time according to General relativity is due to its curvature, identified with the gravitational field, we, studying the motion in the coordinate frame of reference, consider the analogy with the action of forces on the particle.

Taking into account equation (8) a motion equations are found by using Hamilton's principle from variation of energy integral

$$S = \int_{\mu_0}^{\mu_1} L d\mu = - \int_{\mu_0}^{\mu_1} \rho d\mu,$$

where μ_0, μ_1 are values of the affine parameter in points, which are linked by found extremal curve. Energy ρ is non-zero, its variations leave interval to be light-like, and application of standard variational procedure yields Euler-Lagrange equations

$$\frac{d}{d\mu} \frac{\partial \rho}{\partial u^\lambda} - \frac{\partial \rho}{\partial x^\lambda} = 0. \tag{16}$$

The obtained equations of the isotropic critical curve can be rewritten as

$$\frac{dp_\lambda}{d\mu} - F_\lambda = 0. \tag{17}$$

4. ENERGY AND MOMENTUM OF PARTICLE TRANSFERRED TO GRAVITY FIELD

In accordance with conservation laws, the vector of energy and momentum of a system that includes a particle and the gravitational field generated by it, denoted by \bar{p}^k , can be written as the sum of the momentum and energy of the particle itself p^k and transmitted it to the gravitational field \bar{p}^k . The vector \bar{p}^k changes under the influence of the force from the source of gravity:

$$\frac{d\bar{p}^k}{d\mu} = \frac{dp^k}{d\mu} + \frac{d\bar{p}^k}{d\mu} = F^k.$$

Passing in equations (17) to the associated canonical momenta and forces, we obtain

$$F^k = \frac{dp^k}{d\mu} + g^{k\lambda} \frac{dg_{\lambda i}}{d\mu} p^i.$$

Comparing two expressions for F^k and passing to the partial derivatives of metrical coefficients we find the rate of exchange of energy and momentum between particle and gravitational field

$$\frac{d\bar{p}^k}{d\mu} = g^{k\lambda} \frac{\partial g_{\lambda i}}{\partial x^j} u^j p^i.$$

When considering the dynamics of a single particle, this vector is an analogue of the pseudotensor used in the laws of conservation in tensor form.

From the conservation laws it follows that the force acting on the system, including the particle and the gravitational field generated by it, is equal in magnitude and opposite in sign to the force acting on the system of the source of gravitation from the side of the particle system. This is equivalent to fulfilling Newton's third law. Its adherence to the Newtonian limit of gravity means the equality of the passive and active gravitational masses.

5. COMPARISON OF NULL GEODESICS, ENERGY INTEGRAL VARIATION AND FERMAT PRINCIPLES

Let us clear whether proposed variational method conforms to Fermat's principle, which for stationary gravity field [2] is formulated as follows

$$\delta \int \frac{1}{g_{11}} (dl + g_{1k} dx^k) = 0,$$

where dl is element of spatial distance along the ray

$$dl^2 = \left(\frac{g_{1p} g_{1q}}{g_{11}} - g_{pq} \right) dx^p dx^q.$$

Comparing the integrand

$$df = \frac{1}{g_{11}} (dl + g_{1k} dx^k) \tag{18}$$

with equation (5) we write

$$\frac{df}{d\mu} = \rho u^1. \tag{19}$$

Null geodesics and extreme energy integral curves for light-like particle are identical in static space-time [5, 11]. In [28] the generalized Fermat's principle is proposed and it is shown that obtained curves are null geodesics. It is applied Pontryagin's minimum principle of the optimal control theory and obtained an effective Hamiltonian for the light-like particle motion in a curved spacetime. The dynamical equations for this Hamiltonian are

$$Q = u^1$$

and

$$\frac{d}{d\mu} \left(\frac{\partial Q}{\partial \dot{x}^q} \right) - \frac{\partial Q}{\partial x^q} - \frac{\partial Q}{\partial x^1} \frac{\partial Q}{\partial \dot{x}^q} = 0. \tag{20}$$

Function Q coincides with following from (18) expression for $df/d\mu$ under condition that the metric coefficients also depend on time. Following from

(19) expression for energy $\rho = Q/u^1$ substituted in Euler-Lagrange equations (16) yields

$$\frac{1}{u^1} \frac{d}{d\mu} \left(\frac{\partial Q}{\partial u^q} \right) - \frac{1}{(u^1)^2} \frac{\partial Q}{\partial u^q} \frac{du^1}{d\mu} - \frac{1}{u^1} \frac{\partial Q}{\partial x^q} = 0. \quad (21)$$

The Euler-Lagrange equation for the time coordinate obtained from energy integral variation principle is reduced to the form

$$\frac{du^1}{d\mu} + \frac{u^1}{2u_1} \frac{\partial g_{ij}}{\partial x^1} u^i u^j = 0.$$

Comparing its with equations (7) we write

$$\frac{du^1}{d\mu} = (u^1)^2 \frac{\partial(Q/u^1)}{\partial x^1} = u^1 \frac{\partial Q}{\partial x^1}.$$

Substituting this expression in (21) and multiplying it by u^1 gives equations (20), which confirms the consistency of principle of an extremal energy integral of light-like particle and generalized Fermat's principle.

6. PHOTON'S DYNAMICS IN SCHWARZSCHILD SPACE-TIME

6.1. SPHERICAL COORDINATES

A centrally symmetric gravity field in the free space is described by the Schwarzschild metric. At spherical coordinates $x^i = (\tau, r, \theta, \varphi)$ with $\tau = ct$ its line element is

$$ds^2 = \left(1 - \frac{\alpha}{r}\right) d\tau^2 - \left(1 - \frac{\alpha}{r}\right)^{-1} dr^2 - r^2 (d\theta^2 + \sin^2\theta d\varphi^2), \quad (22)$$

where α is constant. To find the photon motion, we solve the Euler-Lagrange equations, which give for Lagrangian (8) a solution that is identical with the geodesics. In plane $\theta = \pi/2$ equations (17) with canonical momenta (9) and forces (10) yield [4, 5, 11]:

$$\frac{d\tau}{d\mu} = 1, \quad \frac{d\varphi}{d\mu} = \frac{B}{r^2} \left(1 - \frac{\alpha}{r}\right), \quad (23)$$

where B is constant. Substituting these values in equation $ds = 0$ we find

$$\frac{dr}{d\mu} = \pm \left[\left(1 - \frac{\alpha}{r}\right)^2 - \left(\frac{B}{r}\right)^2 \left(1 - \frac{\alpha}{r}\right)^3 \right]^{1/2}. \quad (24)$$

The value of the coordinate velocity in the remote frame is

$$v = \sqrt{\left(r \frac{d\varphi}{dt}\right)^2 + \left(\frac{dr}{dt}\right)^2} = c \left(1 - \frac{\alpha}{r}\right).$$

In 4D space-time for the Schwarzschild field the canonical momenta are

$$p_1 = 1, \quad p_2 = \mp \frac{1}{\left(1 - \frac{\alpha}{r}\right)} \sqrt{1 - \frac{B^2}{r^2} \left(1 - \frac{\alpha}{r}\right)}$$

$$p_3 = 0, \quad p_4 = -B.$$

Nonzero components of the contravariant vector of momenta are given by

$$p^1 = \left(1 - \frac{\alpha}{r}\right)^{-1},$$

$$p^2 = \pm \sqrt{1 - \frac{B^2}{r^2} \left(1 - \frac{\alpha}{r}\right)}, \quad p^4 = \frac{B}{r^2}.$$

The physical energy and momentum are matched exactly with the contravariant vector, since in the limit of the Minkovsky space it has momentum components with a sign coinciding with the direction of motion.

6.2. RECTANGULAR COORDINATES

Considering the non-radial motion, in order to avoid the appearance of a fictitious component of momenta and force due to the sphericity of the coordinate system we use the Schwarzschild metric in rectangular coordinates [4, 5, 11]. To the isotropic form of metric one can go from its spherical form (22) with the help of the transformation

$$r = \left(1 + \frac{\alpha}{4\bar{r}}\right)^2 \bar{r}, \quad (25)$$

and it is written as

$$ds^2 = c^2 \left(\frac{1 - \frac{\alpha}{4\bar{r}}}{1 + \frac{\alpha}{4\bar{r}}} \right)^2 dt^2 - \left(1 + \frac{\alpha}{4\bar{r}}\right)^4 (dx^2 + dy^2 + dz^2), \quad (26)$$

where (t, x, y, z) is rectangular frame and

$$\bar{r} = \sqrt{x^2 + y^2 + z^2}.$$

We will consider the motion in the plane $z = 0$ and seek the force acting on the particle at a point $(t,$

$x, 0, 0$) that corresponds to the value of the angular coordinate $\varphi = 0$ in the spherical frame. Coordinate transformations in the plane are

$$x = \bar{r}\cos\varphi, \quad y = \bar{r}\sin\varphi.$$

The nonzero spatial components of the 4-velocity are

$$\bar{u}^2 = \frac{dx}{d\mu} = \frac{d\bar{r}}{d\mu}, \quad \bar{u}^3 = \frac{dy}{d\mu} = \frac{d\varphi}{d\mu}\bar{r}.$$

The transformation (25) implies the relation

$$dr = \left(1 - \frac{\alpha^2}{16\bar{r}^2}\right) d\bar{r}. \tag{27}$$

Equations (24)-(25) yield

$$\bar{u}^1 = 1, \quad \bar{u}_1 = \left(\frac{1 - \frac{\alpha}{4\bar{r}}}{1 + \frac{\alpha}{4\bar{r}}} \right)^2, \tag{28}$$

$$\bar{u}^2 = \pm \frac{\left(1 - \frac{\alpha}{4\bar{r}}\right)}{\left(1 + \frac{\alpha}{4\bar{r}}\right)^3} \left[1 - \frac{B^2 \left(1 - \frac{\alpha}{4\bar{r}}\right)^2}{\bar{r}^2 \left(1 + \frac{\alpha}{4\bar{r}}\right)^6} \right]^{1/2}, \tag{29}$$

$$\bar{u}^3 = \frac{B \left(1 - \frac{\alpha}{4\bar{r}}\right)^2}{\bar{r} \left(1 + \frac{\alpha}{4\bar{r}}\right)^6}. \tag{30}$$

Substitution of these velocities in (11) gives components of associated vector of the canonical momenta

$$\bar{p}^1 = \left(\frac{1 + \frac{\alpha}{4\bar{r}}}{1 - \frac{\alpha}{4\bar{r}}} \right)^2,$$

$$\bar{p}^2 = \pm \frac{1}{\left(1 - \frac{\alpha}{16\bar{r}^2}\right)} \left[1 - \frac{B^2 \left(1 - \frac{\alpha}{4\bar{r}}\right)^2}{\bar{r}^2 \left(1 + \frac{\alpha}{4\bar{r}}\right)^6} \right]^{1/2},$$

$$\bar{p}^3 = \frac{B}{\bar{r} \left(1 + \frac{\alpha}{4\bar{r}}\right)^4}.$$

Passing back from the variable \bar{r} to r , we write, in accordance with equation (13), the value of

the photon energy and momentum in a remote coordinate frame

$$E = \hbar\omega_0 \left(1 - \frac{\alpha}{r}\right)^{-1},$$

$$\bar{P} = [(\bar{p}^2)^2 + (\bar{p}^3)^2]^{1/2} = \frac{1}{\left(1 - \frac{\alpha}{16\bar{r}^2}\right)} \frac{\hbar\omega_0}{c},$$

where ω_0 is the photon frequency at infinity at the world line with unlimited r . Moving to the scale of the length of spherical frame in view of equation (27) we obtain $P = \hbar\omega_0/c$.

Using the analogy of geometrical optics with gravity [6-8, 28] the refraction index (4) is given by

$$n = \left(1 - \frac{\alpha}{r}\right)^{-1}.$$

Turning to ESM we write four-momentum after rotation in the plane (TS) in space $G(1,4)$ (3):

$$\left(\frac{E}{c}, P, p_s \right) = \left(\frac{\hbar\omega}{c \left(1 - \frac{\alpha}{r}\right)}, \frac{\hbar\omega}{c}, \frac{\hbar\omega [\alpha(2r - \alpha)]^{1/2}}{c(r - \alpha)} \right).$$

We obtain the coincidence of the energy and momentum in the embedded four-dimensional space-time in ESM with the result given by variational principle of the stationary energy integral of photon in the Schwarzschild field.

6.3. FORCES AND GRAVITY MASS OF PHOTON

At spherical coordinates the non-zero components of canonical forces vector (10) and associate vector F^k (14) are

$$F_2 = \frac{\alpha}{r^2 \left(1 - \frac{\alpha}{r}\right)} - \frac{B^2}{r^3} + \frac{\alpha B^2}{2r^4},$$

$$F^2 = -\frac{\alpha}{r^2} + \frac{B^2}{r^3} \left(1 - \frac{\alpha}{r}\right) \left(1 - \frac{\alpha}{2r}\right). \tag{31}$$

For a gravitational constant G , active gravitational mass M and $\alpha = 2GM$ the first term of F^2 yields (15) for the radial motion ($B = 0$) twice Newton gravity force acting on a photon

$$Q^2 = -\hbar\omega_0 \frac{\alpha}{r^2}.$$

It corresponds to the passive gravitational mass of the photon

$$m_{gp} = 2\hbar\omega_0 \quad (32)$$

Considering the non-radial motion we use the Schwarzschild metric in rectangular coordinates (26). Substituting nonzero 4-velocity components (28)-(30) in (10), we find nonzero component of the force vector (15) acting on the photon:

$$\bar{Q}^2 = -\hbar\omega_0 \frac{\alpha \left(1 - \frac{\alpha}{8\bar{r}}\right)}{\bar{r}^2 \left(1 + \frac{\alpha}{4\bar{r}}\right)^5 \left(1 - \frac{\alpha}{4\bar{r}}\right)}.$$

Taking into account transformation (25) it is rewritten as

$$\bar{Q}^2 = -\hbar\omega_0 \frac{\alpha \left(1 - \frac{\alpha}{8\bar{r}}\right)}{r^2 \left(1 - \frac{\alpha^2}{16\bar{r}^2}\right)}.$$

Its magnitude does not depend on the direction of motion of the photon. This formula differs from force in spherical coordinates (31) because the expression for the canonical force (10) is non-covariant, that is, with this approach gravity force acting on the photon depends on the choice of the coordinate system. However, in the limit of weak gravity these expressions asymptotically converge and give Newton's law of gravitation with passive gravitational mass of the photon $2\hbar\omega_0$ (32). One conforms to the light deflection in central gravity field, which is twice value being given by the Newton gravity theory.

Obtained gravitational mass of the light-like particle is independent on the direction of its motion. The gravitational mass of a photon for low gravity is equal to doubled mass of a material particle, equivalent to its energy. This corresponds to the result of Tolman [30] for active gravity mass of photon. He applied solutions of Einstein's equation for the electromagnetic field in the case of weak gravity to analyze the gravitational interaction of a light packet or beam with a material particle.

This result can have the following application. At annihilation of an electron and positron the energy determined from non-gravitational interactions and the momentum are preserved. We will consider how the gravitational mass of system changes. Although it is not known exactly whether the gravitational mass of the positron is positive or negative, some estimates give its positive value [31]. Proceeding

from this assumption the total gravitational mass of an electron and positron $2m_e$ is twice less than the gravitational mass of the formed gamma quanta $4m_e$. This raises the question of mass conservation [32]. If to consider energy as a gravitation source, it means that on condition of its preservation at annihilation besides gamma quanta this process has to be allocated the particles g^- which are carrying away negative energy as a source of gravitational field, that is, having negative gravitational mass. Process of annihilation will look as follows

$$e^+ + e^- \rightarrow 2\gamma + 2g^-. \quad (33)$$

The particles g^- with gravitational mass

$m_{g^-} = m_e$ do not have a kinetic momentum and therefore their detection by standard means of particle registration, for example, a bubble chamber, is not possible. With the passage of light beams through the area with negative energy needs to produce the effect of defocusing, opposites focusing of light by the gravitational lens [33].

7. GRAVASTAR STRUCTURE

The gravastar model was offered [21, 22] alternatively to black holes. It is considered as final object, which is formed in because of processes of elementary particles disintegrations. This is static spherically symmetrical field with the metric

$$ds^2 = -f(r)dt^2 + \frac{dr^2}{h(r)} + r^2(d\theta + \sin^2\theta d\varphi^2). \quad (34)$$

In the case of an isotropic medium and a constant density ϵ in the inner region of gravastars the solution of Einstein's equations yields a density $\epsilon^2\epsilon = -p$. This corresponds to the de Sitter metric with coefficients

$$f(r) = Ch(r) = C \left(1 - \frac{r^2}{R_D^2}\right). \quad (35)$$

Here R_D is the radius of a curvature of the de Sitter world and C is arbitrary constant. Radius of a curvature is within the limits corresponding to the shell of gravastar $r_1 < R_D < r_2$ and is $R_D = \sqrt{(r_1)^3 / \alpha}$, where α is a radius of Black Hole with equal mass.

For the spherically symmetric static gravastar-like object with negative central pressure it is found [33] that shell cannot be perfect fluids. Anisotropic pressures in the "crust" are unavoidable. The

anisotropic Tolman-Oppenheimer-Volkoff equation can be used to find them [34]. Existence of rotating gravastars cannot be ruled out by invoking its instability [35]. LIGO's observations of gravitational waves from colliding objects have been found either to not be consistent with the gravastar concept [36, 37], but it does not deny the existence of gravastar in principle.

Accretion of matter onto compact stars causes gamma radiation [38] and creates conditions for the birth of gamma-ray electron-positron pair. This reaction, the inverse of (33), occurs when extracting pairs of particles g^- and opposite to them in "a gravitational charge" particle g^+ from a vacuum. Having negative gravitational mass, particle g^- is absorbed immediately leaving g^+ with a positive gravitational mass:

$$2\gamma \rightarrow e^+ + e^- + 2g^+ .$$

The subsequent collision of a positron with an electron will cause annihilation with the release of a pair of g^- . Gravastar and Black Hole will attract particles g^+ . On g^- the compact stars act like White Hole on particles with positive energy. They push these particles into free deep space. This process results in the compact stars's absorption of positive energy from the vacuum compact star and the release negative energy around. In this sense, it is reversed by Hawking radiation, which leads to the evaporation of Black Holes. The particles g^- initiate the dynamics of cosmological expansion controlled by antigravity [40]. The particles g^+ can form a halo of compact stars. Their ability to be part of dark matter depends on whether they have a rest mass. If it is absent, they will dissipate faster in the outer space.

8. ENERGY DENSITY IN SPHERICAL GRAVITATIONAL SYSTEMS

The gravitational mass of a spherical body[2] described by metric (35) with radius r_1 is given by

$$M = 4\pi \int_0^{r_1} \varepsilon r^2 dr, \tag{36}$$

where ε is proper density of matter. Integration is performed here in case of the element of volume $dV_\varepsilon = 4\pi r^2 dr$, which corresponds to the coordinate frame, whereas in its proper frame the given element of space volume will be $dV_p = 4\pi r^2 b^{(-1)}(r) dr$. Condition $b(r) < 1$ means that the gravitational mass of body is less than the sum of individual gravitational masses

its constituent elements. This interprets as the transfer of energy, as a source of gravitational field, to the vacuum.[5] The whole mass of spherical body is defined as follows:

$$M_p = 4\pi \int_0^{r_1} \varepsilon r^2 h^{-1}(r) dr, \tag{37}$$

In terms of ESM in static case the energy-momentum vector \bar{p} with total density of matter $\varepsilon_p = \varepsilon b^{(-1)}(r)$ can be represented as 5-vector

$$\bar{p}_{mi} = (c\varepsilon h^{-1}(r), 0, c\varepsilon h^{-1}(r)).$$

Its hyperbolic rotation in the plane (TS) (2) on an angle $\phi_{TS} = \ln(b(r))$ yields

$$\bar{p}_{mg} = (c\varepsilon, 0, c\varepsilon).$$

This rotation corresponds transition from the total density of matter to the density as a source of gravity.

Considering the mass of the gravastar we assume for simplicity that all of it is concentrated in interior area. The solution of Einstein equations for metric (34) with coefficients (35) gives [21, 22] the density of matter $\varepsilon = (3c^2 / 8\pi G) H_0^2$, where it is denoted $H_0 = 1/R_D$. Substitution of ε in (36) yields gravitational mass

$$M = \frac{c^2}{2G} H_0^2 r_1^3 . \tag{38}$$

The whole mass (37) turn out to be

$$M_p = \frac{3c^2}{2G} \left(-r_1 + \frac{1}{2H_0} \ln \frac{1+H_0 r_1}{1-H_0 r_1} \right).$$

A particular point of interest for applications to microphysical objects is a possibility of situation when M_p exceeds gravitational mass twice: $M_p = 2M$. For the bubble structures it will take place subject to $H_0 r_1 = 0.998147$. With this condition a particle with the mass of an electron $m_e = 9.1093835 \cdot 10^{-31}$ kg according to equation (38) will have a radius $r_e = 1.3579 \cdot 10^{-57}$ m. This value is less than Planck length by 22 orders of magnitude. It does not include spin, magnetic moment and charge, but this result may be used to estimate the order of the electron radius via gravastar model.

Observation of a single electron in a Penning trap [41] suggests the upper limit of the particle's radius to be 10^{-22} m.

9. CONCLUSIONS

Canonical 4-momentum is given by variational principle of the stationary energy integral of photon. The physical energy and momentum of photon are matched exactly with the contravariant 4-momentum, since in the limit of the Minkovsky space it has momentum components with a sign conforms to the direction of motion. For the Schwarzschild space-time the result coincides with energy and momentum in the embedded four-dimensional space-time obtained by (TS) -turn in ESM that is corresponded to the photon's motion in space with refraction index $n > 1$. One provides localization of the photon and can be considered as the acquisition of rest mass by it.

The identity of the generalized Fermat principles and the stationary energy integral of a light-like particle for velocities is proved. The virtual displacements of coordinates retain path of the light-like particle to be null in the pseudo-Riemann space-time, i.e. not lead to the Lorentz-invariance violation in locality and corresponds to the variational principles of mechanics. The equivalence of the solutions given by the first principle, to the geodesics, means that the use of the second also turns out geodesics. The stationary energy integral principle gives a system of equations that has one equation more. This makes it possible to uniquely determine the affine parameter and energy-momentum vector of the particle.

A definite Lagrangian produces particle canonical momenta and forces acting on it in the coordinate frame. Contravariant forces are mapped to the components of the vector of the gravitational force. The four-force vector is not covariant. The value of the force acting on a particle depends on the choice of the coordinate frame, and therefore the quantities determined through them are meaningful only for weak gravity, for which its values asymptotically converge in the different coordinate frames. The analogy between the mechanics of particle motion in the Schwarzschild space and Newton's gravity theory under this condition allows to determine passive gravitational mass of the photon, which is equal to twice the mass of a material particles of the same energy determined from non-gravitational interactions. This corresponds to the result of Tolman for active gravity mass of photon. This discrepancy suggests that at annihilation of an electron and positron in addition to gamma quanta

the particles are released that have zero kinetic energy and momentum and carrying away negative energy as a source of gravitational field, that is, they have negative gravitational mass.

These particles, together with similar particles with positive energy, can be generated by accretion of matter onto compact stars. As a result, positive energy is absorbed and negative energy is released in free space. Areas containing g^- are characterized by negative pressure and exhibits properties of antigravitation. The presence of such regions in the Universe causes its accelerated expansion. The ability of particles g^+ to be part of dark matter depends on whether they can be at rest.

The (TS) -rotation of energy-momentum 5-vector of matter density describes gravitational defect of static mass. It is shown, that gravastar model can be used to describe the properties of the microworld, giving an estimate of the electron radius.

REFERENCES

1. Sivuhin DV. *Optika* [Optics]. Moscow, Fizmatlit Publ., 2005, 792 p.
2. Landau LD, Lifshitz EM. *The Classical theory of Fields*. Oxford, Butterworth-Heinemann, 1975, 402 p.
3. Perlick V. Gravitational lensing from a spacetime perspective. *Living Rev. Relativity*, 2004, 7:9.
4. Belayev WB. Application of Lagrange mechanics for analysis of the light-like particle motion in pseudo-Riemann space. arXiv:0911.0614 [gr-qc].
5. Belayev WB. *Dinamika v obschei teorii otnositel'nosti: variacionn'ie metod'i* [The dynamics in general relativity theory: variational methods]. Moscow, URSS Publ., 2017, 216 p.
6. Tsipenyuk DYu, Andreev VA. Structure of extended space. *Bulletin of the Lebedev Physics Institute*, 2000, 6:23-34.
7. Tsipenyuk DYu, Andreev VA. Marriage of electromagnetism and gravity in an extended space model and astrophysical phenomena. Amoroso RL, Kauffman LH, Rowlands P (eds.) *Proc. 8th Vigier symposium "The physics of reality"*. Singapore, World Scientific, 2013:171-182.
8. Andreev VA, Tsipenyuk DYu. Problema vvedeniya konechnogo razmera i peremennoy massy fotona [The problem of introducing finite size and variable mass of the photon]. *Inzhenernaya fizika*, 2017, 5:17-28 (in Russ.).

9. Rumer YuB. *Issledovaniya po pyatimernoy optike* [Studies on five-dimensional optics]. Moscow, URSS Publ., 2010, 152 p.
10. Tsipenyuk DYu, Andreev VA. Electromagnetic and gravitational fields in the 5-dimensional extended space model, their localization and interaction with matter. *RENSIT*, 2019, 11(2):93-102; doi: 10.17725/rensit.2019.11.093.
11. Tsipenyuk DYu, Belayev WB. Extended space model is consistent with the photon dynamics in the gravitational field. *J. Phys.: Conf. Ser.*, 2019, 1251:012048.
12. Chernin AD. Dark energy in the nearby Universe: HST data, nonlinear theory, and computer simulations. *Phys. Usp.*, 2013, 56:704-709.
13. Ellis J. Dark matter and dark energy: summary and future directions. *Phil. Trans. Roy. Soc. Lond. A*, 2003, 361:2607.
14. Akrami Y, Kallosh R, Linde A, Vardanyan V. Dark energy, α -attractors, and large-scale structure surveys. *JCAP*, 2018, 1806:041.
15. Karachentsev ID, Telikova KN. Stellar and dark matter density in the Local Universe. *Astronomical notes*, 2018, 339:615.
16. Shafieloo A, L'Huillier B, Starobinsky AA. Falsifying Λ CDM: Model-independent tests of the concordance model with eBOSS DR14Q and Pantheon. *Phys. Rev. D*, 2018, 98:083526.
17. Alam U, Sahni V, Saini TD, Starobinsky AA. Is there supernova evidence for dark energy metamorphosis? *Mon. Not. Roy. Astron. Soc.*, 2004, 354:275.
18. Bondi H. Negative mass in general relativity. *Rev. Mod. Phys.*, 1957, 29:423-428.
19. Rivlin LA. Stopped light: Towards plane-wave-free electrodynamics. *Quantum Electronics*, 2003, 33:777-797.
20. Firstenberg O, Peyronel T, Liang Q-Y, Gorshkov AV, Lukin MD, Vuletić V. Attractive photons in a quantum nonlinear medium. *Nature*, 2013, 502:71-75.
21. Mazur PO, Mottola E. Gravitational vacuum condensate stars. *PNAS*, 2004, 101:9545.
22. Mazur PO, Mottola E. Cosmological dark energy: prospects for a dynamical theory. *Class. Quantum Grav.*, 2015, 32:215024.
23. Berezhin VA, Kuzmin VA, Tkachev II. Dynamics of bubbles in general relativity. *Phys. Rev. D*, 1987, 36:2919.
24. Pannia FAT, Bergliaffa SEP. Evolution of vacuum bubbles embedded in inhomogeneous spacetimes. *JCAP*, 201703:026.
25. Burinskii A. Superconducting source of the Kerr-Newman electron. Efremov AV, Goloskokov SV (eds.) *Proc. of the XIII Adv. Res. Workshop on HEP*, Dubna, 2010:439-442.
26. Fan X-H, Yong G-C, Zuo W. Probing nuclear bubble configurations by proton-induced reactions. *Phys. Rev. C*, 2019, 99:041601(R).
27. Landau LD, Lifshitz EM. *Mechanics*. Oxford, Butterworth-Heinemann, 1982, 224 p.
28. Frolov VP. Generalized Fermat's principle and action for light rays in a curved spacetime. *Phys. Rev. D*, 201388:064039.
29. Okun LB. Photons and static gravity. *Mod. Phys. Lett. A*, 2000,15:1941.
30. Tolman RC. *Relativity Thermodynamics and Cosmology*. New York, Dover Publications, 2011, 528 p.
31. Kalaydzhyan T. Gravitational mass of positron from LEP synchrotron losses. *Sci. Rep.*, 2016, 6:30461.
32. Tsipenyuk DYu. Neizotropnye ob'ekty v rasshirennom prostranstve [Non-isotropic objects in extended space]. *Inzhenernaya fizika*, 2017, 6:20-28 (in Russ.).
33. Tsipenyuk DYu, Andreev VA. Obolocheynye ob'ekty v modeli rasshirennogo prostranstva i mekhanizm obrazovaniya temnoj materii [Shell objects in the model of extended space and the mechanism of formation of dark matter]. *Kratkie Soobshcheniya po Fizike FLAN*, 2004, 9:13-25 (in Russ.).
34. Visser M, Wiltshire DL. Stable gravastars - an alternative to black holes? *Class. Quant. Grav.*, 2004, 21:1135.
35. Cattoen C, Faber T, Visser M. Gravastars must have anisotropic pressures. *Class. Quant. Grav.*, 2005, 22:4189.
36. Chirenti C, Rezzolla L. On the ergoregion instability in rotating gravastars. *Phys. Rev. D*, 2008, 78:084011.
37. Chirenti C, Rezzolla L. Did GW150914 produce a rotating gravastar? *Phys. Rev. D*, 2016, 94:084016.
38. Cardoso V, Franzin E, Pani P. Is the gravitational-wave ringdown a probe of the event horizon? *Phys. Rev. Lett.*, 2016, 116:171101.

39. Bednarek W. Gamma-rays from the vicinity of accreting neutron stars inside compact high-mass X-ray binaries. *Astronomy and Astrophysics*, 2009, 495(3):919-929.
40. Tsipenyuk DYu, Andreev VA. Dark matter and condensed bubble object formation in the 5d extended space model. *Gravitat. Cosmol.*, 2006, 12 (2-3):235-238.
41. Dehmelt HA. Single atomic particle forever floating at rest in free space: new value for electron radius. *Phys. Scr.*, 1988, 22:102-110.

DOI: 10.17725/rensit.2019.11.261

Resonant interference exchange interaction

Gennady V. Mishinsky

Joint Institute for Nuclear Research, <http://www.jinr.ru/>

Dubna 141980, Moscow Region, Russian Federation

E-mail: mish@jinr.ru

Received 20.11.2019, peer reviewed 29.11.2019, accepted 03.12.2019

Abstract. The exchange interaction is manifested not only between identical particles but also between any identical objects or systems. The exchange interaction is responsible for the pairing of atomic electrons in the orthoboson $S=1$ with the formation of a Bose-Einstein condensate in a strong magnetic field. Resonant interference exchange interaction occurs between an object and a system that has resonant R-states with this object. The RIEEX-interaction explains the possibility of carrying out reactions of cold fusion and reactions of low-energy transmutation of chemical elements. The RIEEX-interaction is also realized between systems with excited identical resonant R-states. Since the resonant interaction between objects is, in fact, a RIEEX-interaction, it is based on all fundamental interactions.

Keywords: exchange interaction, resonant interaction, quantum physics, general physics, atomic physics, nuclear physics, cold fusion, nuclear molecules, trans molecules, low-energy nuclear reactions

PACS: 03.75.Mn; 03.75.Nt; 25.60.Pj; 26.20.Cd; 26.65.+t; 32.10.-f; 36.10.-k

For citation: Gennady V. Mishinsky. Resonant interference exchange interaction. *RENSIT*, 2019, 11(3):261-278; DOI: 10.17725/rensit.2019.11.261.

CONTENTS

1. INTRODUCTION (261)
2. EXCHANGE INTERACTION (262)
 - 2.1. HELIUM ATOM (262)
 - 2.2. ATOMS WITH PAIRED ELECTRONS - TRANSATOMS (264)
 - 2.3. TRANSMUTATION REACTIONS AT PROTONS (265)
3. RESONANT EXCHANGE INTERACTION (267)
 - 3.1. RADIATIVE CAPTURE OF NEUTRON (267)
 - 3.2. COLD FUSION (270)
 - 3.3. NUCLEAR MOLECULES (271)
4. RESONANT INTERFERENCE EXCHANGE INTERACTION (274)
 - 4.1. TWO-SLIT INTERFERENCE (274)
 - 4.2. TRANSNUCLEUS, NUCLEAR TRANSMOLECULES AND TRANSMUTATION REACTIONS (275)
5. CONCLUSION (276)
- REFERENCES (276)

1. INTRODUCTION

At present, there are four fundamental interactions known in natural sciences: strong (F), electromagnetic (EM), weak (W) and gravitational (G). Shipov G. in his theory of physical vacuum [1] introduced such notion as “inertia field” (I). The inertia field is associated with the rotational degrees of freedom of material objects. The energy of such inertia field produces torsion of the space around the material object similar to that when the gravitational mass of the material object generates curvature of space. Thus, the gravitational interaction G has been enlarged up to the inertial gravitational interaction IG .

In quantum physics, one more interaction, a fifth one, is manifested during an interaction between identical particles. This interaction is called the exchange interaction [2]. The exchange interaction is connected with the indistinguishability of identical particles. The identity principle says: it is impossible to distinguish identical particles experimentally. So,

if two identical particles are replaced, each with the other, like $\psi_a(1)\psi_b(2) \rightarrow \psi_a(2)\psi_b(1)$, then the result of interaction between them will not change. The result of interaction or the eigenvalues that comply with it will not change if the wave function of the particles is presented as a superposition of wave functions of two states: the eigenstate $\psi_a(1)\psi_b(2)$ and identical state $\psi_b(1)\psi_a(2)$: $\psi^\pm(1,2) = \psi_a(1)\psi_b(2) \pm \psi_a(2)\psi_b(1)$.

In paper [3], the exchange interaction is modernized up to resonant interference exchange interaction. The RIEEX interaction is the exchange interaction between any objects, A and B, which have resonant R-states belonging to a compound system consisting of the objects A and B. Resonant R-states are in a certain approximation identical to the objects A and B.

The nature of resonant interference exchange interaction is associated with the overlapping and interference of the wave functions of identical objects having resonant R-states. The exchange interaction makes an additional contribution into the total energy of the interacting particle-states for all of the fundamental interactions: F , EM , W and IG . This contribution is connected with that the total energy of interaction between the identical objects or objects with the R-states contains an exchange interference member which is not equal to zero due to their identity. With this, the greater is the overlapping of the wave functions of the identical objects or objects with R-states, the greater is the exchange energy.

In this article, the region where resonant interference exchange interaction takes place is considered using a few examples from atomic and nuclear physics.

2. EXCHANGE INTERACTION

2.1. HELIUM ATOM

Let us consider the wave function of two identical fermions 1 and 2 with the spin $s = 1/2$ [4]. The total wave function of two particles is usually represented as the product of the spin wave function of the particles $\{S(1)S(2)\}$ and the wave function of their spatial motion $[\psi_1^V \psi_2^V]$. The

spin wave function of the particle can assume two values: with positive spin projection over the preferential direction S^+ and with negative spin projection over the preferential direction S^- . The spin function of two fermions can be represented as the product of spin functions of separate fermions or a combination of their products. It can be symmetric or antisymmetric. Symmetric spin wave functions describe the triplet state of two fermions with parallel spins ($S = 1, m_s = +1, 0, -1$), while antisymmetric spin wave functions describe the singlet state with antiparallel spins ($S = 0$).

The wave function of the spatial motion of two fermions must satisfy the same requirements as the spin function of two fermions. It can be either symmetric $\psi^+(1,2)$ or antisymmetric $\psi^-(1,2)$:

$$\psi^+(1,2) = [\psi_a(1)\psi_b(2) + \psi_a(2)\psi_b(1)], \quad (1a)$$

$$\psi^-(1,2) = [\psi_a(1)\psi_b(2) - \psi_a(2)\psi_b(1)]. \quad (1b)$$

Since the total wave function of two fermions must be an antisymmetric function, only the following combinations can be considered acceptable:

$$[\psi_a(1)\psi_b(2) + \psi_a(2)\psi_b(1)] \times \{S^+(1)S^-(2) - S^+(2)S^-(1)\}, \quad (2)$$

$$[\psi_a(1)\psi_b(2) - \psi_a(2)\psi_b(1)] \{S^+(1)S^+(2)\}, \quad (3a)$$

$$[\psi_a(1)\psi_b(2) - \psi_a(2)\psi_b(1)] \{S^-(1)S^-(2)\}, \quad (3b)$$

$$[\psi_a(1)\psi_b(2) - \psi_a(2)\psi_b(1)] \times \{S^+(1)S^-(2) + S^+(2)S^-(1)\}. \quad (3c)$$

The wave functions of two fermions ψ_a and ψ_b are written without account of interaction between them and satisfy the eigen-functions of the energies E_a and E_b . In this case, the energy of the system is: $E = E_a + E_b$. In calculations, the energy of interacting particles is quite often defined with the help of the perturbation theory. All of the fundamental interactions (F , EM , W and IG) are always simultaneously in the perturbing potential of the interacting identical particles or other "identical objects". The first

correction to the energy of the system in the perturbation theory is calculated as follows:

$$\Delta E^{(1)} = \frac{\int \psi^*(1,2)[F, EM, W, G]\psi(1,2)dV_1dV_2}{\int \psi^*(1,2)\psi(1,2)dV_1dV_2}, \quad (4)$$

where $\psi(1,2)$ is the corresponding wave functions (2) and (3), $dV_1 = dx_1dy_1dz_1$, $dV_2 = dx_2dy_2dz_2$. The integral in the denominator is normalizing.

Let us consider the interaction between the electrons in a helium atom [4] and between protons in a transhelium molecule. In a helium atom the energy of perturbation between the electrons is defined by the Coulomb interaction potential:

$$V = k \cdot e^2 / r_{12}, \quad (5)$$

where r_{12} is the distance between the electrons, $k = 1/4\pi\epsilon_0 = 8.99 \cdot 10^9 \text{ H} \cdot \text{M}^2/\text{C}^2$ ($\epsilon_0 = 8.85 \cdot 10^{-12} \text{ F/m}$ is the electric constant), $e = 1.6022 \cdot 10^{-19} \text{ C}$ is the electron charge.

Since the perturbation energy V (5) does not depend on the spin variables, there arise identical multipliers, when averaging over such variables in the numerator and denominator (4), and these multipliers then diminish. As a result, $\psi(1,2)$ corresponds to the parts of wave functions (2 and 3), which depend only on the coordinates. Consequently:

$$\begin{aligned} \psi^*(1,2)\psi(1,2) &= \psi_a^*(1)\psi_b^*(2)\psi_a(1)\psi_b(2) + \\ &+ \psi_a^*(2)\psi_b^*(1)\psi_a(2)\psi_b(1) \pm \\ &\pm [\psi_a^*(1)\psi_b^*(2)\psi_a(2)\psi_b(1) + \psi_a(1)\psi_b(2)\psi_a^*(2)\psi_b^*(1)]. \end{aligned} \quad (6)$$

The integrals from the first two members (6) are equal to each other. In the denominator (4), they are equal since the interaction of the electrons is symmetric relative to their coordinates. Now we shall introduce the designations C and A :

$$C = \int |\psi_a(1)|^2 [k \cdot e^2 / r_{12}] |\psi_b(2)|^2 dV_1dV_2. \quad (7)$$

The integral C is responsible for the usual average Coulomb energy of repulsion between the electron clouds. The integral A (8) from the members in the square brackets (6) is the exchange integral arising due to the identity of the electrons. Such energy is called the exchange energy.

$$A = \frac{1}{2} \int [\psi_a^*(1)\psi_b^*(2)\psi_a(2)\psi_b(1) + \psi_a(1)\psi_b(2)\psi_a^*(2)\psi_b^*(1)] \times [k \cdot e^2 / r_{12}] dV_1dV_2. \quad (8)$$

Thus, correction to energy (4) can be presented as:

$$\Delta E^{(1)} = C \pm A, \quad a \neq b, \quad (9a)$$

$$\Delta E^{(1)} = C \pm A, \quad a = b, \quad (9b)$$

C and A have positive values [4]. The positive signs in (9a,b) refer to the singlet state when the electron spins are contrary to each other ($S = 0$), and the wave function of their spatial motion is symmetric: the state $E_a + E_b + C + A$ and $2E_a + C + A$ (Fig. 1). Thus, such states form the electron levels of parahelium. The ground state of parahelium $2E_a + C + A$, 1^1S_0 has the energy of 79.0 eV, while the first excitation of the parahelium state $E_a + E_b + C + A$, 2^1S_0 amounts to 58.4 eV. The energy $2E_a = 108.8 \text{ eV}$ is the doubled energy of ionization of He^+ ion. In the ground state of parahelium the electrons are in the identical state: $a = b$. Therefore, integrals (7) and (8) are equal to each other: $C = A = 15 \text{ eV}$.

The minus sign in (9a) refers to the triplet state when the electron spins are parallel ($S = 1$, $m_s = -1, 0, +1$), while the wave function of their spatial motion is antisymmetric: the state $E_a + E_b + C - A$ (Fig. 1). The ground state of orthohelium $E_a + E_b + C - A$, 2^3S_1 has an energy of 59.2 eV. In orthohelium the exchange interaction attracts the electrons to each other. Orthohelium also has a unique peculiarity: since the spins and magnetic moments of the electrons μ_e in orthohelium are parallel, the orthohelium produces a strong, directional, inhomogeneous

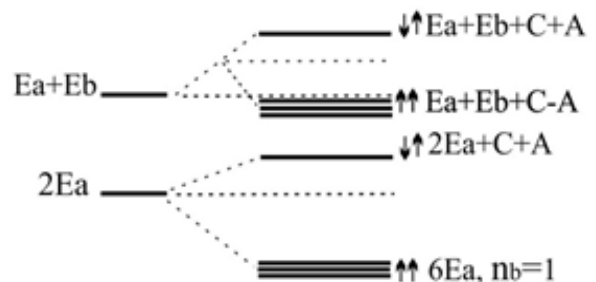


Fig. 1. Scheme of energy levels of helium atom [4] and transhelium under consideration of electron interaction.

and anisotropic magnetic field. At the centre of the orthohelium, magnetic field right at the nucleus is estimated as being $\sim 400 T$, while it is $\sim 70 T$ along its radius $8.76 \cdot 10^{-11} m$. The magnetic field is calculated according to formula [5]:

$$\mathbf{B}_s = \mu_0 \sum_i \frac{3\mathbf{n}_i(\boldsymbol{\mu}_e \cdot \mathbf{n}_i) - \boldsymbol{\mu}_e}{r_i^3},$$

where $\mu_0 = 1.26 \cdot 10^{-6} H/m$ is the magnetic constant; $\mu_e = 9.29 \cdot 10^{-24} J/T = 5.79 \cdot 10^{-5} eV/T$; r is the distance from the electron to the point where the field \mathbf{B}_s is calculated; \mathbf{n} is the unit vector in the direction r ; i is the number of electrons having parallel spins.

If there were an antisymmetric coordinate state with $a = b$ and $S = 1$, then $C = A$, and the exchange energy would compensate fully the energy of Coulomb repulsion: $\Delta E^{(1)} = 0$, the minus sign in (9b). In papers [6, 7], the following is considered: the possibility of existence of atoms with paired electrons which form the Bose-Einstein condensate, including the possibility of existence of transhelium.

2.2. ATOMS WITH PAIRED ELECTRONS - TRANSATOMS

The atoms which have electrons, not necessarily all, in paired state, are called “transatoms”. These states arise in a strong magnetic field of more than $30 T$. In a strong magnetic field, the atoms are inevitably transformed into transatoms! [6] In such a magnetic field the electrons are paired into the orthoboson $S = 1$. The motion of two electrons in orthobosons are rigidly correlated, while the electron spins are parallel to each other, $S = 1$, and both electrons are in one energy state: $a = b$ and $E_a(1) = E_a(2)$.

In paper [6], it is shown that in a strong magnetic field the electrons with parallel spins are paired due to:

- firstly, to the exchange interaction between the electrons, which is of attraction nature; and,
- secondly, due to the arising of electron oscillation around their orbitals (**Fig. 2a**).

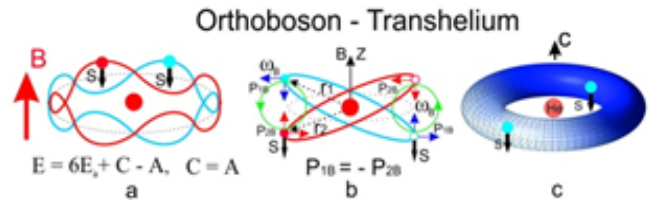


Fig. 2. a - electron oscillations; b – electron oscillations in the longitudinal and in the transverse magnetic field B directions; c – orthoboson - transhelium.

Owing to such oscillations of the electron, a new, additional degree of freedom arises [8], which produces a new quantum number, n_b . Then, correlated oscillations arise as a result of the exchange interaction between two electrons. The quantum number of oscillations of the paired electrons are equal to each other by the module; however, they are contrary in their sign: $n_b^1 = -n_b^2$, $n_b = 1, 2, 3 \dots$. Therefore, the Pauli principle is fulfilled for them.

The frequency of oscillations ω_B is connected with the frequency of rotation of the electron at the orbital $\omega_0 = E_0/\hbar$ and the frequency of precession of its orbital moment ω_ℓ by the following ratio [9, 10]: $\omega_B = n_b \sqrt{\omega_0^2 + \omega_\ell^2}$. The energy of oscillation $E_B = \hbar\omega_B$. The oscillations of the electrons are performed both in the longitudinal and transverse direction relative to the propagation of the magnetic field \mathbf{B} (Fig. 2b). Since the electrons in a pair oscillate in the contra-phase $n_b^1 = -n_b^2$, such motion allows two electrons in identical energy states to be found in non-overlapping spatial regions. The trajectories of motion of the electrons can be represented as closed interleaved helices located at the surface of a toroid [7] (Fig. 2c). Two electron helices resemble the double helix of a DNA molecule. The trajectories of several orthobosons in a multielectron transatom make an interleaved helical twist. This twist is a toroidal spin electron and magnetic twist, let's call it “torsem twist” or “torsem condensate”. So, a quantum paradox arise: “the wave functions of the electrons overlap maximally, and the spatial regions of their motion do not overlap”.

Since in the orthoboson and transhelium the wave function of the spatial motion of the

electrons is antisymmetric ($n_b^1 = -n_b^2$), then $\Delta E^{(1)} = C - A$. Also, because $a = b$, then $C = A$ and $\Delta E^{(1)} = 0$. The exchange Coulomb attraction suppresses the Coulomb repulsion. So, one more quantum paradox arises: “waves extinguish the wind”. For $n_b = 1$ the energy of paired electrons in the helium transatom is: $6E_a = 3 \cdot 108.8 = 326.4$ eV or 163.2 eV for each electron [7] (Fig. 1). The radius of transhelium is less by three times in comparison with the state $2E_a = 108.8$ eV: $R_{\text{THc}} = 8.83 \cdot 10^{-12} \text{ m}$.

Two atoms of hydrogen, which interact in a strong magnetic field due to the arising oscillations of the electrons ω_B , join into a transmolecule of hydrogen “ H_2 ” where the electrons are paired into orthoboson [7] (Fig. 3a). Such orthoboson produces in the hydrogen transmolecule “ H_2 ” an electromagnetic potential well with the magnetic induction vector at the centre $\sim 10^4 \text{ T}$. In such a ultrastrong and inhomogeneous magnetic field the protons ($S_p = 1/2$) will have parallel spins $\uparrow\uparrow$. Like the electrons, the protons in the hydrogen transmolecule form a bound state – the orthoboson $S = 1$ – at the expense of their own exchange interaction and their own correlated oscillations. Similar to the electrons, the exchange Coulomb interaction of the protons in the first order of the perturbation theory fully compensates their Coulomb repulsion. This leads to approaching of the protons to the nuclear distances with the formation of a transmolecule of “helium-pp” (“He-pp”) [7] (Fig. 3b). The protons in the transmolecule “He-pp”

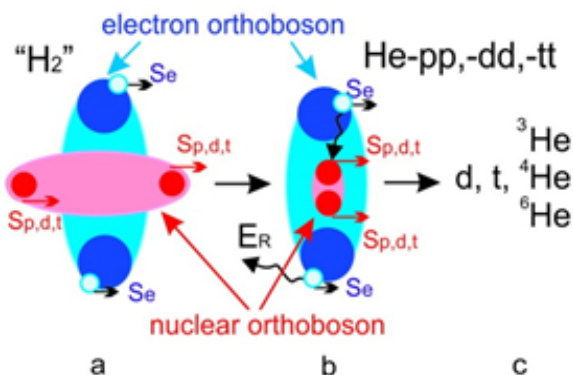


Fig. 3. Transformation of hydrogen transmolecule into “helium” transmolecule.

can be replaced by deuterons d and tritons t . As a result, the transmolecules “He-dd” and “He-tt” are formed. Formation of the transmolecule of hydrogen “ H_2 ” and transmolecule “He-pp” is accompanied by characteristic radiation in the region of deep ultraviolet radiation in the range from 27 eV to 150 eV [7, 11]. Exactly this radiation was registered in the extreme ultraviolet spectroscopy experimental studies of the microwave discharge in the helium-hydrogen plasma [12]. The scheme of electron transitions from the states of atoms and ions of hydrogen, as well as of hydrogen molecules and ions of hydrogen molecules into the hydrogen transmolecules “ H_2 ” and further, into the “He-pp” transmolecule, is presented in Fig. 4. The transitions with emission of two photons are depicted by double lines. The figures are given in electron-volts.

2.3. TRANSMUTATION REACTIONS AT PROTONS

Protons, apart from the electromagnetic interaction $E-M$, enter into a strong interaction: F . The potential F has a negative value. Therefore, the potentials of strong and Coulomb interactions have opposite signs. So, when the proton spins are parallel, they repel each other at the expense of strong interaction [3]. Due to this, reaction (10) in the He-pp transmolecule will be impossible. But an opportunity will be

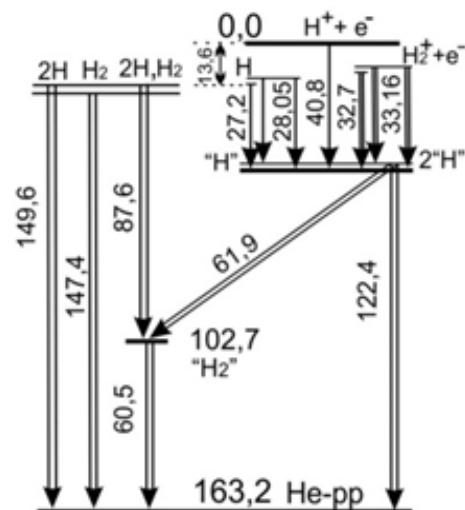
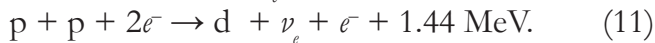


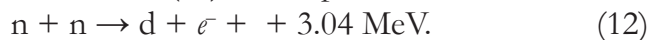
Fig. 4. Scheme of electron transitions in the “hydrogen-helium” transmolecule in He + H_2 plasma.

opened for reaction (11) with the participation of the electron orthobosons $2e^-$.



The protons in the He-pp transmolecule have parallel spins. The strong F -exchange interaction of protons repel them from each other; the Coulomb E -exchange interaction fully compensates the Coulomb repulsion of protons; and the weak W -exchange interaction with the participation of electron orthoboson allows reaction (11).

Let us consider the proton-proton, neutron-neutron and neutron-proton interactions. The proton cannot have a bound state with another proton, just like the neutron does not have a bound state with another neutron. The proton cannot be attracted to another proton, just like the neutron, to another neutron. Therefore, at p - p and n - n interactions at the wavelengths of their wave functions ($\lambda_{p,n} = h/m_{p,n} \cdot v$) the perturbing strong interaction F , which enters into the exchange interaction, will change the antiparallel spins of colliding protons $p\uparrow\downarrow p$ and neutrons $n\uparrow\downarrow n$ into the parallel $p\uparrow\uparrow p$ and $n\uparrow\uparrow n$. Then the spatial wave function of protons or neutrons becomes antisymmetric and the protons or neutrons repel each other because the exchange strong F repulsion surpasses the exchange Coulomb attraction [3]. Due to this, reactions at the expense of strong interaction using free, and even more so, thermonuclear protons (10) or neutrons (12), are impossible:

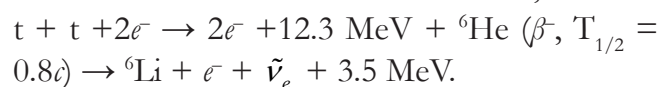
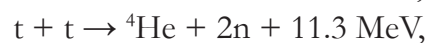
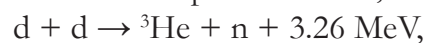
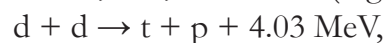


Reactions (10) and (12) at protons and neutrons being in the electromagnetic or nuclear potential well with antiparallel spins are also impossible due to the necessity to fulfill the angular momentum conservation law. The spins of particles e^+ and $\tilde{\nu}_e$ are directed along the momentum direction (they have a right-hand helicity), whereas the spins of particles e^- and ν_e are directed against the momentum (they have a left-hand helicity). Probably, this is why the chief thermonuclear reaction (10) was not fulfilled on

the Earth in laboratory conditions. It cannot pass at the Sun and in stars. Consequently, the stars are not thermonuclear reactors in the channels of reaction (10). In the strong magnetic fields of the stars, the He-pp transmolecules are formed, and in channel (11) low-energy transmutation reactions with participation of electron orthobosons $2e^-$ take place.

The reaction $p + p + 2e^- \rightarrow d + \nu_e + e^- + 1.44 \text{ MeV}$ (11) differs from the reaction with capture of one electron: $p + p + e^- \rightarrow d + \nu_e + 1.44 \text{ MeV}$ (**pep**) where emission of a monoenergetic neutrino takes place. In reactions (11), the neutrino spectrum is continuous. However, it must differ from the neutrino spectrum at beta decay since it occurs with two paired electrons of energy 326 eV. The contribution of reaction (11) was not taken into account when comparing the experimental energy spectrum of solar neutrinos [13], obtained at the Borexino set-up, with the summary theoretical neutrino spectrum produced in a number of nuclear reactions. As a result of comparison, reaction (10) passes with the probability 99%, and the (pep) reaction with the probability 0.24%. Therefore, it is necessary to carry out processing of the experimental neutrino spectrum using reaction (11).

With the production of deuterium and tritium, He-dd and He-tt transmolecules will be formed, which are also nuclear orthobosons. They enter into non-Coulomb nuclear reactions of transmutation, including with the participation of electron orthobosons, with the formation of protons, neutrons, deuterons, tritons, such nuclei as ${}^3\text{He}$, ${}^4\text{He}$, ${}^6\text{He} \rightarrow {}^6\text{Li}$ (Fig. 3c) [6]:



Further on, the atoms of orthohelium of ${}^4\text{He}$ with their own strong magnetic fields ($\sim 70 \text{ T}$) become unified and produce multi-nuclear transmolecules, where multinuclear reactions

with synthesis of heavier chemical elements with the nucleus charge $Z > 6$ take place [14]. Thus, the reactions of low-energy transmutation ensure the star and planetary nucleosynthesis [6, 15, 16]. We shall note that only with the appearance of deuterium at the Sun and in the stars thermonuclear reactions become possible. Therefore, the Sun and stars are reactors of mixed type: transmutational and thermonuclear ones.

Due to the isotopic invariance of the strong interaction, the protons can interact with the neutrons in resonance. The neutron and proton have a bound state, that is the deuteron. The proton captures a thermal neutron with the cross section $\sigma_{\tau} = 0.332$ barn. Such a small cross section of capture, σ_{τ} , is due to that the deuteron has an only bound state being in the nuclear potential well, and it does not have any states close to and higher than the binding energy of the deuteron: $E_d = 2.224$ MeV. As a result, the interaction between the proton and neutron produces a deuteron with the spin $S = 1$. In the deuteron, the spins of the neutron and proton are parallel, and their spatial wave functions are symmetric. With that, their total wave function is antisymmetric due to the antisymmetric isotopic spin component of their wave function: n, p . As a consequence, the neutron and the proton will be attracted to each other because the spatial component of their total wave function is symmetric; however, with this the spin component of their wave function is also symmetric, that is their spins are parallel: $p \uparrow \uparrow n$. The $\sim 65\%$ possibility for the proton and neutron to reside outside of the nuclear potential well of the deuteron can be interpreted as the existing resonant interference exchange interaction between the proton and the neutron (chapter 3).

- In the atom which is in a strong magnetic field, the exchange Coulomb interaction allows the atomic electrons to be paired into the orthobosons with $S = 1$. Thus, a transatom is formed which has a spin electronic Bose-Einstein condensate. The spins and spin

magnetic moments of all the orthobosons of a transatom are oriented in one direction. The spin electronic condensate or torsem condensate produces inside and around the transatom an ultrastrong, directional, inhomogeneous and anisotropic magnetic field.

- The exchange Coulomb attraction between any two identical charged fermions that make up the orthoboson in the first order of the perturbation theory fully compensates the Coulomb repulsion between them.
- The strong exchange interaction between colliding protons and neutrons prohibits them to enter into nuclear and thermonuclear reactions with the formation of the deuteron.

3. RESONANT EXCHANGE INTERACTIONS

3.1. RADIATIVE NEUTRON CAPTURE

In paper [3], the resonant interference exchange interaction was introduced. The RIEEX-interaction is an exchange interaction between any objects, A and B , which have resonant R -states belonging to a compound system composed of objects A and B . The resonant R -states, in some approximation, are identical to the objects A and B . The R -states become real when they are excited at the wavelengths of the wave functions of the A and B objects. Therefore, the spatial region of the exchange interaction for all fundamental potentials: F , EM , W and IG , is defined by the wavelengths of the wave functions of resonantly interacting identical objects A and B . When the wave functions of the objects A and B are overlapped, then they appear simultaneously in two states: in the eigenstate $\psi_a(A)\psi_b(B)$ and in the identical state $\psi_b(A)\psi_a(B)$. Their full wave function is $\psi^{\pm}(A,B) = \psi_a(A)\psi_b(B) \pm \psi_b(A)\psi_a(B)$. The eigen-part $\psi_a(A)$ at its eigen-spot a interacts with the identical part $\psi_a(B)$, while the eigen-part $\psi_b(B)$ at its eigen-spot b interacts with $\psi_b(A)$. Thus, thanks to the resonant interference exchange

interaction, the short-range strong F and locally weak W interactions become long-range ones.

In paper [3], RIEX-interaction of neutrons, protons and deuterons with atomic nuclei is considered. If the compound nucleus consisting of a nucleus target and neutron n , or proton p , or deuteron d , has resonance R -levels, then n or p , or d upon entering into resonance with one of such R -levels start to interact with it through exchange interaction. The resonant R -state is excited at the wavelength of eigen wave functions $\psi_n(n)$ or $\psi_p(p)$ or $\psi_d(d)$. The R -state possesses its eigen wave function $\psi_R(R)$. Due to the exchange interaction the R -state as well as the neutron, the proton, the deuteron in addition to the eigenstates, they have identical states: $\psi_n(R)$, $\psi_p(R)$, $\psi_d(R)$, $\psi_R(n)$, $\psi_R(p)$, $\psi_R(d)$. The full antisymmetric wave function of the R -level and neutron n is:

$$[\psi_n(n)\psi_R(R) - \psi_n(R)\psi_R(n)] \cdot \{S^+(n)S^+(R)\}; \quad (13a)$$

$$[\psi_n(n)\psi_R(R) - \psi_n(R)\psi_R(n)] \cdot \{S^-(n)S^-(R)\}; \quad (13b)$$

$$[\psi_n(n)\psi_R(R) - \psi_n(R)\psi_R(n)] \times \{S^+(n)S^-(R) + S^-(n)S^+(R)\}; \quad (13c)$$

$$[\psi_n(n)\psi_R(R) + \psi_n(R)\psi_R(n)] \times \{S^+(n)S^-(R) - S^-(n)S^+(R)\}. \quad (13d)$$

For the proton, the symbol n in (13) should be replaced with “ p ”. For the deuteron-boson ($S = 1$), the full wave function $\psi(d, R)$ should be symmetric.

The potential making a key contribution into the exchange energy is the strong interaction F :

$$\Delta E_{nR}^{(1)} = \frac{\int \psi^*(n, R)[F]\psi(n, R)dV_n dV_R}{\int \psi^*(n, R)\psi(n, R)dV_n dV_R}. \quad (14)$$

The energy of strong perturbation, F , depends on the spin variables. However, we assume that the perturbation F does not change the R -state and the spin orientation of the neutron (or proton). Therefore, when averaging spin wave functions in the numerator and in the denominator (14), identical multipliers appear which diminish. As a result, $\psi(n, R)$ corresponds to the parts of

wave functions (13) which depend only on the coordinates $\psi(n, R) = [\psi_n^V \psi_R^V]$. Then:

$$\begin{aligned} & [\psi_n^V \psi_R^V]^* \cdot [\psi_n^V \psi_R^V] = \psi_n^*(n)\psi_R^*(R)\psi_n(n)\psi_R(R) + \\ & + \psi_n^*(R)\psi_R^*(n)\psi_n(R)\psi_R(n) \pm \\ & \pm [\psi_n^*(n)\psi_R^*(R)\psi_n(R)\psi_R(n) + \\ & + \psi_n^*(R)\psi_R^*(n)\psi_n(n)\psi_R(R)]. \end{aligned} \quad (15)$$

The integral from the functions represented in the squared brackets is the exchange integral. The plus sign (15) responds to the symmetric coordinate wave function in (13d); and the minus sign, to the asymmetric one in (13a, b, c).

The integrals from the first two members in (15) characterize a strong interaction, F , at the distance exceeding its action between the R -state and the neutron (or proton), as well as between part of the neutron in the R -state and part of the R -state in the neutron. Thus, these integrals are equal to zero:

$$\int |\psi_n(n)|^2 F |\psi_R(R)|^2 dV_n dV_R = 0,$$

$$\int |\psi_n(R)|^2 F |\psi_R(n)|^2 dV_n dV_R = 0.$$

So, one can consider that in numerator (9) for the strong interaction:

$$\begin{aligned} & [\psi_n^V \psi_R^V]^* \cdot [\psi_n^V \psi_R^V] = \\ & = \pm [\psi_n^*(n)\psi_R^*(R)\psi_n(R)\psi_R(n) + \\ & + \psi_n^*(R)\psi_R^*(n)\psi_n(n)\psi_R(R)]. \end{aligned} \quad (16)$$

The potential F has a negative value. The exchange integral in this case also has a negative value. So, the nucleus with the R -state and the neutron (or proton) are attracted to each other when their spatial wave function is symmetric, while their spins are antiparallel. The deuteron-boson is attracted to the nucleus with the R -state when both the spatial and the spin components of the total wave function are symmetric or antisymmetric.

The R -state of the compound nucleus is excited by the neutron (p or d) proportionally to the coefficient K : $\psi_R(R) = K\psi_n(n)$ or $\psi_R(r) = K\psi_n(r)$. The coefficient K characterizes the affinity of the neutron (p or d) with the R -state. Usually $K < 1$ or $K \ll 1$. For each R -state the coefficient K is individual, and correspondingly,

the sum of interactions of the neutrons (p or d) together with all of the R-states of the compound nucleus is individual for the specific isotope. The identical state of the neutron in the R-state equals to its eigen R-state: $\psi_R(n) = \psi_R(R)$. The overlapping in the wave functions of the neutron $\psi_n(n)$ and the R-state in the neutron $\psi_n(R)$ will increase: $\psi_n(n)\psi_n(R) = K^2|\psi_n(r)|^2$, proportionally to the neutron density $|\psi_n(r)|^2$ at the distance r from the nucleus. With the same coefficient the overlapping in the wave functions of the R-state and the neutron in the R-state will grow: $\psi_R(n)\psi_R(R) = K^2|\psi_n(r)|^2$. Eventually, the integral from (16) and the energy of the exchange interaction $\Delta E^{(1)}(r)$ (14) are written as follows:

$$\Delta E_{nR}^{(1)}(r) \sim 2K^4 \int |\psi_n(r)|^2 F |\psi_n(r)|^2 d^2V_n. \quad (17)$$

Since the potential of the strong interaction, F , has a short range and the property of saturation, integral (17) has its value only in the volume which is commensurable with the nucleus volume V_A , the diameter of which is equal $\varnothing A$. Therefore, we will consider the value of action of F at the exchange interaction of the neutron (p or d) with the R-state over the entire length L , from the place where this interaction starts up to the nucleus, as constant: $F_R = const$. That is, F_R does not depend on the distance r between the neutron and the nucleus over the entire length L . The length L correlates with the wavelength of the neutron (p or d) as $L \sim K^4 \cdot \lambda_{n,p,d}$. Since $\lambda_{n,p,d}$ or the wavelength of the wave function of the neutron (p or d) is much greater than the dimensions of the nucleus $\psi_n(r) \gg \varnothing A$, then $\psi_n(r) = const$ in the volume V_A . Consequently, from (17) the energy of the exchange interaction $\Delta E^{(1)}(r)$ is proportional to the squared neutron (p or d) density in the nucleus region V_A , when the neutron is at the distance r from the nucleus.

$$\Delta E_{nR}^{(A)}(r) \sim 2F_R \cdot K^4 |\psi_n(r)|^4 \int_{V_A} d^2V_n. \quad (18)$$

The integral in (18) is the squared volume of the nucleus, V_A^2 . It is proportional to the squared mass number of the nucleus: $V_A^2 = \rho M^2$.

$$\Delta E_{nR}^{(A)}(r) \sim 2F_R \cdot K^4 |\psi_n(r)|^4 \cdot V_A^2. \quad (19)$$

Let us introduce the designation U , which includes $2F_R$, ρ and normalizing integral (9):

$$\Delta E_{nR}^{(A)}(r) = UK^4 M^2 \cdot |\psi_n(r)|^4. \quad (20)$$

The value U , which characterizes the potential of a strong interaction between a neutron or a proton with the R-state, is estimated as follows: $U = 9-12$ MeV [3].

During the interaction between the neutron (p or d) with the R-state, its wave function is transformed from the plane wave into the wave function of the bound state. The orbital moment of the thermal neutron (p or d) interacting with the nucleus: $\ell = 0$. So, we will represent the wave function $\psi_n(r)$ [or $\psi_p(r)$, or $\psi_d(r)$] as the radial part of the S -wave function of the electron which was on the orbital with the radius a_0 and rotates around the nucleus with the quantum numbers $n = 1$ and $\ell = 0$. The density distribution of such an electron in the radial direction is characterized

by the function: $P(r) = C \left[r^2 \exp\left(-\frac{2r}{a_0}\right) \right]$, where C is the normalizing constant, a_0 is the radius of the electron orbital [4]. **Fig. 5** provides in relative units: the red line which corresponds to the values of the function from the nucleus up to a_0 (500 fm); the green line shows the neutron (p or d) density in the nucleus, when neutron resides at the distance r from the nucleus: $|\psi_n(r)|^2 = P(L-r)$; and the blue line indicates the potential of

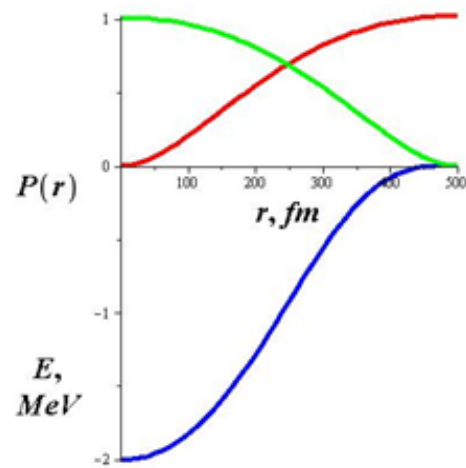


Fig. 5. The red line is the radial density of the orbital electron; green – neutron density in the nucleus located at a distance r from a neutron; blue – RIEEX potential.

the exchange interaction $\Delta E_{nR}^{(1)}(r) = -[P(L-r)]^2$ (the values $a_0 = L = 500$ fm and $UK^4M^2 = -2$ MeV are chosen arbitrarily).

Thus, during the interaction of a neutron with the R-state of the compound nucleus at the distance $L \sim K^4 \lambda_n$ up to the nucleus there is a potential pit of depth equal to UK^4M^2 . In Fig. 6, the red line shows the nuclear potential of nickel, for example, ^{64}Ni ; the blue line indicates the potential of the RIEX-interaction; and the green line corresponds to the total potential (the value $UK^4M^2 = -2$ MeV is chosen arbitrarily).

Upon coming into the potential pit, the neutron finds itself in the region which is lower than the binding energy of the neutron, where the density of neutron energy levels is considerable and, therefore, the resonant interaction of the neutron with them is also great. Thus, thanks to the resonant interference exchange interaction the neutron is captured by the nucleus at the distance L .

3.2. COLD FUSION

In contrast to the neutron, both the proton and the deuteron have electric charge, therefore when they approach the nucleus they experience a Coulomb barrier. However, behind the Coulomb barrier of a compound nucleus, the proton, apparently, as well as the deuteron, has a large quantity of resonance levels up to the Coulomb barrier height (Fig. 7). The energy of the proton and deuteron can range from the thermal one up to the energy equal to the Coulomb barrier height. Therefore, when losing its energy on the way of approaching the nucleus, the proton

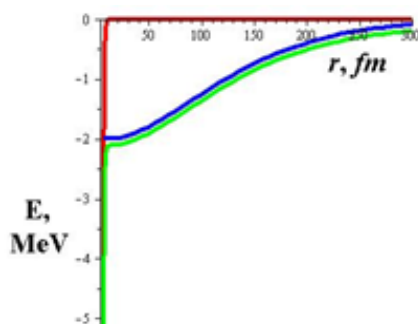


Fig. 6. Red line - nuclear potential Ni; blue - RIEX potential Ni-n; green - total potential Ni+n.

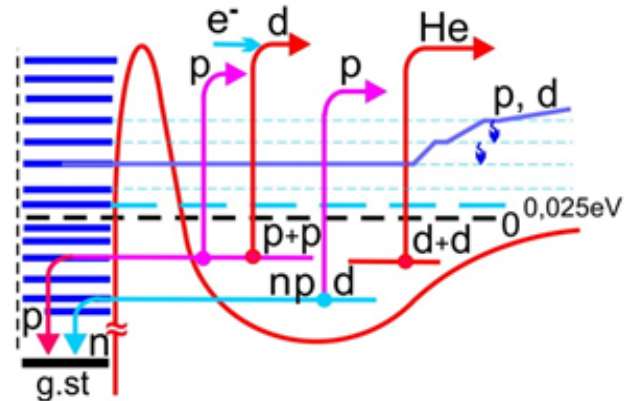


Fig. 7. The levels of the compound nucleus $A + p$ (d) beyond the Coulomb barrier and the interaction with them of a proton or deuteron.

or deuteron “scan” the energy levels of the nucleus behind the Coulomb barrier, up to the moment when they enter into resonance with the suitable R-level (Fig. 7). The suitable R-level is defined by the requirement of supremacy of its exchange energy with the proton over the energy of Coulomb repulsion of the proton off the nucleus. The suitable R-levels may exist above the “room” energy 0.025 eV. In such a case, the RIEX interaction requires energy stimulation. Such stimulation can be supplied by heating the “working body” or by affecting it using external sources of supplementary energy (laser, microwave radiation, etc.). Thus, during an interaction of the proton or a deuteron with the R-state at the length $L \sim K^4 \lambda_{p,d}$ from the nucleus, there arises formation of a potential well. The potential well depth and the distance from the well bottom to the nucleus are defined by the difference between the attracting energy of the exchange interaction $-UK^4M^2 |\psi_p(r)|^4$ and the energy of the Coulomb repulsion $V = k \cdot Ze^2/r$, where Z is the nucleus charge. In Fig. 8, the red line refers to the nuclear potential of Ni (nickel) plus the Coulomb potential Ni+p, and the blue line corresponds to the RIEX potential (values $400 F_m$ and $UK^4M^2 = -2$ MeV are chosen arbitrarily), and the green line indicates the summed potential.

As a result, an “exchange” potential well is formed at the Coulomb barrier of the nucleus A. A nuclear molecule is created as follows: $A + p$

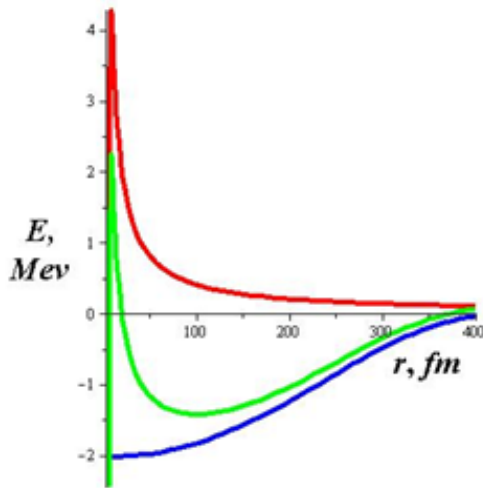
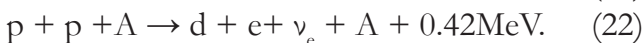
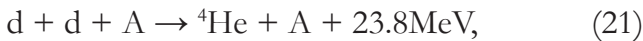
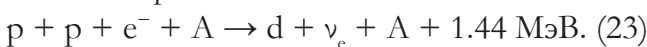


Fig. 8. Red line - nuclear plus Coulomb potentials $Ni+p$; blue - RIEEX potential $Ni+p$; green - total potential $Ni+p$.

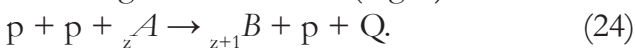
and $A+d$. At a large concentration of protons (deuterons) for one nucleus of the main element, a second proton and a second deuteron may fall into the exchange well: $A+p+p$ and $A+d+d$. The proton-fermions in the well will have antiparallel spins in the ground state. The deuteron-bosons may have differently oriented spins as the deuteron levels are closely-spaced triplet states ($S_d = 1, m_s = +1, 0, -1$). This opens a possibility for the reactions of cold fusion (Fig. 7):



As was explained in 2.3, the protons with antiparallel spins cannot perform reaction (22). Therefore, this gives a possibility for the reaction with the capture of the orbital K -electron:



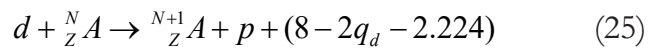
When two protons are in the exchange well, there arises a possibility for tunneling of one of the protons through the Coulomb barrier right into the ground state of the compound nucleus without gamma emission (Fig. 7).



This reaction will compete with reaction (17).

We shall note that the deuteron which resides in the exchange well of the nuclear molecule is polarized by the Coulomb field of the nucleus: the neutron is placed closer to the nucleus than the proton. Therefore, the neutron may perform radiationless transition into the ground state of the nucleus A with proton emission (Fig. 7). The

proton energy, with accuracy up to the nucleus recoil energy, will be equal to the neutron bounding energy in the nucleus ~ 8 MeV minus double energy of the level (neutron energy plus proton energy), occupied by the deuteron in the exchange potential well q_d and minus deuteron binding energy 2.224 MeV:



where N is the number of neutrons in the nucleus. The level occupied by the deuteron in the potential well q_p can be nominally assumed as its depth. This reaction is possible also because the proton and neutron are above the nuclear potential well of the deuteron with the probability $\sim 65\%$. Reaction (19) is even more so probable if the neutron has a resonance level behind the Coulomb barrier of the compound nucleus. Thus, at dissolving of deuterium in a thin layer or powder of titanium or palladium, one can register protons with the energy defined by the depth of the potential well q_d .

The proton and neutron in a deuteron exist 65% of their time in the quasi-free state. So, they interact independently with their R -states. It follows from this that the reactions of cold fusion on deuterons must have notable cross sections for the isotopes, for which the cross sections of radiative capture of neutrons are substantial as well.

Besides that, due to the isotopic invariance of strong interaction, the proton can interact resonantly with the neutron R -levels both, as being behind the Coulomb barrier, and belonging to the isotopes with substantial resonant absorption of neutrons [17]. In this case, the proton is attracted to the nucleus which has resonant neutron R -levels, when their spins are parallel.

3.3. NUCLEAR MOLECULES

As a result of RIEX-interaction between the proton or deuteron with the atomic nucleus ${}_Z A$, a nuclear potential well is formed at the Coulomb barrier of the nucleus. Due to this nuclear molecules are created as follows: ${}_Z A + p$

and ${}_Z A+d$. The lifetime of the corresponding molecule is defined by the transparency of the Coulomb barrier. Also, in spite of the decrease in the height and width of the Coulomb barrier, the nuclear molecules ${}_Z A+p$ and $A+d$ which have been formed may be stable ($A+d$ is stable with an accuracy up to the reaction of neutron capture; see 3.2). Implicitly, it is confirmed by the absence of gamma radiation when dissolving hydrogen or deuterium in titanium, nickel or palladium. The mass of a nuclear molecule ${}_Z A+p$ differs from the atom mass of ${}_{Z+1} B$ by the difference between the proton binding energy Q_p in the ${}_{Z+1} B$ nucleus and the depth of the potential well q_p of the nuclear molecule. Depending on ${}_{Z+1} B$, the difference $Q_p - q_p$ or the nuclear-molecule mass defect can amount to several MeV. The difference in the mass of a few tens of keV can be at present determined using time-of-flight and quadrupole mass-spectrometers, including quadrupole ion traps [18]. From such measurements, the depth of the potential well q_p can be determined.

It is also evident that the electron levels in a nuclear molecule will shift relative to the electron levels in the ${}_{Z+1} B$ atom. In the first approximation, this nuclear molecule electron shift (NME shift) will not lead to the appearance of differences in the chemical properties of ${}_{Z+1} B$ atom as well as of the ${}_Z A+p$ nuclear molecule. The same cannot be remarked about their optical spectra. In optical measurements of atomic electron levels, the isotope shift is known which is related to the changes in the number of neutrons in the isotopes of one and the same chemical element [19]. The isotope shift consists of two parts: mass and field shifts. The mass shift between the neighbouring isotopes is connected with the change in the isotope mass by the neutron mass (~ 940 MeV). The field shift is associated with the change in the shape and volume of the nucleus when a neutron is added to the nucleus. As this takes place, the distribution of the electric charge in the nucleus or its mean-square charge radius change as well. In the nuclear molecule,

the mass shift is negligibly small (\sim several MeV) in comparison with the isotope mass shift. But on the other hand, the field shift in the ${}_Z A+p$ nuclear molecule considerably surpasses the isotope field shift in ${}_{Z+1} B$. Such NME shifts can be registered using common atomic optical spectrometers. The more so they can be observed when using lasers with the variable wavelength of the radiation (for example: dye lasers), as well as in a complex with the quadrupole ion trap. Owing to the indicated reasons, it is necessary to study, first and foremost, such "chemical elements" (possible nuclear molecules) as vanadium ($V = Ti+p,d$), copper ($Cu = Ni+p,d$), silver ($Ag = Pd+p,d$). These chemical elements are obtained through the cold fusion reactions with the participation of hydrogen or deuterium and such basic elements as Ti (titanium), Ni (nickel), and Pd (palladium).

The nuclear molecules of vanadium, copper, silver with a proton or deuteron will have the atomic mass which is greater by one or two (p or d) than the atomic mass of stable isotopes of titanium, nickel and palladium. Vanadium, copper and silver have two stable isotopes, each: V-50, 51; Cu-63, 65; Ag-107, 109. Titanium and nickel have five stable isotopes each: Ti-46÷50; Ni-58, 60÷62, 64; and palladium has six stable isotopes: Pd-102, 104÷106, 108, 110. The nuclear molecules of V, Cu and Ag can be registered using mass spectroscopy after their chemical separation from Ti, Ni and Pd.

If the existence of nuclear molecules with a proton or a deuteron is possible, then the question about a possible existence of nuclear molecules in a pair with other nuclei, starting with helium nuclei, ${}^4 He$, arises. However, in condensed matter the atoms with the nucleus charge $Z \geq 2$ with thermal energy cannot lose all their electrons and enter into the RIEX-interaction with its nuclei with the nuclei of the main element, even if the potential of such an interaction is considerable. Consequently, in order to obtain heavy nuclei molecules, it is necessary to use heavy ions accelerated up to several MeV. These heavy ions

should be accelerated so that the nuclei of heavy ions could approach closely the target nuclei of the main element.

Since the exchange potential well is lower than the zero line of the potential energy, and internal potential well 2 of the nuclear molecule is less than external one 1 (Fig. 9), there exists a non-zero probability of spontaneous decay of a single nucleus into two cluster nuclei, and its transition into the state of a nuclear molecule consisting of two such cluster nuclei. At the transition into the state of a nuclear molecule there is a release of energy. Such energy can realize itself at the expense of neutron or gamma-quanta emission. In this case, a stable nuclear molecule is formed. In other case, the energy is released as kinetic energy of the cluster nuclei, and the nuclear molecule does not form at all. Only two nuclei are formed then. The latter case resembles the fission process of nuclei.

In nuclear physics such a notion as cluster radioactivity is known [20]. At cluster decay heavy and transuranium nuclei radiate spontaneously nuclei of light clusters which are heavier than the α -particle but lighter than the products of spontaneous fission. Up to now, over two dozens of decays have been observed experimentally for nuclei from ^{221}Fr to ^{242}Cm with the production of such clusters as: ^{14}C , ^{20}O , ^{24}Ne , ^{26}Ne , ^{28}Mg , ^{30}Mg , ^{32}Si and ^{34}Si . Since the energy of the yielding cluster in all of the decays is less than the height of the potential barrier,

U_B , the cluster decay is due to the tunneling of the light cluster through barrier 1 (Fig. 9). The probability of such processes in relation to the main modes of decay of mother nuclei is within the range from 10^{-9} to 10^{-16} . In all of the observed cases, the residual nucleus is the double magic nucleus of lead (^{208}Pb) or its closest neighbours. Therefore, sometimes the cluster decay is called the “lead” decay. The presence of closed magic nucleon shells in the formed nuclei considerably increases the probability of the cluster decay.

The “tin” radioactivity of nuclei is predicted for the range ^{112}Ba – ^{116}Ce , for which the decay with the formation of ^{12}C , ^{16}O nuclei and double magic nucleus ^{100}Sn is anticipated. By present time, the emission of ^{12}C from the ^{114}Ba nucleus with a relative probability of decay of $\sim 3.0 \cdot 10^{-5}$ is observed. It is deemed that the cluster decay, like in the case of α -radioactivity, take place in two stages: at first a cluster is formed at the surface of the mother nucleus, which then tunnels through Coulomb barrier 1 of the nucleus (Fig. 9). Since the internal potential well of the nuclear molecule is less than the outer one, the spontaneous transition is possible for the $_{56}\text{Ba}$ and $_{58}\text{Ce}$ nuclei into the state of nuclear molecules, $_{50}\text{Sn}$ - $^{12,14}\text{C}$ and $_{50}\text{Sn}$ - $^{16,18}\text{O}$, correspondingly. For the same reason it is not excluded that the cluster “lead” decay occurs at first into the state with the formation of a nuclear molecule and its subsequent dissociation into clusters.

Since the cluster decay resembles the fission process when the motion of the nucleons proceeding in the mother nuclei due to its oscillation leads to the production of fragments in the course of deformation of the nucleus, the transitions of $_{56}\text{Ba}$ and $_{58}\text{Ce}$ nuclei into nuclear molecules, apparently, can be stimulated using gamma quanta of energy ~ 14 - 18 MeV, by exciting in $_{56}\text{Ba}$ and $_{58}\text{Ce}$ a giant dipole resonance. Observation of $_{50}\text{Sn}$ - $^{12,14}\text{C}$ and $_{50}\text{Sn}$ - $^{16,18}\text{O}$ nuclear molecules, as has been pointed out earlier, can be made by the mass defect or optical NME shift. Another way of observing a nuclear molecule

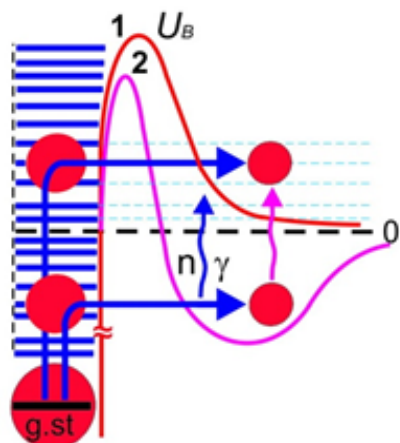


Fig. 9. Cluster decay through barrier 1 and the formation of a nuclear molecule through barrier 2.

is the acceleration of this molecule, preferably up to one MeV/nucleon, with subsequent dissociation of the molecule at the fixed target nuclei. Dissociation of the nuclear molecule leads to the formation of two-nucleus clusters, which can be registered separately using a semiconductor detectors.

Apparently, such events were observed by the authors of paper [21] in the experiments on elastic scattering of the fragments produced in a common binary fission of atomic nuclei in a thin foil. From the obtained data, one can assume that after its binary fission the fragment can come into the state which resembles a two-nucleus system consisting of a magic cluster and a lighter cluster. A recent experiment [22] showed that the cluster decay of the fragments produced in a binary fission is characteristic of both heavy and light fragments. In a light fragment, one of the clusters forming a nuclear molecule is a deformed magic isotope, ^{85}As or ^{77}Zn ; and in a heavier fragment such deformed and spherical magic isotopes can be: ^{85}As , ^{82}Ge , ^{84}Se , ^{98}Sr , ^{108}Mo , ^{121}Ag , ^{123}Cd , ^{132}Sn , ^{138}I , ^{148}Ce , ^{150}Ce . In the cluster decay of a heavy fragment, there must be “tin” radioactivity in the range of $^{144,146}\text{Ba}$ and $^{148,150}\text{Ce}$, for which formation of molecules is expected: $^{12,14}\text{C}$ and $^{16,18}\text{O}$ with double magic spherical nucleus of ^{132}Sn ($T_{1/2} = 40$ s).

As a result:

- The resonant exchange interaction is realized between any objects, A and B, which possess resonant R-states belonging to a compound system. Consequently, the resonant interaction is an exchange interaction. At resonant interaction between the objects, a supplementary exchange energy is produced, which attracts them to each other, thus increasing the cross section of the reaction between the interacting objects.
- The resonant exchange interaction explains how the reactions of cold fusion on protons and deuterons take place.
- The resonant exchange interaction predicts the existence of nuclear molecules.

4. RESONANT INTERFERENCE EXCHANGE INTERACTION

4.1. TWO-SLIT INTERFERENCE

Resonant interference exchange interaction passes between the particle at its wavelength and the resonant R-state which is had by any object (R-object). The RIEX-interaction can take place in the condensed matter, with a large concentration of identical R-objects. If the distance between the R-objects is less than the given wavelength of the particle $K^4\lambda$ with the affinity coefficient K , then the particle excites all of the R-objects in the sphere with the radius $K^4\lambda$. In such a case the wave functions which arose for multiple R-objects, interact simultaneously both with the wave functions of the particle and with each other. The R-objects have additional exchange interaction. Thus, the RIEX-interaction allows one to produce correlated ensembles of identical particles and objects.

When in the condensed medium all identical R-objects move, they will affect chaotically the travelling particle. If the objects are fixed, their total influence on the particle will become quite definite, and it will change in dependence from the location of the R-objects and from the direction of the particle motion.

Let us fix two R-objects which are equidistant from the particle that is moving opposite to them. The wave functions of the two R-objects will interfere with each other, producing an interference field. The particle entering into a RIEX-interaction with the R-objects will deviate to one side or another due to this interference field. Now, let us replace these two R-objects with two R-resonators. In resonator cavities tuned to the required wavelength of the particle, oscillations are excited which interfere and resonantly interact with the particle. This RIEX-interaction also deviates the particle from its way.

Two slits with the parameters corresponding to the oncoming particle, similarly to two resonator cavities, produce interference fields in front of the particle travelling opposite to them

and behind the particle that is moving away from two-slits. The particle while interacting with the interference fields produced by the two-slits will make an interference picture on the screen behind the slits. When doing so, the particle will travel through one slit. The slits interacting with the particle represent active elements. Thus, the paradox of travelling by the quantum particle simultaneously through two slits is annihilated.

4.2. TRANSNUCLEI, NUCLEAR TRANSMOLECULES AND TRANSMUTATION REACTIONS

The multiple and variable experiments in low-energy transmutation of chemical elements prompt us that the condensed matter is ionized when externally influenced, and at a certain charge density, stable local electron-ion formations are produced inside it – capsules with a strong magnetic field \mathbf{B} inside ($> 30T$). In the strong magnetic field \mathbf{B} , the atomic electrons are paired into orthobosons, and the atoms are inevitably transformed into transatoms.

The electronic orthobosons make the spin Bose-Einstein condensate in the atom or the torsem-condensate. The magnetic moments of the electrons, μ_e , in the torsem condensate are oriented in one direction, and they generate inside and around the transatom the ultrastrong, directional, inhomogenous and anisotropic magnetic field $\mathbf{B}_s \sim 10^5-10^{10}$ T [5, 23]. The internal ultrastrong magnetic field \mathbf{B}_s , while interacting with the magnetic and magnetic orbital moments of the nucleons in the nucleus, change the nucleus structure by transforming it into a transnucleus.

In a strong magnetic field, the atom from its “amorphous state” is transformed into a well-ordered magnetic “crystal”, that is into a transatom. Being in the state of the torsem condensate, the transatom practically loses its individuality. The transatoms with an even number of the electrons begin to resemble inert gases, while uneven transatoms resemble alkaline chemical elements with one outer electron. The difference between the transatoms lies in the

number of orthobosons residing at the electron shells [23].

The same occurs with the nucleus but already in an ultrastrong magnetic field of the torsem condensate. The transnucleus is an ordered nuclear magnetic “crystal”. The nucleons in the nucleus, just like the electrons in an atom, can produce nucleon orthobosons: proton-proton and neutron-neutron ones. Proton-proton and neutron-neutron orthobosons form nucleon shells. The transnuclei lose their individuality. Their structures begin to resemble each other. The structure of a light transnucleus will be identical to the component of the structure of a heavier transnucleus. These identical parts of the transnuclei can enter into an exchange interaction.

The ultrastrong magnetic fields of orthobosons and their torsem condensate attract transatoms to each other. The torsem condensate of transatoms get collectivized. The transnuclei of the transatoms get collectivized as well. Binuclear and multinuclear molecules called transmolecules are produced. **Fig. 10** depicts as an example the formation of a sodium transmolecule, ${}_{11}\text{Na}$, from the transatoms of boron, ${}_{5}\text{B}$, and carbon, ${}_{6}\text{C}$. Transmolecules consist of transnuclei, parts of which are identical to each other. The transnuclei in the transmolecule enter into the low-energy multinuclear reactions of transmutation. As a result of transmutation reactions, other chemical elements are produced. The atomic nuclei of these chemical elements are non-radioactive since the weak exchange interaction and electronic orthobosons take part in the transmutation reactions.

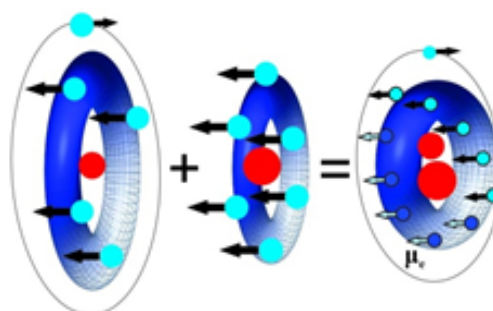


Fig. 10. The formation of sodium transmolecule from boron and carbon transatoms.

The transatoms with transnuclei are steady, stable formations. However, being in the environment, the transatoms using their ultrastrong magnetic fields transform common atoms into transatoms at collisions. The transatoms form transmolecules at once, which enter into the transmutation reactions with its transnuclei. The products of transmutation reactions, if they are not in a strong magnetic field, are found as common atoms with common nuclei. Thus, in a medium of common atoms the transatoms with the transnuclei are non-steady, non-stable formations.

The experiments and theoretical calculations in low-energy transmutation of chemical elements have shown that in the yielding reaction channel there is such an ensemble of new nuclei which is different, minimally, in the total mass from the total mass of the ensemble of nuclei at the entrance channel. In other words, the energy produced in the transmutation reactions is not large and amounts from tens of keV up to several MeV. In usual nuclear reactions, the greater the difference in the energies between the initial and final states, the greater is the probability of this reaction. The reactions with the participation of two and more objects with a small production of energy proceed with a larger cross section only in the case when they have a resonant character; in other words, if there is resonant interference exchange interaction between them. Consequently, low-energy multinuclear reactions of transmutation of chemical elements take place at the expense of the RIEEX-interaction.

5. CONCLUSION

The Universe consists of identical particles, mostly of fermions, $s = 1/2$: protons, neutrons, electrons. They, in their turn, form a great number of varied and, at the same time, similar, in a certain sense “identical” objects and a variety of different and, at the same time, identical systems. Each system is composed of interacting objects in it, which simultaneously

present “a system”. Each such system enters as an object into a more unified system. Among the particles, objects and systems there exist all types of fundamental interactions, including the RIEEX-interaction.

The objects where the compound systems have resonance states, come into a resonant interaction, but in fact into the resonant interference exchange interaction. The RIEEX-interaction attracts the objects to each other. Thus, knowing the properties of the object, its resonances, one can determine its location by coming into the RIEEX-interaction with it. Using the RIEEX-interaction one can “find a black cat in a dark room”.

As a rule, if some process passes with a surprisingly high yielding cross section, it is necessary to search for the resonance for the interacting objects.

The resonances “permeate” the entire Universe, starting with the elementary particles up to complex social systems. The more complex is the system, the more resonant states and resonant vibrations it possesses. The RIEEX-interaction does not only join the objects into systems, but when doing this it simultaneously makes the choice and natural selection of suitable objects from a greater number of other different objects. This mechanism is vitally important for the biological systems, for instance, in replication of the DNA molecule.

The RIEEX-interaction is universal since it includes all of the fundamental interactions. The RIEEX-interaction creates more complex systems from isolated objects, and thus prevents their destruction. So, the resonance interference exchange interaction is defined as AntiEntropy one.

REFERENCES

1. Shipov GI. *Teoriya fizicheskogo vakuuma, teoriya, eksperimenty, tekhnologii* [The theory of physical vacuum, theory, experiments, technology]. Moscow, Nauka Publ., 1997, 450 p.

2. Heisenberg W. Über die Spektra von Atomsystemen mit zwei Elektronen. *Z. Phys.*, 1926, 39(7):499-518.
3. Mishinsky GV. Theory of cold fusion reactions. *Radioelectronics. Nanosystems. Information Technologies (RENSIT)*, 2019, 11(2):125-142. DOI: 10.17725/rensit.2019.11.125, <http://en.rensit.ru/>.
4. Matveev AN. *Atomnaya fizika* [Atomic physics]. Moscow, Vysshaya shkola Publ., 1989, 439 p.
5. Landau LD, Lifshitz EM. *The Classical theory of Fields*. Oxford, Butterworth-Heinemann, 1975, 402 p.
6. Mishinsky GV. Atom in a strong magnetic field. Transformation of atoms to transatoms. *RENSIT*, 2017, 9(2):147-160. DOI: 10.17725/rensit.2017.09.147.
7. Mishinsky GV. Non-Coulomb nuclear reactions of transatoms. Stellar energy and nucleosynthesis. *RENSIT*, 2018, 10(1):35-52. DOI: 10.17725/rensit.2018.10.035.
8. Kadomtsev BB. Tyazhely atom v sverkhsil'nom magnitnom pole [Heavy atom in an ultrastrong magnetic field]. *ZhETF*, 1970, 58(5):1765-1769 (in Russ.).
9. Fock VA. Bemerkung zur Quantelung des harmonischen Oszillators im Magnetfeld. *Z.Phys.*, 1928, 47:446-448.
10. Heiss WD, Nazmitdinov RG. Orbital magnetism in small quantum dots with closed shells. *Pis'ma v ZhETF*, 1998, 68(12):870-875 (in Russ.).
11. Mishinsky GV. Spin electron condensate. Spin nuclide electron condensate. *RENSIT*, 2018, 10(3):411-424. DOI: 10.17725/rensit.2018.10.411.
12. Mills R, Ray P. Extreme ultraviolet spectroscopy of helium-hydrogen plasma. *J. Phys. D:Appl. Phys.*, 2003, 36:1535-1542.
13. Borexino Collaboration: Bellini G., Benziger J., Bick D. et al. Neutrinos from the primary proton-proton fusion process in the Sun. *Nature*, 2014, 512:383-386.
14. Mishinsky GV. Multinuclear reactions in condensed helium. *RENSIT*, 2017, 9(1):94-105. DOI: 10.17725/rensit.2017.09.094.
15. Mishinsky GV, Kuznetsov VD. Element distribution in the products of low energy transmutation. Nucleosynthesis. *Annales de la Fondation Louis de Broglie*, 2008, 33(3-4):331-356.
16. Mishinsky GV, Kuznetsov VD, Penkov FM. Nizkoenergeticheskaya transmutatsiya atomnykh yader khimicheskikh elementov. Raspredelenie po elementam v produktakh transmutatsii. nukleosintez [Low energy transmutation of atomic nuclei of chemical elements. Element distribution in the products of low energy transmutation. Nucleosynthesis]. *International Journal of Unconventional Science (IJUS)*, 2017, 17-18(5):61-81 (in Russ.), <http://www.unconv-science.org/>.
17. Klimov AI. Will Russia be among the leaders of new energy technologies? *LA REGNUM*, 2019, (in Russ.); <https://regnum.ru/news/2625783.html>.
18. Hoffmann E de, Stroobant V. *Mass spectrometry : principles and applications*. 3rd ed. John Wiley & Sons Ltd, 2007, 489 p.
19. Angeli I, Marinova KP. Table of experimental nuclear ground state charge radii: An update. *Atomic Data and Nuclear Data Tables*, 2013, 99(1):69-95.
20. Tchuvil'sky YuM. *Cluster radioactivity*. Moscow, Moscow University Publ., 1997, 166 p.
21. Kamanin DV, Pyatkov YuV, Strekalovsky AO, Alexandrov AA, Alexandrova IA, Goryainova ZI, Mkaza N, Kuznetsova EA, Malaza V, Strekalovsky OV, Zhuchko VE. Manifestation of clustering in low energy fission - new results. *Izvestiya Rossiiskoi Akademii Nauk. Seriya Fizicheskaya*, 2018, 82(6):719-722 (in Russ.).
22. Strekalovsky AO, Kamanin DV, Pyatkov YuV, Goryainova ZI, Zhuchko VE, Alexandrov AA, Alexandrova IA, Korsten R, Malaza V, Kuznetsova EA, Strekalovsky

- OV. Fission fragments binary brake-up at crossing of the carbon foll. *International Conference "Nucleus-2019"*, July 1-5, 2019, Dubna. *Izvestiya Rossiiskoi Akademii Nauk. Seriya Fizicheskaya*, 2019, (in press).
23. Mishinsky GV. Magnitnye polya transatomov. Spinovy-nuklidny-elektronny kondensat [Magnetic fields of transatoms. Spin-nuclide-electronic condensate]. *IJUS*, 2017, 15-16(5):6-25 (in Russ.).

DOI: 10.17725/rensit.2019.11.279

Paper is devoted to 150-year of Mendeleev's Periodic Table

Numerical representation of fractals in physical chemistry of material sciences

Alexander D. IzotovKurnakov Institute of General and Inorganic Chemistry, Russian Academy of Sciences, <http://igic.ras.ru/>
Moscow 119991, Russian Federation*E-mail: izotov@igic.ras.ru***Feodor I. Mavrikidi**Oil and Gas Research Institute, Russian Academy of Sciences, <http://www.ipng.ru/>
Moscow 119333, Russian Federation*E-mail: mavrikidi@mail.ru**Received 05.11.2019, peer reviewed 18.11.2019, accepted 25.11.2019*

Abstract. The paper substantiates the promise of the model of numerical asymmetry of fractals, which allows, from a single point of view, to cover modern approaches to modeling in chemistry and physics. The basis of the model is the synthesis of two basic number systems of mathematics - real and p- adic numbers. A physical chemistry interpretation of p-adic numbers and their properties is given. The physical chemistry space of the model becomes hyperbolic. The conclusion is made about the need to take into account duality in chemistry. As an illustration serves a model of matter based on Stone duality, which formally represents a pair "substance - properties". The identity of nonlinear models of the atom and the Universe is shown, which serves as a justification for the periodicity of properties and is consistent with the hyperbolicity of the space of the general theory of relativity. The existence of the "golden section" number as a unit of a new number model is theoretically substantiated. The natural connection between the model and quantum mechanics by means of quantum numbers extracted from the model is shown. This opens up possibilities for the synthesis and interaction of the natural sciences, physics and mathematics, which, in the future, can serve as a model for the co-evolution of nature and technology.

Keywords: material science, fractals, p-adic numbers, number asymmetry, "golden section", duality of chemistry, Mendeleev's Periodic Table

PACS: 81.00.00; 05.45.Df; 02.10+p.

For citation: Alexander D. Izotov, Feodor I. Mavrikidi. Numerical representation of fractals in physical chemistry of material sciences. *RENSIT*, 2019, 11(3):279-290; DOI: 10.17725/rensit.2019.11.279

CONTENTS

1. INTRODUCTION (279)
 2. FRACTALS AND NUMBERS IN CHEMISTRY (281)
 3. P-ADIC NUMBERS IN PHYSICAL CHEMISTRY INTERPRETATION (282)
 4. NONLINEARITY OF CHEMICAL SPACE (286)
 5. CONCLUSIONS (288)
- REFERENCES (289)

1. INTRODUCTION

Modern materials science is a physical chemistry science. In this chemistry uses

mathematics mediated by physics [1], which strongly impoverishes specificity of chemistry. So, for example, the balance equations of chemical reactions do not say anything about the very essence of qualitative transformations of matter, only its mechanical face is modeled as the only available. Therefore, all the calculation schemes for parameters of chemical phenomena, elements, the periodic system, as well as their descriptions by linear language, are equivalent and, ultimately, to mechanics. Since the physical component of materials science is informative, the main focus of the work

will be on chemistry, in which the concept of fractality is also represented by physics. The physical side of the issue was highlighted in the works of the authors [2, 3] and others.

The linearity inherent in physical and mathematical models is, in general, foreign to chemistry, because, obviously, all substances are binary formations consisting of material atoms/molecules held by intangible/invisible, field bonds. Therefore, more adequately chemistry concept is not atomic-molecular, but *web-like* substance whose properties are equally defined by its material and immaterial parts. The mathematics of networks that are also subject to (chemical) transformations is very poorly developed. In particular, the rules of arithmetic, which, in fact, introduce unaccounted mechanistic linearity into the model, do not act on networks without distorting the essence of the problem. This problem should be discussed separately, the scope of the article does not allow the development of argumentation more fully.

In summary, the problem of "reduction of chemistry to physics" looks as follows. In the chemical – qualitative, transformation of matter, the substance participates in the interaction of its *binary internal* space with external forces, phenomena, factors. The external becomes internal and vice versa, the boundary of the body becomes conditional. While in physics the internal space of bodies does not take any part – the boundary is absolute. This is the meaning of heating and/or other energy penetrating effects on the body, dispersion and mixing of substances that enter into a reaction, etc. These mathematical flaws are complemented by many unsolved problems of nucleosynthesis and elementary particle theory. The issues of nucleosynthesis are closely related, on the one hand, to questions of the evolution of stars, and, on the other, to the properties of nuclear interactions.

[4]. This is a well-known problem in natural science of the connection between the local (atoms) and the global (Universe), also known as the problem of "part and whole". In this point converges the problem of uncertainty of logical consequence, the notion of truth and the existence in contradiction. For biology, chemistry, and other natural sciences, these generally accepted concepts of logic do not exist now. Moreover, duality and contradictions in them are (naturally) scientific facts. This incompleteness gives rise to the contradictory semantic variability of many concepts and, as a result, prevents the formation of a holistic picture of science and the completeness of the model – at least in some approximation, when the truth of the part means consistency with the truth of the whole. For example, as an alternative, a test suggests itself instead of the traditional abstraction of separation, the abstraction of interpenetration with its obvious chemical meaning.

In the modeling of materials science, the main difficulty is its chemical part, which one usually tries to reduce to physics. During the existence and development of chemistry have been numerous attempts of its formalization by giving its basic law – the periodic system of Mendeleev mathematical form drawn via different sections of it – geometry, topology, group theory, etc. [5-14]. As far as the authors know, none of the approaches has given the fruitful development of mathematical methods for solving specific chemical (i.e., non-mathematical) problems and tasks. As recent work [15] showed, the form of the Periodic system changes depending on the choice of the properties of the elements, representing a hypergraph in which various types of periodicity and order can be detected. In other words, the Periodic system of elements is a *system* in the sense of the general systems theory, i.e. is special, distinct from physical

and mathematical, but closely connected with other sciences, space. The difference lies in the synthesis of many irreducible (i.e., mutually negating) formal languages that make up the model. Such objects lie at the intersection of all natural sciences, being their common part, which is consistent with a similar position in chemistry.

Today formed withdrawal line from standard models through engaging analysis and Fibonacci hyperbolic geometry, matrix structures [16-18]. In this direction, with general theoretical depth stands out book [19], in which the analysis of the periodic system is directly connected with the properties of numbers and the most general of the geometries – projective, i.e. the foundation of chemistry is associated with the fundamental concepts of mathematics, the closeness of the projective plane as a model of space, and the common constant of natural science – the number of the golden ratio. Therefore Fibonacci-like idea as closely related to the number of the golden section, looks very promising. In general, we can say that today there are numerous scattered model results related to the periodic table. The general physical and mathematical picture is not yet visible.

In this regard, it makes sense to pay attention to the following circumstance. Chemical elements make up the table as a whole – an *image*, i.e. *heterogeneous, integral in some sense*, formation. Such objects do not belong to the field of standard mathematics (except for tables, as auxiliary means of numerical methods). In contrast, *images* are typical for the fractal geometry of nature. A study conducted by the authors showed that empirical fractals are accompanied by an *already existing* logically connected line of mathematical constructions, which allows to look at the problems of materials science from a new point of view [2]. It arises when formalizing the idea of I.M.

Tananayev – to consider the particle size of the substance, i.e. the property of divisibility of matter (obviously also atoms – Auth.) by a separate degree of freedom. This formalization introduces into the arsenal of modeling the *second fundamental number system of mathematics* – *p*-adic numbers Q_p , which formalize this degree of freedom, thereby expanding the possibilities of modeling.

The aim of this work is to demonstrate that fractals via its formal analog – numerical asymmetry are promising candidate for the construction of adequate mathematical models of physico-chemical materials science. As new theoretical facts interpretation of *p*-adic numbers by S. Ulam, and their physico-chemical connotation by Tananaev, logical-linguistic idea of A.N. Parshin are introduced. These facts are described in detail in [20]. Mathematical modeling now operates in an expanded numerical space, making it possible to perceive the chemical subspace in it. This constitutes the content of the constructions.

2. FRACTALS AND NUMBERS IN CHEMISTRY

The periodic table as an *image* is semantically two-dimensional – along with an increase in the mass of elements, i.e. of their physical characteristics, it reflects a change in properties – qualitative, non-physical entities. One axis of the two-dimensionality is the mass axis or axis aggregation/divisibility of matter. It can be called the axis of nucleosynthesis. The second axis is the field axis – a set of electronic shells that determines the properties of elements. This is the axis of oxidation-reduction. This semantic two-dimensionality allows supplementing the physical types of duality – wave-particle, electromagnetic and thermodynamic ones by conjugated pairs having purely chemical specifics, such as “reaction-diffusion”, “oxidation-reduction”. These two pairs of oppositions correspond to

two basic numerical systems of mathematics – real R and p -adic numbers Q_p (here p is a prime number). Because of these numbers are the basis of the novelty of the method, here will be given the necessary information, equipped with physical and chemical interpretation. (more details in [20, part 1]).

3. p-ADIC NUMBERS IN PHYSICO-CHEMICAL INTERPRETATION

Real R and p -adic numbers Q_p are two basic number systems of mathematics. They are equally represented by formal power series in powers of the base equal to one of prime numbers $p = 2, 3, 5, \dots, 13, \dots, 41, \dots$, (which, however, to this day do not have a generally accepted natural-science interpretation):

$$\begin{aligned}
 x &= a_{-n}p^{-n} + a_{-n+1}p^{-n+1} + \dots + \\
 &+ a_{-1}p^{-1} + a_0 + a_1p + a_2p^2 + \dots + a_kp^k + \dots = \quad (1) \\
 &= \sum_{i=-n}^{\infty} a_i p^i, a_i \in A = \{0, 1, 2, \dots, p-1\}.
 \end{aligned}$$

In the same way, the positional record of both kinds of numbers is the same:

$$x = a_{-n}a_{-n+1} \dots a_0 a_1 \dots a_k \dots \quad (1^*)$$

This gives rise to measurable quantities of two kinds with the help of number metric functions, which are formal functional analogues of a universal pair of processes “convergence-divergence”. Real numbers are obtained from (1)-(1*) by adding (“nucleosynthesis”) all the digits and then all the digits disappear, p -adic – by distinguishing the digits (“splitting”) in the positional notation. The quantities (metrics) of these numbers have the form

$$x \in R, |x|_{\infty} = |x|, \quad \xi \in Z_2, |\xi|_2 = p^{-(-n)}. \quad (2)$$

More precisely, for p -adic numbers there are two metrics – multiplicative and additive:

1. Additive one gives the coordinate on the n axis of divisibility (*nucleosynthesis*) of matter. Its physical interpretation is the energy of particle formation/decay:

$$\begin{aligned}
 v_p(\xi) &= ord_p(\xi) = -n = -\ln |\xi|_p^{\alpha} \Rightarrow \quad (2^*) \\
 &\Rightarrow v_p(\xi + \eta) \geq \min \{ v_p(\xi) + v_p(\eta) \}.
 \end{aligned}$$

2. Multiplicative one gives the size of the particles when dispersed, physically – their mass:

$$|\xi|_p^{\alpha} = p^{-\alpha n}, \quad \alpha > 0 \Rightarrow |\xi + \eta|_p^{\alpha} \leq \max \{ |\xi|_p^{\alpha}, |\eta|_p^{\alpha} \}. \quad (2^{**})$$

If one do not take into account the genesis, then on the material axis $|x|_{\infty}$ and $|\xi|_2$ are indistinguishable. It is easy to verify that these two quantities are connected by a hyperbolic relation, known as power laws, which allows them to be distinguished by behavior:

$$|x|_{\infty} = c \cdot |x|_2^D, \quad (2^{***})$$

where D is the fractal dimension.

Expansions (1)-(1*) have a double meaning. When reading from right to left or from the reverse side of the sheet are converted into correct entry of real numbers. In other words, two kinds of numbers are connected by *negation*. In the proposed model (1)-(1*), the numbers are considered partly as p -adic, partly as real, i.e. on both sides of the sheet. For example, with $n > 0$, the decomposition to the right is a p -adic number, and to the left is a real number. Forms (1)-(1*) are also a numerical and coordinateless prototype of an iterated functions system, which is the main generator of fractals and the intersection of physics, language, biology, etc., where it is known as a hierarchy. Its action is the divisibility of matter, decomposability of systems, distinction and boundaries, disturbance of connectivity. For the first time such an interpretation of p -adic numbers S . Ulam suggested in the study of multiplicative processes arising in the fission chain reaction in 1955. Infinite division leads to zero dimensional sets or fractals. Therefore, like fractals, p -adic numbers are everywhere. Zero-dimensional sets do not have physical properties, they are invisible, they are numerical candidates for the role of fields of

various nature – physical (electromagnetic, gravitational, etc.), morphogenetic in biology, various linguistic ones. Moreover, all these heterogeneous fields coexist at every point in physical space, i.e. p -adic numbers are *multimodal*. In a recent work [21], the authors conclude – “The existence of a minimum length in quantum mechanics and a maximum speed of light are artifacts of the Archimedean basis of physics. Both of these assumptions are not supported by non-Archimedean (ie p -adic – Auth.) Physics.” Therefore, the number of mathematical systems makes up a pair of “material-ideal”. Ideal, symbolic, presents the properties of materials, often associated with human perception.

Geometrically real and p -adic numbers are represented by two oppositely directed trees. This mirror picture – numerical asymmetry $U = R \times Z_p$, is a formal analogue of the two-dimensional semantics of chemistry, which turns out to be consistent with all manifestations of duality in mathematics. Duality as the existence in a logical negation becomes one of the natural relationships and *mathematical operations*. It combines determinism with chance, gravity with repulsive force, compression with expansion, entropy processes are inextricable with energy. As a result, the resulting two trees – real and p -adic numbers are a condition for the existence of one another, they are connected as *real and possible, continuous and discrete*. Their combination provides another universal image of natural systems – the scale-invariant network, known in materials science as the atomic-molecular structure, Voronoi and Delaunay partitions.

The order of two numerical systems is reciprocal. They implement *two types of causality*, known as *compression, aggregation, materialization* and *expansion, dissipation, dematerialization* – synonyms of a universal pair of processes generated by a universal pair of *attractive*

and repulsive forces. Then, negation can be understood as complementarity – causality, the direction of time, topology, and the properties of members of the opposition are combined. The combination of two methods of coordination: physical and p -adic, provides the basis for adequate consideration of the geometry of the physico-chemical-symbolic space – it becomes locally hyperbolic, globally – projective (projective plane) Formally:

$U = R \times Z_2$, $u = x \cdot \xi$, $x \in R$, $\xi \in Z_2$ – space and number;

$$P^2(R) = R^2 \cup P^1(R) \text{ – projective plane; } (3)$$

$R = \text{inv } Z_2 = \neg Z_2$ – "coordinate axes" of the U (inv – involution, \neg – negation). Any statement of the logic P , formulas, equations, makes sense in both numerical systems:

$$R \leftarrow P \rightarrow Z_2, \tag{3*}$$

however, with different numerical results. This is the transfer principle, which includes the duality principle for networks.

p -Adic numbers are spatially-geometric numerical system because it is isomorphic to the conventional iterated functions system (*IFS – iterated function system*) – the basic unit for obtaining fractal images of various shapes. This property allows to cover, from a single point of view, the various versions of the images of the periodic table proposed by researchers – spiral, pyramidal, disconnected, network, etc. [see site *meta-synthesis.com*]. In this case, a computer that implements such correspondences acts as a theoretical tool – an operator specific to chemical (and not only) science, the only one that can match *strings* and *images* [22], giving them numerical content using a *non-linear* language (see above). In other words, having received on the monitor screen a picture of a mixture of two/three reacting substances that differ in color (see **Fig. 1**), the computer as an operator assigns a certain number to each micro-region the corresponding color, thus turning the reaction region into a numerical

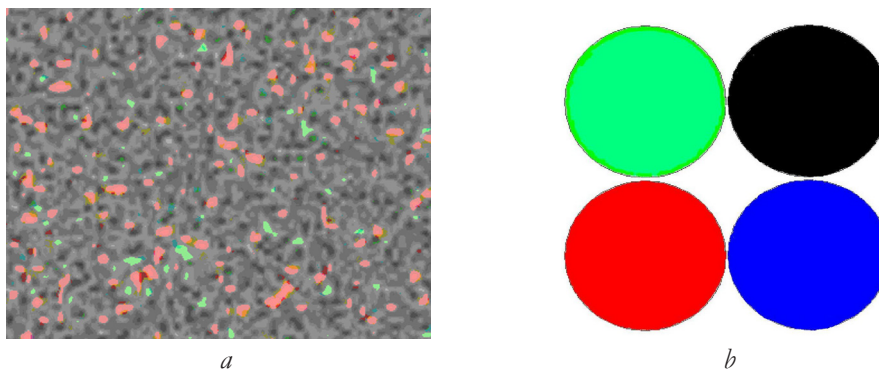


Fig. 1. The numerical image of a) the reaction as chemical addition; b) physical addition.

field, with the possibility of subsequent application of analytical/chemical calculation methods, the inclusion of motion, the contact of the valence orbits of atoms, etc.

Measurements: definability of the “golden section”. In the space of numerical asymmetry $U = R \times Z_2$, consisting of two subspaces with different topologies, the mathematical method of measurement – the axiom of Archimedes takes an unusual form. Since the number in U has the form $\|u\| = |x|_\infty \cdot |\xi|_2$, its measurement consists of the measurements of its two factors. In view of the fact that p -adic numbers are invariants of infinite divisibility, there is no definable unit in U (just as in ordinary mathematics, the unit is indefinable). And the axiom of Archimedes has a double meaning – as an additive and as a multiplicative process. Moreover, it can be written only recursively, in the sense of “the next result is equal to the sum of the previous ones and at the same time their product”. Formally:

$$u_{n+2} = u_{n+1} + u_n \text{ and } u_{n+2} = u_{n+1} \times u_n. \quad (4)$$

But these are the Vieta formulas of the quadratic equation $x^2 - u_{n+2}x - u_{n+2} = 0$. His decisions are known

$$x_{1,2} = u_{n+2} \cdot \frac{1 \pm \sqrt{5}}{2} = u_{n+2} \tau^\pm, \quad (5)$$

where the $\tau^+ = \frac{1}{\tau}$ number of the golden ratio = 1.618. In (5), it u_{n+2} is a large-scale factor manifesting τ on all floors of the natural hierarchy. Since a real number in U is defined as $\|u\| = |x|_\infty \cdot |\xi|_2$, due to the mutual

indeterminacy of two types of metrics, one of them is random in relation to the other. In physical space, random is ultrametric. If you write the "golden equation" in the form

$$\frac{x}{1-x} = \frac{1}{x}, \quad (6)$$

then, using the Logit-transform $z = \ln\left(\frac{x}{1-x}\right)$ for $\|u\|$ we obtain a distribution function $P(z) = \frac{1}{\|u\| \cdot \frac{1}{\|u\|}}$, that is very close to the Gaussian normal distribution, but with a finite support. Therefore, we find that the frequency of occurrence of “golden quantities” has a pronounced maximum and a clear dispersion [23].

Thus, this number is *determined* by the structure of the self-dual number system. Therefore, it τ can be taken as the natural base of τ -adic numerical system Q_2^τ . And decomposition (1) will take the form analogous to the Bergman system [24], which, like the 2-adic one, has same alphabet/digits, but also has additional useful properties, such as redundancy – any number can be represented by different Bergman codes [25]:

$$\begin{aligned} x &= a_{-n} \cdot \tau^{-n} + a_{-n+1} \cdot \tau^{-n+1} + \dots + \\ &+ a_{-1} \tau^{-1} + a_0 + a_1 \cdot \tau + a_2 \cdot \tau^2 + \dots + a_k \cdot \tau^k + \dots = \quad (7) \\ &= \sum_{i=-n}^{\infty} a_i \cdot \tau^i \quad a_i \in A = \{0, 1\}. \end{aligned}$$

The unit is determined in two ways. Additively as $1 = \tau^1 + \tau^2$. And multiplicatively as $1 = \tau^+ \times \tau$. Fibonacci numbers F_n are related to the τ

by relations $\lim_{n \rightarrow \infty} \frac{F_n}{F_{n-1}} = \tau$ and $F_n = \frac{1}{\sqrt{5}}(\tau^n - (-\tau)^n)$ for $n > 4$ with an error of less than 0.01. And also via the Binet formula:

$$F_n = \frac{\tau^n - (-\tau)^{-n}}{\tau - (-\tau)^{-1}}. \tag{8}$$

A useful property of this numerical system is that as it follows from (5) $\tau^+ \cdot \tau^- = 1$. Comparing this relation with (2**), which determines the relationship between two numerical metrics, we see that the two roots of the golden equation can be taken as real and ultrametrics, the constant c turns out to be computable and equal to the diameter of the scale level. And expansion (7) turns out to be an accurate representation of two numerical systems on a “golden” basis. In addition, the redundancy of the representation of an object by various codes of this system opens up the space for the existence of isotopes and isomers of chemical elements.

Global periodicity. Correspondingly, the expression for the ultrametrics (2*) and (2**) is corrected with the substitution of the bases 2 and p by τ . Written together on the plane $(|\cdot|_\infty, |\cdot|_\tau)$ isomorphic plane of complex numbers C , both metrics (2) and (2*) in the form:

$$n \mapsto r = \tau^{\pm i \alpha \cdot n}, \tag{9}$$

where $r, n \in R$ give a famous expression for the “golden spiral”. Its peculiarity is that it does not spin on a plane, but around the axis of mass – nucleosynthesis. This axis is the axis of the 2-adic tree. Therefore, summing up, we arrive at a spatial hyperbolic model [16] that reproduces, according to Mendeleev, the bodily and discrete characters of the system (Fig. 2), reproducing the numerous chemical properties of elements. A similar model was proposed by the authors of [19], calling this spiral a global periodic function. Their work contains a link between local and global in chemistry. Reducing these poles - the atom

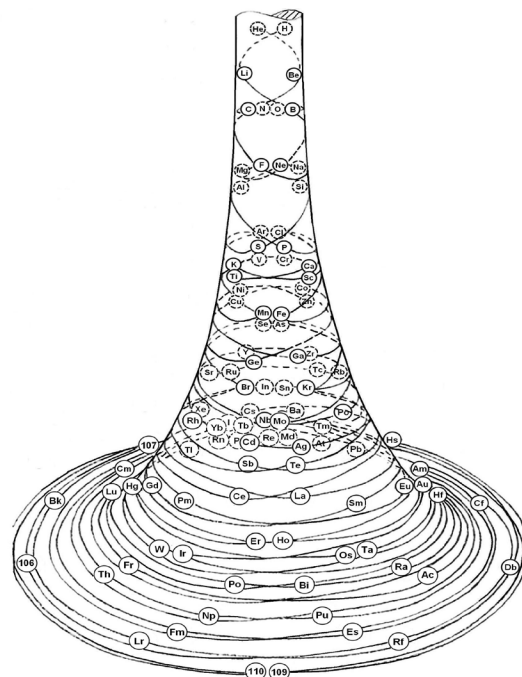


Fig. 2. The solid and discrete (according to Mendeleev) image of the periodic system.

and the Universe, through fractal geometry (it’s 2-adic!), they thus come to a projective model of the *chemical* universe. Clarification is required here. The authors obtain a projective plane by identifying infinity $+\infty = -\infty$ on the real axis. But by virtue of what was said above about the indeterminacy of unity, and, therefore, zero, the minus sign ($-$) has a conditional character, introduced for convenience, and often serving as an “operator” of time reversal, without a noticeable natural-science meaning. The Fibonacci series and 2-adic numbers do not contain it. Instead, the projective plane is obtained by identifications $|\cdot|_\infty \rightarrow \infty = |\cdot|_2 \rightarrow 0$ and $|\cdot|_2 \rightarrow \infty = |\cdot|_\infty \rightarrow 0$. In this case, the global periodicity of matter becomes a consequence of the closeness of space (see (3)). The work mentioned above [15] gives a scaled invariant network (hypergraph) as a model of the chemical Universe, and curvature can also be determined on it [26]. As a result, we get a variant of the Universe in which there is a place of duality-complementarity, i.e. chemistry and other natural sciences.

The general expression of a real number leads to a power law, which is similar to flicker noise – “amplitude-frequency”. Here, the additive variable is represented by mass m , and the multiplicative by frequency f . Since the golden section number that has a *Logit* distribution is included in this ultrametric, the obtained law of distribution of elements by mass (amplitudes) of nuclei has the form of a distorted hyperbola [4, Introduction, Fig. 8]. It is symptomatic that all these power-law dependencies have a completely different form in the sense of proximity of functions – from a smooth hyperbola (E. Fermi) to a “sawtooth” one (Ishkhanov B.I. et al.). Such power laws are typical for evolving systems and, in principle, can serve as an entry point for introducing p -adic numbers into the model. In this case, the periodic table is really seen “... as if by the reflection of a stopped some unknown yet dynamic process of development of inorganic matter” [30]. Thus, the model includes the idea of evolution of the composition of chemical elements.

4. NONLINEARITY OF CHEMICAL SPACE

The arguments of the previous section allow us to formalize the chemical Universe (for the developed theory, see [31]) as the resultant of the forces of aggregation (synthesis) and scattering (dispersion), formally represented by numerical asymmetry, $U = R \times Z_2$, $u = x \cdot \xi$, where R is the axis of nucleosynthesis, and Z_2 is the field measurement, the axis of oxidation-reduction, the axis of the electron shells. The motion along the field axis changes the properties of the elements, which is expressed by a change in the electronic composition of atoms. Stone duality allows us to imagine the volume of matter in two ways – as a material entity and as a formal language. From theoretical informatics it is known that language and property are one and the same thing (text and graphic editors of modern computers are

an example of this). Here, the properties of a substance are understood widely, including phase transitions between aggregate states. An expanded form of Stone duality is given in [20] (C is a Cantor perfect set, a classic example of a fractal $C \cong Z$, (not to be confused with C is complex numbers)):

$$C \cong C_{\text{matter}} \cong \exp(C) \cong 2^C \cong Z_\tau \cong [IFS \equiv \{0,1\}^N] \cong \\ \cong [Z_\tau \rightarrow Z_\tau] \cong C(Z_\tau, Z_\tau) \cong H \cong C_{\text{Bool}} \cong C. \quad (10)$$

Here: Z_τ is the set of numbers of the form (7), and the signs of equivalence (isomorphism) “ \cong ” mean in order from left to right:

- (1) C_{matter} is a model of fractal matter,
- (2) C is exponentially complete, i.e. mechanical transformations of matter do not change its numerical nature, τ -adic numbers Z_τ are an example of a spatially geometric numerical system, i.e. can encode objects of various shapes.
- (3) Such a distribution of matter is a spectrum of truth functions of Boolean algebra.
- (4) This is matter with numerical properties; there is Z_τ a topological algebra.
- (5) Such a structure of matter (zero-dimensional, discountual, fractal) coincides with the formal languages of theoretical informatics, is a domain in theoretical informatics (iterated functions system, is the central technique for generating fractals). This is a symbolic space, the scope of symbolic dynamics.
- (6) As a lattice, it coincides with the space of continuous functions above itself.
- (7) Such a numerical or algebraic image of matter can be represented by its field of continuous functions by Stone duality theorem.
- (8) The set of 2-adic numbers is a Hilbert space. This means that its elements can be interpreted in the form of vectors of the Hilbert space and in the form of functions. Thus, p -adic numbers can be regarded as a Banach algebra with involution, that is, a C^* -algebra. Z_τ – a discontinued version of the Hilbert space. In this form, it Z_τ is also Boolean algebra – the

basis of the symbolic technique (according to the same Stone theorem).

(9) The fractal distribution of *matteris*, according to the statement of M. Stone, the flip side of Boolean algebra, i.e. perfect, symbolic object.

Then a substance can be defined as a system of its properties using the reflective properties of p -adic numbers:

$$\forall n \in N, \forall p = \tau,$$

$$Q_\tau \cong Q_\tau \times Q_\tau \times \dots \times Q_\tau = Q_\tau^n, \tag{11}$$

$$Z_\tau \cong Z_\tau \times Z_\tau \times \dots \times Z_\tau = Z_\tau^n.$$

Here, each factor corresponds to one of the property fields. Since they are zero-dimensional formations, (11) answers the question – how can different fields coexist at one point in space, not only physical, but also linguistic and morphogenetic fields of biology. Using (10) and (11), it is possible to solve the problems of “material equivalent of function and properties” of material science and a similar “structure-function” of biology. As shown by the authors of [32], the stationary orbit of an electron is the resultant of the forces of Coulomb attraction and centrifugal repulsion. The electron orbit in this case, according to Bertrand’s theorem, has a two-loop form. The same image has numerical asymmetry, i.e. globally chemical universe U .

The multilayered image of the Universe as applied to an atom means many of its electronic orbits (**Fig. 3**). The image of the nucleus in the first figure, in comparison with its absence of m in the second, means just the presence of the axis of nucleosynthesis (2^{**}), while the second figure is simple $U = R \times Z_2$, i.e. image of electronic orbits. Attractors of nonlinear

systems have the same two-loop images (see [20, Appendix to Chapter 7]). The authors’ conclusion [19] on the identity of the micro- and macrocosms of the chemical universe has a formal justification.

Quantum numbers. This section outlines the reasons for using the τ -adic numerical system Z_τ as a model of the chemical properties. As a first step, the interpretation of Z_τ as a coordinateless functional space of quantum mechanics and the relationship of quantum numbers with it is proposed. According to the arguments of S. Ulam, at subnuclear distances, space cannot be smooth, it demonstrates a strong violation of local behavior, which entails the possibility of irregular topologies similar to p -adic ones [33].

The general structure of chemical elements is a dense core surrounded by an electron cloud, similar to the binary structure of chemistry. Then the physical meaning of the base $p = \tau$ of the numerical system of τ -adic numbers is a pair of “*matter (core) – field (e-cloud)*” or, mathematically, “*connectivity-discreteness*”. Then Z_τ is a Hilbert space consisting of wave functions as a zero-dimensional space; it is capable of generating field and matter in addition (i.e., the known wave nature of matter). The quantum mechanical properties are preserved under such an interpretation.

The hypothesis of a τ -adic relation of quantum numbers is as follows. Consider Z_τ as the union of four self-similar “circles”. Visually, these are 4 binary trees with a common root (**Fig. 4**).

On this tree, we consider the trajectories, i.e. functions – paths connecting vertices. For example, the vertices of the upper right branch with the vertices of the lower right. Then, if we put the principal quantum number n equal to the number of the level of the division hierarchy, then the orbital quantum number $l = (0, 1, 2, \dots, n-1)$ coincides with the set of levels of the hierarchy. In Fig. 4 $n = 4, l = (0, 1, 2, 3)$. These

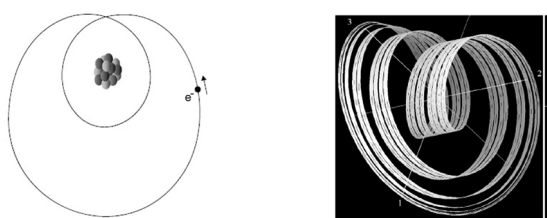


Fig. 3. The nonlinearity of the atom and space.

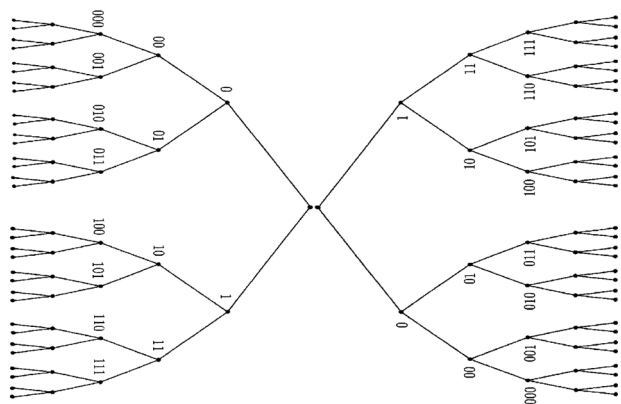


Fig. 4. 2-adic space of waves and particles.

two numbers are common to all four branches. The magnetic quantum number m_l coincides with the segment $(-l, l)$. When moving to the root, the path is deterministic, from the root it is non-deterministic. The left and right half of the figure are associated with a spin quantum number $m_s = (1/2, -1/2) \cong (\alpha, \beta)$.

Thus, the considered trajectories $\xi^- = a_0 a_1 \dots a_n \in Z_2$ as wave functions that have a double – deterministic and nondeterministic meaning, and as elements of the numerical system Z_2 naturally connect all four quantum numbers. Based on the foregoing, the closest seems to be the interpretation of the periodic law as an infinite-dimensional functional space [11]. The stated hypothesis concerns the periodic system of free atoms, which, however, is different from the periodic system of chemical elements [34].

5. CONCLUSIONS

Based on the analysis of mathematical models of materials science, the introduction of a new degree of freedom is substantiated – the divisibility of matter and its digitization by p -adic numbers. Physicochemical and general scientific interpretations of p -adic numbers are given.

Together with real numbers, they form a physic-chemical space that allows the existence of the properties of substances, as illustrated by the expanded form of Stone duality. In this space, the axis of nucleosynthesis and the axis

of oxidation-reduction are distinguished, which makes it possible to introduce, in addition to the known physical pairs of oppositions, pairs inherent in chemistry. The existence of two types of causality, expressed by the pairs “attraction-repulsion”, “synthesis-decay”, “convergence-divergence”, “aggregation-dissipation”, and others synonymous with them, is shown. The formal model of material science as a physical and chemical science is a self-dual numerical system that expands the modeling arsenal in the direction of increasing its adequacy.

As an alternative to disparate theories, an approach based on Fibonacci numbers as the common constant of natural sciences is chosen. It has been formally proved that the number of the “golden ratio” is the base of the numerical system of the physico-chemical space, which is largely analogous to 2-adic numbers. Thus, all disparate works on the models of the periodic table of Mendeleev gain a single framework and reliable formal justification.

The periodicity of matter as a consequence of the identity of nonlinear models of the atom and the Universe is substantiated. Geometrically, it follows from the projective model of space. The consistency of the proposed model with quantum representations by extracting quantum numbers from the structure of the model without additional assumptions and calculations is shown.

In general, it has been demonstrated that the proposed numerical version of physico-chemical materials science is consistent with the known results, providing their empirical nature with mathematical validity.

Special mention should be made of the nonphysical properties of materials. Properties are described in formal languages. By the Rice-Uspensky theorem, any non-trivial property of a language is undesirable, i.e. it is impossible to single out any specific property of a material

in a formally familiar language. The question remains whether this solution is possible within the framework of the proposed approach.

REFERENCES

1. Kurashov VI. *History and philosophy of chemistry*. M., 2009.
2. Izotov AD, Mavrikidi FI. *Fractals: divisibility of matter as a degree of freedom in materials science*. Samara, SSAU, 2011, 128 p.
3. Izotov AD, Mavrikidi FI. Numerical asymmetry of the internal space of non-crystalline materials. *Bulletin of the Samara Scientific Center of the Russian Academy of Sciences*, 2017, 19(1):5-24.
4. Ishkhanov BI, Kapitonov IM, Tutyn IA. *Nucleosynthesis in the universe*. M., Moscow State University Publ., 1998, Introduction.
5. Mazurs EG. *Graphic Representations of the Periodic Table System During One Hundreds Years*. Alabama, 1974.
6. Imyanitov NS. The equation for the law of Mendeleev. *Nature*, 2002, 6:65-69 (in Russ.).
7. Imyanitov NS. The Periodic Law. Formulations, Equations, Graphic Representations. *Russian Journal of Inorganic Chemistry*, 2011, 56(14):2183-2200 (in Russ.).
8. Restrepo G, Pachon L. Mathematical Aspects of Periodic Law. *Foundations of Chemistry*, 2007, 9:189-214.
9. Korotky VM, Melentyev GB. On the spiral-matrix structure of a periodic law. *Proc. of the International Scientific and Practical. Conf. "Prospects for the development of modern mathematical and natural sciences"*. Voronezh, ITSRON, 2015, Issue II, p. 30-33 (in Russ.).
10. Scerri ER. *The Periodic Table*. Oxford, University Press, 2007.
11. Korableva TP, Korolkov DV. *Theory of the periodic system*. SPbSU Publ., 2005, 172 p., (in Russ.).
12. Rouvray DH, King RB. The Periodic Table: Into the 21st Century. *Journal of chemical education*, 2006, 83(6); DOI: 10.1021/ed083p849.
13. Didyk YuL, Astafyeva EM. *Mirror symmetry in the structure of an atom and the periodicity of elements*. St. Petersburg, Khimizdat Publ., 2008, p. 106, (in Russ.).
14. Chernyshev SL. *Four Dimensions of the Periodic System of Elements*. M., Lenand, 2019.
15. Leal W, Restero G. *Formal structure of Periodic System*. arXiv: 190210753v1. [CS.DM] 27Feb, 2019.
16. Shilo NA, Dinkov AV. The phenotypic system of atoms in the development of D.I. Mendeleev. "Academy Trinitarizm", M., El № 77-6567, publ.14630, 09.11.2007. (in Russ.).
17. Petoukhov S.V. Metaphysical aspects of the matrix analysis of genetic coding and the golden ratio. *Metaphysics*. Moscow, Binom, 2006, p. 216-250, (in Russ.).
18. Stakhov A, Rozin B. The Golden Section, Fibonacci series and new hyperbolic models of Nature. *Visual Mathematics*, 2006, 8(3), <http://www.mi.sanu.ac.yu/vismath/stakhov/index.html>.
19. Boeyens JCA, Levendis DC. *Number Theory and Periodicity of Matter*. Springer, 2008.
20. Mavrikidi FI. *Numerical asymmetry in applied mathematics*. M., Delfis Publ., 2016, 416 p.
21. Rosinger EE, Khrennikov AYu. Beyond Archimedean Space-Time Structure. *Advances in Quantum Theory*, 2011, 1327:520-526.
22. Izotov AD, Mavrikidi FI. Computer and numerical asymmetry in the engineering sciences. *Proc. Prokhorov Academy of Engineering Sciences*, 2013, 2:31-42 (in Russ.).
23. Izotov AD, Mavrikidi FI. Numerical asymmetry, golden ratio and quasicrystals. *Bulletin Prokhorov Academy of Engineering Sciences*, 2015, 1:3-6, (in Russ.).

24. Bergman G. A Number System with an Irrational Base. *Math. Mag.*, 1957, 31(2):98-110.
25. Stakhov A. *Numerical Systems with Irrational Bases for Mission-Critical Applications*. World Scientific Publ., 2018, 284 p.
26. Leal W, Restero G, Stadker PF, Jost J. Forman-Ricci Curvature for Hypergraphs. arXiv:1811.07825 [cs.DM] Nov 19, 2018.
27. Fermi E. *Lectures in atomic physics*. M., RHD, 2011 P.46.
28. Saito K. (ed.) *Chemistry and the periodic table*. Moscow, Mir Publ., 1982, p.14.
29. Frank-Kamenetsky D.A. The origin of chemical elements. *Soviet Physics Uspekhi*, 1959, 68(3):529-556.
30. Kedrov B.M. *Microanatomy of the great discovery*. Moscow, Nauka Publ., 1970, 245 p.
31. Boeyens JCA. *Chemical Cosmology*. Springer, 2010.
32. Ceulemans A, Thyssen P. The Chemical Mechanics. In Scerri E, Restero G. (eds.) *Mendeleev to Oganesson: Multidisciplinary Perspective on the Periodic Table*. Oxford University Press, 2018, Ch 5.
33. Everett CJ, Ulam S. On Some Possibilities of Generalizing the Lorentz Group in the Special Relativity Theory. *J. of Combinatorial Optimization*, 1966, 1:248-270.
34. Izotov AD, Izotova VO, Mavrikidi FI. Geometry as a parameter in the processes of creating materials. *Solid state chemistry: nanomaterials, nanotechnology*. Abstracts of the XI International Scientific Conference. Stavropol, 2012, SevKavSTU, p. 215-217, (in Russ.).

DOI: 10.17725/rensit.2019.11.291

Improving the accuracy of measurement time intervals of radio reception in the framework of recursive multi-stage Bayesian estimates

Yuri N. Gorbunov

A.I. Berg Central Research Institute of Radioengineering, <http://www.cnirti.ru/>
Moscow 107078, Russian Federation

Kotelnikov Institute of Radioengineering and Electronics of RAS, Fryazino branch, <http://fire.relarn.ru>

Fryazino 141190, Moscow region, Russian Federation

E-mail: gorbunov@ms.ire.rssi.ru

Received 03.12.2019, peer reviewed 18.12.2019, accepted 20.12.2019

Abstract. The conditions of increasing the accuracy of digital measurement of repeating signal parameters (increasing the resolution) in measuring radio reception systems by reducing sampling and quantization errors, with a random nature of the change in the measurement conditions (experiment conditions) are analyzed. The method of reducing the errors of digital measurement during random modulation of the phase of the quantizing sequence and conducting multi-stage measurements using recursive optimal estimates from the theory of statistical estimation is analyzed in detail. By analogy with adaptive digital filters, a hypothesis is put forward about the possibility of increasing instrumental accuracy (reducing instrumental errors) in measuring repeated time intervals with random modulation of the initial phase of quantizing pulses and using feedback in the experiment. Thus, the fundamental possibility of creating the fundamental basis of ultra-precise measurements is proved. Similarly, an increase in image sharpness along the X, Y axes is realized, for example, the aperture of the line of receiving sensors and the use of rough ("Boolean") statistics of the input signal. The approach based on the recursion of measurements due to changes in the conditions of the experiment using the statistical test method (Monte Carlo method) is considered. To clarify (interpolate) the position of the end of the measured segment inside the resolution element and thus achieve the effect of "instrumental overresolution" of multiple measurements.

Keywords: chaotization of measurements (randomization), chaotic modulation of the phase, rough counting, measurement recursion, instrumental accuracy, discretization and quantization effects, feedback, stochastic linearization

UDC 621.396.96

For citation: Yuri N. Gorbunov. Improving the accuracy of measurement time intervals of radio reception in the framework of recursive multi-stage Bayesian estimates. *RENSIT*, 2019, 11(3):291-298; DOI: 10.17725/rensit.2019.11.291.

CONTENTS

1. INTRODUCTION (292)
 2. PROBLEM STATEMENT (292)
 3. BAYES ESTIMATES OF PROBABILITY ON FREQUENCY AND MAXIMUM LIKELIHOOD ESTIMATES (294)
 4. FEEDBACK COUPLING IN A TIME INTERVAL METRE A METHOD OF STATISTICAL TRIALS (295)
 5. CONCLUSION (296)
- REFERENCES (296)

1. INTRODUCTION

In a number of problems of a radiolocation and the radio measuring technics it is not required derivings of exact instant references of time intervals, therefore measuring process can be organised not on one, and on a series (pack) n of impulses. In that case when the modification of the measured parametre can be neglected, an instrumental error reduce at the expense of randomization of algorithms of measuring at usage of statistical handling of "rough" current references of time intervals. As a result of it high-speed performance of equipment, in particular metering circuits (measuring of time intervals by the specified mode makes a subject of engineering application of a known Monte-Carlo method in calculus mathematics [1, 2]) decreases. Enough the close engineering problem (to the mentioned measurer). The image processing problem is. As in that, and other case, it is primary (at measuring)

it is used the method of the direct account, however remains some error of step-type behaviour which cannot be subjected a method of the direct account any more since it becomes less prices of division of a measuring dial of the tool.

2. PROBLEM STATEMENT

Immediate usage of a Monte-Carlo method (method of statistical trials of SI) does not allow to gain, unfortunately, enough effective valuation because of low speed of convergence of evaluations. We will illustrate it on an example of measuring of an iterated time interval. Measuring (estimation) by a SI method is led [3] by count of number m of coincidence of two independent sequences. The first sequence consists of short quantizing impulses (scores) with known reference phase τ_0 , second – from n times of an iterated measured time interval duration τ . The second sequence has the phase of a recurring modulated on the casual law T . Modulation of phase of a recurring of measured impulses can be created artificially, for example by insert in a chain of start radar station (RLS) of the wobbler of repetition frequency.

If the moments of occurrence of measured intervals are independent and are uniformly proportioned within an

interval τ_0 "rough" references of time intervals on separate trials will differ on magnitude $\mu_i \tau_0$ [3], where

$$\mu_i = \begin{cases} 1, & \text{with probability } p = R\{\tau / \tau_0\}, \\ 0, & \text{with probability } q = 1 - p, \end{cases}$$

$R\{\tau / \tau_0\}$ function of a fractional share of the ratio τ / τ_0 .

The statistics of coincidence $m = \sum_{i=1}^n \mu_i$ in n trials is proportioned under the binomial law:

$$W\left(\frac{m}{n} / p\right) = c_n^m p^m q^{n-m}, \quad (1)$$

c_n^m – number of combinations of n by m .

The probability p can be estimated on frequency of coincidence $p^* = m/n$ therefore a τ^* time interval estimate τ

$$\tau^* = \tau_0(E\{\tau / \tau_0\} + p^*) = \tau_0(E\{\tau / \tau_0\} + m/n). \quad (2)$$

$E\{\tau / \tau_0\}$ function of an integer part of the ratio τ / τ_0 .

Medial on all m quadrature of an error of estimation (2) taking into account expression (1) we will gain in an aspect

$$\begin{aligned} M\{(\tau^* - \tau)^2 / p\} &= \tau_0^2 M\{(p^* - p)^2 / p\} = \\ &= \tau_0^2 D_0 = \tau_0^2 \sigma^2, \end{aligned} \quad (3)$$

where $\sigma = \sqrt{D_0} = \sqrt{M\{(p^* - p)^2 / p\}} = \sqrt{pq/n}$ mean squared error of measuring of probability p on frequency m/n , $M\{\cdot\}$ expectation operation.

From the equation (3) we will discover a mean squared error of estimation σ_τ оценки интервала of an interval τ

$$\sigma_\tau = \sqrt{M\{(\tau^* - \tau)^2 / p\}} = \tau_0 \sigma. \quad (4)$$

From the formula (4) it is visible that the error σ_τ of measuring of an interval τ (at admissible on high-speed performance of applied equipment a quantization interval τ_0) is completely spotted by an error of measuring σ of probability p which depending on number n of processed impulses decreases rather slowly and has the order $n^{1/2}$.

It is easy to show that the $p^* = m/n$ probability estimate p is a maximum likelihood estimate converting into a maxima function of verisimilitude (1), in a sense understood as function from a variable p .

Lowering reviewing of obvious problems on a competence and efficiency of a maximum likelihood estimate, it is necessary to score that the lower bound of its error gained from an inequality of Rao-Kramera [4], is spotted also by expression (4).

In paper the answer to a problem is given: whether it is possible to raise in addition a measurement accuracy of probability p if field of maximum likelihood estimates to dilate more blanket nonrecursive and recursive Bayes estimates. In a sense this problem can be considered as a problem of "an instrumental supersolution».

3. BAYES ESTIMATES OF PROBABILITY OF A SOFTWARE TO FREQUENCY AND MAXIMUM LIKELIHOOD ESTIMATES

If the aprioristic cumulative distribution function to designate through $W(p)$, posteriori – $w(p/m/n)$ verisimilitude function – $w(m/n/p)$ at a quadratic loss function the Bayes estimate p_{opt}^* of probability p will be noted as follows:

$$p_{opt}^* = \int_0^1 pW\left(\frac{p}{m/n}\right)dp = \int_0^1 \frac{pW\left(\frac{m/n}{p}\right)}{G\left(\frac{m}{n}\right)}W(p)dp. \quad (5)$$

Here $G\left(\frac{m}{n}\right) = \int_0^1 w\left(\frac{m/n}{p}\right)W(p)dp$ normalising coefficient. In the formula (5) it is possible to use floppy enough aprioristic probability density $W(p)$ in the form of [5] β allocations:

$$W(p) = \frac{\tilde{A}(v_1 + v_2)}{\tilde{A}(v_1)\tilde{A}(v_2)} p^{v_1-1}(1-p)^{v_2-1}, \quad p \in [0, 1], \quad (6)$$

where $\Gamma(v)$ – γ function.

Selection of parameters v_1 also v_2 it is possible to gain a major set of allocations (including uniform at $v_1 = v_2 = 1$), practical problems corresponding to a wide range. Association on p the conditional medial quadrature of an error $M\{(p^* - p)^2/p\}$ for a maximum likelihood estimate and a bayesian estimate is reduced in a **Fig. 1**.

By means of formulas (1), (5), (6) we will gain a bayesian (optimal) estimate

$$p_{opt}^* = (m + v_1) / (n + v_1 + v_2). \quad (7)$$

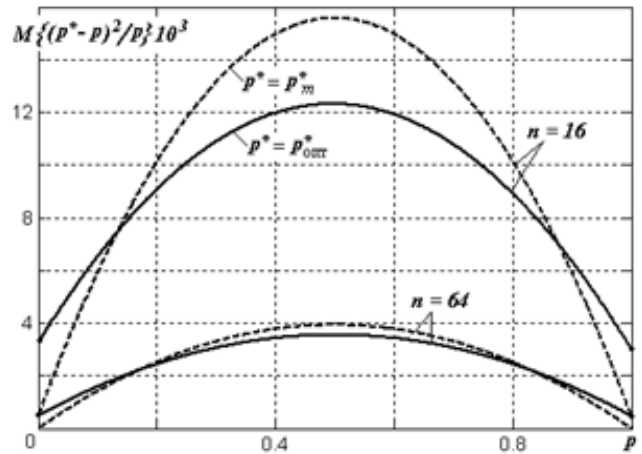


Fig. 1. Medial quadrature of an error for a maximum likelihood estimate (a shaped line) and a bayesian estimation (solid line) for $n = 16$ and $n = 64$.

Medial quadrature of an error of measuring of probability p for the uniform aprioristic law $W(p) = 1$ ($v_1 = v_2 = 1$):

$$M\{(p_{i\text{ML}}^* - p)^2 / p\} = \frac{np(1-p) + (1-2p)^2}{(n+2)^2}. \quad (8)$$

Comparing medial quadratures of errors of Bayes and maximum probable p_m^* estimates, it is possible to discover cross points (drawing) of curves $M\{(p_{opt}^* - p)^2 / p\} = \frac{np(1-p) + (1-2p)^2}{(n+2)^2}$. Differently, in a gamut $p < 0.15$ and $p > 0.85$ it is necessary to use a maximum likelihood estimate, in a remaining gamut the p Bayes estimate is better. However advantages of a maximum likelihood estimate in the specified gamuts are reached only when the measurand lies in them, i.e. the aprioristic information concerning magnitude of measured probability is necessary.

For a raise of a measurement accuracy or cutting of number of trials when all aprioristic informations are settled, it

is necessary to discover new reserves. Step-by-step procedure of measuring of probability when observed datas at the previous stages are considered as the aprioristic informations for the subsequent stages, does not give additional scorings. Really, if by results of measuring at each stage to take a maximum likelihood estimate

$$p^*(m_i) = m_i / n_i, \quad i = 1, 2, 3, \dots, l,$$

where l number of stages of measuring; n_i sizes of each stage on observed datas after l stages it is possible to generate a resultant an estimate:

$$p_{\Sigma}^* = \sum_{i=1}^l \eta_i p^*(m_i) \quad (9)$$

(η_i – unknown weighting coefficients), and

$$\sum_{i=1}^l \eta_i = 1. \quad (10)$$

Taking into account limiting (10), optimum weighting coefficients $\eta_{i\text{opt}}$, $i = 1, 2, \dots, l$ error of estimations (9) minimising the conventional medial quadrate, are gained in an aspect

$$\eta_{i\text{opt}} = n_i / \sum_{i=1}^l n_i. \quad (11)$$

Substituting the equation (11) in (9), we will have

$$p_{\Sigma}^* = \sum_{i=1}^l m_i / \sum_{i=1}^l n_i = m / n.$$

Thus, the total estimate p_{Σ}^* coincides with a maximum likelihood estimate одноэтапной procedures for $n = \sum_{i=1}^l n_i$.

4. FEEDBACK COUPLING IN THE TIME INTERVAL METER THE METHOD OF STATISTICAL TRIALS

The previous outcomes have spotted limits of a method of statistical trials at the expense of use of the aprioristic informations. In that case when the aprioristic informations are settled completely, it is necessary to discover essentially new reserve of a raise of accuracy of a method of statistical trials. The supposition about a possibility of application of feedback coupling in estimation procedure is with that end in view made. We will divide all volume of trials n into two and more stages. The first stage in volume n_1 represents the classical plan of independent trials of Bernulli. At development of an estimate p_1^* of initial probability $p = R\{\tau/\tau_0\}$ at the first stage it is necessary to use all available aprioristic informations. Differently, the estimate p_1^* is optimum Bayes. Further on an estimate p_1^* the correcting reference component δ which is added to an initial unknown quantity of measured probability is made p . Thus, at the second stage in volume n_2 measuring of new magnitude is spent

$$p_2 = p + \delta. \quad (12)$$

The estimate p_2^* by results of the second stage depends on observed datas at the first stage. Following the results of two stages the resultant an

estimate $p_{1,2}^* = p_1^* \eta_1 + (p_2^* - \delta) \eta_2$, where η_1, η_2 weighting coefficients is made, $\eta_1 + \eta_2 = 1$.

It is necessary to note that the assumption about a feedback coupling possibility at measuring is not always realizable. However measuring of time intervals by a method of statistical trials - an ideal case of embodying of offered idea. For introduction of the reference component, obviously, it is possible to apply a lag line with switching of taps. The reference component δ is equivalent to a delay of back edge of a measured interval at the second stage for a while $\delta \tau_0$. In some measure related idea is the urn plan of Polya [5]. However in the plan of Polya magnitude of the correcting component (number of full-spheres of certain colour) is constant, its sign (colour of added full-spheres) changes only. The prospective correcting component δ is function of the previous measurements $\delta = \delta(p_1^*)$.

As a matter of fact developed idea two-staged procedures the estimate after the first stage p_1^* is used for making of the best requirements of measuring of probability at the second stage. The previous outcomes testify that total measuring $p + \delta = 1$ as at $p = 0$ or $p = 1$ the conventional medial quadrate of an error the least will be the best requirement of measuring.

Thus, the algorithm of the correcting reference component is extremely simple:

$$\delta(p_1^*) = 1 - p_1^* \tag{13}$$

Let's note expression for medial quadrate of an error of a resultant of an estimate $p_{1,2}^*$

$$\begin{aligned} M_{1,2} \{ (p_{1,2}^* - p)^2 \} &= \int_0^1 \left\{ \sum_{m_1=0}^{n_1} \left[\sum_{m_2=0}^{2n_2} (p_1^* + \eta_2(p_2^* - 1) - \right. \right. \\ &- p)^2 W \left(\frac{m_2}{n_2} / m_1, p \right) \right] \times W \left(\frac{m_1}{n_1} / p \right) \right\} W(p) dp = \\ &= \int_0^1 \left\{ \sum_{m_2=0}^{n_1} \left[(p_1^* - p)^2 - 2\eta_2(p_1^* - p) \sum_{m_2=0}^{2n_2} (p_2^* - 1) \times \right. \right. \\ &\times W \left(\frac{m_2}{n_2} / m_1, p \right) + \\ &+ \eta_2^2 \sum_{m_2=0}^{2n_2} (p_2^* - 1)^2 W \left(\frac{m_2}{n_2} / m_1, p \right) \right] W \left(\frac{m_1}{n_1} / p \right) \right\} W(p) dp = \\ &= D_1 - 2\eta_2 D_1 + \eta_2^2 D_2, \end{aligned} \tag{14}$$

where

$$D_1 = \int_0^1 \left[\sum_{m_1=0}^{n_1} (p_1^* - p)^2 W \left(\frac{m_1}{n_1} / p \right) \right] W(p) dp,$$

Optimising (14) on η_2 we will gain

$$\begin{aligned} M_{1,2opt} \{ (p_{1,2}^* - p)^2 \} &= \\ &= (D_1 - 2\eta_2 D_1 + \eta_2^2 D_2) / \eta_2 - \eta_{2opt} = \\ &= \frac{D_1}{D_2} (D_2 - D_1). \end{aligned} \tag{15}$$

Comparing $M_{1,2opt}$ with D_0 under condition of identical total amount of trials $n = n_1 + n_2$ for a case small $n = 2, 3, 4$ (see the **Table**), it is possible to draw following deductions:

1. The partition reduces medial quadrate of an error of measuring by stages in comparison with one-staged procedure at identical total volume of trials

Table
Calculation of the relative scoring B in percentage % for various relations between stages n_1 and n_2 for двухэтапной procedures.

Designation	"1+1"	"2+1"	"1+2"	"2+2"
n_1	1	2	1	2
n_2	1	1	2	2
γ_{2opt}	9/32	32/129	18/41	64/161
D_2	16/31	43/256	123/972	161/1536
D_1	1/18	1/24	1/18	1/24
D_0	1/24	1/30	1/30	1/36
$M_{1,2opt}$	23/576	27/3096	23/738	94/3864
$B = (D_0 - M_{1,2opt})/D_0$	4	5.9	6.5	9.5

2. With growth the n medial quadrate of an error at двухэтапной to procedure impinges faster, than at одноэтапной so the scoring grows.
3. The scoring depends on a relation of volumes between stages.

The analysis of medial quadrate (15) for a case of the major $n \geq 1$ is hampered owing to sectionally continuous exposition D_2 on the statistican m . However the analysis somewhat becomes simpler if to consider normalisation of function of probability $W(p_2/p)$ with growth n_1 . Outcomes of the basic calculations are tabulated.

From formulas (12), (13) and (7) it is visible that probability function $W(p_2/p)$ is actually binomial. Hence, with growth the n_1 asymptotics of the Moavre-Laplace, therefore is valid

$$W(p_2 / p) \cong \frac{1}{\sqrt{2\pi\sigma_{p_2}}} \exp\left\{\frac{(p_2 - a)}{2\sigma_{p_2}^2}\right\},$$

where a $\sigma_{p_2}^2$ variance of a frequency function an $W(p_2/p)$, a - average (on all m_1) value p_2 .

Considering conversions (12), (13) and (7), it is possible to show that

$$\sigma_{p_2}^2 = n_1 p(1 - p) / (n_1 + 2)^2, \\ a = (n_1 + 1 + 2p) / (n_1 + 2).$$

As a result of an average on m_2, m_p, p expressions D_1 and D_2 from (15) taking into account approximations

$$\{\Phi(a / \sigma_{p_2}) - \Phi(a / \sigma_{p_2} - 2)\} \cong 2, \\ \exp\{-(1 / 2\sigma_{p_2}^2)(2 - a)^2\} \cong 0,$$

где $\Phi(u) = \frac{1}{\sqrt{2\pi}} \int_0^u e^{-t^2/2} dt$ integral of Laplace, we will gain

$$D_2 = \frac{1}{3(n_1 + 2)^2} + \frac{n_1(n_2 - 1)}{n_2(n_1 + 2)} \frac{1}{6} + \frac{1}{4} \sqrt{\frac{\pi}{2}} \frac{1}{n_2 \sqrt{n_1}},$$

$$D_1 = 1 / 6(n_1 - 2).$$

As $n_1, n_2 \gg 1$ that

$$D_2 \cong 1 / 6n_1 + (1 / 4)\sqrt{\pi / 2}(1 / n_2 \sqrt{n_1}),$$

$$D_1 \cong 1 / 6n_1.$$

Expression for medial quadrate of an error at двухэтапной to procedure looks like

$$M_{1,2opt} \cong D_2 - D_1 = (1 / 4)\sqrt{\pi / 2}(1 / n_2 \sqrt{n_1}).$$

Examination $M_{1,2opt}$ on an extreme (minimum) at the fixed $n = n_1 + n_2$ gives a following optimum relation between stages: $n_2 = 2n_1$. Then

$$M_{1,2opt} \cong 3\sqrt{3\pi} / (8\sqrt{2}n\sqrt{n}) = 3^{3/2} \pi^{1/2} / (2^{7/2} n^{3/2});$$

$$\sigma_{1,2opt} = \sqrt{M_{1,2opt}} \cong 3^{3/4} \pi^{1/4} / (2^{7/4} n^{3/4}).$$

5. CONCLUSION

Modulation of phase of a recurring of measured impulses under the casual law at measuring of iterated time intervals by

a Monte-Carlo method allows to raise at handling of impulses a measurement accuracy in \sqrt{n} time.

The raise of a measurement accuracy within the limits of nonrecursive (ОДНОЭТАПНЫХ and МНОГОЭТАПНЫХ) Bayes estimates is impossible without usage of the aprioristic informations concerning a measured interval.

The supposition about a feedback coupling possibility in a Monte-Carlo method is made and proved that an additional raise of a measurement accuracy of time intervals probably within the limits of the recursive Bayes estimates.

Application of recursive (2-etaпnyh) Bayes estimates of measuring of time intervals gives the chance to increment a measurement accuracy in $n^{1/2} - n^{3/4}$ time.

REFERENCES

1. Sobol IM. *Chislennye metody Monte-Karlo* [Numerical Monte-Carlo methods]. Moscow, Nauka Publ., 1973, 312 p.
2. Ermakov SM. *Metod Monte-Karlo i smezhnyye voprosy* [Monte-Carlo method and the adjacent problems]. Moscow, Nauka Publ., 1975,
3. Balashov VP, Valitov RA, Vikhrov GP at all; Ed. VP Balashov. *Avtomatizatsiya radioizmereniy* [Automation of radio measurements]. Moscow, Sov. radio Publ., 1966, 527 p.
4. Wilks S. *Matematicheskaya statistika* [The mathematical statistics]. Moscow, Nauka Publ., 1967, 632 p.
5. Feller V. *Vvedenie v teoriyu veroyatnostey i ee prilozheniya* [Introduction in probability theory and its applications]. Vol. 1, 2. Moscow, Mir Publ., 1967.

DOI: 10.17725/rensit.2019.11.299

About AlGaAs-heterostructures CVC kinetics simulation**Natalia A. Vetrova, Evgeny V. Kuimov, Sergey A. Meshkov, Vasily D. Shashurin**Bauman Moscow State Technical University, <http://bmstu.ru/>

Moscow 105005, Russian Federation

E-mail: vetrova@bmstu.ru, ekjmo@mail.ru, sb67241@mail.ru, schashurin@bmstu.ru

Received 21.08.2019, peer reviewed 20.09.2019, accepted 23.09.2019

Abstract. A model of degradation of AlGaAs-heterostructures is presented. The model of dissipative processes was extended to the case of a diffusion-blurred aluminum profile. The definition of the Γ -X-mixing operator is generalized for potentials without explicit heterojunctions. The effect of degradation processes on inelastic scattering is taken into account by applying the diffusion equation to the optical potential profile. The self-consistency algorithm was optimized in order to reduce the calculation time. This paper proposes a faster method based on the reduction in the number of calculated integrals for electrons density. A number of test structures were simulated via developed algorithm. The deviation of the calculation results from the experimental data on the curvature of CVC initial section does not exceed 3%. Thus, we can conclude that it is expedient to use the model to calculate the kinetics of heterostructures CVC initial section at elevated temperatures, including within the framework of the task of predicting the GIC and MIC UHF reliability indicators based on multilayer AlGaAs-heterostructures.

Keywords: heterostructures, nanoelectronics, mathematical modeling, structure degradation, self-consistent potential, dissipative processes.

UDC 004.052, 538.91

Acknowledgments: This work was financially supported by the Ministry of Education and Science of the Russian Federation, project No. 16.1663.2017 / 4.6.

For citation: Natalia A. Vetrova, Evgeny V. Kuimov, Sergey A. Meshkov, Vasily D. Shashurin. About AlGaAs-heterostructures CVC kinetics simulation. *RENSIT*, 2019, 11(3):299-306; DOI: 10.17725/rensit.2019.11.299.

CONTENTS

- 1. INTRODUCTION (299)**
 - 2. STRUCTURE DEGRAGATION (300)**
 - 3. DISSIPATIVE PROCESSES (301)**
 - 4. SELF-CONSISTENT POTENTIAL (302)**
 - 5. RESULTS (304)**
 - 6. CONCLUSION (304)**
- REFERENCES (305)**

1. INTRODUCTION

Today, one of the most important design issues for nanoelectronic devices based on AlGaAs-heterostructures is the prediction of their reliability indicators. Firstly, such devices are promising for use as the basis for ultrafast devices of a new generation [1,2] in industries related to high requirements for reliability [3,4]. Secondly, a high cost of testing and

the time constraints on their implementation makes physical and mathematical simulation of aging devices [5] more attractive compared with a classical statistical method of the theory of reliability tests.

Degradation of AlGaAs-heterostructures is attributed [6] to diffusion processes in semiconductor layers. A profile of molar fraction of aluminum is blurred under effect of high temperatures, which affects the potential energy of electrons and a position of metastable levels. The concentration profile of silicon (a donor impurity in the contact layers) is blurred too [7]. Also, metals of the contacts and contact areas penetrate into the layers of the heterostructure over time,

which leads to an increasing of resistance of contact areas [8].

Existing mathematical models of current transfer in AlGaAs-heterostructures are based on the assumption that the transitions between the layers are localized. A calculation of the tunnel transparency coefficient within framework of the formalism of wave functions is easily generalized to the case of a continuous profile by replacing a stepped profile of potential energy with a continuous one. However, models of dissipative processes [9, 10] require coordinates of the heterointerfaces be explicitly specified, which is impossible to do in the case of the diffusion-blurred profile of the molar fraction of aluminum. Consequently, such models are not suitable for current transfer simulations with taking into account the diffusion blurring of a profile of aluminum.

Thus, the task of predicting the reliability of devices based on AlGaAs-heterostructures includes the following subtasks: structure degradation simulation (i.e., diffusion blurring of impurity profiles and resistance growth of contact areas calculation) and generalizing current transfer models to the case of structures with a continuous impurity profile along with optimization self-consistent procedures.

A numerical calculation of the current-voltage characteristics (CVC) of heterostructures is characterized by a high time complexity, which causes a problem with kinetics of CVC simulation because of repeated self-consistent calculation. The most resource-intensive part of the calculation algorithm is the step of calculating the electron concentration within the calculation of the self-consistent potential [11,12]. Optimization of this procedure allows to

reduce the calculation time for both a single CVC and their kinetics.

2. STRUCTURE DEGRADATION

In this paper, the model of structure degradation is based on the position of the dominant role of diffusion in degradation processes. Thus, the degradation of AlGaAs-heterostructures in the framework of the models presented is due to the diffusion of aluminum and silicon, as well as the penetration of metal from ohmic contacts into semiconductor contact layers, which causes their resistance increases.

The diffusion of aluminum and silicon can be described using the Fick equation [13]. As the boundary conditions, the condition of equality to zero of the substance flow at the boundaries of the simulated region was chosen, and the step profile approximation was taken as the initial condition. The diffusion coefficient was estimated using the Arrhenius equation with activation energy of 3.5 eV and a pre-exponential factor of $0.17 \text{ cm}^2/\text{s}$ [8].

Fick's equation was solved using the finite difference method. In this case, one grid was used to simulate diffusion and calculate the electron wave functions to avoid loss of accuracy when interpolating grid values of impurity concentrations. To solve this problem, elements of finite difference equations are obtained by averaging the terms of the Fick equation on the grid cells. The result of solving the obtained equations is the average fractions of aluminum and the average concentrations of silicon in the grid cells. These quantities were later used to construct a finite difference Hamiltonian, which allows not to construct a separate grid for solving the Schrödinger equation.

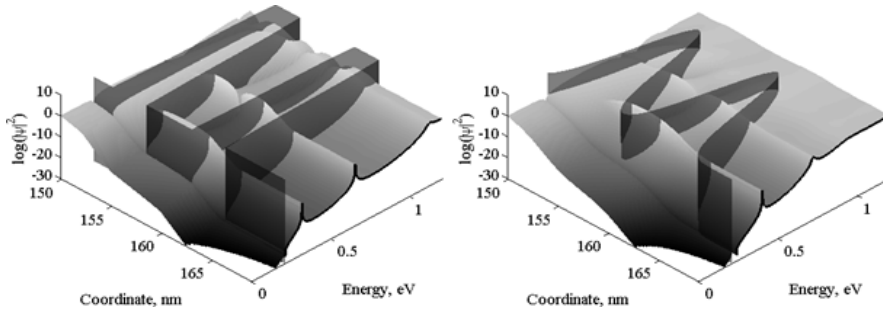


Fig. 1. The electron density logarithm before (left) and after (right) annealing. Black surfaces - the profile of the potential energy of an electron.

To estimate the effect of structure degradation, technological annealing of a resonant tunneling structure (RTS) was simulated at a temperature of 800°C [14–17]. The duration of annealing is 30 s, but in order to make the calculation results more distinguishable, the simulated annealing time is increased 4 times. The diffusion processes of aluminum and silicon were simulated. The results of calculating the electron density and the tunnel transparency coefficient are shown in Fig. 1. The wave functions were calculated at zero voltage in the self-consistent field approximation [11].

As can be seen from the figures, diffusion blurring leads to a shift of the resonance levels to high energies, as well as the broadening of the resonance levels. This leads to an

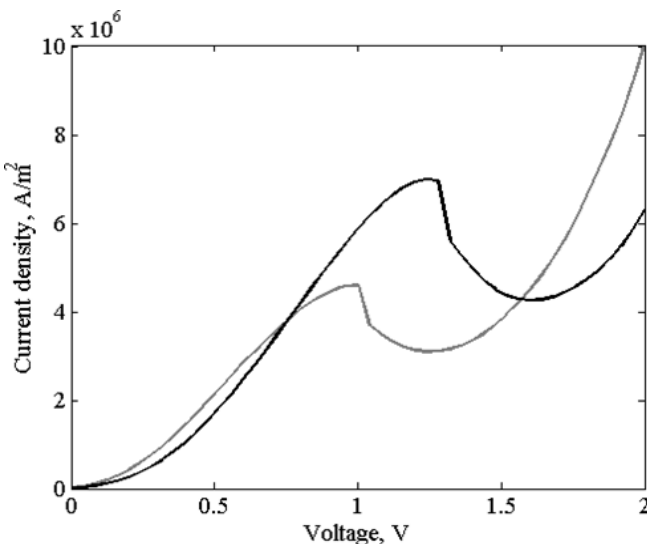


Fig. 2. CVC RTS before (grey line) and after (black line) annealing.

increase in peak voltage and peak current, in addition, to an increase in the slope of CVC characteristic, as shown in Fig. 2. The duration of annealing in calculating CVC characteristic in Fig. 2 corresponds to the duration of the simulated technological process and is 30 s.

3. DISSIPATIVE PROCESSES

The model of current transfer includes two types of electron scattering — intervalley scattering at heterointerfaces [9] and inelastic scattering by phonons [10]. The inter-valley scattering is taken into account by the two-channel model, and the scattering on phonons is taken into account using the optical potential method. In [9, 10] models of dissipative processes were developed for the case of precise heterointerfaces. However, it is difficult to determine the positions of heterointerfaces, when taking into account diffusional changes in the aluminum profile; therefore, these models require generalization. The motion of electrons in the two-channel model is described by the Schrödinger equations for an open system, in which a communication operator is included that describes the mixing of electronic states in the channels

$$\begin{pmatrix} H^\Gamma - E + \Sigma^\Gamma & A \\ A & H^X - E + \Sigma^X \end{pmatrix} \begin{pmatrix} \psi^\Gamma \\ \psi^X \end{pmatrix} = \begin{pmatrix} S^\Gamma \\ 0 \end{pmatrix}, \quad (1)$$

where $\psi^{\Gamma(X)}$ – electrons wave function in $\Gamma(X)$ -channel, E – electrons energy, $H^{\Gamma(X)}$

–isolated $\Gamma(X)$ -channel Hamiltonian, $\Sigma^{\Gamma(X)}$ –operator of electrons extraction from $\Gamma(X)$ -channel, S^{Γ} – electron injection into Γ -channel function [18], A – coupling between channels operator.

The definition of a communication operator presented in [9] is not suitable for the case of a blurred aluminum profile, since it requires given coordinates of heterointerfaces; therefore, this definition is generalized to the case of a continuous aluminum profile.

$$A = \alpha \left| \frac{d}{dz} x \right|, \quad (2)$$

where α – inter-valley interreaction constant, x – aluminium molar fraction, z – coordinate.

The optical potential is included in the Hamiltonian of the Γ -channel and is assumed to be zero in spacer regions and barriers and a constant in quantum wells (in this work the value 0.02 eV was used), thus the model includes an additional mechanism for the release of electrons from the quantum well. Again, such an optical potential distribution is not suitable for use in the case of the absence of explicit heterointerfaces. To take into account the effect of structure degradation on inelastic scattering processes, diffusion blurring of the optical potential profile was simulated using equations describing the diffusion of aluminum. The distribution of the optical potential as a sum of rectangular functions was used as the initial condition.

4. SELF-CONSISTENT POTENTIAL

The high time complexity of calculating the self-consistent potential (described in [11]) is associated primarily with the calculation of the concentration of electrons by formulaw

$$n_{L(R)} = \frac{\sqrt{2kT}}{(2\pi)^2 \hbar^3} (m^*)^{\frac{3}{2}} \times \\ \times \int_{U_{L(R)}}^{\infty} |\psi_{L(R)}|^2 \ln \left(1 + e^{\frac{-E+E_F+U_{L(R)}}{kT}} \right) \frac{1}{\sqrt{E-U_{l(r)}}} dE, \quad (3) \\ (H - E + \Sigma)\psi_{L(R)} = S_{L(R)}, \\ n = n_L + n_R,$$

where n – electrons concentration, k – Boltzmann constant, T – temperature, m^* – electrons in reservoirs effective mass, \hbar – Dirac constant, $U_{L(R)}$ – electron in source (drain) potential energy, $U_{l(r)}$ – electron potential energy at channel boundary with source (drain), $S_{L(R)}$ – electrons injection from source (drain) function, E_F – Fermi level, φ – envelope electrons wave function.

As can be seen from the above formulas the calculation of the electron concentration in the channel requires a separate calculation of the electron concentration from the source and drain, for which it is necessary to solve the Schrödinger equation twice, and then to calculate the integral in formulas (3) two times. Integration is complicated by the fact that the wave function has a number of narrow peaks (see **Fig. 3**) therefore, it is required to use multiple calculations with decreasing grid step or grid adaptation procedure.

Because ψ_L and ψ_R have resonances at the same energy levels, to reduce the computation time, you can use the same grid to calculate n_L and n_R . However, it is possible to propose a method that does not require the calculation of partial concentrations. By simple algebraic calculations, their formulas (3) can be obtained

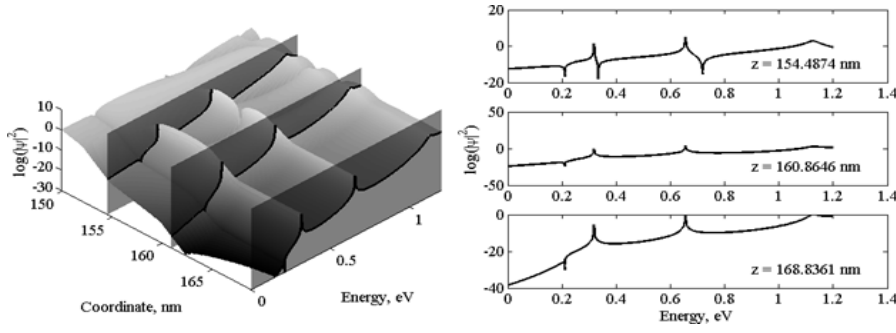


Fig. 3. The natural logarithm of the square of the modulus of the wave function of electrons from the source for fixed values of the coordinate.

$$n = \frac{\sqrt{2kT}(m^*)^{\frac{3}{2}}}{(2\pi)^2 \hbar^3} \int_{U_L}^{\infty} \varphi dE,$$

$$(H - E + \Sigma)\varphi = S_L f_L + S_R f_R,$$

$$|f_{L(R)}|^2 = \begin{cases} \ln\left(1 + e^{\frac{-E + E_F + U_{L(R)}}{kT}}\right) \frac{1}{\sqrt{E - U_{L(R)}}} & \text{for } E > U_{L(R)} \\ 0 & \text{for } E \leq U_{L(R)} \end{cases} \quad (4)$$

Calculating the electron concentration using formulas (4) allows solving the Schrödinger equation and integrating it once (for a given energy level), unlike calculating using formulas (3).

It is worth noting that if the Schrödinger equation for an open system [18] contains the functions of injection of electrons from the source S_L and drain S_R , then in the continuity equation there appear interference components whose physicality is in question [14].

$$div \bar{j} = |S_L|^2 + |S_R|^2 + S_L S_R^* + S_L^* S_R, \quad (5)$$

where \bar{j} – probability flow.

As a result of numerical experiments, it was found that the contribution of interference terms to electrons density in spacers and potential barriers regions is negligible compared to the contribution of these terms to electrons density in potential well region. However, knowing the position of the potential well relative to the electron sources, it is possible to

minimize the influence of interference terms by varying the arguments of complex S_L and S_R , which is equivalent to the choice of the initial phases of the electrons wave functions.

The self-consistent potential was not significantly affected by interference terms. Thus, comparing the results of calculations of the self-consistent potential when using formulas (3) and (4) for calculating the concentration, no significant deviations were found (the maximum deviation is $1.5 \cdot 10^{-5} \%$). The results of calculating the self-consistent potential are shown in **Fig. 4**. The calculation time for various external voltages is presented in **Fig. 5**.

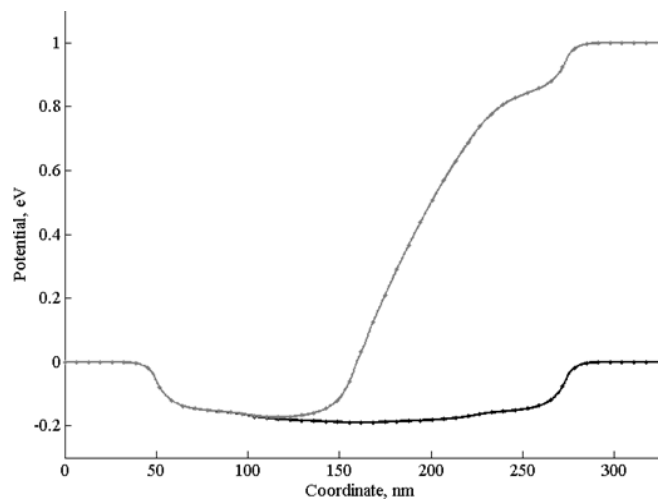


Fig. 4. Self-consistent potential at 0 V (black) and 1 V (gray). Lines – the original algorithm, points – an optimized algorithm.

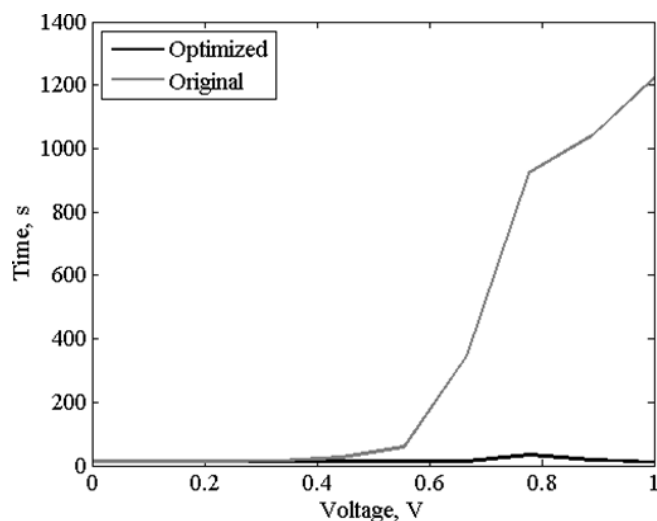


Fig. 5. Calculation time self-consistent potential.

Thus, the use of this approach made it possible to reduce the time for calculating the electron concentration by half without significant losses in accuracy.

5. RESULTS

For the validation of the presented model, the current-voltage characteristics of a number of RTS were calculated taking into account diffusion changes at the technological stage of annealing the structure for 30 s at 800°C [15-19]. The simulation was carried out self-consistently with regard to dissipative processes (the number of self-consistency iterations is 20, the inter-valley interaction constant is 0.7 eV Å, the optical potential in the quantum well is 0.02 eV). The results of the calculation compared with the experimental data are shown in **Fig. 6**.

As can be seen from the graphs, the developed algorithm allows, with satisfactory accuracy, to model the CVC of the RTS in the region of positive differential resistance — the deviation of the calculation results from the experimental data on the curvature of the initial portion does not exceed 3%. Thus, the presented model can be used to predict the parameters of devices whose

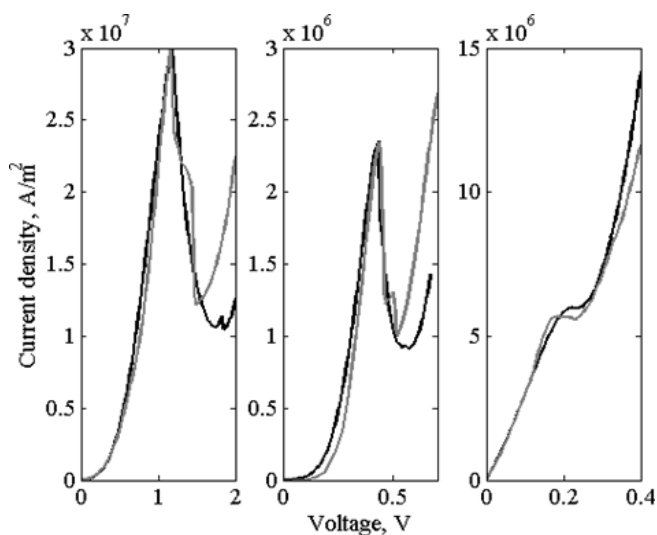


Fig. 3. The results of calculations IVC RTS. Grey lines — experimental data, black — the results of the calculation.

performance characteristics are determined by the initial section of the CVC RTS.

6. CONCLUSION

A mathematical model of the degradation of AlGaAs-heterostructures based on diffusion models of atoms in a crystal lattice has been developed. The diffusion of aluminum and silicon was simulated using the Fick equation with the second-type boundary conditions. For the numerical calculation, the finite-difference method was used, and the finite-difference scheme was built on the basis of a unified spatial grid for modeling both diffusion processes and transverse carrier transport, which made it possible to avoid loss of accuracy during interpolation. The blurring of the ohmic contacts was taken into account as an increase in the resistance of the contact layers. Accounting models of dissipative processes are generalized to the case of a continuous impurity profile. The operator of communication between the Γ - and X-valleys was calculated on the basis of the aluminum fraction profile, thus, it was possible to take into account the effect of aluminum diffusion on the inter-valley

scattering processes. In order to reduce the time complexity of the CVC calculation algorithm, the procedure for calculating the self-consistent potential is optimized at the stage of calculating the electron concentration by reducing the number of calculated integrals, thus, the time for calculating the self-consistent potential is reduced by half.

According to the results of validation of the presented model, it was concluded that it is useful to simulate the kinetics of the initial section of CVC of heterostructures at elevated temperatures, including within the framework of the task of predicting the GIC and MIC UHF reliability indicators based on multilayer AlGaAs-heterostructures.

ACKNOWLEDGMENTS

This work was financially supported by the Ministry of Education and Science of the Russian Federation, project №16.1663.2017/4.6.

REFERENCES

- Nadar S, Zaknoune M, Wallart X. High performance heterostructure low barrier diodes for sub-THz detection. *IEEE Transactions on Terahertz Science and Technology*, 2017, 7(6):780-788.
- Magruder KC, Levi AFJ. Optimal design of heterostructure tunnel diode with nonlinear current-voltage characteristic. *Physica E*, 2012, 44(7-8):1503-1509.
- Bonsendorf D, Schneider S, Meinschien J, Tamm JW. Reliability of high power laser diodes with external optical feedback. *Proc. of SPIE*, 2016, 9733:973302.
- Sin Y, Presser N, Lingley Z, Brodie M, Foran B, Moss S. Reliability, Failure Modes, and Degradation Mechanisms in High Power Single and Multi-Mode InGaAs-AlGaAs Strained Quantum Well Lasers. *Proc. of SPIE*, 2016, 9733:973304.
- Lu Y, Nie Z, Zhang P, Wang Z, Xiong L, Wang S, Wu D, Liu X. Numerical simulation of thermo-mechanical behavior in high power diode laser arrays. *ICEPT*, 2016:76-83.
- Jimenez J. Laser diode reliability: crystal defects and degradation modes. *Comptes Rendus Physique*, 2003, 4(6):663-673.
- Ushanov VI, Chaldyshev V, Preobrazhenskii VV, Putyato MA. Diffusion Blurring of GaAs Quantum Wells Grown at Low Temperature. *Semiconductors*, 2018, 52(13):1704-1707.
- Makeev MO, Ivanov YA, Meshkov SA, Litvak YN, Vetrova NA. Issledovaniya degradatsii rezonansno-tunelnykh diodov na baze AlAs/GaAs nanoheterostruktury [Studies of the degradation of resonant tunneling diodes based on AlAs/GaAs nanoheterostructures]. *Inzhenernyy zhurnal: nauka i innovatsii*, 2013, 6(18):48 (in Russ.).
- Abramov II. *Osnovy modelirovaniya elementov mikro- i nanoelektroniki* [Fundamentals of modeling elements of micro- and nanoelectronics]. Saarbrücken, LAP LAMBERT Academic Publ., 2016, 444 p.
- Bennabi Y, Hammou AB, Nouredine Z. Scattering and Tunneling in Active Systems. *Mod. Phys. Lett. B*, 2011, 25(20):1691-1700.
- Wang J, Wasige E. Self-consistent analysis of the IV characteristics of resonant tunnelling diodes. *Int. J. Terahertz Sci. Tech.*, 2012, 5(4):153-162.
- Mennemann JF, Kosina H, Jungel A. J. Transient Schrodinger-Poisson Simulations of a High-Frequency

- Resonant Tunneling Diode Oscillator. *Comput. Phys.*, 2013, 239:187-205.
13. Schowalter M. Investigation of diffusion in AlAs/GaAs distributed Bragg reflectors using HAADF STEM imaging. *J. Phys.: Conf. Ser.*, 2011, 326:012035.
 14. Kruglyak Y. Non-Equilibrium Green's Function Method in Matrix Representation and Model Transport Problems of Nanoelectronics. *Nanomaterials: Applications And Properties*, 2013, 2(1):01001(6pp).
 15. Macherzynski W, Gryglewicz J, Stafiniak A, Prazmowska J, Paszkiewicz R. Formation Process and Properties of Ohmic Contacts Containing Molybdenum to AlGa_N/Ga_N Heterostructures. *Advances in Electrical and Electronic Engineering*, 2016, 14(1):83-88.
 16. Piotrowska A. Ohmic Contacts to GaAs: Fundamentals and Practice. *Acta Physica Polonica Series A*, 1993, 84(3):491-504.
 17. Nishi H, Inada T, Saito J, Ishikawa T, Hiyamizu S. Implantation into an AlGaAs/GaAs Heterostructure. *Jpn. J. Appl. Phys.*, 1983, 22:pp.401-404.
 18. Yanxu Z., Weiwei C., Yuyu F., Ye D., Chen X. Effects of rapid thermal annealing on ohmic contact of AlGa_N/Ga_N HEMTs. *Journal of Semiconductors*, 2014, 35(2):6004.
 19. Pillet CA. A Mathematical Account of the NEGF Formalism. *Annales Henri Poincaré*, 2018, 19(2):411-442.

DOI: 10.17725/rensit.2019.11.307

Reduction of graphene oxide by supercritical isopropanol: definition of acetone in the composition of the multicomponent mixture by gc-ms method

ElenaV. Fatyushina, ElenaYu. Buslaeva

Kurnakov Institute of General and Inorganic Chemistry. Russian Academy of Sciences, <http://www.igic.ras.ru/>
Moscow 119991, Russian Federation

E-mail: fat@igic.ras.ru, buslaeva@igic.ras.ru

Received 20.08.2019, peer reviewed 20.09.2019, accepted 23.09.2019

Abstract. The analytical procedure of the reduction products of inorganic oxides and graphene oxide by supercritical isopropanol (propanol 2) has been developed. The method is based on the analytical control of acetone yield, which is always formed as a result of supercritical isopropanol reduction of these compounds. The presence of acetone is a confirmation of the reduction processes found by other methods. The problem of acetone identification, eluting as one peak with propanol 2, which is present in a high concentration in a multicomponent mixture, is the "pass" of the substance in the sample under standard analysis conditions.

Keywords: graphene oxide, gas chromatography-mass spectrometry, selective detection, isomers, quantitative analysis of acetone

UDC 541.64.543.422.4

For citation: ElenaV. Fatyushina, ElenaYu. Buslaeva. Reduction of graphene oxide by supercritical isopropanol: definition of acetone in the composition of the multicomponent mixture by gc-ms method. *RENSIT*, 2019, 11(3):307-314. DOI: 10.17725/rensit.2019.11.307.

CONTENTS

1. INTRODUCTION (307)
 2. MATERIALS AND METHODS (308)
 3. RESULTS AND DISCUSSIONS (309)
 4. CONCLUSION (313)
- REFERENCES (314)

1. INTRODUCTION

In some cases, when there is no direct evidence of the processes of transformation of the substance in the solid phase, or it is difficult for a number of reasons (for example, an insufficient amount of the sample for the study by RFA), the presence of indirect evidence-acetone, which is always formed as a result of the interaction of supercritical alcohols and inorganic compounds-is indispensable. In other cases, the presence of acetone is a confirmation of the recovery processes detected by other methods. The presence of complex salts and mixtures of components in graphene oxide reduction products imposes additional

requirements for the selectivity of acetone determination, which is satisfied by the gas chromatography-mass spectrometry (GCMS) method and makes it difficult to identify it by chromatographic methods. It was found that the main factors leading to false negative results of HCMS analysis are the presence of background components eluting together with the target substances. The problem of identifying acetone eluting by a single peak with propanol 2 (isopropanol) present in a high concentration is the "pass" of the substance in the sample under standard analysis conditions.

The aim was to develop a method of analysis of the solutions of complicated composition, resulting from the interaction of supercritical alcohol 2 propanol and inorganic compounds, based on analytical control of the yield of acetone as a witness and criterion of recovery of oxides and complex salts (including graphene oxide), to find the optimal conditions of analytical control of the recovery processes,

ensuring the separation selectivity of overlapping chromatographic peaks.

Propanol 2 with acetone is usually divided into polar columns with polyethylene glycol (PEG). Many polar phases have disadvantages (relative to mid-polar, low-polar and non-polar). Among such disadvantages is a relatively low tolerance to oxidants. This should be taken into account when developing a technique on columns with PEG or its derivatives, which include the fixed liquid phase: FFAP, DB-WAX, DB-FFAP. The service life of the PEG speaker is significantly shorter than that of the HP-5 speaker and does not exceed one year.

To determine the complex composition of a mixture of near-boiling components, it is recommended to use a column with a nonpolar phase (polydimethylsiloxane) [1]. In cases where this fails, it is necessary to resort to high-resolution mass spectrometry, or to methods that "shift" the analytical peaks to a different region of mass numbers, for example, to other methods of ionization or to obtain derivatives for which the masses of the characteristic ions of the analyzed compounds have different values. Obviously, increasing the resolution leads to a decrease in signal intensity.

This complicates and increases the cost of the analysis procedure, in addition, it makes it difficult to obtain quantitative results.

In this paper, an attempt is made to develop a method for determining acetone in a near-boiling isopropyl alcohol without preliminary sample preparation and separation of components of a complex mixture, providing quantitative results and a low detection limit.

2. MATERIALS AND METHODS

The work was carried out on the chromatomass spectrometry system of the company "Agilent" (USA), consisting of a quadrupole mass analyzer Agilent 5973, gas chromatograph Agilent 6890. Chromatography was performed on capillary column HP-5 with fixed phase -5%

diphenylsiloxane and 95% dimethylsiloxane, column dimensions 0.32 mm×50 m×0.52 μm.

The initial temperature of the column was 30° C, the temperature programming speed – 10°C/min, the final temperature of the column – 250°C/min.

Ionization of substances in the mass spectrometer was carried out in the mode of electronic shock, registration of chromatograms was carried out both on the total ion current and in the mode of measuring the current created by individual ions or their groups.

Conditions for registration of chromatograms and mass spectra:

- interface temperature 280°C;
- detector temperature 150°C;
- ionizing electron energy 70 eV;
- recorded mass interval 12-350 a. e. m.;
- the scanning speed of 4.27 scans/sec.;
- the voltage at the multiplier 70 V;
- resolution 0.5 a.e.m.;
- dosing of the sample was carried out with the help of "Hamilton" microsyringes with a volume of 10 μl, the volume of the dosed sample was 0.4 μl.

Before the analysis of samples under the same conditions, blank samples of isopropyl alcohol containing no target component-acetone were analyzed.

During the evaporation of the sample, the "split" mode was used with the ratio of the amount of injected substance into the capillary column-discharge, 1:10, respectively.

The volumetric velocity of the carrier gas is 1 ml/min.

CHECKING THE MASS DEVICE SETTINGS AND MONITORING THE STABILITY OF THE CALIBRATION CHARACTERISTIC

This procedure was carried out on perfluorotributylamine supplied to the device according to the instructions "Autotune" [2].

The molecular composition was determined by comparing the obtained mass spectra with the library mass spectra given in the MSD ChemStation data collection and processing program.

PREPARATION OF CALIBRATION SOLUTIONS OF ACETONE IN PROPANOL

Calibration solutions were prepared as follows: to 10 aliquot volumes (1 ml) propanol 1 and propanol 2 were added 2, 5, 10, 20, 50, 100, 200 μl of acetone solution, while its concentration made up 0.02; 0.06; 0.16; 0.25; 0.49; 0.98; 1.96; 4.55; 8.3; 14.28; 20.0 (%vol.), respectively. An internal standard (propanol 1) was added to the acetone calibration solution in propanol 2 and subjected to GCMS analysis. The concentration of propanol 1 in the calibration mixture was 0.5% vol.

3. RESULTS AND DISCUSSIONS

It is established that the main factors leading to false negative results and the impossibility of visual identification are the presence of background components eluting together with the target substances. Fig. 1 the fragments

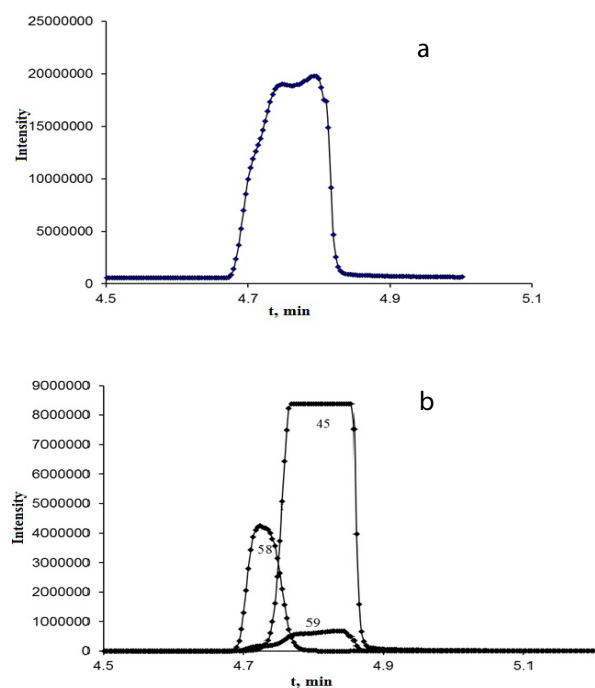


Fig. 1. The fragments of mass chromatograms of near-boiling compounds in the full-scan mass detection (a) and selected ion monitoring (SIM) (b).

of mass chromatograms of near-boiling compounds in the full-scan mass detection total ion current (a) and selected ion monitoring (SIM) in the extraction mode of characteristic ions (b) are presented.

Due to these factors, especially at low acetone content in the solvent propanol 2, the method of determination, providing for the detection of the total ion current, was unsuitable. This fact is confirmed by a fragment of the chromatogram of the undivided components (a).

If the mass spectra of the undivided components have specific peaks characterizing each of the components and are absent (or insignificant) in the spectra of the other components, the ionic mass chromatograms for each of these characteristic peaks show the elution of each of their respective components regardless of whether the chromatograms (b) overlap.

Determination of the acetone content in the matrix of near-boiling propanol 2 was carried out in the mode of ion chromatogram extraction and selective detection of characteristic lines 43 and 58 m/z from the mass spectra without preliminary separation of these compounds during sample preparation.

A low-intensity peak 59 m/z from the mass spectrum of propanol 2 was used as a label characterizing the change in chromatography and detection conditions to assess the true value of the acetone peak area. Additional information to control the stability of the measurement conditions was a constant ratio between the characteristic ions of the substance being determined.

Identification of acetone occurred by coincidence of maxima and character of curvature of peaks of ion chromatograms extracted from the total ion current. From Fig. 1b it can be seen that it was possible to separate the chromatographic peaks and detect acetone.

The criterion of absence process reduction of oxides and complex salts was the absence of

one chromatographic peak of the characteristic acetone ion within 0.05 min retention time in the presence of all other peaks.

In order to evaluate and eliminate interfering factors and obtain peaks of analytical ions free from superposition, isomers were used for calibration as analogues of the matrix component, but with different chromatographic characteristics, in this case: propanol 1. The physical properties of propanol 1 and propanol 2 are different: propanol 2 has a lower boiling point than propanol 1. It differs from its analogue retention time, the shift is about 2 min. Chemical properties of these isomers, differing in the position of the functional group, differ slightly, because they have the same qualitative composition and nature of the bond between the atoms in the molecule. **Fig. 2** illustrates the chromatographic peaks of acetone in propanol 2 (a) and in propanol 1 (b). It is seen that the peak of acetone overlaps with the peak of near-boiling propanol 2 and is independently measured in propanol 1.

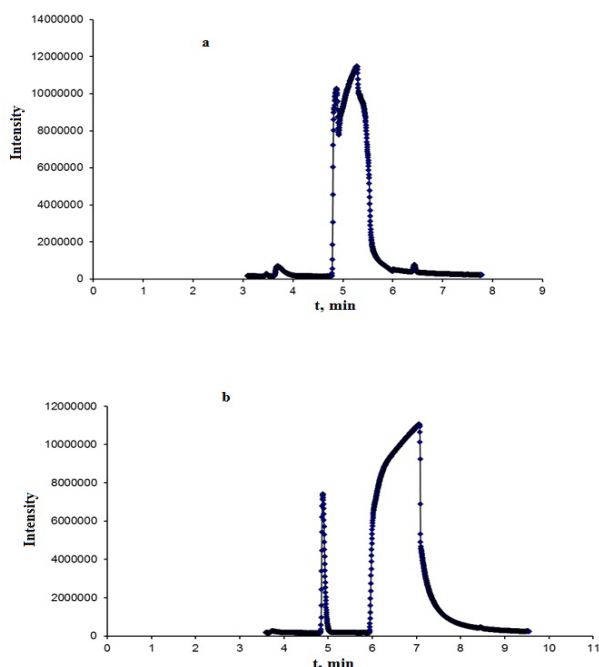


Fig. 2. Chromatographic peaks of acetone in propanol 2 (a) and in propanol 1 (b). It is seen that the peak of acetone overlaps with the peak of near-boiling propanol 2 and is independently measured in propanol 1.

Fig. 3 illustrates the difference between the mass spectra of propanol 2 and its isomer propanol 1, due to which separation by extractable ions is possible.

Mass chromatograms and mass spectra are given to illustrate the absence of the influence of solvent peaks of propanol 1 on the accuracy of the determination results (Fig. 2, 3) due to the absence of Isobaric interference.

QUANTITATIVE GS MS ANALYSIS OF ACETONE IN A NEAR BOLING MULTICOMPONENT MIXTURE WITH ISOPROPANOL

Achieving high precision and the reproducibility of the quantitative results it is possible only with the right choice of quantitative analysis method and chromatographic analysis conditions. Quantification of identified compounds was performed by the method of "internal standard", for which a pre-determined calibration correction factor, indicating how many times the response of the mass-selective detector (area of the chromatographic peak is independent of the characteristic ion m/z 58) per unit mass of a substance is different from the response of the mass-selective detector per unit mass "internal standard" [3]. Its advantages are that it largely eliminates the impact of sample dosing error on the reproducibility of the analysis results.

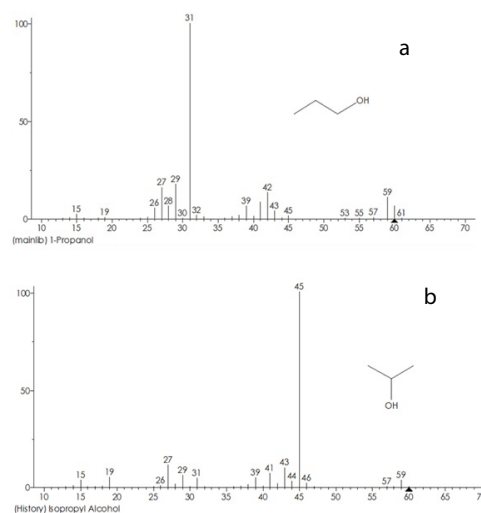


Fig. 3. Mass spectrum of propanol 1 (a) and propanol 2 (b).

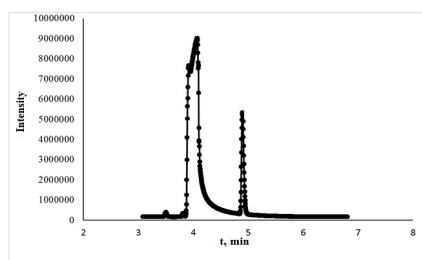


Fig. 4. Fragment of mass chromatogram of acetone in propanol 2 with internal standard propanol 1.

As an internal standard, propanol 1 was used, which has the same functional group with the matrix component propanol 2, but with different chromatographic and mass- spectral characteristics (**Fig. 4**).

The basis of quantitative chromatographic analysis dependence of peak height h or its area S on the amount of substance. **Fig. 5** presented dependency relationship of the intensities of chromatographic peaks of acetone (corresponding to 58 ion) and propanol 1 in the propanol 2 matrix, calculated from the area and height of chromatographic peaks.

Using the t -criteria, it was found that the systematic error was significant against the background of a random spread in the calculation using the height of the peaks (**Fig. 6**), therefore, the quantitative assessment of the

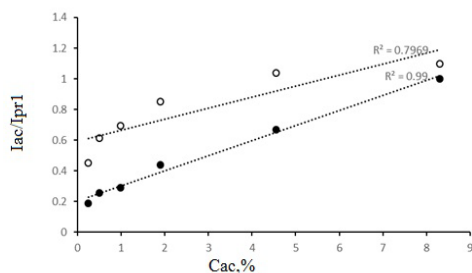


Fig. 5. Relations of analytical signals of acetone and internal standard of propanol 1 (I_{ac}/I_{pr1}) depending on acetone content ($C_{ac},\%$) calculated by area (●) and by heights (○) of chromatographic peaks.

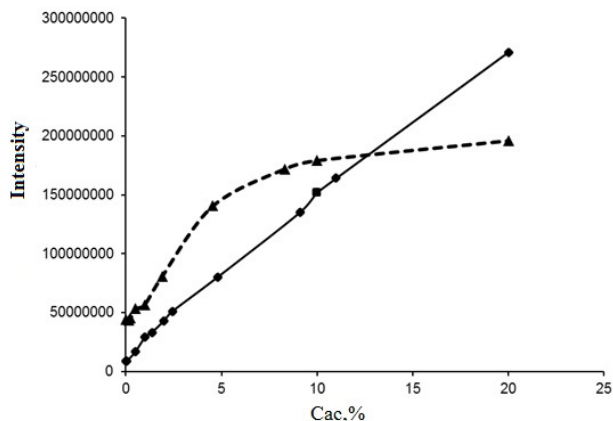


Fig. 6. Dependence of peak intensity on the amount of acetone analyzed in propanol 2 (---) and propanol 1 (-).

acetone content was carried out on the area of chromatographic peaks.

When working in the detector linearity range this dependence can be represented by the linear regression equation:

$$C_{ac} = K_i * C_{pr1} \times S_{ac} / S_{pr1},$$

where K_i — coefficient of relative sensitivity of acetone as the internal standard — propanol 1, C_{pr1} — 1 propanol content in the mixture of sample and solvent (propanol 2), S_{ac} and S_{pr1} — square peaks on the chromatogram, corresponding to ion m/z 58 acetone peak and the internal standard propanol 1. The value of K does not depend on the amount of the determined component in the analyzed sample, in principle, should remain unchanged even when changing the conditions of chromatography and detection, unless, of course, these changes did not cause a violation of the linearity of the detector and the true value of the area was used as the peak parameter. This calculation scheme is widely used, but does not provide adequate results for nonlinear calibration dependencies. The use of calibration coefficients taken from the literature for quantitative calculations also leads to errors. In fact, it may be necessary to use combined versions of definitions or more complex modifications, in particular, the method of internal standard and absolute calibration [4].

QUANTITATIVE ANALYSIS OF SINGLE-PEAK ELUTING SUBSTANCES UNDER NONLINEAR DETECTION CONDITIONS

The main disadvantage of the quantitative analysis method proposed above is the need for non-overlapping characteristic ions to identify each compound, which is especially difficult to perform when analyzing compounds with similar structure, for which, as a rule, chromatographic and spectral overlap is most likely. A significant deviation of the calibration graph from the linearity can lead to the complete disappearance of small peaks.

Under these conditions, distortion of the shape and change in the area of the peaks were observed.

In order to expand the possibilities of quantitative analysis (the range of determined contents), it is additionally proposed to correct analytical signals using an external standard. To obtain peaks of analytical ions free from superposition, it is proposed to use isomers-analogues of the matrix component, having the same functional group, but with different chromatographic characteristics, in this case - propanol 1. The value of K_i was determined by additional experiments involving a known amount of substance i .

On the example of a model mixture of acetone-propanol 1, acetone-propanol 2 (Fig. 6) the advantage of calibration using isomers is shown. Checking the isotope ratio revealed overlaps, which was expressed in a deviation from the linearity of the dependence of the intensity of the analytical signal of acetone on its content in propanol 2 (Fig. 6, dashed line). The most pronounced deviations in the calculation of height. This can be explained by the fact that the peak of acetone comes out just before the peak of propanol 2. This causes the acetone to enter the desorption zone, which gives its false peak at the same location. As a result, not only can the relative intensity of ion peaks in the mass

spectra be distorted, but also excess peaks that are not characteristic of the analyzed substances may appear. The contribution to the intensity of peaks of characteristic background ions or peaks of ions of other components leads to overestimated results in determining the concentration of the analyte. It should be borne in mind that the amount of overlap can be large if it is due to the components present in the mixture in much larger quantities than those analyzed.

The distortion of the acetone peak shape was observed when the column was overloaded with a solvent eluting in a high concentration - propanol 2.

The absence of interfering factors is illustrated by the linear dependence of the analytical signals of acetone on its content in propanol 1, including the imposition of a matrix "tail" is minimized (values on the y -axis are close to zero at "0"acetone concentration). In this case, the change in the analytical signals of acetone from its content in propanol 2 should be corrected beyond the linearity of the detector (Fig. 6). The effect of acetone concentration on the change in the ratio of acetone and propanol 1 peak areas is illustrated in Fig. 7.

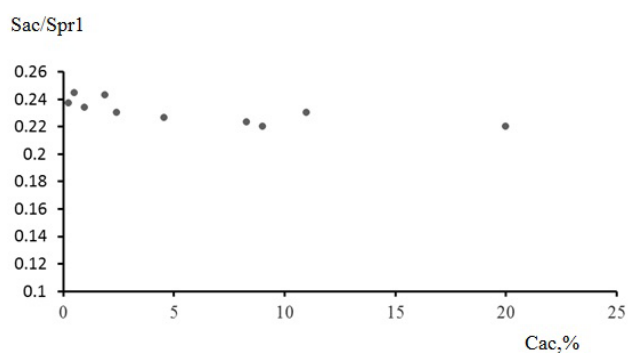


Fig. 7. Ratio of acetone and propanol 1 peak areas (S_{ac}/S_{pr1}) depending on acetone concentration (C_{ac} , %) in solvent.

The correctness of the values of the calibration coefficient of acetone analytical signals corrected according to the external standard is confirmed by a small variation in the values of the relations between the areas of acetone peaks and the standard-propanol 1 present in equal concentrations.

If this condition is not met, the resulting errors can be compensated by using a combined version using an internal standard, wherein, in which the isomer of the matrix component is not an extraneous interfering component in the initial mixture. Uncontrolled changes in the absolute intensities of analytical signals are corrected relative to the internal standard or by the method of internal normalization to assess the relative amounts of components of mixtures [5]. The value of the ratio of the peak areas of the component and the introduced standard was determined and, using the previously obtained dependence of the ratio of the peak areas on the ratio of the quantities of these components in the model mixture, the content of the analyzed component was determined.

The amount of the *i*-th component (Q_i) was calculated taking into account the known concentration of the standard (C_{stk}) in the calibration solution, the detector response to the internal standard (S_{st}) and the calibration dependence of the component-internal standard (K_{st}):

$$Q_i = K_{st} C_{ik} * S_{st} / C_{stk}$$

where Q_i is the amount of the component equal to the product of its concentration on the injected volume, C_{ik} - the concentration of the component in the calibration solution. The formula corrects the position of the calibration points along the component quantity axis, leaving the detector response value as it is obtained in the experiment.

The numerical values of the relative response coefficients of the detector are obtained from chromatographic data of calibration mixtures

Table

The method "introduced-found", mode SIM.

Detected Content Range	Introduced mg/l	Experimentally found value
0.2 - 0.5	0.3	0.35 ± 0.07
0.5 - 1.5	1.0	1.12 ± 0.13
1.5 - 4.5	2.8	3.04 ± 0.26
4.5 - 20.0	15.0	16.2 ± 0.17

with known concentrations of standard and investigated impurities.

The estimation of the relative random component of the error of the results of quantitative determinations by the method of absolute calibration [6] was carried out according to the ratio:

$$\delta_{G_i} = (\delta_{ki} + \delta_{Si}) / 2,$$

where δ_{ki} - the relative error of the K_i coefficients, δ_{Si} - the same for the chromatographic peak areas of the substances to be determined.

The accuracy of the analysis was estimated by determining the boundaries in which the error of the results of the unit analysis is with a given probability $P = 0.95$.

The reproducibility of the introduction of samples was 1.5-2.5%, the reproducibility of fixed retention times was not worse than ± 0.05 min. The results of the determination of acetone in propanol 2 according to the developed method are presented in the **Table**.

4. CONCLUSION

The developed algorithm is useful for searching, identifying and determining the contents of overlapping a priori known components in a complex mixture (the qualitative composition is known) with a high degree of reliability.

The use of an isomer as an analogue of one of the undivided components for comparison made it possible to prevent overlaps of extracted ions, to increase isotopic sensitivity due to the absence of Isobaric interferences and to exclude the influence of the matrix effect on the analysis result. In addition, this eliminates the procedure of introducing a foreign component into the original mixture.

REFERENCES

1. Berezkin VG, Lapin AB, Lipsky JB. Investigations of a new field in gas chromatography: Capillary columns with a super-thick layer of stationary liquid phase. *J. Chromatogr. A*, 2005, 1084(1-2):18-23.
1. Reese A, Prest H. Retention time locked GC-MS analysis of phenols. *Agilent Technologies application*, 2001, 28(9):3934-5988.
2. Kai Meng C. Identification and Quantitation of Pesticides in the partsper-trillion range using retention time locking and GC/MS. *Agilent Technologies application*, 2001, 14(11):4392-5988.
3. Kioussia MK, Angelisa YS, Cawleyc AT, Koupparisb M, Kazlauskasc R, Brennad JT, Georgakopouloa CG. External calibration in GasChromatography–Combustion–Isotope Ratio Mass Spectrometry measurements of 92 endogenous androgenic anabolic steroids in sports doping control. *J. Chromatogr. A*, 2011, 1218:5675-5682.
4. Zenkevich IG, Kosman VM. *Metody kolichestvennogo kbromatograficheskogo analiza lekarstvennykh veshchestv* [Methods of quantitative analysis of pharmaceutical substances]. S-P., SP KHFA Publ., 1999, 80 s.
5. Vial J., Jardy A. *Quantitation by standard addition*. *Encyclopedia of Chromatography* [Ed. J. Cazes], Taylor & Francis, 2010, 3: 1975-1976.

DOI: 10.17725/rensit.2019.11.315

Conduction mechanism of nanographite formed by methane plasma deposition and subsequently heat treatment

Efim P. Neustroev, Aisen R. Prokopiev

Ammosov North-Eastern Federal University, <https://www.s-vfu.ru>
Yakutsk 677000, Russian Federation

E-mail: neustr@mail.ru, aisenprokopiev@mail.ru

Received 01.11.2019, peer reviewed 11.11.2019, accepted 18.11.2019

Abstract. Samples of nanographite films obtained by carbon deposition in a methane plasma and subsequent heat treatment at a temperature of 650°C were studied. Thickness of obtained films was 1-2 nm. The results of measurements of a temperature dependency of the resistance ($R(T)$) shows that when a temperature changes from 80°K to 300°K the resistance changes by about three orders of magnitude. The temperature dependency of the activation energy has a non-Arrhenius character corresponding to the variable range hopping mechanism. An analysis of the dependency of the reduced activation energy versus the natural logarithm of temperature showed that the electric conductivity of graphite nanoflakes corresponds to the Efros-Shklovsky mechanism. Size of graphite nanoflakes was estimated to be ~1.7 nm from the obtained results.

Keywords: plasma-enhanced deposition, methane, heat treatment, nanographite, electrical conductivity

PACS: 73.25.+i, 73.50.Mx, 73.61.-r.

Acknowledgements: This work was carried out within the framework of projects of the Ministry of Science and Higher Education of the Russian Federation (project FSRG-2017-0017) and a grant from the Russian Science Foundation (project 19-32-90133 Postgraduate students).

For citation: Efim P. Neustroev, Aisen R. Prokopiev. Conduction mechanism of nanographite formed by methane plasma deposition and subsequently heat treatment. *RENSIT*, 2019, 11(3):315-320; DOI: 10.17725/rensit.2019.11.315.

CONTENTS

- 1. INTRODUCTION (315)
- 2. MATERIALS AND METHODS (316)
- 3. RESULTS (316)
- 4. CONCLUSION (318)
- REFERENCES (319)

1. INTRODUCTION

Nanographite can serve as a precursor for producing graphene [1]. Graphene and its derivatives are of interest not only because of their high electrical and thermal conductivity as well as mechanical strength [2, 3], but also due to their sensory properties for

creation of optoelectronic, biological, gas and mechanical sensors [2, 4] and wide possibilities for practical application. The most popular methods for producing graphene are Chemical Vapor Deposition (CVD) [5] and its modification – plasma-enhanced chemical vapor deposition (PECVD) [5]. As a rule, PECVD method uses hydrocarbons (CH_4 or C_2H_2) as sources of carbon [6, 7]. PECVD method possesses numerous advantages including the possibility of temperature drop to 450°C without using catalysts [6] and increase in the deposition rate [6] during the process. At the same time, direct plasma exposure can lead to the formation of a high density of defects [8] in the films formed and the formation of vertical carbon structures due to the intrinsic electric field [5]. The formation of defects and vertical growth can be reduced by the remote plasma-enhanced chemical deposition method, in which the reaction chambers of the plasma system and the CVD devices are spatially separated while the gas flows are combined [9]. On the other hand, such method complicates the installation for producing graphene and increases its cost. This study used the method of separate use of plasma deposition and heat treatment in the form of two independent sequential stages. The electrical and structural properties of the obtained material were investigated.

2. MATERIALS AND METHODS

First stage of obtaining the samples involved deposition of carbon on the surface of SiO_2 in a CH_4 methane plasma at temperatures that were close to ambient. The power of the generated inductively coupled plasma (13.56 MHz) ranged from 150 to 200W. The reaction was carried out in a chamber previously evacuated to pressure of 0.001 mbar. When methane was launched at a flow rate of $30\text{cm}^3/\text{min}$, the operating pressure in the chamber rose to 0.03 mbar. Total time of processing samples in plasma was up to 12 min. At the second stage, the samples were subjected to heat treatment at a temperature 650°C for 30 min in an argon atmosphere. The obtained carbon films were studied by Raman spectroscopy (Ntegra Spectra), Atomic Force Microscopy (AFM) (Ntegra Spectra), and temperature dependencies of the resistances, measured in the range from 80°K to 300°K using a two-probe method.

3. RESULTS

Fig. 1a shows the Raman spectra of a sample treated in CH_4 plasma with a power of $P = 200\text{ W}$ for 12 min before and after annealing. A wide photoluminescence band observed after plasma exposure is typical for hydrogenated amorphous carbon film (a-C:H) [10]. After heat treatment, this

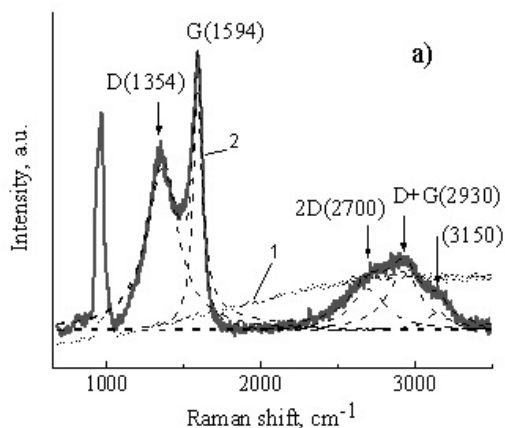


Fig. 1a. Raman spectra of the sample: 1 - after processing in plasma ($P = 200\text{ W}$, 12 min), 2 - after annealing.

band practically disappears. D-, G-peaks and their overtones (2D, D+G) corresponding for nanocrystalline graphite structures appear [11]. The nature of the peak at the $\sim 3150\text{cm}^{-1}$ connects with vibrations of the carbon-hydrogen bonds of the aromatic carbon ring [11]. The band observed in the range from 920cm^{-1} to 1050cm^{-1} is connected with the SiO_2 substrate [12]. An increase in its intensity after heat treatment can be explained by a decrease in the thickness of the deposited amorphous film, which was confirmed by the results of AFM measurements.

Fig. 1b shows the $R(T)$ -dependency normalized relatively to resistance at a temperature of 80° K . At the temperature less than 300° K , $R(T)$ has a nonlinear character and changes by more than three orders of magnitude with a decrease temperature to 80°

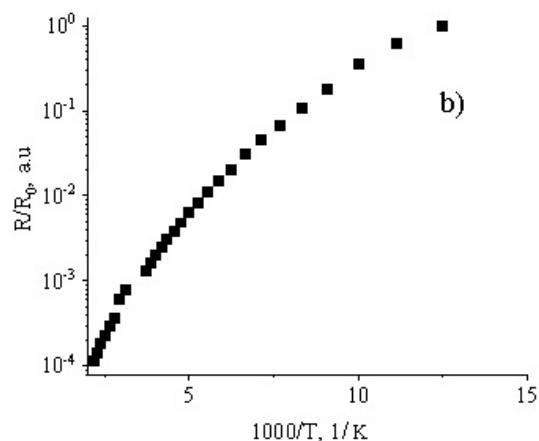


Fig. 1b. The dependency of the value of relative resistance on the return temperature.

K . In this case, it can be described by following equation [13]:

$$R(T) = R_0 \exp\left(\frac{T_0}{T}\right)^n, \quad (1)$$

where R_0 is a constant coefficient and T_0 is a characteristic temperature.

The exponent depends on the mechanism of conductivity and takes values of $1/2$, $1/3$ or $1/4$ depending on the model of transfer of charge carrier. Values $n = 1/2$, $1/3$ and $1/4$ correspond to variable range hopping mechanisms in accordance with the Efros-Shklovsky model, for 2D and 3D systems, respectively [13, 14]. Value n can be determined from the dependency of $\ln R$ on T^{-n} although graphs for n shown on Fig. 1b are equal to $1/2$, and $1/3$ do not allow to determine exactly which of them more accurately describes the experimental data. Therefore, the self-consistent method was used to refine the value of n [13]. Such method allows to determine $\ln W = A - n \times \ln T$ using

the equation, where W is the reduced activation energy determined from the following expression:

$$W = -\frac{\partial \ln R(T)}{\partial T} = n \left(\frac{T_0}{T} \right)^n \quad (2)$$

Fig. 1c shows the dependency of $\ln W$ on $\ln T$ from the slope to which a value of $n = 1/2$ was found which corresponds to the law of Efros-Shklovsky. A slight deviation with increasing temperature can be caused by the influence of the thermo-activation mechanism prevailing at the T less than 300° K.

For the Efros-Shklovsky model, the characteristic temperature T_0 is determined by the following expression [13]:

$$T_0 = T_{ES} = \frac{2.8e^2}{4\pi\epsilon\epsilon_0 k_B \xi}, \quad (3)$$

where e is the electron charge, ϵ_0 is the electric constant, ϵ is the relative permittivity, and ξ is the length of the range of localization of the electron wave function that corresponds to the

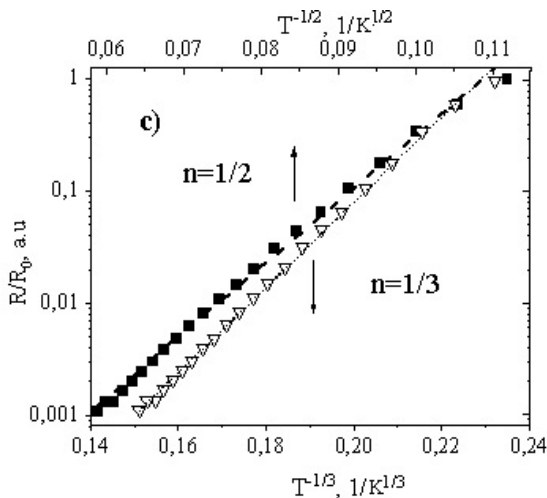


Fig. 1c. Dependencies of relative resistances on $T^{-1/2}$ and $T^{-1/3}$.

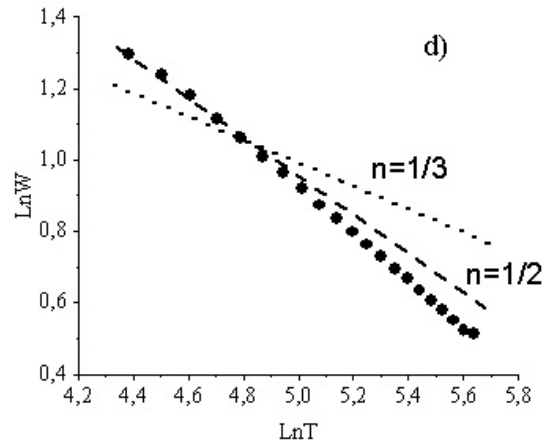


Fig. 1d. Graph of the reduced activation energy versus the temperature on a logarithmic scale.

half-length of the graphene domain. The value of the characteristic temperature T_0 was determined from the slope of the $\ln R$ dependency on $T^{-1/2}$ (Fig. 1c) which was $\sim 13500^\circ$ K. From the AFM measurements, the thickness of the investigated film and the number of layers $L = 3-4$ were determined (with a graphene layer thickness of 3.41 Å). Taking $\epsilon = 4$ for graphene flakes with the number of layers L [15], a value of $\xi = 0.85$ nm was found from (3). Thus, a size of the graphene domain equal to $d = 2 \xi \sim 1.7$ nm in nanocrystalline graphite.

4. CONCLUSION

The properties of carbon films formed as a result of plasma treatment in methane and subsequent annealing at $T = 650^\circ$ C were studied. Peaks typical for nanocrystalline graphite are observed in the Raman spectra of the samples obtained. Mechanism of electrical conductivity was

established out of $R(T)$ dependency corresponding to the Efros-Shklovsky law for localized states in graphene domains. Based on this, the size of graphite nanocrystallites was estimated and the value of ~ 1.7 nm was obtained.

ACKNOWLEDGMENTS

The reported study was funded by Ministry of Science and Higher Education of the Russian Federation (project FSRG-2017-0017) and RFBR project number 19-32-90133.

REFERENCES

1. Çelik Y, Flahaut E, Suvacı E. A comparative study on few-layer graphene production by exfoliation of different starting materials in a low boiling point solvent. *FlatChem.*, 2017, 1:74-88.
2. Novoselov KS, Fal'ko VI, Colombo L, Gellert PR, Schwab MG, Kim K. A roadmap for graphene. *Nature*, 2012, 490(7419):192.
3. Papageorgiou DG, Kinloch IA, Young RJ. Mechanical properties of graphene and graphene-based nanocomposites. *Progress in Materials Science*, 2017, 90:75-127.
4. Chen D, Feng H, Li J. Graphene oxide: preparation, functionalization, and electrochemical applications. *Chemical reviews*, 2012, 112(11):6027-6053.
5. Tan H, Wang D, Guo Y. Thermal growth of graphene: A review. *Coatings*, 2018, 8(1):40.
6. Azam MA, Zulkapli NN, Dorah N, Seman R-A, Ani M, Sirat M, Ismail E, Fauzi F, Mohamed M, Majlis B. Critical considerations of high quality graphene synthesized by plasma-enhanced chemical vapor deposition for electronic and energy storage devices. *ECS Journal of Solid State Science and Technology*, 2017, 6(6):M3035-M3048.
7. Khan A, Islam SM, Ahmed S. Direct CVD Growth of Graphene on Technologically Important Dielectric and Semiconducting Substrates. *Advanced Science*, 2018, 5(11):1800050.
8. Neustroev EP, Burtseva EK, Soloviev BD, Prokopiev AR, Popov VI, Timofeev VB. Modification of graphene oxide films by radiofrequency N_2 plasma. *Nanotechnology*, 2018, 29(14):144002.
9. Cuxart MG, Šics I, Goñi AR, Pach E, Sauthier G, Paradinas M, Foerster M, Aballe L, Moreno Fernandez H, Carlino V, Pellegrin E. Inductively coupled remote plasma-enhanced chemical vapor deposition (rPE-CVD) as a versatile route for the deposition of graphene micro- and nanostructures. *Carbon*, 2017, 117:331-342.
10. Ferrari AC, Robertson J. Interpretation of Raman spectra of disordered and amorphous carbon.

- Physical review B*, 2000, 61(20):14095.
11. Beams R, Cançado LG, Novotny L. Raman characterization of defects and dopants in graphene. *Journal of Physics: Condensed Matter*, 2015, 27(8):P.083002.
 12. Uchinokura K, Sekine T, Matsuura E. Raman scattering by silicon. *Solid State Communications*, 1972, 11(1):47-49.
 13. Joung D, Khondaker SI. Efros-Shklovskii variable-range hopping in reduced graphene oxide sheets of varying carbon sp^2 fraction. *Physical Review B*, 2012, 86(23):235423.
 14. Muchharla B, Narayanan TN, Balakrishnan K.. Temperature dependent electrical transport of disordered reduced graphene oxide. *2D Materials*, 2014, 1(1):011008.
 15. Santos EJG. Electric field effects on graphene materials. *Exotic Properties of Carbon Nanomatter*. Springer, Dordrecht, 2015, p. 383-391.

DOI: 10.17725/rensit.2019.11.321

Binding of short DNA oligonucleotides to the surface of reduced graphene oxide to create biological sensors

Ivan A. Komarov, Alexander N. Kalinnikov, Sergey N. Shcherbin, Vyacheslav A. Seleznev

Bauman Moscow State Technical University, <http://www.bmstu.ru/>

Moscow 105005, Russian Federation.

Olga M. Antipova

Lomonosov Moscow State University, <https://www.msu.ru/>

Moscow, 119991 Russian Federation

Nikolay S. Struchkov

National Research University of Electronic Technology, <https://miet.ru/>

124498, Moscow, Zelenograd, Russian Federation.

E-mail: ikomarov@emtc.ru, alexandr.kalinnikov@emtc.ru, sshcherbin@emtc.ru, vseleznev@emtc.ru, antipovachem@gmail.com, struchkov.nikolaj@gmail.com

Received 31.10.2019, peer reviewed 11.11.2019, accepted 18.11.2019

Abstract. The study examined the possibility of immobilization of short DNA oligonucleotides (aptmers) on the surface of reduced graphene oxide, with the aim of forming a bio-sensitive sensory layer. The features of laser reduction of graphene oxide were considered, and the parameters of reduction were determined, which were implicated in achieving partial reduction. The possibility of immobilization of aptamers on graphene oxide with a low degree of reduction and the response of sensory structures formed on the basis of this basis is shown. A significant difference between the response of the sensors to the effects of thrombin (target protein) and albumin (comparison protein) was demonstrated.

Keywords: aptamers, biosensors, immobilization, nucleotides, graphene oxide

UDC 620.3

Acknowledgements: This work was financially supported by the grant of the Ministry of Education and Science of the Russian Federation No. 14.574.21.0182 (unique identifier RFMEFI57417X0182).

For citation: Ivan A. Komarov, Olga M. Antipova, Nikolay S. Struchkov, Alexander N. Kalinnikov, Sergey N. Shcherbin, Vyacheslav A. Seleznev. Binding of short DNA oligonucleotides to the surface of reduced graphene oxide to create biological sensors. *RENSIT*, 2019, 11(3):321-330; DOI: 10.17725/rensit.2019.11.321.

CONTENTS

1. INTRODUCTION (321)
2. MATERIALS AND METHODS (323)
3. RESULTS AND DISCUSSION (324)
 - 3.1. AFM IMAGING OF GRAPHENE OXIDE FILMS (324)
 - 3.2. INVESTIGATION OF THE FEATURES OF THE RECOVERY OF GRAPHENE OXIDE FILM (325)
 - 3.3. IMMOBILIZATION OF APTAMERS (325)
 - 3.4. STUDY OF THE FEATURES OF IMMOBILIZATION (326)
 - 3.5. SENSOR RESPONSE RESEARCH (328)
4. CONCLUSION (328)
- REFERENCES (329)

1. INTRODUCTION

The market for electronic devices is growing rapidly and shifting more and more towards the personalized devices with large number of different sensors. Among them devices for health monitoring are most claimed. In addition, 5th generation mobile networks that allow data collection and transfer from a large number of different sensors have recently appeared. Another important trend of the world healthcare is remote patient control without the need to visit a hospital. Based on the abovementioned trends, we can conclude that in the nearest future diagnostics

of some diseases will be held completely online. And in the far future diagnostics of the wide spectrum of diseases will be made remotely that requires sophisticated systems for personal diagnostic. One of the main requirements for such systems is the creation of sensors that can directly measure presence of specific pathogens since far from all diseases and pathologies can be determined by such indirect measurements as heart rate, pressure or ECG (today the most sophisticated smart bracelets and watches allow such measurements). Preferably new generation of biological sensors should detect the presence of pathogens or their markers in physiological fluids or human breathing. The development of affordable sensors of this kind could greatly simplify the chain that include taking medical tests; movement samples from the clinic to the laboratory, processing samples in the laboratory by qualified personnel, results transfer to the patient, results transfer to the doctor. According to last advances in data transfer technologies and in case of the presence of highly sensitive and selective sensors the abovementioned chain can be reduced to sample deposition on sensors and transfer results of measurement to the patient and doctor. Great advance of such approach is that results can be obtained in a few minutes.

Based on foregoing, it is possible to determine the basic requirements for biosensors: high accuracy, selectivity and velocity of the test with minimal usage skills, possibility of on-site detection and low cost of the tests.

Taking into account the above requirements for the biosensor, one of the most promising materials is reduced

graphene oxide, obtained by reduction of suspensions, films, or graphene oxide powders. Due to the presence of functional groups and relatively high conductivity, reduced graphene oxide can be successfully used both for the formation of a sensitive layer and transducer [1]. The advantage of graphene oxide is its good dispersibility, which makes possible graphene oxide deposition on various substrates by liquid methods, in particular, drop-casting [2], spin-coating [3] or aerosol deposition [4]. The reduction of graphene oxide can be carried out with the retention of a part of the functional groups, which subsequently can be used to immobilize bioavailable agents [5].

Several mechanisms of reduction of graphene oxide can be distinguished: thermal [6], chemical [7] and photochemical realized using UV radiation [8], as well as methods based on the use of lasers [9].

In this paper we showed the possibility of graphene oxide films formation with further local reduction of these films using laser irradiation. The possibility of controlled reduction of graphene oxide with the presence of a certain number of functional groups and conductivity is also shown. Moreover, we immobilized short DNA oligonucleotides (aptamers) to reduced graphene oxide film through a modified EDC/HNS reaction. Aptamers as biosensitive agents have such advantages over antibodies as higher stability, much simpler and cheaper synthesis [10-14]. As a final point we demonstrated selective response of sensors structures based on reduced graphene oxide with the binded aptamers to the target and reference proteins.

2. MATERIALS AND METHODS

As the substrate for graphene oxide film deposition we used polyethylene terephthalate (PET) with a thickness of 175 μm and a lateral size of the substrate of 40×40 mm. We used PET is due to the relatively high melting point, significantly exceeding 250°C that makes possible the heat treatment of the deposited films, and acceptable mechanical characteristics, at a low cost. The preparation of the substrates for the deposition of graphene oxide consisted in mechanical cleaning in 2-propanol (ECOS-1, Extra Pure, TU 2631-064-44493179-01).

An aqueous suspension of graphene oxide (4.7 mg/ml) obtained by the advanced Hammers method (MIP Graphene LLC, Russian Federation) [15] was diluted with deionized water to a concentration of 1.5 mg/ml and deposited on PET surface by spin-coating with the number of iterations from 5 to 15. Obtained films were dried at a temperature of 110°C for 20 minutes. The thickness of the obtained films was in range from 40 to 100 nm (according to atomic force microscopy).

Local restoration of the graphene oxide film was carried out by an automated setup which included a diode laser (445 nm wavelength) and a motorized sample table [16]. Control of the laser power in the range of 10-400 mW was carried out by pulse-width modulation with a frequency of 30 MHz. The pulse width ranged from 1 to 20 μs . The processing time at the point was 30 ms (the size of the laser beam was about $1.5 \cdot 10^3 \mu\text{m}^2$).

For the formation of a biosensitive layer, amine modified thrombin aptamers AmTBA with a nucleotide sequence (5'-GGTTGGTGTGGTTGG-3') were

used. Aptamers were synthesized using standard chemistry of phosphoramidites and purified by liquid chromatography (Apto-Farm, LLC, Russia). The amino group was introduced as a modified thymine residue at the 5'-end of the DNA sequence. The binding of aptamers to carboxyl groups contained in reduced graphene oxide was carried out using a commercially available electrophilic activator EDC (1-ethyl-3-(3-dimethylaminopropyl)-carbodiimide (Sigma-Aldrich, USA). The reaction was carried out in 100 mM buffer a solution of MES (2-(N-morpholino) ethanesulfonic acid, Sigma-Aldrich, USA), pH = 6.0, with the addition of 25% ethanol, at room temperature in an inert gas atmosphere. The final concentration of the aptamer in the conjugation reaction amounted to 50 μM . Binding occurred within 1 hour, after The solution was collected, centrifuged and analyzed by HPLC.

HPLC measurements were performed on an Agilent Technologies 1200 instrument with a DNA PAC 100 chromatographic column (particle diameter 4×250 mm and 13 μm , Thermo Scientific, USA). The mobile phases were as follows: A: 10 mM Tris, 1 mM EDTA, pH = 7.5, 5% acetonitrile; B: 10 mM Tris, 1 mM EDTA, pH = 7.5, 1 M NaCl, 5% acetonitrile. The gradient program included two stages: 0-1 min - 30% B, 1-20 min 30-50% B. The column temperature was 60°C, the flow rate was 1 ml/min. Detection was carried out by absorption at a wavelength of 254 nm.

Raman spectra were obtained on a Centaur U HR combined AFM/Raman complex (NanoScanTechnology Ltd, Russian Federation).

Fourier-IR spectroscopy was carried out on a Nicolet iS10 FTIR spectrometer (Thermo Fisher Scientific, USA) by the method of impaired total internal reflection.

The surface topography of the graphene oxide films was obtained using a Solver P47-Pro scanning probe microscope (NT-MDT, Russia).

Thrombin was used as the target protein, and albumin was used as the reference protein. The response of biosensors to the effects of proteins was recorded using an IPS-16 sensor parameters meter (Pracktik NC Ltd., Russian Federation).

3. RESULTS AND DISCUSSION

3.1. AFM IMAGING OF GRAPHENE OXIDE FILMS

We measured thickness of the obtained films by atomic force microscopy and made correlation with made correlation with the transmittance of the same films made by spectrophotometry. By the correlation between the spectrophotometric data, it is subsequently possible to make a fast control the thickness of the deposited films. The dependence of film thickness and optical transmittance on the number of deposition iterations in on **Fig. 1**.

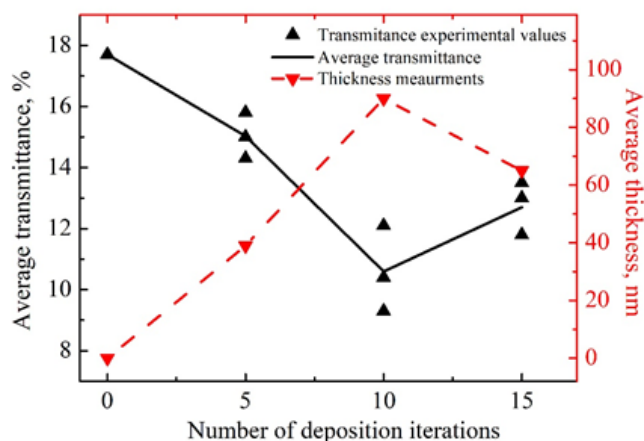


Fig. 1. Dependence of the thickness of the formed films and the optical transmittance on the number of deposition iterations.

The thickness of the obtained films was determined using atomic force microscopy according to the following procedure: a graphene oxide film was partially removed from the substrate with the end face of another PET substrate so that a step formed between the substrate and the graphene oxide film. The height of the step was determined by the surface topography (**Fig. 2**). The morphology of the film surface is typical for graphene oxide films and is similar to the morphology of the film presented in [17].

Based on the data obtained, it is possible to note the presence of a threshold number of depositions - 10, at which the maximum film thickness is achieved. It is assumed that this threshold is due to the fact that upon depositions the film does not have time to completely dry. In this case the adhesion of the upper layers of the film is less than the centrifugal force for a given solution concentration and substrate rotation speed.

From the obtained data, it can be noted that the film thickness and optical transmittance have a linear dependence on the number of deposition iterations and are inversely proportional to each other. The maximum film thickness is achieved at 10 iterations of deposition and is 90 nm. In this case, the optical transmittance is about $10 \pm 2\%$, which was used in the further preparation of the sensor structures.

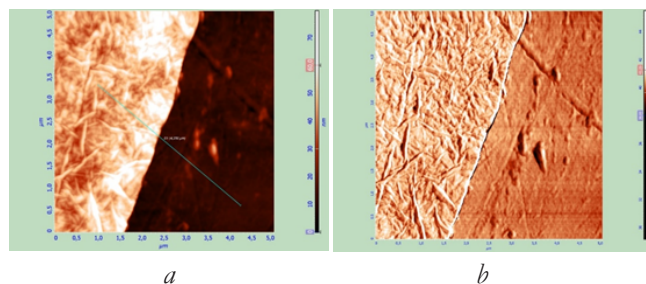


Fig. 2. The topography of the graphene oxide film (a) and the image of the boundary of the graphene oxide film and the PET substrate in the phase contrast mode.

3.2. INVESTIGATION OF THE FEATURES OF THE RECOVERY OF GRAPHENE OXIDE FILMS

The thickest graphene oxide films were used to study the features of reduction by laser irradiation. The films were treated with laser fluence from 15.2 to 59.4 J/cm². We assumed that at low fluence it will be weak reduction of graphene oxide but with conductive channels formation and residual amounts of functional groups, that will be sufficient for aptamer binding. From the obtained results (Fig. 3) we can note that the ratio I_D/I_G is reduced to about 0.4 with increasing fluence to about 37 J/m², which means that there is a removal of structural defects, primarily due to removal oxygen-containing functional groups. When fluence is more than 60 J/cm² we observed destruction of the film with partial ablation of substrate. The maximum degree of graphitization and according to Raman spectroscopy is achieved at a fluence of 48.3 J/cm², which follows from the ratios I_D/I_G and I_{2D}/I_G . But considering the fact that the resistance and ratio I_D/I_G and I_{2D}/I_G vary in the range from 35 to 50 J/cm², it is assumed that the resulting energy is sufficient to heat the graphene oxide film over the

entire thickness. Increasing I_{2D}/I_G ratio tells us about structuring of reduced graphene oxide due to the presence turbostratic graphite consisting of several graphene flakes which have a random orientation in the layer. It is interesting to note that there is a significant correlation between the resistance of the reduced areas and the I_D/I_G ratio, that assumes quasi-linear nature of the energy distribution in the irradiated graphene oxide film.

Based on the data of Raman spectroscopy it can be concluded that the maximum number of functional groups (i.e., structural defects) observed in 15-25 J/cm² fluence range but nevertheless reduced graphene oxide film in this case shows conductivity. This fluence values were used in further work for sensor structures formation.

3.3. IMMOBILIZATION OF APTAMERS

To study the specific features of the binding of DNA nucleotides to reduced graphene oxide, we used a well-studied aptamer with affinity for thrombin [18] with amino modification (Am-TBA). The nucleotide sequence of this aptamer: 5'-GGT'TGGTGTGGT'TGG-3'. As it was shown in [19], TBA recognizes thrombin with very high affinity using its TT loops, and the core structure of the G quadruplex stabilizes the exact location of the loops. In this case we used the 5'-amino-thymidine modification of the aptamer (Am-TBA), due to the fact that the addition of nucleotide residues and functional groups at the 5'-end of the TBA does not change the structure of the aptamer that binds thrombin and does not affect binding to the target protein [20]. The amine group in Am-TBA is necessary for covalent bonding by carboxyl groups

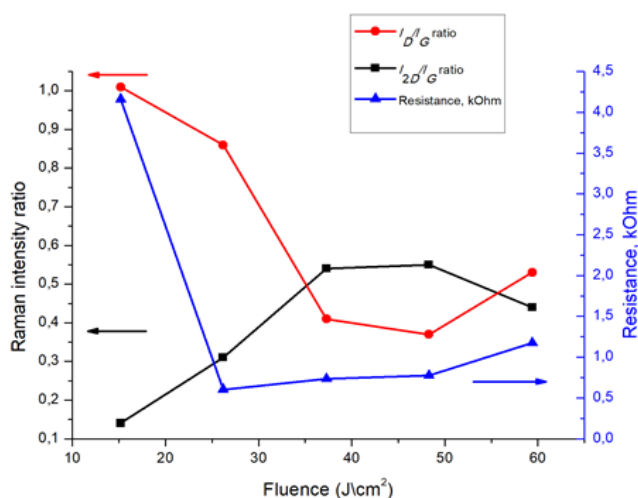


Fig. 3. Dependence of the intensity ratios D, G, and 2 D of Raman peaks and the resistance of the reduced regions on the laser fluence.

of the reduced graphene oxide film pre-activated with carbodiimide (EDC).

The EDC conjugation method is an extremely common practice for bioconjugation: the coupling reaction proceeds with a quantitative yield. However, when we applied this method to conjugate an amino-modified aptamer derivative with a reduced graphene oxide film, we saw that the hydrophobic surface effect of the reduced graphene oxide plays an important role. We did not get a satisfactory yield with the standard reaction method. We have shown that the addition of 25% vol. of ethanol to the reaction mixture improves the yield of the reaction.

HPLC analysis of AmTBA amount allows only reactive carboxyl groups to be calculated. However, it is the number of active carboxyl groups that determines the number of conjugated sensitive molecules on the surface of the reduced graphene oxide and, therefore, it determines the effectiveness of the biosensor.

Based on the amount of the amino-modified AmTBA aptamer, we calculated that the specific number of carboxyl groups reaches 29 pmol per 1 mm², maximum at fluence 42 J/cm², 32 pmol per 1 mm², at fluence 35 J/cm² and 43 pmol per 1 mm² films at a minimum fluence of 25 J/cm² (Table).

Table

Aptamer conjugation results.

Laser fluence, J/cm ²	The percentage change in the concentration of AmTBA, %	Quantitative change in the quantity of AmTBA, nmol	The specific amount of reactive carboxyl groups per unit area, 10 ¹² /nm ²
25	32	3.2	43
35	29	2.9	32
42	26	2.6	29

Thus, we observed a tendency to increase the presence of carboxyl functional groups with a decrease in the laser fluence and determined that laser treatment with a fluence of about 25 J/cm² is suitable for aptamer communication and, therefore, for the entire sensor.

3.4. STUDY OF THE FEATURES OF IMMOBILIZATION

The Raman spectra from the sensor structures before and after the aptamer interaction are shown in Fig. 4. In these spectra, we can observe *D* (~1350 cm⁻¹), *G* (~1600 cm⁻¹) and *2D* (~2700 cm⁻¹) bands respectively. It is known that the *D* band arises due to *A_{1g}* symmetry and originates from the zone boundary phonons. The *D* band is usually attributed to various defects in the graphite lattice. The *G* band on the other hand is first-order scattering, related to *E_{2g}* symmetry and corresponds to the Brillouin zone of crystalline *sp*² lattices in graphite [21].

Higher ID/IG ratio in the reduced graphene oxide indicates larger defect density [22, 23] i.e. including functional groups. Thus in our case we observe large defect presence in the sensitive area of biosensor including functional groups. It

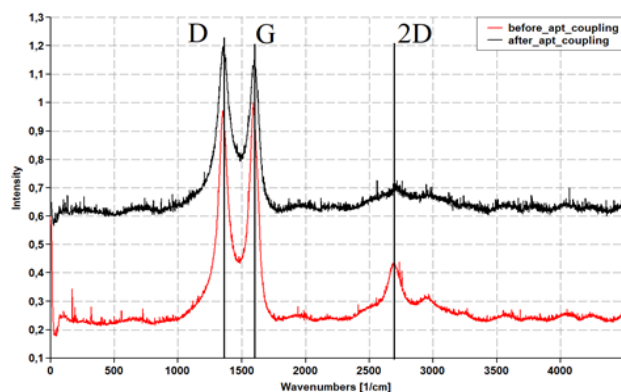


Fig. 4. Raman spectra on the reduced surface of graphene oxide before and after aptamer interaction.

has been reported that the 2D peak profile is sharp for pristine graphene, whereas low and wide 2D peak intensity as compared to D and G peaks indicates higher disorder rate in the GO structure [24]. From figure 5 and abovementioned information on the nature of Raman bands we can make next observations and deduction. One can see that there are 2 main features in spectra after coupling: change in ID/IG ratio (0.98-0.99 before to 0.86-1.13 after aptamer coupling) and decrease of 2D peak intensity. As we assume these effects could be corresponded to increase of defect number due to presence of aptamer-rGO conjugates with the trend and values ID/IG ratio before and after aptamer coupling very similar to the effects obtained in [25, 26]. Authors of [26] correspond this effect to the coupling of polyethylenimine (PEI) to the graphene oxide. In our case, such comparison is legal due to low reduction rate of graphene oxide that thus contains different functional groups. Based on abovementioned information we have indirect confirmation of aptamer coupling that is confirmed further by FTIR spectroscopy (Fig. 5).

From Fig. 5 we can mention presence of several characteristic peaks we attribute to hydroxyl, carboxyl, carbonyl and epoxide. Broad peak at $\sim 3400\text{ cm}^{-1}$ could be attributed to O-H stretching vibrations, i.e. hydroxyl groups presence [27]. One should note that this peak is clearly observed only in sensitive area after coupling reaction. Minor peaks at 2847 cm^{-1} (symmetric) and 2917 cm^{-1} (asymmetric) are $-\text{CH}_2$ absorption band that was split into two sub-bands and can be assigned to alkyl moieties (as a result of the reduction of COOH to $-\text{CH}_3$ segment) [28]. Relatively intensive peak at $\sim 1720\text{ cm}^{-1}$ in case of reduced graphene oxide in contact area should be attributed to carboxyl groups presence, which means that reduction with low fluence doesn't remove all functional groups. On the other hand, large decrease in this peak intensity after aptamer coupling means that we observe reaction between aptamer and carboxyl group. The same situation is described in [29] for 6 arm polyethylene glycol amines conjugated with graphene oxide. According to [30] the peak at $\sim 1720\text{ cm}^{-1}$ should be attributed to $\text{C}=\text{O}$ carboxyl and carbonyl groups, peak at 1640 cm^{-1} can be attributed to the skeletal vibrations of un-oxidized graphitic domains. Wide band at about $\sim 1080\text{ cm}^{-1}$ appears due to hydroxyls [31].

From FTIR spectra we can make a conclusion that after the graphene oxide reduction. A number of functional groups still remain in the film. Moreover, after aptamer coupling, we observe decrease of the carboxyl peak intensity, which means transformation of this groups after coupling reaction. It is that we want and predict for low reduction ratio.

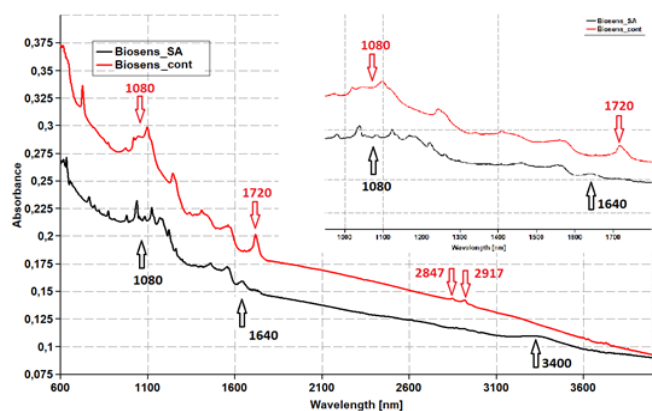


Fig. 5. FTIR spectra of the biosensor in the region of the reduced oxide with and without aptamers applied.

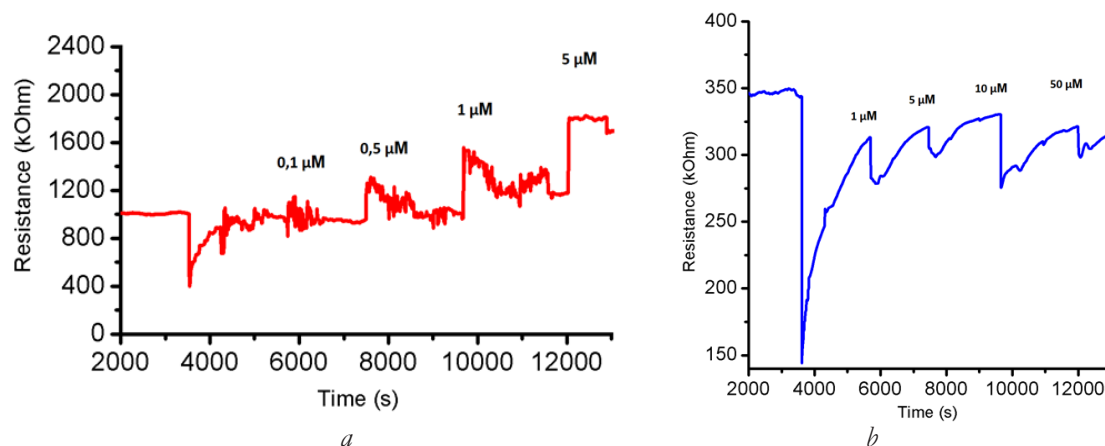


Fig. 6. Response of sensory structures to thrombin (a) and albumin (b).

3.5. SENSOR RESPONSE RESEARCH

We exposed the sensitive area with thrombin (target) and albumin proteins (reference) to get a response from the sensor. Sensors with a coupled thrombin-binding aptamer were exposed to thrombin (**Fig. 6a**) and albumin (**Fig. 6b**). We observed a significant difference between sensory signals acting on different proteins. The sensors also showed various signs of resistance change,

Fig. 6 shows that there is a reaction to thrombin in which the response increases with increasing concentration of thrombin, while in the case of albumin there is no noticeable difference in response even at concentrations differing by 2 orders of magnitude. The latter fact suggests that albumin interacts nonspecifically with aptamers, whereas in the case of thrombin, it is precisely the selective interaction of the aptamer with thrombin that is observed. In addition, it is noticeable in Fig. 6a that, after reaching the maximum response, a resistance fluctuation is observed with a trend towards a return to the initial resistance. We attribute the fact of resistance fluctuation to protein desorption process, while in case of albumin we observe nonspecific interaction of albumin with aptamers, cause in case of interaction

with reduced graphene oxide surface we should observe must observe non-recovery response due strong coupling of rGO with albumin like in [32]. The detection limit of the developed sensor on thrombin is in range from 1 to 10 μM.

CONCLUSION

In this work, we showed the possibility of the formation and controlled reduction of graphene oxide films using laser radiation. The possibility of binding short DNA oligonucleotides (aptamers) with reduced graphene oxide through the carboxyl groups of the latter was shown. The optimal range of fluence values for the reduction of graphene oxide is 15-25 J/cm². Optimal binding of aptamers is achieved with minimal fluence. The response of the sensors to the target and reference protein is shown, and there are noticeable differences in the response to thrombin and albumin with a minimum detectable concentration of the first 1 μM.

ACKNOWLEDGEMENTS:

This work was financially supported by the grant of the Ministry of Education and Science of the Russian Federation No. 14.574.21.0182 (unique identifier RFMEFI57417X0182).

REFERENCES

1. Celik N, Balachandran W, Manivannan N. Graphene-based biosensors: methods, analysis and future perspectives. *IET Circuits Devices Syst.*, 2015, 9:434-445.
2. Xiaoning Tang, Xiansheng Zhang, Huiping Zhang, Xingmin Zhuang and Xiong Yan. Facile dip-coating process towards multifunctional nonwovens: Robust noise reduction, abrasion resistance and antistatic electricity. *Textile Research Journal*, 2018, 88(22):2568-2578.
3. Kymakis E, Stratakis E, Stylianakis MM, Koudoumas E, Fotakis C. Spin coated graphene films as the transparent electrode in organic photovoltaic devices. *Thin Solid Films*, 2011, 520:1238-1241.
4. HongFei Shi, Can Wang, ZhiPei Sun, YueLiang Zhou, KuiJuan Jin, GuoZhen Yang. Transparent conductive reduced graphene oxide thin films produced by spray coating. *Science China Physics, Mechanics & Astronomy*, 2015, 58(1):1-5
5. Zhang Y-L, Guo L, Xia H, Chen Q-D, Feng J, Sun H-B. Photoreduction of Graphene Oxides: Methods, Properties, and Applications. *Advanced Optical Materials*, 2013, 2(1):10-28.
6. McAllister MJ et al. Single Sheet Functionalized Graphene by Oxidation and Thermal Expansion of Graphite. *Chem. Matter*, 2007, 19:4396-4404.
7. Stankovich S et al. Synthesis of graphene-based nanosheets via chemical reduction of exfoliated graphite oxide. *Carbon*, 2007, 45(7):1558-1565.
8. Rabchinskii MK, Shnitov VV, Dideikin AT, Aleksenskii AE, Vul' SP, Baidakova MV, Pronin II, Kirilenko DA, Brunkov PN, Weise J, Molodtsov SL. Nanoscale Perforation of Graphene Oxide during Photoreduction Process in the Argon Atmosphere. *The Journal of Physical Chemistry C*, 2016, 120(49):28261-28269.
9. Gengler RYN, Badali DS, Zhang D, Dimos K, Spyrou K, Gournis D, Miller RJD. Revealing the ultrafast process behind the photoreduction of graphene oxide. *Nature Communications*, 2013, 4(1).
10. Röthlisberger P, Gasse C, Hollenstein M. Nucleic Acid Aptamers: Emerging Applications in Medical Imaging, Nanotechnology, Neurosciences, and Drug Delivery. *Int J Mol Sci.*, 2017, 18(11):E2430.
11. Park KS. Nucleic acid aptamer-based methods for diagnosis of infections. *Biosens Bioelectron.*, 2018, 102:179-188.
12. Shigdar S et al. Aptamers as theranostic agents: modifications, serum stability and functionalization. *Sensors (Basel)*, 2013, 13(10):13624-13637.
13. Pu F, Ren J, Qu X. Nucleobases, nucleosides, and nucleotides: versatile biomolecules for generating functional nanomaterials. *Chem Soc Rev.*, 2018, 47(4):1285-1306.
14. Hughes RA, Ellington AD. Synthetic DNA Synthesis and Assembly: Putting the Synthetic in Synthetic Biology. *Cold Spring Harb Perspect Biol.*, 2017, 9(1):023812.
15. Alexandrov GN, Smagulova SA, Kapitonov AN, Vasil'eva FD, Kurkina II, Vinokurov PV, Timofeev VB, Antonova IV. Thin partially reduced oxide-graphene films: Structural, optical, and electrical properties. *Nanotechnologies in Russia*, 2014, 9(7-8):363368.
16. Struchkov NS, Kondrashov VA, Rozanov RY, Nevolin VK. Research and development of the method of graphene oxide thin films local reduction by modulated laser irradiation. *18th Russian*

- Youth Conference on Physics of Semiconductors and Nanostructures, Opto- and Nanoelectronics*, 2016, Peter Great St Petersburg Polytechn Univ, St Petersburg, RUSSIA, 2016, vol. 816, BRISTOL: Iop Publishing Ltd, 2017.
17. Yamaguchi H, Eda G, Mattevi C et al. Highly uniform 300 mm wafer-scale deposition of single and multilayered chemically derived graphene thin films. *ACS Nano*, 2010, 4:524-528.
18. Bock LC, Griffin LC, Latham JA, Vermaas EH, Toole JJ. Selection of single-stranded DNA molecules that bind and inhibit human thrombin. *Nature*, 1992, 355(6360):564-566.
19. Pica A, Krauss RI, Merlino A, Nagatoishi S, Sugimoto N, Sica F. Dissecting the contribution of thrombin exosite I in the recognition of thrombin binding aptamer. *FEBS J.*, 2013, 280:6581-6588.
20. Musumeci D, Oliviero G, Roviello GN, Bucci EM, Piccialli G. G-quadruplex-forming oligonucleotide conjugated to magnetic nanoparticles: synthesis, characterization, and enzymatic stability assays. *Bioconjug Chem.*, 2012, 23(3):382-391.
21. Yang D. et al. Chemical analysis of graphene oxide films after heat and chemical treatments by X-ray photoelectron and microRaman spectroscopy. *Carbon*, 2009, 47:145-152.
22. Ferrari AC et al. Raman spectrum of graphene and graphene layers. *Phys. Rev. Lett.*, 2007, 97:187401-187404.
23. Kotakoski J et al. From point defects in graphene to two-dimensional amorphous carbon. *Phys. Rev. Lett.*, 2011, 106:105505-105508.
24. Malard LM, Pimenta MA, Dresselhaus G, Dresselhaus MS. Raman spectroscopy in graphene. *Phys. Rep.*, 2009, 473:51-88.
25. Kurapati R, Bonachera F, Russier J et al. Covalent chemical functionalization enhances the biodegradation of graphene oxide. *2D Mater.*, 2018, 5:015020.
26. Rodriguez-Silva AA, Movil-Cabrera O, Oliveira dos Anjos CT, Staser JA. Supercapacitor-Based Biosensor for Low Density Lipoprotein Detection. *Journal of The Electrochemical Society*, 2016, 163(6):B256-B263.
27. Lee D, Cho H, Han D, Chand R, Yoon T, Kim Y. *J. Mater. Chem. B*, 2017, DOI: 10.1039/C6TB03357A.
28. Bhavana Gupta, Niranjana Kumar, Kalpataru Panda et al. Role of oxygen functional groups in reduced graphene oxide for lubrication. *Scientific Reports*, 7:45030. DOI: 10.1038/srep45030.
29. Eluyemi MS, Eleruja MA, Adedeji AV et al. Synthesis and Characterization of Graphene Oxide and Reduced Graphene Oxide Thin Films Deposited by Spray Pyrolysis Method. *Graphene*, 2016, 5(03):143-154.
30. Akbar Bagri, Cecilia Mattevi, Muge Acik et al. Structural evolution during the reduction of chemically derived graphene oxide. *Nature Chemistry*, 2010, 2:581-587.
31. Xitong Liu, Chenxu Yan, and Kai Loon Chen. Adsorption of Human Serum Albumin on Graphene Oxide: Implications for Protein Corona Formation and Conformation. *Environ. Sci. Technol.*, 2019, 53:8631-8639.

DOI: 10.17725/rensit.2019.11.331

Spectral and conductive properties of film heterostructures based on fullerene-containing material and 4-methylphenylhydrazone N-isoamilisatine

Alexey N. Gusev, Alim S. Mazinov, Andrey S. Tyutyunik, Vladimir S. Gurchenko

V.I. Vernadsky Crimean Federal University, <https://cfuv.ru/>

Simferopol 295007, Russian Federation

E-mail: galex0330@rambler.ru, mazinovas@cfuv.ru, real-warez@mail.ru, gurchenko_v@mail.ru.

Received 22.11.2019, peer reviewed 29.11.2019, accepted 02.11.2019

Abstract. The 4-methylphenylhydrazone N-isoamylisatin method consists of 4-methylphenylhydrazone and a diode heterostructure. The best method for producing, synthesizing, microscopy of carbon films and an organic precursor. The results of the successive x-ray phase analysis of the materials used are presented. Also, the optical spectra of isatins having short wavelength (420-500 nm) and long wavelength (850-900 nm) extrema giving absorption peaks at 3-3.1 eV and luminescence at 1.4 eV. The results of studies of IR spectroscopy of primary carbon films and an organic composite are obtained. The current-voltage characteristics of a thin-film heterostructure based on a fullerene-accessible material and an organic precursor with ITO-aluminum strapping are presented. It was shown that the experimental structures have rectifying diode characteristics with hysteresis of the forward branch of the I-V characteristic.

Keywords: organic heterostructure, thin-film structures, current-voltage characteristics, X-ray phase analysis, fullerene-containing material, hydrazone

PACS 61.48.+c, 61.66.Hq, 73.61.-r

Acknowledgments: The reported study was funded by RFBR, project number 19-32-90038.

For citation: Alexey N. Gusev, Alim S. Mazinov, Andrey S. Tyutyunik, Vladimir S. Gurchenko. Spectral and conductive properties of film heterostructures based on fullerene-containing material and 4-methylphenylhydrazone N-isoamilisatine. *RENSIT*, 2019, 11(3):331-336; DOI: 10.17725/rensit.2019.11.331.

CONTENTS

1. INTRODUCTION (331)
 2. COMPOSITION OF HETEROSTRUCTURES (332)
 3. HETEROSTRUCTURE SPECTROSCOPY (333)
 4. ELECTRICAL PARAMETERS OF THE HETEROJUNCTION (334)
 5. CONCLUSION (334)
- REFERENCES (335)

1. INTRODUCTION

The future simplification in the construction of electronic circuits is directly related to the printing technologies of flexible microcircuits, in which, to date, carbon materials demonstrate relatively high performance [1, 2]. Such composites are of particular interest when combined with organic and inorganic materials [3, 4]. On the other hand, the

achievements of thin film organic electronics optimistically promise to enable the creation of stable and fully functional devices on organic structures in the near future [5]. The construction of heterostructures based on organics with the addition of fullerenes allows not only to provide an acceptable quantum yield [6], but also makes it possible to construct 3D bulk barrier structures [7]. The use of organic materials as a donor allows us to create a potential barrier similar to diode structures. The simplicity and cheapness of the production of organic functional layers and fullerene-containing materials (FCM) is an indisputable advantage over the more expensive and complex analogues in production [8].

Based on the above assumptions, in this work, an attempt was made to build an organic heterostructure based on FCM and organic material, 4-methylphenylhydrazone N-isoamylisatin (IMPH). We also attempt to draw analogies with classical solid state barrier structures in terms of their optical and electrical properties. The FCM obtained by the low-temperature cracking method [9] was used as an acceptor. The synthesis of the organic precursor was carried out according

to the technique presented in previously published works [10, 11].

2. COMPOSITION OF HETEROSTRUCTURES

To determine the composition of fullerene-containing soot and to confirm the molecular structure of IMPH, methods of X-ray phase analysis and IR spectroscopy were used. The X-ray diffraction patterns of FCM and IMPH were recorded on a DRON-3 general-purpose X-ray diffractometer (Bragg-Brentano focusing scheme using a graphite monochromator) in the angular range - 2θ from 7° to 110° . An X-ray tube with a copper anode λ ($K\alpha$) = 0.154184 nm was used. The primary and secondary beams were limited by slits: horizontal — 0.25 mm, vertical — 6 mm, and Soller slits — 0.5 mm. The detector rotation speed is $0.5^\circ/\text{min}$, the time constant is $1 \cdot 10^3$ imp/s. Sample rotation speed –120 rpm (axis in the survey plane) (**Fig. 1**).

The proportion of 2.7% C_{60} (Buckminsterfullerene, **Table**) in the total share of 93% in the carbon component of the entire starting material and the corresponding peaks in the X-ray diffraction pattern (**Fig. 1**) allow us to classify the starting carbon powder as a fullerene-containing material

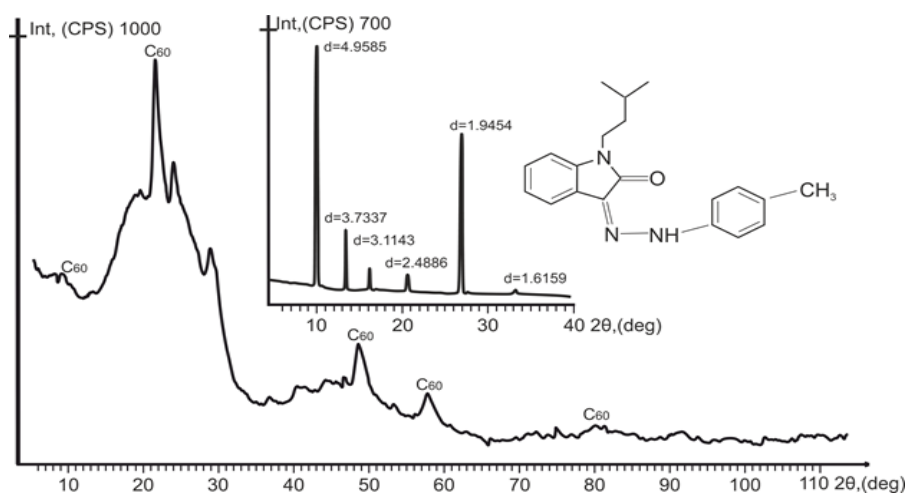


Fig. 1. X-ray diffraction pattern of FCM sample (main graph) and 4-methylphenylhydrazone N-isoamylisatin (inset).

Table

Key FCM components

International name	Mass fraction, %	COD ID	International name	Mass fraction, %	COD ID
Carbon Lonsdaleite	28.9	1100004	Buckminsterfullerene	2.7	9011073
Carbon	13.2	9012588	Supercubane	2.2	9012241
Carbon	12.9	2101499	Carbon	2.0	9012593
Carbon	12.2	9014004	Carbon	0.7	9012592
Carbon Graphite 3R	9.7	1101021	Carbon Graphite 2H	0.4	1011060
Carbon	7.7	9012594	Carbon	0.4	9012590

[9]. An X-ray phase analysis of IMPH in the solid phase showed that the organic precursor has a tetragonal system with sides: $a = 19.27609045 \text{ \AA}$; $b = 19.27609045 \text{ \AA}$; $c = 14.14478333 \text{ \AA}$. In this case, the simplest space group P4 can line up at angles: $\alpha = 90^\circ$; $\beta = 90^\circ$; $\gamma = 90^\circ$ (inset in Fig. 1).

3. HETEROSTRUCTURE SPECTROSCOPY

Spectral analysis in the visible range (400–900 nm) involved using a prismatic monochromator with a halogen lamp, with appropriate filters after normalization to the hydrogen line. Each of the constituent functional layers of the general heterostructure was separately deposited on coverslips with corresponding volume fractions. The dependences of the intensities of the transmitted (T) and reflected (R) signals normalized to the spectra of the initial substrates had at least $1.5 \cdot 10^3$ points

with a prism rotation duration of at least 30 minutes (Fig. 2a).

The relatively even spectra of R and T IMPH films 2.2–2.3 μm thick had short-wave (420–500 nm) and long-wave (850–900 nm) extrema giving absorption peaks at 3–3.1 eV and luminescence in the region of 1.4 eV (insets in Fig. 2a).

An attempt to preliminary estimate the band gap using the Tauc equation, by analogy with [12], showed the presence of an energy barrier of 3.05 eV. FCM films deposited from a benzene solution had practically zero transmission and reflection spectra lying at the noise level of the photomultiplier with an absorption coefficient even lower than that of pure fullerene.

A characteristic feature of the IR spectra of IMPH and FCM (inset in Fig. 2b), in the

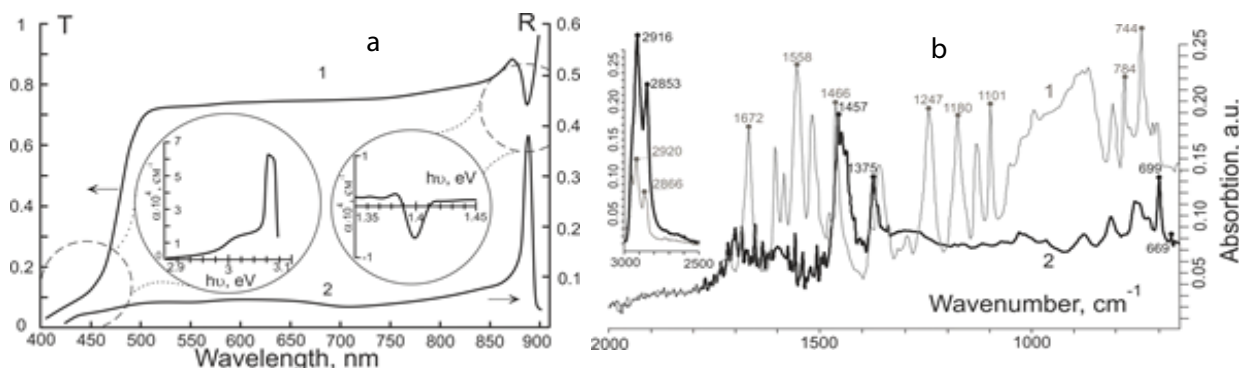


Fig. 2. Optical spectra of IMPH (a) — transmission (1), reflection (2), absorption peaks (insets). IR spectra (b) - IMPH (1) and FCM (2).

region of small wavelengths (3000–2500 cm^{-1}), is the presence of several absorption bands associated with vibrations of the C-H group [11]. The intensity of the FCM peaks in this range is several times higher than the IMPH peaks. In the region of lower frequencies (2000–650 cm^{-1}), the bands of 1375 and 1457 cm^{-1} are inherent for FCM, which can be assigned to the C_{sp^3} -H group, and peaks 669, 699 cm^{-1} to C_{sp^2} -H [13]. In the range (2000–650 cm^{-1}), IMPH is characterized by the presence of peaks of 1672 and 1558 cm^{-1} associated with C = O and C = N groups, the peaks in the region of 1610–1364 cm^{-1} are due to stretching vibrations of C = C of benzene rings. The range of 1295–1054 cm^{-1} is C-N, C-C, C-H oscillations. Deformation vibrations of C-H groups at 1128–744 cm^{-1} are observed in benzene rings and an alkyl substituent.

4. ELECTRICAL PARAMETERS OF THE HETEROJUNCTION

To determine the electrical parameters, the heterojunction was created in the form of a “sandwich” structure (insert in **Fig. 3**). As the contact group, we used aluminum (Al) on a setall, 120 nm thick, with a specific resistance of 40 Ω/sq and indium tin oxide (ITO) with a specific resistance of 16–18 Ω/sq having a transparency of at least 82%. By the method of pouring from a solution, IMPH was applied to ITO, and FCM to aluminum. Volume resistivity measurements were made at least 10 times using the Keysight B1500 Semiconductor Analyzer. Samples were placed in a sealed shielding chamber with a lighting matrix at a temperature of 20–25°C.

The current dependences of the assembly were built according to the averaged eightfold

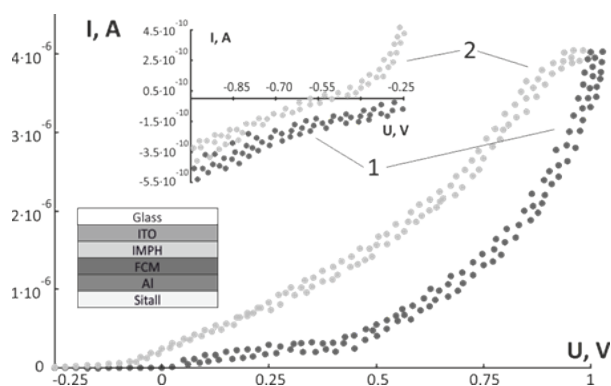


Fig. 3. The current – voltage characteristics of the FCM heterostructure is 4-methylphenylhydrazone of *N*-isoamylisatin (1-straight branch; 2-reverse branch).

point measurement with a voltage scan duration of 5, 10, 15 minutes. The ratio of the forward current to the reverse one in the interval from -1 V to +1 V, averaged over five cycles, amounted to 104 with apparent hysteresis in the positive quarter of the I–V characteristics (Fig. 3). By analogy with classical semiconductor devices, for a carbon-organic heterostructure, it is also possible to derive bias voltages at direct connection of 0.45–0.5 V with access to a linear current section at 4.1 μA (Fig. 3). At the same time, the achievement of reverse currents of 530 pA at a voltage of -1 V may be due to the not ideal construction of the space charge region and the presence of recombination levels, which reduce the photosensitivity of the FCM-IMPH heterostructure to zero, in comparison with C_{60} -4-methylphenylhydrazone of *N*-isoamylisatin [11].

5. CONCLUSION

The key result of the study is a demonstration of the possibility to build a potential barrier on the basis of fullerene-containing material and the organic precursor 4 - methylphenylhydrazone *N*-isoamylisatin.

Determination of the studied materials composition by X-ray phase analysis confirmed the molecular structures of the

samples. Spectral analysis in the visible range yielded the characteristics of reflection, absorption, and transmission, and also made it possible to calculate the energy barrier. The study of IR spectra showed the presence of peaks characteristic of both IMPH and FCM used. The addition of an organic compound made it possible to significantly enhance the conductive properties of the thin film structure of a fullerene-containing material and to achieve a direct and reverse current ratio of 4 orders.

The type of current-voltage characteristic indicates that there is a potential barrier due to different morphologies of basic molecular systems which requires additional studies.

In general, the results confirm the prospects for research into organic quantum electronics, which, together with nanostructured carbon materials, will significantly expand the frontiers of modern instrument engineering.

ACKNOWLEDGMENTS: *The reported study was funded by RFBR, project number 19-32-90038.*

REFERENCES

1. Cao X, Lau C, Liu Y, Wu F, Gui H, Liu Q, Zhou C. Fully Screen-Printed, Large-Area, and Flexible Active-Matrix Electrochromic Displays Using Carbon Nanotube Thin-Film Transistors. *ACS Nano*, 2016, 10(11):9816-9822.
2. Chortos A, Koleilat GI, Pfattner R, Kong D, Lin P, Nur R, Bao Z. Mechanically Durable and Highly Stretchable Transistors Employing Carbon Nanotube Semiconductor and Electrodes. *Advanced Materials*, 2015, 28(22):4441-4448.
3. Romanov NM, Zaharova IB, Malova MM, Elistratova MA, Mysihin SF. Vliyanie gamma izlucheniya na tonkie nanokompozitnye plenki MEH-PPV/C₆₀ [The effect of gamma radiation on thin nanocomposite films MEH-PPV/C₆₀]. *St. Petersburg Polytechnic University Journal - Physics and Mathematics*, 2018, 11(4):24-34 (in Russ.).
4. Zaharova IB, Zimirov VM, Romanov NM, Kvyatkovskii OE, Makarov TL. Opticheskie i strukturnye svoystva plenok fullerena s dobavleniem tellurida kadmiya [Optical and structural properties of fullerene films with the addition of cadmium telluride]. *Fizika tverdogo tela*, 2014, 56(5):1024-1029 (in Russ.).
5. Izawa S, Shintaku N, Kikuchi M, Hiramoto M. Importance of interfacial crystallinity to reduce open-circuit voltage loss in organic solar cells. *Appl. Phys. Lett*, 2019, 115(6):153301.
6. Awartani O, Kudenov MW, Kline RJ, O'Connor BT. In-Plane Alignment in Organic Solar Cells to Probe the Morphological Dependence of Charge Recombination. *Adv. Funct. Mater*, 2015, 25(8):1296-1303.
7. Page ZA, Liu Y, Duzhko VV, Russell TP, Emrick T. Fulleropyrrolidine interlayers: Tailoring electrodes to raise organic solar cell efficiency. *Science express*, 2014, 346(6208):441-444.
8. Nimith KM, Satyanarayan Nagarajan, Govindarao Umesh. Enhancement in fluorescence quantum yield of MEH-PPV:BT blends for polymer light emitting diode applications. *Optical Materials*, 2018, 80:143-148; DOI: 10.1016/j.optmat.2018.04.046.
9. Rabotyagov KV, Shevchenko AI, Mazinov AS. Issledovanie struktury i fiziko-khimicheskikh svoystv poristykh uglerodnykh materialov, poluchennykh nizkotemperaturnym krekingom [Study of the structure and physicochemical properties of porous carbon materials obtained by low temperature cracking]. *Uchenye zapiski Krymskogo federalnogo universiteta i. V.I. Vernadskogo, Ser. Biology. Chemistry*, 2015, 1(67):125-131 (in Russ.).
10. Cigáň M, Jakusová K, Gáplovský M, and Filo J, Donovalová J, Gáplovský A. Isatin phenylhydrazones: Anion enhanced photochromic behavior. *Photochem. Photobiol.*

- Sci*, 2015, 14:2064-2073.
11. Gusev AN, Mazinov AS, Shevchenko AI, Tyutyunik AS, Gurchenko VS, Braga EV. Volt-ampernye kharakteristiki i fotoelektricheskiy effect geterostruktur fulleren C_{60} -4-methylphenylhydrazone N-isoamylisatin [Current-voltage characteristics and photoelectric effect of heterostructures of fullerene C₆₀-4-methylphenylhydrazone N-isoamylisatin]. *Pis'ma v ZHTEF*, 2019, 45(19):40-43 (in Russ.).
 12. Evstropiev SK, Kylagina AS, Evstropiev KS, Kolobkova EV, Nikonorov NV, Soshnikov IP, Oreshkina KV, Hrebtov AI. Vliyaniye molekulyarnogo vesa polivinilpirrolidona na strukturu, spektral'nyye i nelineynno-opticheskiye svoystva kompozitsionnykh materialov, sodержashchikh nanochastitsy CdS/ZnS.[The effect of the molecular weight of polyvinylpyrrolidone on the structure, spectral and nonlinear optical properties of composite materials containing CdS/ZnS nanoparticles]. *Optika i spektroskopiya*, 2018, 125(5):608-614 (in Russ.).
 13. Rabotyagov KV, Mazinov AS, Gurchenko VS, Tyutyunik AS, Shevchenko AI, Ivanchenko IO, Arutinov NE. Sravnitel'naya kharakteristika tonkoplenochnykh fullerensoderzhashchikh struktur [Comparative characteristics of thin-film fullerene-containing structures]. *Uchenye zapiski Krymskogo federalnogo universiteta i. V.I. Vernadskogo, Ser. Biology. Chemistry*, 2019, 5(2):210-218 (in Russ.).

DOI: 10.17725/rensit.2019.11.337

Source detection in dispersive environment

Venedikt M. Kuz'kin

Wave Research Center, A.M. Prokhorov General Physics Institute of RAS, <http://www.gpi.ru/>
Moscow 119991, Russian Federation

E-mail: kumiov@yandex.ru

Sergey A. Pereselkov, Sergey A. Tkachenko

Voronezh State University, <http://www.vsu.ru/>
Voronezh 394006, Russian Federation

E-mail: pereselkov@yandex.ru; sega-tk@mail.ru

Yuri V. Matvienko

Institute of Marine Technology Problems of Far Eastern Department of RAS, <http://www.imtp.febras.ru/>

Vladivostok 690091, Russian Federation

E-mail: yamat@marine.febras.ru

Received 10.10.2019, peer reviewed 01.11.2019, accepted 07.11.2019

Abstract. The theory and implementation of a new information technology for passive source detection in a dispersive environment is presented. The method is based on the processing of the interference pattern formed by broadband noise source. The estimation of noise immunity of interferometric processing is received. The results of numerical analysis of noise source detection using the Neumann-Pearson criterion in oceanic waveguides are considered.

Keywords: dispersion, interferometry, hologram, noise source, Neumann-Pearson test, detection characteristics

UDC 004.052.34

Acknowledgments: This work was financially supported by grants from the Russian Foundation for Basic Research (projects No. 19-08-00941, No. 19-29-06075) and the Presidium of the Russian Academy of Sciences No. 5 "Photonic Technologies in Sensing of Inhomogeneous Media and Bioobjects".

For citation: Venedikt M. Kuz'kin, Sergey A. Pereselkov, Yuri V. Matvienko, Sergey A.

Tkachenko. Source detection in dispersive environment. *RENSIT*, 2019, 11(3):337-344; DOI: 10.17725/rensit.2019.11.337.

Contents

1. Introduction (337)
 2. Noise immunity of interferometric signal processing (331)
 3. Source detection by the Neumann-Pearson criterion (333)
 4. Conclusion (335)
- References (335)

1. INTRODUCTION

In dispersing media, when multi-wave (multipath) propagation takes place, a mechanism of self-organization of the interference pattern (interferogram) of a moving (or stationary) broadband noise source is possible. The interference pattern formats the stable system of

localized bands in the frequency-time variables [1]. The slope of the bands is determined by the radial velocity of the source (the projection of the velocity towards the receiver). The frequency dispersion can be due to both the physical properties of the environment and the presence of the boundaries of the environment in which the waves propagate (waveguide propagation).

The information technology for signal processing of the source noise field (interferometric processing) is proposed by based on properties of interference pattern in waveguide. The offered information technology implements coherent accumulation of spectral intensity along localized bands by using 2D Fourier transform of interferogram. At the output of the 2D Fourier transformation of interferogram, the spectral density of the signal is localized in a narrow band in the form of focal spots caused by interference of modes (normal waves) of different numbers. In contrast of noise, the accumulation of interference along the interferogram bands is incoherent. The proposed interferometric signal processing makes it possible to solve the problem of localization of low-noise sources with high noise immunity: detection, direction, determination of radial velocity, distance and resolution [2-6].

The 2D Fourier transform of an interferogram is called a hologram, since it records and reconstructs the wave field of the source. Image

reconstruction is achieved by filtering the 2D spectral density of the source on the hologram and application of the 2D Fourier inverse transform [2-6]. This clearing of the source signal from noise does not require knowledge of the nature of the signal, noise and transfer function.

The application of the proposed signal processing does not depend on the nature of the dispersion. At the same time, the quantitative parameters of the dispersion determine the effectiveness of its use. The proposed signal processing allows a new understanding of the statistical problem of passive detection of a noise signal at presence of noise background. This paper presents a solution of this problem based on the Neumann-Pearson criterion [7]. Its solution focuses on an advanced example of sound propagation in an oceanic waveguide (the case of waveguide dispersion) by using a single receiver.

2. NOISE IMMUNITY OF INTERFEROMETRIC SIGNAL PROCESSING

The efficiency of interferometric processing is characterized by the limit (minimum) input ratio – signal/noise (s/n): q_{lim} . When value $q_0 \geq q_{lim}$ coherent accumulation of spectral intensity along interference bands is realized [2]. At this condition the source detection is stable and estimates of the source parameters are close to real values. For the scalar component of the source noise field and isotropic noise $q_{lim} \approx 1.5/J^2$ [3]. Here J – is the number of time intervals (samples)

at which coherent accumulations of spectral maxima of the wave field along the interference bands are realized

$$J = \frac{\Delta t}{T + \delta T}, \quad (1)$$

where Δt – time of observation, T – duration of noise realization of the source, δT the interval between samples. In order to noise realization to be independent, the duration δT must satisfy the condition $\delta T > \Delta f_1$, where Δf_1 noise source spectrum width.

Next, let's limit the area of input values $q_0 \geq 1.5/J$. That is practical interest. Signal and noise are considered independent Gaussian random processes with zero mathematical expectations. Let's put that in the band $\Delta\omega_1 = 2\pi\Delta f_1$ provides W localized bands with width $\Delta\omega_2 = 2\pi\Delta f_2$ and the contrast of the interferogram, i.e. the visibility of the bands, is equal to one. Along the interference bands, the intensity of the useful signal accumulates coherently, and the noise – incoherently. These provisions are not fulfilled accurately. But as it is shown by the results of computer modeling and nature experiments [2-6], the estimations remain quite correct.

Under the s/n ratio q_0 at the input of a single receiver at the initial time $t = 0$ refers to the value of

$$q_0 = q(0) = \frac{\overline{E_s(0)}}{\overline{E_n(0)}}, \quad (2)$$

where

$$\overline{E_s(0)} = \frac{1}{\pi} \int_0^\infty |s(0, \omega)|^2 d\omega = \frac{1}{\pi} \Delta\omega_1 |s(0, \omega_s')|^2, \quad (3)$$

$$\overline{E_n(0)} = \frac{1}{\pi} \int_0^\infty |n(0, \omega)|^2 d\omega = \frac{1}{\pi} \Delta\omega_1 |n(0, \omega_n')|^2 \quad (4)$$

– average energy of useful signal and noise. Here ω_s' and ω_n' – selected signal frequencies and noise in the band $\Delta\omega_1$. The stroke above means averaging over the ensemble of realizations. In accordance with (3), (4), the input ratio s/n (2) is equal to

$$q_0 = \frac{|s(0, \omega_s')|^2}{|n(0, \omega_n')|^2}. \quad (5)$$

The values in the numerator and denominator (5) are equal to the mathematical expectations of the signal intensity and noise at the initial time

$$M_s(0) = |s(0, \omega_s')|^2, \quad M_n(0) = |n(0, \omega_n')|^2. \quad (6)$$

Signal dispersion and noise at the initial moment is [8]

$$D_s(0) = 2 \left[|s(0, \omega_s')|^2 \right]^2, \quad D_n(0) = 2 \left[|n(0, \omega_n')|^2 \right]^2. \quad (7)$$

The average useful signal energy and noise during time accumulation Δt can be written in the form of the addition of energies at time intervals of duration T along the interference bands

$$\overline{E_s}(\Delta t) = \frac{1}{\pi} \int_0^\infty \left| \sum_{j=1}^J W s(t_j, \omega) \right|^2 d\omega, \quad (8)$$

$$\overline{E_n}(\Delta t) = \frac{1}{\pi} W J \sum_{j=1}^J \int_0^\infty |n(t_j, \omega)|^2 d\omega. \quad (9)$$

Suppose that the mathematical expectations of the signal and interference do not depend on the moment of reference t_j , that is $|s(t_j, \omega)|^2 = |s(\omega)|^2$ and $|n(t_j, \omega)|^2 = |n(\omega)|^2$. Then expressions (8), (9) take the form

$$\overline{E_s}(\Delta t) = \frac{1}{\pi} W^2 J^2 \overline{|s(\omega_s'')|^2} \Delta \omega_2, \quad (10)$$

$$\overline{E_n}(\Delta t) = \frac{1}{\pi} W J \overline{|n(\omega_n'')|^2} \Delta \omega_2, \quad (11)$$

so at the output of the time accumulation, the ratio s/n is equal to

$$q(\Delta t) = \frac{\overline{E_s}(\Delta t)}{\overline{E_n}(\Delta t)} = W J \frac{\overline{|s(\omega_s'')|^2}}{\overline{|n(\omega_n'')|^2}}. \quad (12)$$

Here ω_s'' и ω_n'' – selected frequency of the signal and noise in the band $\Delta \omega_2$.

Using the input ratio s/n (5), the expression (12) is represented in the form

$$q(\Delta t) = W J \frac{\overline{|s(\omega_s'')|^2} \overline{|n(\omega_n'')|^2}}{\overline{|n(\omega_n'')|^2} \overline{|s(\omega_s'')|^2}} q_0. \quad (13)$$

At the initial time, the average useful signal energies (3) and noise (4) can also be expressed as

$$\overline{E_s}(0) = \frac{1}{\pi} W^2 \overline{|s(\omega_s'')|^2} \Delta \omega_2, \quad (14)$$

$$\overline{E_n}(0) = \frac{1}{\pi} W \overline{|n(\omega_n'')|^2} \Delta \omega_2. \quad (15)$$

From the comparison of expressions (3), (4) and (14), (15) we find

$$\overline{|s(\omega_s'')|^2} \Delta \omega_1 = W^2 \overline{|s(\omega_s'')|^2} \Delta \omega_2, \quad (16)$$

$$\overline{|n(\omega_n'')|^2} \Delta \omega_1 = W \overline{|n(\omega_n'')|^2} \Delta \omega_2 \quad (17)$$

and then the expression (13) takes the form

$$q(\Delta t) = J q_0. \quad (18)$$

According to (10), (11) during the accumulation of mathematical expectations and dispersion of useful signal intensity and noise are equal

$$M_s(\Delta t) = W^2 J^2 \overline{|s(\omega_s'')|^2}, \quad M_n(\Delta t) = W J \overline{|n(\omega_n'')|^2}, \quad (19)$$

$$D_s(\Delta t) = 2W^4 J^4 \overline{|s(\omega_s'')|^2}^2, \quad D_n(\Delta t) = 2W^2 J^2 \overline{|n(\omega_n'')|^2}^2. \quad (20)$$

Thus, the multiple coherent summation of the interference maxima of the noise source wave field along the localized bands increases the output s/n ratio $q(\Delta t)$ by J times with respect to the input value q_0 . This increase becomes quite clear if we consider an analogy with the coherent spatial signal processing of a multi-element antenna containing Q receivers: with respect to a single receiver, the ratio of s/n increases Q -times.

Recording an interferogram onto a hologram and clearing the domain of spectral density localization from interference leads to an additional increase in the output ratio s/n compared to $q(\Delta t)$. The 2D Fourier transform of the interferogram localizes the 2D spectral density of the useful signal within a narrow hologram band, the area of which can be estimated as

$$S_s = \frac{\tau_{M-1}}{\Delta t}. \quad (21)$$

Here τ_{M-1} – position of the main maximum (M-1)-th focal spot on the time axis due to interference between extreme modes, where M – the number of modes forming the source field at the receiving point [2]. Outside this band, the spectral density is practically suppressed. The spectral density of the noise is distributed over the entire domain of the hologram, the area of which is equal to

$$S_n = |v_{M-1}| \tau_{M-1}, \quad (22)$$

where $v_{M-1} = -\omega_1 h_{1M}$ – position of the main maximum (M-1)-th focal spot on the axis of cyclic frequency [2]. Here $h_{1M} = h_1 - h_M$, h_m – horizontal wave number of m -th mode; ω_1 – average frequency of spectrum width $\Delta\omega_1$; ω – radial velocity of the source. In the 2D Fourier transformation, the energy does not change. Therefore, assuming that the noise power is uniformly distributed in the hologram region, the s/n ratio in the localization band of the spectral density of the useful signal (at the output of interferometric processing) will be

$$q_{hol} = \frac{S_n}{S_s} q(\Delta t). \tag{23}$$

According to (18), (21), (22), expression (23) takes the form

$$q_{hol} = J\gamma q_0 \tag{24}$$

where is the concentration coefficient $\gamma = |v_{M-1}| \Delta t$. In the case of a unmovable source, the value $|v_{M-1}|$ replaced by the width of the spectrum Δv in the hologram domain.

For shallow water in the low frequency range (several hundred hertz) and source velocities $\omega \approx 1-10$ m/s value $|v_{M-1}| \approx 0.07-0.7$ Gz [2–6]. Setting accumulation time $\Delta t = 100$ s, we obtain estimation $\gamma = 7-70$. The difference in the mechanism of accumulation of spectral intensity along the interference bands and the distribution of the spectral density of the wave field of the source and the noise on the hologram gives a high s/n ratio at the output of the interferometric processing.

3. DETECTION OF THE SOURCE BY THE NEUMAN-PIRSON CRITERION

Neumann-Pearson criterion optimizes the probability of correct detection p_1 (exceeding of given level at the output of the processing at the presence of useful signal) for a given probability of false alarm p_2 , those. exceeding given level at the absence of useful signal due to noise [7].

Probability density $p_{sn,n}(x)$ of random value $I_{sn,n}(\Delta t)$ equal to temporary accumulation of spectral density

$$I_{sn,n}(\Delta t) = \sum_{j=1}^J \overline{|s_j(t, \omega) + n_j(t, \omega)|^2} \tag{25}$$

has a complex form defined by the composition of generalized χ^2 -distributions and probability density determined by the Hankel function of zero order of the imaginary argument [8]. Here, the subscripts «sn» and «n» note the cases of presence and absence of a useful signal, respectively. In accordance with the central limit theorem for a large number of terms J probability density $p_{sn,n}(x)$ approximates for Gaussian distribution. Since value $I_{sn,n}(\Delta t) \geq 0$, so $p_{sn,n}(x) = 0$ at $x < 0$ and for probability density $p_{sn,n}(x)$, when $J \gg 1$, obtain [8]

$$p_{sn,n}(x) = \frac{1}{\sqrt{2\pi D_{sn,n}(\Delta t)}} \left\{ \exp \left[-\frac{(x - M_{sn,n}(\Delta t))^2}{2D_{sn,n}(\Delta t)} \right] + \exp \left[-\frac{(x + M_{sn,n}(\Delta t))^2}{2D_{sn,n}(\Delta t)} \right] \right\}, x \geq 0, \tag{26}$$

Here $M_{sn,n}(\Delta t)$ and $D_{sn,n}(\Delta t)$ – expectation and variance of a random variable $I_{sn,n}$ at

time moment Δt . According to (19), (20), (25) we have

$$M_{sn}(\Delta t) = W^2 J^2 \overline{|s(\omega_s'')|^2} + WJ \overline{|n(\omega_n'')|^2}, \quad (27)$$

$$D_{sn}(\Delta t) = 2 \left[W^2 J^2 \overline{|s(\omega_s'')|^2} + WJ \overline{|n(\omega_n'')|^2} \right]^2. \quad (28)$$

At the absence of a noise, the mathematical expectation $M_n(\Delta t)$ and variance $D_{sn}(\Delta t)$ are determined by expressions (19), (20). The linear $2D$ Fourier transform has the Gaussian probability density as well. Therefore, the probability density of the localized energy on the hologram has form similar to (26) by replacing expressions (27) and (28) by the relations

$$M_{sn(hol)}(\Delta t) = \gamma W^2 J^2 \overline{|s(\omega_s'')|^2} + WJ \overline{|n(\omega_n'')|^2}, \quad (29)$$

$$D_{sn(hol)}(\Delta t) = 2 \left[\gamma W^2 J^2 \overline{|s(\omega_s'')|^2} + WJ \overline{|n(\omega_n'')|^2} \right]^2. \quad (30)$$

Probability of false alarm p_2 at the output of interferometric signal processing equals to the probability that the noise level is more than given level g . So, probability of false alarm equals to

$$p_2 = \frac{1}{\sqrt{2\pi D_n(\Delta t)}} \int_g^\infty \left\{ \exp \left[-\frac{(x - M_n(\Delta t))^2}{2D_n(\Delta t)} \right] + \exp \left[-\frac{(x + M_n(\Delta t))^2}{2D_n(\Delta t)} \right] \right\} dx. \quad (31)$$

After simple transformations, taking into account the relationship (19), (20) between the quantities $M_n(\Delta t)$ and $D_n(\Delta t)$, expression (31) is reduced to the following form

$$p_2 = 1 - 0.5 [\Phi(\kappa_n - 0.5) + \Phi(\kappa_n + 0.5)], \quad (32)$$

where $\kappa_n = g/2M_n(\Delta t)$, $\Phi(x)$ – error integral

$$\Phi(x) = \frac{2}{\sqrt{\pi}} \int_0^x e^{-t^2} dt.$$

The probability of a false alarm is determined by the parameter κ_n . Expectation $M_n(\Delta t)$, according to (4), (17), can be represented as

$$M_n(\Delta t) = \frac{\pi}{\Delta\omega_2} J \overline{E_n}(0) = JM_n(0) \frac{\Delta\omega_1}{\Delta\omega_2}, \quad (33)$$

The noise energy density at the output of the temporary accumulation (for fixed input power and samples) is higher, than it is greater the ratio of the bands of the signal spectrum and the interferogram.

Probability of correct detection p_1 at the output of interferometric signal processing

$$p_1 = \frac{1}{\sqrt{2\pi D_{sn(hol)}(\Delta t)}} \int_g^\infty \left\{ \exp \left[-\frac{(x - M_{sn(hol)}(\Delta t))^2}{2D_{sn(hol)}(\Delta t)} \right] + \exp \left[-\frac{(x + M_{sn(hol)}(\Delta t))^2}{2D_{sn(hol)}(\Delta t)} \right] \right\} dx, \quad (34)$$

By using the ratios (12), (18), (24), (29), (30), can be represented as

$$p_1 = 1 - 0.5 [\Phi(\eta_1) + \Phi(\eta_2)], \quad (35)$$

where

$$\eta_1 = \frac{2\kappa_n - 1 - q_{hol}}{2(1 + q_{hol})}, \quad (36)$$

$$\eta_2 = \frac{2\kappa_n + 1 + q_{hol}}{2(1 + q_{hol})}. \quad (37)$$

One can see the probability of correct detection is determined by the parameter κ_n and the s/n ratio q_{hol} (24) at the output of interferometric processing.

The given false alarm probability p_2 determines the level of g . This level g determines the probability of correct

detection p_1 . Thus, it is possible to calculate the useful signal detection curves, representing the dependence of the probability of correct detection on the output (or input) s/n ratio at a fixed probability of false alarm p_2 . The range of input relations of s/n $q_0 = 1.5/J^2$ corresponds to the range of output values of s/n $q_{hol} \geq 1.5\gamma/J$. One can see, that the possibility of correct detecting of useful signal in interferometric signal processing for given probabilities p_1 and p_2 is not depend upon signal form and type of interference. The possibility of correct detecting is determined only by the energy density of the interference $M_n(\Delta t)$, the number of samples J and the concentration coefficient γ .

The **Fig. 1** shows the curves for correct detecting of useful signal as dependence of input s/n ratio q_0 for concentration coefficient $\gamma = 10$. Probability of false alarm $p_2 = 10^{-3}, 10^{-6}, 10^{-9}$. Number of samples $J = 15, 30$. These values corresponds to the limiting input relations of s/n $q_{lim} = 0.00667, 0.00167$. The decreasing of the

probability of false alarm leads to the probability of correct detection decreasing for a given input s/n ratio. At the samples increasing, the source detection efficiency increases.

4. CONCLUSION

In dispersing environment, the information technology for processing of signal interferograms of broadband sources is proposed. This information technology allows to solve the problem of localization of low-noise sources with high noise immunity. Of course, for each type of dispersing environment, the preliminary analysis of the efficiency of the offered signal processing is required.

The offered signal processing effectiveness is demonstrated by the example of waveguide dispersion of oceanic waveguides for the problem of noise source detection by the Neumann-Pearson criterion by using a single receiver. Noise immunity of signal processing is estimated. Analytical dependences of detection curves are obtained. The results of numerical calculations are presented.

ACKNOWLEDGMENTS: *This work was financially supported by grants from the Russian Foundation for Basic Research (projects No. 19-08-00941, No. 19-29-06075) and the Presidium of the Russian Academy of Sciences No. 5 "Photonic Technologies in Sensing of Inhomogeneous Media and Bioobjects".*

REFERENCES

1. Chuprov SD. The interference structure of the sound field in a layered ocean. In: *Acoustics of Ocean. The current situation*. Moscow, Nauka Publ., 1982, p. 71-82.

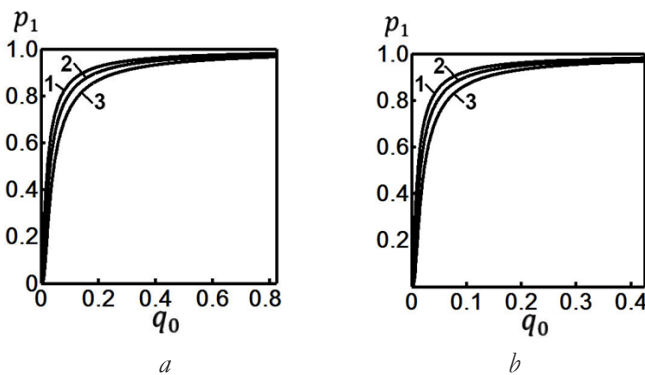


Fig. 1. The dependence of the probability of correct detection p_1 upon the input relations s/n q_0 for different values of the probability of false alarm p_2 : (a) $J = 15$; (b) $J = 30$. Concentration coefficient $\gamma = 10$. Curve 1 - $p_2 = 10^{-3}$; curve 2 - $p_2 = 10^{-6}$; curve 3 - $p_2 = 10^{-9}$.

2. Kuznetsov G.N., Kuzkin V.M., Pereselkov S.A. Spectrogram and localization of the sound source in the shallow sea. *Akust. zhurn.*, 2017, 63(4):406-418 (in Russ.).
3. Kaznacheev I.V., Kuznetsov G.N., Kuzkin V.M., Pereselkov S.A. Interferometric method for detecting a moving sound source by a vector-scalar receiver. *Akust. zhurn.*, 2018, 64(1):33-45 (in Russ.).
4. Kuz'kin VM, Pereselkov SA, Kuznetsov GN, Kaznacheev IA. Interferometric direction finding by a vector-scalar receiver. *Phys. Wave Phenom.*, 2018, 26(1):63-73.
5. Kuz'kin VM, Kuznetsov GN, Pereselkov SA, Grigor'ev VA. Resolving power of the interferometric method of source localization. *Phys. Wave Phenom.*, 2018, 26(2):150-159.
6. Kuznetsov GN, Kuz'kin VM, Lyakhov GA, Pereselkov SA, Prosovetskiy DYu. Direction finding of a noise sound source. *Phys. Wave Phenom.*, 2019, 27(3):237-241.
7. Tikhonov VI. *Optimum signal reception*. Moscow, Radio i svyaz' Publ., 1983, 320 pp.
8. Tikhonov VI. *Statistical radio engineering*. Moscow, Radio i svyaz' Publ., 1982, 624 p.

DOI: 10.17725/rensit.2019.11.345

Calculation the earthquake stability of various structures using the grid-characteristic method

^{1,2,3}Alena V. Favorskaya, ^{1,2}Igor B. Petrov

¹Moscow Institute of Physics and Technology, <https://mipt.ru/>
Dolgoprudny 141700, Moscow region, Russian Federation

²Scientific Research Institute of System Analysis of RAS, <https://www.niisi.ru/>
Moscow 117218, Russian Federation

³National Research Centre "Kurchatov Institute", <http://www.nrcki.ru/>
Moscow 123182, Russian Federation

E-mail: aleanera@yandex.ru, petrov@mipt.ru

Received 15.10.2019, peer reviewed 23.10.2019, accepted 31.10.2019

Abstract. Building in earthquake-prone regions requires the development of new methods for computer simulation in order to assess the safety of exploitation of constructed structures and design new structures. In this paper, we propose to use the grid-characteristic method on structured curvilinear grids to calculate the elastic and acoustic wave fields in the structure under consideration, containing the geological massif and surrounding water bodies. Then, based on the calculated field of the Cauchy stress tensor, the possible damaged regions are determined. To highlight the complex shape of the boundaries, multiple contacting separate computational grids are used, between which the contact condition of continuity of speed and traction is used. Test calculations of the earthquake resistance of a multi-story residential building, metro station, footbridge with elevator shaft and dam of hydroelectric power station were carried out. The used grid-characteristic method allows us to accurately solve the boundary-value problem of elastic and acoustic wave equations in the integration domain of complex shape.

Keywords: computer simulation, grid-characteristic method, structural curved grids, earthquake resistance, residential building, footbridge, dam, metro station

UDC 519.63

Acknowledgments: The study was carried out at the Moscow Institute of Physics and Technology with a grant from the Russian Science Foundation (project No. 17-71-20088).

For citation: Favorskaya A.V., Petrov I.B. Calculation of seismic resistance of various structures using the grid-characteristic method. *RENSIT*, 2019, 11(3):345-350; DOI: 10.17725/rensit.2019.11.345.

CONTENTS

1. INTRODUCTION (345)
 2. MODELS AND METHODS (346)
 3. RESULTS AND DISCUSSION (348)
 4. CONCLUSION (348)
- REFERENCES (349)

1. INTRODUCTION

Nowadays the study of earthquake resistance is carried out using high-quality computer

modeling. The finite element method is mainly used [1-3] for this in up-to-date software. For simulation the propagation of seismic waves through the geological rock, finite-difference methods might be used [4].

The grid-characteristic method was proposed in [5]. Recently, new modifications of this method [6] and the corresponding computational algorithms for high-performance

computer systems [7] are being developed. The grid-characteristic method has been successfully applied to solve direct [8-10] and inverse [11] seismic prospecting problems. The grid-characteristic method was also applied to investigate the seismic stability of high-rise buildings [12,13], seismic isolation [14], composite oil pipelines [15], and nuclear power plants [16].

2. MODELS AND METHODS

To describe the behavior of the simulated materials and water under intense seismic influences, the boundary-value problem of elastic wave equation:

$$\rho \frac{\partial}{\partial t} \mathbf{v}(\mathbf{r}, t) = (\nabla \boldsymbol{\sigma}(\mathbf{r}, t))^T, \quad (1)$$

$$\begin{aligned} \frac{\partial}{\partial t} \boldsymbol{\sigma}(\mathbf{r}, t) = & (\rho c_p^2 - 2\rho c_s^2)(\nabla \cdot \mathbf{v}(\mathbf{r}, t)) \mathbf{I} + \\ & + \rho c_s^2 (\nabla \otimes \mathbf{v}(\mathbf{r}, t) + (\nabla \otimes \mathbf{v}(\mathbf{r}, t))^T). \end{aligned} \quad (2)$$

and acoustic wave equation:

$$\rho \frac{\partial}{\partial t} \mathbf{v}(\mathbf{r}, t) = -\nabla p(\mathbf{r}, t), \quad (3)$$

$$\frac{\partial}{\partial t} p(\mathbf{r}, t) = -\rho c^2 (\nabla \cdot \mathbf{v}(\mathbf{r}, t)). \quad (4)$$

is solved jointly.

Hereinafter, \mathbf{v} is the vector field of the local velocity of the medium (displacement derivative on time), $\boldsymbol{\sigma}$ is the tensor field of the symmetric second-order Cauchy stress tensor, p is the scalar field of pressure in the acoustic medium, ρ is the density, c_p , c_s are the longitudinal (P-) and transverse (S-) waves speeds in an elastic medium and the speed of sound in an acoustic medium, respectively, ∇ is the gradient vector, \mathbf{I} is the unit tensor of the second rank, \otimes is the symbol of the tensor product of vectors, \cdot .

The condition of the free boundary was set at the boundaries with air, having the following forms for systems (1), (2) and (3), (4), respectively:

$$\boldsymbol{\sigma} \cdot \mathbf{m} = 0, \quad (5)$$

$$p = 0.$$

In expression (5), \mathbf{m} is the external unit normal to the boundary.

At the contact boundaries between subdomains with structured and unstructured computational grids and subdomains with various parameters of the media, the contact condition of complete adhesion was used for system (1), (2):

$$\boldsymbol{\sigma}_1 \cdot \mathbf{m} = \boldsymbol{\sigma}_2 \cdot \mathbf{m}, \quad (6)$$

$$\mathbf{v}_1 = \mathbf{v}_2, \quad (7)$$

and system (3), (4):

$$p_1 = p_2, \quad (8)$$

$$\mathbf{v}_1 \cdot \mathbf{m} = \mathbf{v}_2 \cdot \mathbf{m}. \quad (9)$$

In expressions (6)-(9) \mathbf{m} is the external unit normal to the boundary of the body 1; the indices 1 and 2 correspond to different contacting bodies.

At the contact boundaries between elastic and acoustic media, the following condition was used:

$$p = -(\boldsymbol{\sigma} \cdot \mathbf{m}) \cdot \mathbf{m}, \quad (10)$$

$$\boldsymbol{\sigma} \cdot \mathbf{m} - ((\boldsymbol{\sigma} \cdot \mathbf{m}) \cdot \mathbf{m}) \mathbf{m} = 0, \quad (11)$$

$$\mathbf{v}_A \cdot \mathbf{m} = \mathbf{v}_E \cdot \mathbf{m}. \quad (12)$$

In expressions (10)-(12), \mathbf{m} is the external unit normal to the boundary of the elastic body; the indices E and A correspond to elastic and acoustic bodies.

To obtain numerically solution the systems of equations (1), (2) and (3), (4), the grid-characteristic method was used, which was described in detail in works [17, 18]. The Rusanov scheme was used [19]. For this, the system of equations is written in the following form:

$$\frac{\partial}{\partial t} \mathbf{q} + \mathbf{A}_1 \frac{\partial}{\partial \xi_1} \mathbf{q} + \mathbf{A}_2 \frac{\partial}{\partial \xi_2} \mathbf{q} + \mathbf{A}_3 \frac{\partial}{\partial \xi_3} \mathbf{q} = 0.$$

Here \mathbf{q} is the vector of unknowns composed of components of \mathbf{v} and p for system (1), (2) and

composed of components of \mathbf{n}_j and for system (3), (4). The directions of the coordinate system either coincide with the coordinate axes when using structured computational grid, or locally in each cell coincide with the axes of a curved computational grid. In this case, one can enter a vector \mathbf{n}_j along the direction under consideration :

$$\mathbf{n}_j = \nabla \xi_j(x, y, z).$$

The eigenvalues of each of the matrices will run through the following sets of values for systems (1), (2) and (3), (4), respectively:

$$\{|\mathbf{n}_j|c_p, -|\mathbf{n}_j|c_p, |\mathbf{n}_j|c_s, -|\mathbf{n}_j|c_s, 0\}, \quad (13)$$

$$\{|\mathbf{n}_j|c, -|\mathbf{n}_j|c, 0\}. \quad (14)$$

The use of curved computational grids requires not only large computational resources, but may also require a decrease in the time step to ensure the stability of the method due to the effective growth of wave propagation speeds in accordance with expressions (13), (14).

Models of structures and the host geological massif were used with the following elastic and acoustic parameters shown in **Table 1**.

The integration steps in time and coordinates were varied for different calculations and for different subregions in one calculation in accordance with **Table 2**. A seismic wave, longitudinal or transverse, with a wavelength of 50 m was set at an angle of 15° to the Earth's surface. The maximum amplitudes of these waves for various calculations are also given in Table 2.

Table 1

Elastic and acoustic parameters of simulated media.

Material	P-wave speed, m/s	S-wave speed, m/s	Density, kg/m ³
Concrete	4250	2125	2300
Geological rock	2300	1400	2500
Ground under riverbed	2200	400	2400
Water	1500	-	1000

Table 2

Computational parameters.

Computation	Maximal coordinate step, m	Minimal coordinate step, m	Time step, mks	Total time, s	Maximal value of v in P-wave/S-wave, m/s
Building	0.05	0.025	5.875	0.47	0.24/0.25
Dam	0.5	0.07576	30	1.0	0.375/1.0
Station	0.04	0.02	4.7	0.141	0.1/0.1
Foot-bridge	0.02	0.02	4.7	0.47	0.25/0.25

The total time was selected in such a way that after the propagation of the wave under consideration, new damage would no longer be formed.

An example of using separate computational grids to describe the complex geometry of the computational domain is shown in **Fig. 1** on the example of the hall of the metro station. Note that fragments of computational grids at the edges of the figure are shown. The used integration steps on coordinates in different calculation grids for this calculation are presented in **Table 3**.

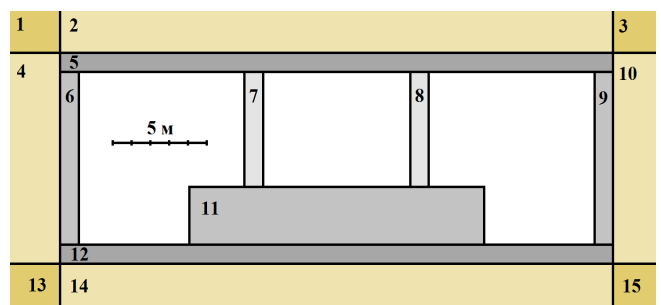


Fig. 1. Separate computational grids: metro station.

Table 3

Steps of separate computational grids: metro station.

Grids numbers	1, 3, 13, 15	4, 10	2, 14	5, 6, 7, 8, 9, 11, 12
Step along OX, m	0.04	0.04	0.02	0.02
Step along OY, m	0.04	0.02	0.04	0.02
Material	Geological rock	Geological rock	Geological rock	Concrete

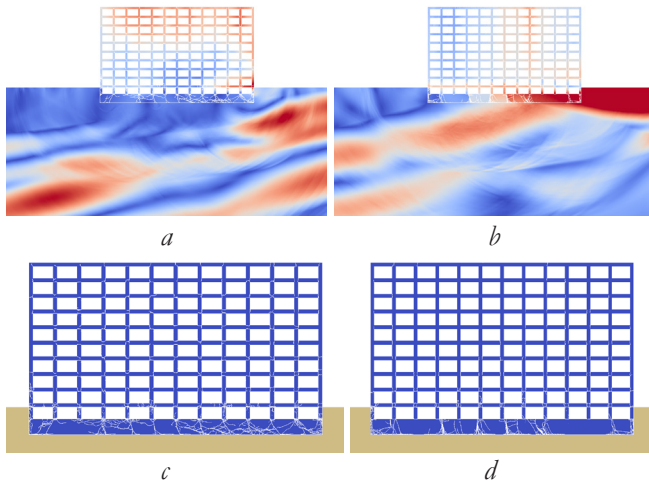


Fig. 2. Multi-story residential building.

To simulate the destruction of materials, the criterion for the main stress was used. Concrete with a strength of 1 MPa was considered. In this case, the bearing walls of the footbridge and the columns of the metro station were considered reinforced with a strength of 2.5 MPa. When modeling the dam, soil with a strength of 3 MPa was considered.

3. RESULTS AND DISCUSSION

In Figs. 2-5 the earthquake resistance calculations of a multi-story residential building, an earth dam of a hydroelectric power station, a metro station, and a footbridge under roadway are shown respectively. A dam with a height of 56 m and a base area of 66 m was considered. The metro station was located at a depth of 25 m.

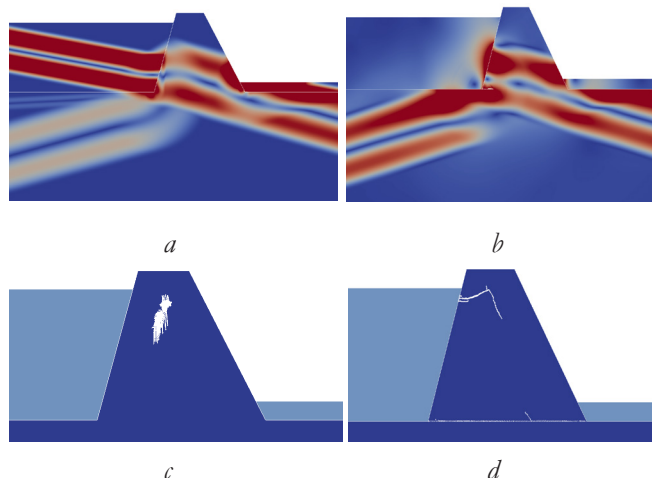


Fig. 3. Dam of hydroelectric power station.

Table 4

Time moments in wave patterns presented in the paper.

Computation	Building		Dam		Station		Footbridge	
	P-wave	S-wave	P-wave	S-wave	P-wave	S-wave	P-wave	S-wave
Time moment, ms	94	141	43.33	224.1	21.15	35.25	28.2	25.85
Figure number	Fig. 2a	Fig. 2b	Fig. 3a	Fig. 3b	Fig. 4a	Fig. 4b	Fig. 5a	Fig. 5b

Figs. 2a, 2c, 3a, 3c, 4a, 4c, 5a, and 5c correspond to the action of the P-wave, Figs. 2b, 2d, 3b, 3d, 4b, 4d, 5b, and 5d correspond to the action of the S-wave. The corresponding time moments are presented in Table 4. In Figs. 2a, 2b, 3a, 3b, 4a, 4b, 5a, and 5b the wave patterns are shown, in Fig. 2c, 2d, 3c, 3d, 4c, 4d, 5c, and 5d the areas of destruction are shown.

The calculations performed demonstrate the possibility of joint solution of systems (1), (2) and (3), (4) in heterogeneous regions of complex shape and the subsequent determination of the weaknesses of the structures under consideration depending on the type of seismic impact.

4. CONCLUSION

The grid-characteristic method on structured and combined structured and curved grids allows to successfully calculate the localization of the damaged areas of complex objects: multi-story buildings, metro stations, footbridges, hydroelectric power stations dams. The main features of this modification of the

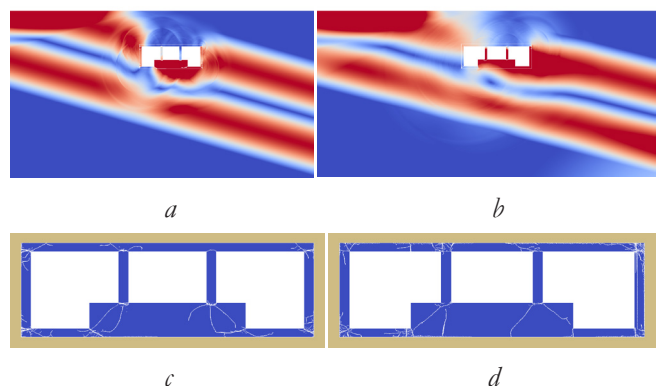


Fig. 4. Metro station.

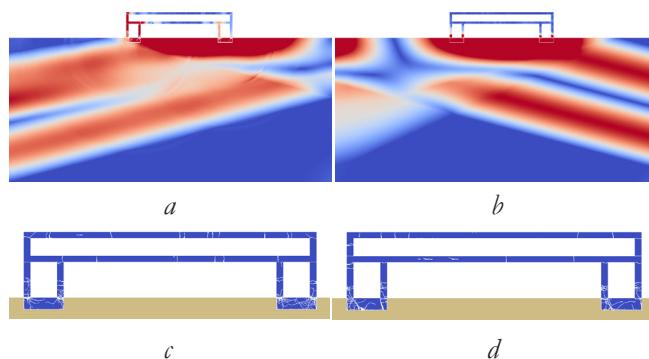


Fig. 5. Footbridge over a roadway.

grid-characteristic methods are described in the paper. Particular attention is paid to the use of separate computational grids to describe the complex geometry of the computational domain and to vary the step along the coordinate axes. Test calculations of seismic resistance of various structures were carried out. The use of combined structured regular and curved grids allows to save computing resources and to use more detailed computational grids and models of the structures under consideration. It is shown that the grid-characteristic method allows highly accurate calculation of elastic and acoustic wave processes in heterogeneous objects of complex shape.

ACKNOWLEDGMENTS

This work has been performed at Moscow Institute of Physics and Technology and supported by the Russian Science Foundation, grant no. 17-71-20088.

REFERENCES

1. Yaghin ML, Hesari MA. Dynamic analysis of the arch concrete dam under earthquake force with ABAQUS. *J.Appl.Sci.*, 2008, 8(15):2648-2658.
2. Xunqiang Y, Jianbo L, Chenglin W, Gao L. ANSYS implementation of damping solvent stepwise extraction method for nonlinear seismic analysis of large 3-D structures. *Soil. Dyn.Earthq.Eng.*, 2013, 44:139-152.
3. Nikolic Z, Zivaljic N, Smoljanovic H, Balic I. Numerical modelling of reinforced concrete structures under seismic loading based on

- the finite element method with discrete inter element cracks. *Earthq.Eng.Struct.D.*, 2017, 46(1):159-178.
4. Moczo P, Robertsson JO, Eisner L. The finite-difference time-domain method for modeling of seismic wave propagation. *Adv. Geophys.*, 2007, 48:421-516.
5. Magomedov KM, Kholodov AS. *Setochno-kharakteristicheskie chislennye metody* [Grid-Characteristic Numerical Methods]. Moscow, Nauka Publ., 1988, 287 p.
6. Khokhlov NI, Golubev VI. On the class of compact grid-characteristic schemes. *International. Conf. on 50 years of the develop. of grid-characteristic method, SIST Ser.*, 2019, 133:64-77.
7. Ivanov AM, Khokhlov NI. Efficient Inter-process Communication in Parallel Implementation of Grid-Characteristic Method. *Conf. on 50 years of the develop. of grid-characteristic method, SIST Ser.*, 2019, 133:91-102.
8. Stognii PV, Khokhlov NI. 2D seismic prospecting of gas pockets. *Conf. on 50 years of the develop. of grid-characteristic method, SIST Ser.*, 2019, 133:156-166.
9. Petrov DI Application of grid-characteristic method to some seismic exploration problems in the Arctic. *J.Phys.:Conf.Ser.*, 2018, 955(1).
10. Favorskaya AV, Petrov IB. The use of full-wave numerical simulation for the investigation of fractured zones. *Math. Models Comput. Simul.*, 2019, 11(4):518-530 (in Russ.).
11. Golubev VI. The Usage of Grid-Characteristic Method in Seismic Migration Problems. *Conf. on 50 years of the develop. of grid-characteristic method, SIST Ser.*, 2019, 133:143-155.
12. Favorskaya A, Golubev V, Khokhlov N. Two approaches to the calculation of air subdomains: Theoretical estimation and

- practical results. *Procedia Comput. Sci.*, 2018, 126:1082-1090.
13. Breus A, Favorskaya A, Golubev V, Kozhemyachenko A, Petrov I. Investigation of seismic stability of high-rising buildings using grid-characteristic method. *Procedia Comput. Sci.*, 2019, 154:305-310.
 14. Favorskaya AV, Breus AV, Galitskii BV. Application of the grid-characteristic method to the seismic isolation model. *Conf. on 50 years of the develop. of grid-characteristic method, SIST Ser.*, 2019, 133:167-181.
 15. Beklemysheva KA, Vasyukov AV, Golubev VI, Zhuravlev YI. On the estimation of seismic resistance of modern composite oil pipeline elements. *Dokl.AN*, 2018, 97(2):184-187 (in Russ.).
 16. Favorskaya A, Golubev V, Grigoriev D. Explanation the difference in destructed areas simulated using various failure criteria by the wave dynamics analysis. *Procedia Comput. Sci.*, 2018, 126:1091-1099.
 17. Favorskaya AV, Petrov IB. Grid-characteristic method. *Innov. in Wave Process. Modelling and Decision Making, SIST Ser.*, 2018, 90:117-160.
 18. Favorskaya AV, Zhdanov MS, Khokhlov NI, Petrov IB. Modeling the wave phenomena in acoustic and elastic media with sharp variations of physical properties using the grid-characteristic method. *Geophys.Prospect.*, 2018, 66(8):1485-1502.
 19. Magomedov KM, Kholodov AS. The construction of difference schemes for hyperbolic equations based on characteristic relations. *Zhurn,vych.mat. i vych fiz.*, 1969, 9(2):158-176 (in Russ.).

DOI: 10.17725/rensit.2019.11.351

Modeling vertical fractures using the Schoenberg model on structured grids by grid-characteristic method

Polina V. Stognii

Educational Scientific and Experimental Center of Moscow Institute of Physics and Technology, <http://kmipt.ru/>
Dolgoprudny 141700, Moscow region, Russian Federation

E-mail: stognii@phystech.edu

Nikolay I. Khokhlov, Igor B. Petrov

Scientific Research Institute for System Analysis of Russian Academy of Sciences, <https://www.niisi.ru/>
Moscow 117218, Russian Federation

E-mail: k_b@inbox.ru, petrov@mipt.ru

Received 28.08.2019, peer reviewed 16.09.2019, accepted 30.09.2019

Abstract. Seismic prospecting is one of the most popular methods of revealing oil and gas reservoirs in the North seas. Geological media, which contain hydrocarbon layers, often include different heterogeneities, for example, fractures. Many scientific works are devoted to modelling fractures and ways of considering them in various mathematical problems, but the Linear Slip model, known as Schoenberg model of fracture, is still the most actual, though this model was developed at the end of the last century. This model is characterized by the presence of an additional parameter — so called fracture opening parameter, describing fractures. In this work, we present the algorithm of introducing the Schoenberg fracture model in the grid-characteristic method. The fracture is organized to be parallel to the boundaries of the modelling grid. The fracture is situated on the border of the two media with the same characterizing parameters. We describe in detail the algorithm of computing the meanings of velocity and stress tensor in the points on the border with the fracture. In order to verify the correctness of the developed approach to modelling a fracture using the Schoenberg fracture model, we carry out the test calculations of seismic waves spread in a homogeneous media with the vertical extremely thin fracture, described by the not equal to null normal component of the fracture opening coefficient and with the equal to null tangential component of the fracture opening coefficient.

Keywords: seismic prospecting, numerical modelling, grid-characteristic method, fractured media

UDC 519.63

Acknowledgments: This work was financially supported by the Russian Federal Property Fund in the framework of scientific project No. 19-01-00281.

For citation: Polina V. Stognii, Nikolay I. Khokhlov, Igor B. Petrov. Modeling vertical fractures using the Schoenberg model on structured grids by grid-characteristic method. *RENSIT*, 2019, 11(3):351-356; DOI: 10.17725/rensit.2019.11.351.

CONTENTS

1. INTRODUCTION (351)
 2. DETERMINANT EQUATIONS (352)
 3. NUMERICAL METHOD (352)
 4. RESULTS (354)
 5. CONCLUSION (355)
- REFERENCES (355)

1. INTRODUCTION

Fractures are often a barrier on the way of exploring the chosen territory during conducting the

geological works on oil and gas deposits extraction [1, 2]. They bring in a significant summary into the seismograms, got as a result of geological layers exploration. Therefore, it is necessary to take into account fractured media while modelling the chosen area in order to obtain more accurate results of seismic data processing.

In reality, the sizes of most fractures are of that sort that the ratio of their width to their height is equal to zero in the limit [3]. These fractures are described by an abstract model of an extremely thin

fracture. In this work, we explore only models of extremely thin fractures. A fracture is described by a set of contact and border conditions in the place of its establishment in the computational area.

There are different ways of modelling the seismic waves spread in fractured media. For example, hierarchical grids are applied to modelling static fractures [4]. In the work [5], authors use the pseudospectral method for modelling fractures with not equal to zero parameter of viscosity.

Hudson model [6] and Schoenberg model [7] are the most well-known models, used for describing fractures. In the Hudson model, a fracture is described by the parameter of effective stiffness, which is linearly or quadratic (first or second order of accuracy, accordingly) dependent from the so-called parameter of fracture density [8].

In Schoenberg model [9, 10], the condition of equal normal components of the stress tensor is set on the boundary of a fracture. In addition, the way of computing the normal components through special parameters of fracture opening, dependent from the medium, filling the fracture, is supposed. The Schoenberg model was already introduced in the well-known Galerkin method, the results can be found in [11].

In this work, we introduce the method of computing geological media with a fracture with the help of the grid-characteristic method and the induced Schoenberg model for the 2D case, which is done for this method for the first time. The contact conditions on the boundary with the fracture are described in detail. In addition, we present the example of numerical modelling for the seismic reflection from the fracture on the boundary of two media.

2. DETERMINANT EQUATIONS

For describing the spread of elastic waves in a homogeneous medium, we used the system of linear-elastic equations [12]:

$$\rho \frac{\partial}{\partial t} v = (\nabla \cdot \sigma)^T, \tag{1}$$

$$\frac{\partial}{\partial t} \sigma = \lambda (\nabla \cdot v) I + \mu ((\nabla \times v) + (\nabla \times v)^T), \tag{2}$$

where ρ is the medium density, v is the speed of elastic waves spread in the medium, σ is the Cauchy stress tensor, λ and μ are the Lamé parameters, determining the properties of the elastic material.

For fracture describing, we used the equations from the model of Schoenberg [13]:

$$\sigma_{xx}^{left} = \sigma_{xx}^{right}, \tag{3}$$

$$\sigma_{xy}^{left} = \sigma_{xy}^{right}, \tag{4}$$

$$\frac{\partial \sigma_{xx}}{\partial t} = K_N (v_x^{right} - v_x^{left}), \tag{5}$$

$$\frac{\partial \sigma_{xy}}{\partial t} = K_T (v_y^{right} - v_y^{left}). \tag{6}$$

In (3)-(6) the indexes «left» and «right» denote the medium on the one side (left) and the medium on the other side (right) from the fracture.

K_N and K_T are the normal and tangential components of the parameter of fracture opening. These characteristics are known beforehand or can be calculated. The description of the theoretical computation of normal and tangential components of fracture opening are presented in the work [14], the description of calculating the parameter of fracture opening as a result of the laboratory experiment is presented in the work [15]. The width of the fracture is considered to be extremely small.

3. NUMERICAL METHOD

For solving the system of linear-elastic equations (1), (2) we used the grid-characteristic method [16]. For computing the homogeneous medium, we applied the Laks-Wendroff scheme of the second order of accuracy [17]:

$$u_i^{n+1} = u_i^n - \frac{ct}{2h} (u_{i+1}^n - u_{i-1}^n) + \frac{c^2 t^2}{2h^2} (u_{i+1}^n + u_{i-1}^n - 2u_i^n). \tag{7}$$

In order to compute fractures, we also used the grid-characteristic method, but with some modifications. Now, we examine the algorithm of computing points on the boundary with the fracture in more detail.

For this, we present the system of equations (1), (2) in the following form:

$$\frac{\partial q}{\partial t} + A_x \frac{\partial q}{\partial x} + A_y \frac{\partial q}{\partial y} = 0, \tag{8}$$

where $q = \{\sigma_{xx}, \sigma_{xy}, \sigma_{yy}, v_x, v_y\}$. A_x and A_y are matrixes, made up from the corresponding components of the equations (1), (2):

$$A_x = \begin{pmatrix} 0 & 0 & -\frac{1}{p} & 0 & 0 \\ 0 & 0 & 0 & 0 & -\frac{1}{p} \\ -\lambda - 2\mu & 0 & 0 & 0 & 0 \\ 0 & -\lambda - 2\mu & 0 & 0 & 0 \\ 0 & -\mu & 0 & 0 & 0 \end{pmatrix}. \tag{9}$$

$$A_y = \begin{pmatrix} 0 & 0 & 0 & 0 & -\frac{1}{p} \\ 0 & 0 & 0 & -\frac{1}{p} & 0 \\ 0 & -\lambda & 0 & 0 & 0 \\ -\lambda & 0 & 0 & 0 & 0 \\ -\mu & 0 & 0 & 0 & 0 \end{pmatrix}. \tag{10}$$

As a result of adopting the method of coordinates splitting in space, we obtain two 1D systems of equations:

$$\frac{\partial q}{\partial t} + A_i \frac{\partial q}{\partial i} = 0, \quad i = x, y. \tag{11}$$

Now, we examine the system of equations (11) for the x -coordinate:

$$\frac{\partial q}{\partial t} + A_x \frac{\partial q}{\partial x} = 0. \tag{12}$$

Hereinafter, we consider the fracture, situated perpendicular to the X -axis, parallel to the boundaries of the computational grid cells. We can make analogous transformations, which are presented lower, for the case, when the fracture is located perpendicular to the Y -axis.

The system of equations (12) is hyperbolic, therefore it can be represented in the form :

$$\frac{\partial q}{\partial t} + \Omega_x \Lambda_x \Omega_x^{-1} \frac{\partial q}{\partial x} = 0, \tag{13}$$

where Ω_x is the matrix, made of the eigenvectors, Λ_x is the matrix with the eigenvalues on the diagonal.

The eigenvalues of the matrixes A_x, A_y are: $\{-c_p, c_p, -c_s, c_s, 0\}$, where c_p is the longitudinal sound velocity, c_s is the transverse sound velocity.

After the variable change, the system (13) will look as following:

$$\frac{\partial p}{\partial t} + \Lambda_x \frac{\partial p}{\partial x} = 0. \tag{14}$$

The system (14) contains five independent equations, which can be solved by any differential scheme [17].

We examine the case of computing points on the boundary of the fracture with the help of the CIR scheme [17]. The scheme looks as follows:

$$u_i^{n+1} = u_i^n - \frac{ct}{h} (u_{i+1}^n - u_i^n), \quad \text{if } c > 0, \tag{15}$$

$$u_i^{n+1} = u_i^n - \frac{ct}{h} (u_{i-1}^n - u_i^n), \quad \text{if } c < 0. \tag{16}$$

In (15), (16) the index i signifies the number of coordinate (for example, x), the index n denotes the number of time, t is the time step, h — is the coordinate step, c is velocity. From equations (15), (16), it follows that points on the left side of the fracture can be calculated only for vectors, corresponding to negative eigenvalues $(-c_p, -c_s)$. Points on the right side of the fracture can be calculated only for vectors, corresponding to positive eigenvalues (c_p, c_s) . For solving the remaining two systems of equations on the left and on the right, we need additional boundary conditions (3)-(6).

Now, we explore in detail the algorithm of computing points on the left side of the fracture for positive characteristics (the algorithm of computing points on the right side of the fracture for negative characteristics is the same). For this, we introduce an additional ghost-node $border+1$ on the right side of the border node [18] into the examined computational grid and place such values into the node $border+1$, so that the conditions (3), (4) are fulfilled on the boundary of the fracture on the next time step. The conditions (5), (6) allow to calculate the values σ_{xx}, σ_{xy} on the $(n+1)$ -th time step. In this work, we solved

the equations (5), (6) with the help of the Euler method:

$$\sigma_{xx}^{left,n+1} = \sigma_{xx}^{left,n} + K_N (v_x^{right,n} - v_x^{left,n}), \quad (17)$$

$$\sigma_{xy}^{left,n+1} = \sigma_{xy}^{left,n} + K_T (v_y^{right,n} - v_y^{left,n}). \quad (18)$$

For describing the boundary conditions, we used the non-reflecting boundary conditions [19]:

$$\Omega^{out} u = 0, \quad (19)$$

where Ω^{out} is the matrix of the eigenvectors, corresponding to the outgoing characteristics (in other words, negative meanings of the characteristics for the matrixes A_x, A_y).

4. RESULTS

We carried out the numerical modelling of the seismic response from an extremely long fracture in a homogeneous medium for the 2D formulation of the problem. The initial impulse was described through the definition of the stress tensor inside a unit circle with the help of the following formula:

$$\begin{aligned} \sigma_{xx}(x, y) = \sigma_{yy}(x, y) = \\ = \exp\left(\frac{-(x-2.2)^2}{0.035} - \frac{(y-3.0)^2}{0.035}\right), \end{aligned} \quad (20)$$

$$1.7 < x < 2.7, 2.5 < y < 3.5.$$

The homogeneous medium was described by the following parameters. The speed of the longitudinal waves was equal to 2 m/sec., the speed of the transverse waves — 1 m/sec. The medium density was equal to 1 kg/m³. The computational area was 9 m along the X-axis and 6 m along the Y-axis. The extremely thin fracture along the whole computational grid was situated vertically on the boundary $x = 3$ m (Fig. 1).

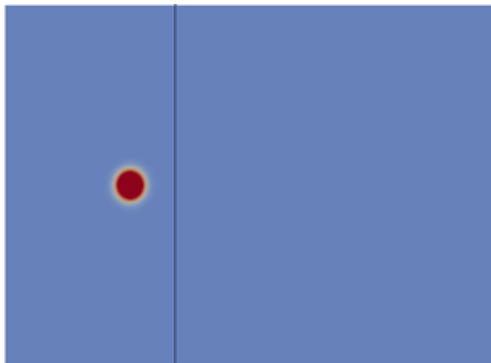


Fig. 1. Wave patterns for the seismic impulse spread (namely, the normal component of the stress tensor σ_{xx}) in the homogeneous medium at different consistent moments of time.

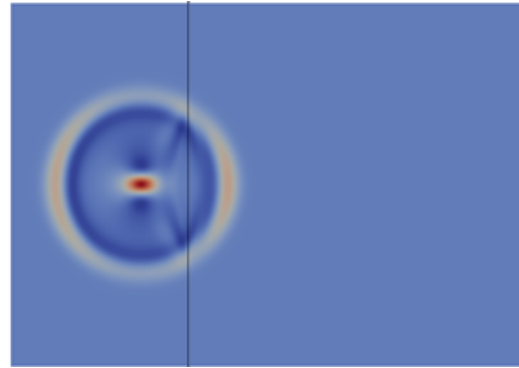


Fig. 2. The seismic impulse at time 0.7 sec.

In the calculations, the time step was equal to 0.005 sec., the coordinate step for X- and Y-axis was 0.025 m. The value of the normal component of the fracture opening parameter K_N was equal to 400 Pa/m, the value of the tangential component of the fracture opening parameter K_T was 0 Pa/m. The same medium with the parameters, described earlier in this section, is situated on the left and on the right side of the fracture. We calculated the spreads of the seismic impulse in the right and left areas relative to the fracture independently, excepting the border points, where we changed the values of the normal and tangent components of the stress tensor (according to the border conditions (3)-(6)). At this stage, we made all the calculations one after the other. Later on, the calculations will become faster with the help of parallelization, for example, using the MPI technology [20].

Figures 1, 2, 3 depict wave patterns of the seismic impulse spread (namely, the normal component of the stress tensor σ_{xx}). Fig. 1 presents the seismic impulse at the initial moment of time. Figs 2, 3 introduce the consistent moments of the seismic wave reflection from the fracture and its further spread in the homogeneous medium.

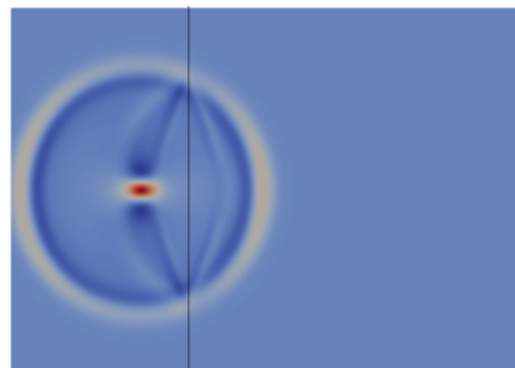


Fig. 3. The seismic impulse at time 1.0 sec.

5. CONCLUSION

In this work, we introduced the realization of the Schoenberg fracture model into the grid-characteristic method. We interposed the Schoenberg model, which is widely used for modelling fractured media, in the grid-characteristic method with the help of the additional corresponding boundary conditions in the computational area, where the fracture is situated. We presented the detailed description of calculating the points on the boundary of the fracture for the 2D case. The boundary conditions were introduced through the CIR scheme of the first order of accuracy, while the other points of the computational grid were calculated using the Laks-Wendroff scheme of the second order of accuracy.

As an example, we carried out the test calculation of the seismic waves spread in the homogeneous medium with the vertical fracture for the case, when the tangential component of the fracture opening parameter was equal to zero. Wave patterns, depicting the normal component of the stress tensor, showed the reflected wave from the fracture and further spread of the seismic wave across the homogeneous medium.

Later on, we suppose to make the parallelization of the introduced algorithm for computing the seismic waves spread in a homogeneous medium with a fracture. It will help to speed up the computations significantly. In addition, the logic continuation of this work is the development of the analogous algorithm for computing fractured media for the 3D case.

ACKNOWLEDGMENTS

The reported study was funded by RFBR according to the research project № 19-01-00281.

REFERENCES

1. Muratov MV, Petrov IB. Application of Fractures Mathematical Models in Exploration Seismology Problems Modeling. *Smart Innovation, Systems and Technologies*, 2019. DOI: 10.1007/978-3-030-06228-6_11.
2. Bakulin A, Grechka V, Karaev N, Anisimov A, Kozlov E. Physical modeling and theoretical studies of seismic reflections from a fault zone. *Society of Exploration Geophysicists Annual Meeting*, 2004, 1674-1677.

3. Leviant VB, Miryakha VA, Muratov MV, Petrov IB. Seismic responses of vertical fractures depending on their thickness. *Tekhnologii seysmorazvedki*, 2015, 3:16-30 (in Russ.).
4. Leviant VB, Petrov IB, Muratov MV. Numerical simulation of wave responses from subvertical macrofractures system. *Tekhnologii seysmorazvedki*, 2012, 1:5-21 (in Russ.).
5. Carcione J. Scattering of elastic waves by a plane crack of finite width in a transversely isotropic medium. *Int. J. Numer. Anal. Meth. Geomech.*, 1998, 22(4):263-275.
6. Hudson, JA. Overall properties of a cracked solid. *Mathematical Proceedings of Cambridge Philosophical Society*, 1980, 88:371-384.
7. Schoenberg M. Elastic wave behavior across linear slip interfaces. *The Journal of the Acoustical Society of America*, 1980, 68(5):1516-1521.
8. Grechka V, Kachanov M. Effective elasticity of fractured rocks: A snapshot of the work in progress. *Geophysics*, 2006, 71:W95-W58.
9. Qiwei Zhan, Qingtao Sun, Qiang Ren, Yuan Fang, Hua Wang, Qing Huo Liu. A discontinuous Galerkin method for simulating the effects of arbitrary discrete fractures on elastic wave propagation. *Geophysical Journal International*. 2017, 210(2):1219-1230.
10. Coates RT, Schoenberg M. Finite-difference modeling of faults and fractures. *Geophysics*, 1995, 60:1514-1523.
11. Zhan Q, Sun Q, Zhuang M, Mao Y, Ren Q, Fang Y, Huang W, Liu Q. A new upwind flux for a jump boundary condition applied to 3D viscous fracture modeling. *Comput. Methods Appl. Mech. Eng.*, 2018, 331:456-473.
12. Novatskii VK. *Teoriya uprugosti* [Elasticity theory]. Moscow, Mir Publ., 1975.
13. Hsu CJ, Schoenberg M. Elastic waves through a simulated fractured medium. *Geophysics*, 1993, 58(7):964-977.
14. Liu E, Hudson JA, Pointer T. Equivalent medium representation of fractured rock. *J. geophys. Res.*, 2000, 105:2981-3000.
15. Zhang J. Elastic wave modeling in fractured media with an explicit approach. *Geophysics*, 2005., 70:75-T85.

16. Magomedov KM, Kholodov AS. *Setochno-karakteristicheskie chislennye metody* [Grid-characteristic numerical methods]. Moscow, Nauka Publ., 1988.
17. Petrov IB, Lobanov AI. *Lektsii po vychislitelnoy matematike* [Computational mathematics lectures]. Moscow, Internet-University of Informational Technologies Publ., 2006.
18. LeVeque R. *Finite-Volume Methods for Hyperbolic Problems*. Cambridge University Press, 2002.
19. Petrov D. Application of grid-characteristic method to some seismic exploration problems in the Arctic. *Journal of Physics Conference Series*, 955(1):012029.
20. Ivanov A, Khokhlov N. Efficient inter-process communication in parallel implementation of grid-characteristic method. *Smart Innovation, Systems and Technologies*, 2019. DOI: 10.1007/978-3-030-06228-6_9.

DOI: 10.17725/rensit.2019.11.357

Eliminating unauthorized access to the frequency resource of the geostationary satellite repeater

Andrey V. Sukhov

Moscow Aviation Institute, <https://mai.ru/>

Moscow 125993, Russian Federation

Anton L. Tovbin

Informatics Research Center at the Ministry of Foreign Affairs of Russia, <https://newnici.mid.ru/>

Moscow 119200, Russian Federation

Vladislav V. Osipov

Scientific Research Institute for System Analysis of the Russian Academy of Sciences

Moscow 117218, Russian Federation

E-mail: suhov@g-tl.ru, 195555@list.ru, kt-mati@mail.ru

Received 28.08.2019, peer reviewed 16.09.2019, accepted 30.09.2019

Abstract. The technique of elimination of unauthorized use of the information transmission channel through the geostationary satellite repeater, based on the analysis of its information resource. The methodological approach is based on the application of differential entropy. The definition of information frequency resource is formulated, its properties are described. The method of calculating the a posteriori probability density of the coordinate vector of an unauthorized radio electronic means for the purpose of calculating the information frequency resource of the geostationary repeater satellite is presented.

Keyword: spectrum monitoring, information model, interference effect, electromagnetic compatibility, entropy.

UDC: 681.513.6

Acknowledgments. This work was carried out as part of the state assignment of the Federal State Institution Scientific Center for Research and Development of the Russian Academy of Sciences (RAS) (basic research 14) on the topic No. 0065-2019-0001 "Software and tools for modeling, designing and developing elements of complex technical systems, software systems and telecommunication networks in various problem-oriented areas "(AAAA-A19-119011790077-1).

For citation: Andrey V. Sukhov, Anton L. Tovbin, Vladislav V. Osipov. Eliminating unauthorized access to the frequency resource of the geostationary satellite repeater.

RENSIT, 2019, 11(3):357-368; DOI: 10.17725/rensit.2019.11.357.

CONTENTS

- | | |
|---|--|
| <p>1. INTRODUCTION (358)</p> <p>2. MATHEMATICAL MODEL OF THE INFORMATION TRANSMISSION CHANNEL (358)</p> <p>3. ESTIMATION OF COORDINATE VECTOR OF AN UNAUTHORIZED TRANSMITTING STATION (359)</p> | <p>4. SATELLITE INFORMATION FREQUENCY RESOURCE (361)</p> <p>5. OPTIMAL ESTIMATION OF THE STATE VECTOR OF AN UNAUTHORIZED ELECTRONIC STATION (363)</p> <p>6. CONCLUSION (367)</p> <p>REFERENCES (368)</p> |
|---|--|

1. INTRODUCTION

Nowadays a lot of information is transmitting through geostationary satellite transponder (GST) because of the development of needs for the global informational exchange among multiply users. The using of this method of informational exchange is especially convenient when transferring information is over long distances, in conditions of sufficiently long sessions of information exchange and when sufficiently large amounts of information are transferring.

But such channels are not always used sanctioned. There are a lot of opportunities for the opening of the protection of informational exchange networks and the gaining access to the data channels (DC) because of the development of the computer technologies. The struggle against unauthorized using of DC with GST may be organized with the using of one or two GST and Earth control stations (ECS) associated with it. The determination of coordinates of an unauthorized radio electronic station (URES) is made by using ECS, the unauthorized access session is logged and the application to the Radiocommunication Bureau of the International telecommunication community (ITC) is being prepared, on the basis of which administrative measures are taken to prevent the operation of the URES. Such a problem for the present situation to determine the coordinates of the transmitter by various methods devoted a lot of publications [1 - 4, etc.].

This article discusses the method of the determining of the coordinates of the URES using one GST and one associated ECS. The scheme of the information exchange is shown in **Fig. 1**. This figure also shows the

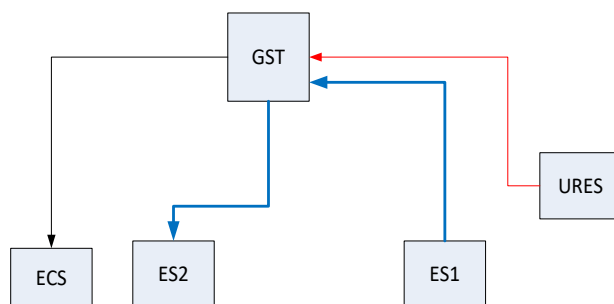


Fig. 1. The scheme of the information exchange through GST.

authorized DC between the first and second Earth stations (ES).

The URES transmitter uses the frequency resource of GST and essentially it is a source of interference. It is possible to determine its coordinates by a small Doppler shift of the received frequency, formed as a result of the constant movement of GST in some area of space relative to the position given for it in the geostationary orbit. Such shifts may be tens of kilometers [1] and the trajectory of the GST are known.

2. MATHEMATICAL MODEL OF THE INFORMATION TRANSMISSION CHANNEL

Consider the phenomenological model of the data channel, for which the important factors are the signal received at the input of the receiver of the Earth control station, the coordinates of the transmitter and the carrier frequency of the signal emitted by the transmitter.

According to [5] the observation equation has the form:

$$z(t) = U(t)\cos(\omega_c t + \varphi(t)) + n(t), \tag{1}$$

where $U(t)$ – the signal amplitude; $n(t)$ – the channel additive white Gaussian noise with characteristics:

the mathematical expectation:

$$M(n(t)) = 0, \tag{2}$$

the dispersion (second central moment):

$$M(n(t_2)n(t_1)) = \sigma_n^2 = N_0 / 2\delta(t_2 - t_1), \quad (3)$$

N_0 – the one-way spectral noise power density, $\delta(\cdot)$ – Delta function; the density of the channel noise:

$$p(n) = \frac{1}{\sqrt{2\pi\sigma_n}} e^{-\frac{n^2}{2\sigma_n^2}}, \quad (4)$$

$\varphi(t)$ – the random phase shift, determined by the double Doppler frequency shift on the signal propagation paths transmitter URES – GST and GST – Earth receiving station, and described in accordance with the models of parameters of radio signals presented in [6], the equation of state:

$$\begin{cases} \dot{\varphi}(t) = \omega(t), \\ \dot{\omega}(t) = -\alpha\omega(t) + n_\omega(t), \end{cases} \quad (5)$$

n_ω – the parametrical Gaussian noise, same described in (2) – (4) with the zero mathematical expectation and the dispersion (standard deviation) σ_ω^2 .

The results of the frequency measurements at the Earth control station is used for the estimation of the location of the unauthorized signal source. The frequency of the received signal f_R is associated with the coordinates of the transmitting station r_T in the form:

$$f_R = \left[f_T \left(1 + \frac{v'_s(r_T - r_s)}{c \|r - r_s\|} \right) + \Delta_f \right] \left(1 + \frac{v_D}{c} \right), \quad (6)$$

where f_R – the carrier frequency of the received signal; f_T – the carrier frequency of the transmitting signal; v_s – the velocity vector of the satellite in the observation period

$v'_s = (\dot{x}_s, \dot{y}_s, \dot{z}_s)$, r_s – the position vector of the satellite in the observation period $r'_s = (x_s, y_s, z_s)$, r_T – the position vector of the transmitter $r'_T = (x_T, y_T, z_T)$, Δ_f – the frequency offset in the satellite repeater; v_D – the scalar rate of range change between satellite and receiver; c – the spread speed of the signal, c

$= 3 \cdot 10^8$ m/c; the upper index «t» denotes an algebraic transposition operation.

Cartesian geocentric coordinate system is used to determine vectors r_s и r_T

3. ESTIMATION OF COORDINATE VECTOR OF THE UNAUTHORIZED TRANSMITTING STATION

We will use the expression (6) to determine the coordinates of the unauthorized transmitter.

It is fair for frequency of the received signal with expression (1) and with that frequency is derivative on time from a phase of a signal:

$$f_R = \frac{1}{2\pi} (\omega_T + \dot{\varphi}(t)). \quad (7)$$

We will use the geocentric Cartesian coordinate system as the coordinate system. In this coordinate system, the difference between the position vectors of the GST and the transmitter has the following representation:

$$r_T - r_s = \begin{pmatrix} x_T - x_s \\ y_T - y_s \\ z_T - z_s \end{pmatrix}. \quad (8)$$

The norm of the difference of these vectors has the following representation:

$$\|r_T - r_s\| = \sqrt{(x_T - x_s)^2 + (y_T - y_s)^2 + (z_T - z_s)^2} \quad (9)$$

In consideration of (7) – (9) expression (6) has the representation:

$$\begin{aligned} & \frac{1}{2\pi} (\omega_T + \dot{\varphi}(t)) = \\ & = \left[f_T \left(1 + \frac{\dot{x}_s(x_T - x_s) + \dot{y}_s(y_T - y_s) + \dot{z}_s(z_T - z_s)}{c\sqrt{(x_T - x_s)^2 + (y_T - y_s)^2 + (z_T - z_s)^2}} \right) + \Delta_f \right] \times \\ & \times \left(1 + \frac{v_D}{c} \right). \end{aligned} \quad (10)$$

Convert expression (10) to a more convenient representation. Enter the designation for this:

$$B_s = 1 + v_D/c,$$

and we present the dependence of the measured parameter, which is a random component of the signal phase $\varphi(t)$, from the unknown parameters of the unauthorized RES – coordinates of the transmitter and the carrier frequency of the transmitter:

$$\begin{aligned} \dot{\varphi}(t) = & \\ = B_s \omega_T & \frac{\dot{x}_s(x_T - x_s) + \dot{y}_s(y_T - y_s) + \dot{z}_s(z_T - z_s)}{c\sqrt{(x_T - x_s)^2 + (y_T - y_s)^2 + (z_T - z_s)^2}} + \quad (11) \\ + \omega_T(B_s - 1) & + \Delta_\omega B_s, \end{aligned}$$

where $\Delta_\omega = 2\pi\Delta_f$, $\omega_T = 2\pi f_T$.

In order to be able to estimate the parameters of the unauthorized RES, we will use the decomposition of the right part of the expression (11) into a Taylor series in the vicinity of the current estimate of the coordinates of the URES on the ground and the current estimate of the transmitter frequency and limit ourselves to members of the first order of smallness.

It is required to find the partial derivatives of the right part of the expression (11) on the vector of the estimated parameters $g(t)$ of the URES for this purpose. The vector of the estimated URES parameters consists of the following components: the coordinates of the URES on the ground and the carrier frequency of the transmitted signal:

$$g^*(t) = \begin{pmatrix} x_T^*(t) \\ y_T^*(t) \\ z_T^*(t) \\ \omega_T^*(t) \end{pmatrix}. \quad (12)$$

The estimation of the parameters of the vector $g(t)$ will be carried out at a sufficiently long interval of observation time to ensure the required accuracy. So even if the components of this vector are stationary, the current estimates will change over time.

The partial derivatives of the function $\omega(g(t), t) = \dot{\varphi}(t)$ on the vector $g(t)$ on the basis of (11) have the following form:

$$\begin{aligned} \Omega_x(t) &= \frac{\partial \omega(g(t), t)}{\partial x_T} = \\ &= \frac{B_s \omega_T \dot{x}_s}{c\sqrt{(x_T - x_s)^2 + (y_T - y_s)^2 + (z_T - z_s)^2}} - \\ &- \frac{B_s \omega_T (x_T - x_s)}{c} \times \end{aligned} \quad (13)$$

$$\begin{aligned} \Omega_y(t) &= \frac{\partial \omega(g(t), t)}{\partial y_T} = \\ &= \frac{B_s \omega_T \dot{y}_s}{c\sqrt{(x_T - x_s)^2 + (y_T - y_s)^2 + (z_T - z_s)^2}} - \\ &- \frac{B_s \omega_T (y_T - y_s)}{c} \times \end{aligned} \quad (14)$$

$$\begin{aligned} \Omega_z(t) &= \frac{\partial \omega(g(t), t)}{\partial z_T} = \\ &= \frac{B_s \omega_T \dot{z}_s}{c\sqrt{(x_T - x_s)^2 + (y_T - y_s)^2 + (z_T - z_s)^2}} - \\ &- \frac{B_s \omega_T (z_T - z_s)}{c} \times \end{aligned} \quad (15)$$

$$\begin{aligned} \Omega_f(t) &= \frac{\partial \omega(g(t), t)}{\partial \omega_T} = \\ &= B_s \frac{\dot{x}_s(x_T - x_s) + \dot{y}_s(y_T - y_s) + \dot{z}_s(z_T - z_s)}{c\sqrt{(x_T - x_s)^2 + (y_T - y_s)^2 + (z_T - z_s)^2}} + \\ &+ (B_s - 1). \end{aligned} \quad (16)$$

We expand the function $\omega(g(t), t) = \dot{\varphi}(t)$ in the vicinity of some point t_k into Taylor series [9]:

$$\begin{aligned} \omega(g(t), t) &\approx \dot{\varphi}(t) \approx \\ &\approx \Omega_x(t_k)(x_T(t) - x_T(t_k)) + \\ &+ \Omega_y(t_k)(y_T(t) - y_T(t_k)) + \\ &+ \Omega_z(t_k)(z_T(t) - z_T(t_k)) + \\ &+ \Omega_f(t_k)(f(t) - f(t_k)) + n_\Omega(t_k), \end{aligned} \quad (17)$$

where in the undefined parameter $n_\Omega(t_k)$ we take into account the residual term of

the decomposition and a set of random factors with Gaussian behavior affecting the measurement results.

Given a sufficiently large number of such factors, as well as, considering the smallness of the remainder term of the series expansions, you can make the assumption about the Gaussian nature of the behavior parameter $n_{\Omega}(t_k)$. Then the distribution of the parameter $n_{\Omega}(t_k)$ will be described similarly to (2) – (4) with dispersion σ_{Ω}^2 .

Thus, when measuring the frequency of the signal from the URES transmitter quite a long time and a priori knowing the location of the GST at a given time, it is possible to filter the vector of unknown parameters of the URES. For this purpose, a system of equations (17) on a sufficient array of frequency measurements at different times t_k should be used.

4. SATELLITE INFORMATION FREQUENCY RESOURCE

To determine the information space in which the information resource should be considered, we will use the differential entropy introduced by K. Shannon [7] and correctly defined by A.N. Kolmogorov [8], who called it differential entropy.

Differential entropy has been defined as a measure of uncertainty for continuous random variables. But it should be borne in mind that its absolute values are associated with the coordinate system in question, which does not allow one random variable entropy to make sufficiently reasonable judgments. At the same time, when comparing random variables, the use of the difference in their entropies avoids this drawback.

For a continuously distributed random variable x with a distribution density $p(x)$, the differential entropy is defined as follows:

$$H(x) = - \int_{-\infty}^{\infty} p(x) \log p(x) dx. \tag{18}$$

For the concept of entropy, the base of the logarithm is not essential, because the base of the logarithm determines the units of information. For the base of the logarithm, two units will be bits, and for the natural logarithm, the units will be nats. It is more convenient to use natural logarithms, operations on which do not lead to the appearance of additional coefficients in mathematical transformations. Therefore, in the future, if no special reservations are made, it is assumed to use only natural logarithms.

In our case, the frequency resource of GST is considered. As the frequency parameter resource should take the distribution of the frequency of the received signal from URES. It is necessary to set as a measure some reference distribution for the URES resource for the correct application of differential entropy. This reference distribution is the distribution of the authorized operating frequency of the signal from the frequency range under consideration. For the operating frequency of the received authorized signal, the necessary statistical characteristics are a priori known, which makes it possible to determine the reference frequency distribution. Taking into account the impact on the transmission channel of information only Gaussian noise density distribution of the authorized frequency will also be subject to the normal distribution law:

$$p(f_{ref}) = \frac{1}{\sqrt{2\pi}\sigma_{ref}} e^{-\frac{(f_{ref}-m_{ref})^2}{2\sigma_{ref}^2}}, \tag{19}$$

where m_{ref} – the mathematical expectation of the authorized frequency, σ_{ref} – standard

deviation of the values of the authorized frequency.

The value of its differential entropy for the normal distribution law (the differential entropy of the authorized frequency access) is known [7]:

$$H(f_{ref}) = \log(\sigma_{ref} \sqrt{2\pi e}), \quad (20)$$

where e – the basis of the natural logarithm.

We will use its entropy to determine the information frequency resource (IFR).

Definition: information frequency resource of the GST is the deviation of the differential entropy of the authorized frequency received by the Earth control station, due to interference from the URES.

Thus, the information frequency resource is presented in the form of:

$$R_{ifr} = H(f_{ref}) - H(f_{unref}), \quad (21)$$

where $H(f_{unref})$ – differential entropy of unauthorized frequency of the received signal (differential entropy of unauthorized frequency access).

This definition of information frequency resource allows you to get the following important properties:

1. The information frequency resource is not bound to the differential entropy measurement scale. This property is determined by the presence of a difference term, which eliminates the dependence of the differential entropy on the coordinates.
2. In the absence of a signal from the URES, the value of the information frequency resource corresponds to the value of the differential entropy of the authorized access of GST, which characterizes the potential accuracy characteristics of GST, and that, in turn, can be used as a comparative indicator of GST.

3. The values of the information frequency resource due to its independence from the coordinates can be used as regulatory parameters at the conclusion of international agreements on the sharing of frequencies.
4. Tables and graphs of information frequency resource dynamics can be used in the preparation of universal calendar plans and recommendations to eliminate unauthorized access to the frequency resource.

In the whole statement of the problem, the information frequency resource should be maximized, and ideally, when operating of URES, it should be as close to zero as possible, which corresponds to the definition of the URES coordinate vector with the potential accuracy of the system with GST.

In the absence of unauthorized frequency access to the GST, the differential entropy of unauthorized access is zero due to the zero value of the density distribution of the frequency of unauthorized access in the entire area of its definition and the value of the information frequency resource is equal to:

$$R_{ifr} = H(f_{ref}). \quad (22)$$

The expression (17) shows the dependence of the unauthorized frequency of the received signal on the vector of coordinates of the URES. This expression is used to determine the location of the URES transmitter. And also on the basis of this expression it is possible to determine the differential entropy of the unauthorized frequency of the received signal.

Expression (17) is a linear function of its random parameters. Therefore, according to the properties of differential entropy, the value of the total differential entropy is also

INFORMATION TECHNOLOGIES

determined by the linear function of the entropy distributions of the random variables included in this function. In this case, we take into account the earlier conclusion about the normality of the laws of distributions of these random variables.

Based on the above, we obtain the following expression to determine the differential entropy of the unauthorized frequency:

$$H(f_{unref}) = \Omega_x(t_k)H(x_T) + \Omega_y(t_k)H(y_T) + \Omega_z(t_k)H(z_T) + \Omega_f(t_k)H(f), \tag{23}$$

where $H(x_T)$, $H(y_T)$, $H(z_T)$ – differential entropies for Cartesian coordinates of URES, $H(f)$ – the differential entropy of the frequency of the transmitter URES.

It should be noted that in the expression (23) there is no dependence on the parameters that determine the mathematical expectation of the laws of distribution of random variables, since they do not affect the differential entropy of the normal distribution law [7].

The technological cycle of the information monitoring process of the frequency resource consists of the following stages:

1. Monitoring of the Earth control station for authorized use of GST channels.
2. Detection of ground control station unauthorized use of GST in any frequency channel.
3. The inclusion of a ground control station of the optimal determinant of the coordinates of the URES and the optimal evaluation of the vector coordinates of the URES to obtain estimates with the required accuracy.

4. Carrying out organizational measures to disable the transmitter and prevent its further work.
5. Continuing of the monitoring of the ground control station for authorized use of GST channels.

5. OPTIMAL ESTIMATION OF THE STATE VECTOR OF UNAUTHORIZED RADIOELECTRONIC WORKSTATIONS

The estimation of the coordinate vector will be carried out in discrete time. Therefore, the transition from the equations of observation (1) and state (5) in continuous time should be made to the equations in finite differences. The observation equation for the k moment of time will take the form:

$$Z_k = U_0 \cos(\omega_{Tk}t_k + \omega_k) + n_k. \tag{24}$$

The differential equation of state in finite differences presents as follows:

$$g_{k+1}^f = \Phi_{k+1}g_k^f + n_{fk+1}g_{k+1}^f = \Phi_{k+1}g_k^f + n_{fk+1}. \tag{25}$$

In this case, taking into account the linearity of the equation of state (25), it is fair [6]:

$$\Phi_{k+1} = \begin{pmatrix} 1 & 1/\alpha(1-e^{-\alpha\Delta t}) \\ 0 & e^{-\alpha\Delta t} \end{pmatrix}, \tag{26}$$

where Δt – sampling interval.

The expression for APD can be represented as follows [5]:

$$p(g_{k+1} | \{z_{k+1}\}) = \frac{p(z_{k+1} | g_{k+1})p(g_{k+1} | \{z_k\})}{p(z_{k+1} | \{z_k\})}, \tag{27}$$

where $\{z_k\} = z_0, z_1, z_2, \dots, z_k$ – a set of implementations of the observed process.

As an approximate algorithm of optimal nonlinear filtering we will use the approximation of APD in the form of point masses on a rectangular lattice of indices [11–14]. We present APD as follows:

$$p(\mathbf{g}_k | \{z_k\}) \approx \sum_{\lambda_k} p(\lambda_k) \delta(\mathbf{g}_k - \lambda_k) \Delta \lambda_k, \quad (28)$$

where $\Delta \lambda_k = \Delta \lambda_1 \Delta \lambda_2 \dots \Delta \lambda_m$, $\Delta \lambda_i$, $\Delta \lambda_i$ – the lattice spacing in the i coordinate of the vector \mathbf{g} ; $\delta(\mathbf{g}_k - \lambda_k)$ – Delta function; $p(\lambda_k)$ – function, satisfying the normalization condition:

$$\sum_{\lambda_k} p(\lambda_k) \Delta \lambda_k = 1, \quad \forall k : p(\lambda_k) \geq 0. \quad (29)$$

Given the approximation (28), the expression (27) will take the form:

$$p(\mathbf{g}_k | \{z_k\}) \approx \frac{p(z_k | \mathbf{g}_k)}{C_k} \sum_{\lambda_k} p(\lambda_k) p(\mathbf{g}_k, \lambda_k) \Delta \lambda_k. \quad (30)$$

where

$$p(\mathbf{g}_k, \lambda_k) = \int_{\mathbf{g}_{k-1}} p(\mathbf{g}_k | \mathbf{g}_{k-1}) \delta(\mathbf{g}_{k-1} - \lambda_k) d\mathbf{g}_{k-1} = p(\mathbf{g}_k | \lambda_k). \quad (31)$$

The normalizing constant C_k is defined as follows:

$$C_{\lambda k} = \sum_{\lambda_k} \sum_{\mathbf{g}_k} p(\lambda_k) p(z_k | \mathbf{g}_k^\lambda) p(\mathbf{g}_k^\lambda, \lambda_k) \Delta \lambda_k \Delta \mathbf{g}_k^\lambda, \quad (32)$$

where \mathbf{g}_k^λ – the values of the vector \mathbf{g} given on the set of lattice values λ_k .

The likelihood function $p(z_{k+1} | \mathbf{g}_{k+1})$, included in the expression (27) depends linearly only on random variables with a Gaussian distribution, so it also has a Gaussian distribution:

$$p(z_{k+1} | \mathbf{g}_{k+1}) = \frac{1}{\sqrt{2\pi\sigma_n^2}} \exp\left\{-\frac{1}{2\sigma_n^2} (z_{k+1} - s(\mathbf{g}_{k+1}^\lambda))^2\right\}, \quad (33)$$

where $\sigma_n^2 = N/2\Delta t$ – the variance of the channel noise.

The nodes of the grid shall conform to the following restrictions on the set of $T_k(\lambda_k)$:

$$T_k(\lambda_k) = \{\lambda_{kj} \in R^M \mid p(\lambda_k) \geq \delta_0\}, \quad (34)$$

where δ_0 – a predetermined threshold level; M – the dimension of the vector \mathbf{g} .

The threshold level is determined by the noise intensity in the observation and state equations, and should be set to ensure stable operation of the filter. This practical recommendation is given by the authors [12].

The lattice nodes are given in the form of a uniform scale along the coordinates of the vector \mathbf{g} as follows:

$$T_k(\lambda_k) = \{\lambda_{kj} \in R^M \mid \forall j = 1, \dots, m : |\lambda_{jk}| < \mu \sigma_\lambda\}, \quad (35)$$

where μ – the value selected experimentally [12], its value is recommended to be set in the range from 1.5 to 3; σ_λ – standard deviation for the corresponding component of the coordinate vector.

Given (31), the joint density can be determined as follows:

$$p(\mathbf{g}_k, \lambda_k) = \frac{1}{(2\pi)^{M/2} |D|} \exp\left\{-1/2 (\mathbf{g}_k - \lambda_k)^t D^{-1} (\mathbf{g}_k - \lambda_k)\right\}. \quad (36)$$

where superscript t stands for transpose; D – covariance matrix of the vector $\mathbf{g}(t)$, which, taking into account the independence of the coordinates of the vector \mathbf{g} has a diagonal form:

$$D = \begin{pmatrix} \sigma_{xx}^2 & 0 & 0 & 0 \\ 0 & \sigma_{yy}^2 & 0 & 0 \\ 0 & 0 & \sigma_{zz}^2 & 0 \\ 0 & 0 & 0 & \sigma_{ff}^2 \end{pmatrix}. \quad (37)$$

Since it is assumed that the URES coordinates do not change in time and the vector of the coordinates being determined is subject only to Gaussian noise during the measurements, in accordance with [6] the equation of state in finite differences has the form:

$$\mathbf{g}_{k+1} = \mathbf{g}_k + D_\sigma n_g, \quad (38)$$

where n_g – parametric noise; D_σ – matrix of standard deviations of parameters of URES vector:

$$D_\sigma = \begin{pmatrix} \left(\frac{\Delta\sigma_{xx}^2}{2}\right)^{1/2} & 0 & 0 & 0 \\ 0 & \left(\frac{\Delta\sigma_{yy}^2}{2}\right)^{1/2} & 0 & 0 \\ 0 & 0 & \left(\frac{\Delta\sigma_{zz}^2}{2}\right)^{1/2} & 0 \\ 0 & 0 & 0 & \left(\frac{\Delta\sigma_{ff}^2}{2}\right)^{1/2} \end{pmatrix}. \quad (39)$$

The covariance error matrix of vector estimates is defined as follows:

$$K_k = C_{ik}^{-1} \sum_{\lambda_k} \sum_{g_k^*} p(\lambda_k) (g_k^i - g_k^{*i}) (g_k^i - g_k^{*i})' p(z_k | g_k^i) p(g_k^i, \lambda_k) \Delta g_k^i \Delta \lambda_k, \quad (40)$$

where g_k^* – estimation of the coordinate vector at the k step according to the selected Bayesian criterion of the average risk minimum, which can be obtained using the current approximation of the APD on a rectangular lattice of indices.

Based on the above expressions, the following algorithm of optimal nonlinear filtering is proposed (the block diagram of the filtering algorithm is shown in **Fig. 2**.)

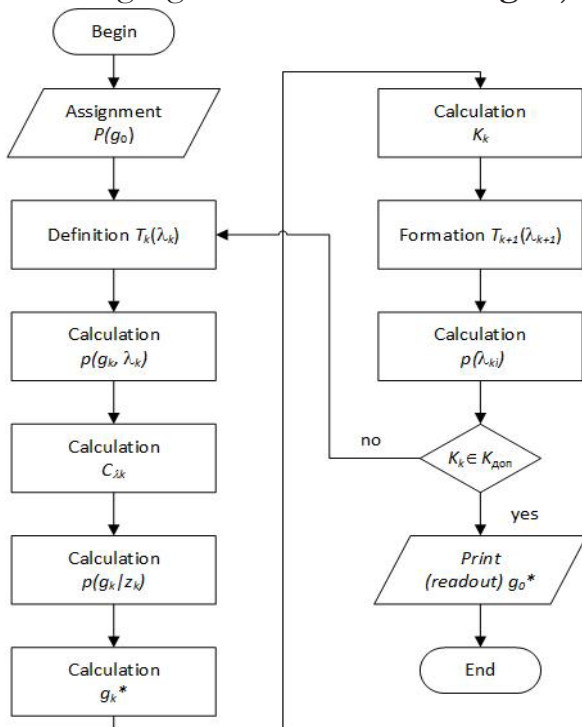


Fig. 2. The block diagram of the filtering algorithm of the URES coordinate vector.

1. At the first step of the filter operation using a priori information, truncated normal distribution laws are set for the coordinates of the unauthorized transmitter vector.
2. The nodes of the lattice $T_k(\lambda_k)$ are determined in accordance with the expressions (34), (25) and the density of the distribution in the nodes is given by the a priori distribution.
3. The joint density $p(g_k, \lambda_k)$ is calculated based on the expression (36).
4. According to the expression (32) is calculated selection constant C_{ik} .
5. APD $p(g_{k+1} | z_{k+1})$ is calculated by expression (33).
6. Calculation of the current estimate of the vector of coordinates of g_k^* according to selected functions of fines:
 - a. For a simple function of fines the coordinate with the maximum value of APD is determined.
 - b. For quadratic functions of fines is determined by the mathematical expectation for APD.
7. The covariance matrix of errors K_k is calculated by expression (40).
8. In accordance with the obtained estimation of the coordinate vector, a lattice of indices is formed for the next step.
9. According to the expression (31) distribution in the lattice $p(\lambda_{k+1})$ is calculated.
10. The calculations are repeated for items 2 ... 9 before reaching the covariance matrix of the errors K_k valid values for the precision of the coordinates. After that, the calculations are stopped and the results with the coordinates of the URES are transmitted to the coordinating bodies.

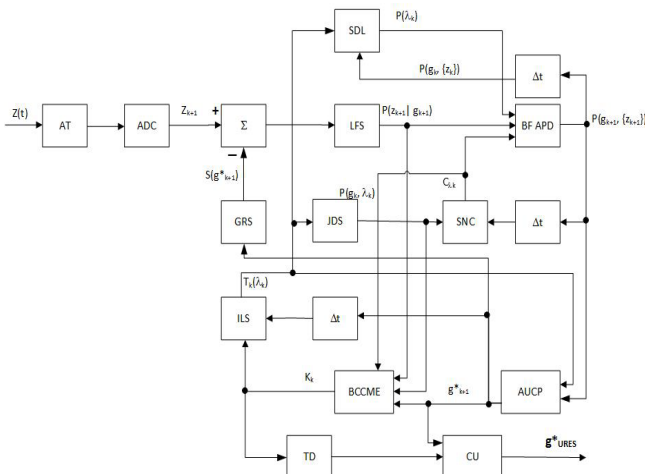


Fig. 3. The block scheme of the optimal digital filter.

Thus, an estimate of the URES coordinate vector can be obtained, but it is still necessary to estimate the information resource of GST in accordance with the recommendations given in section 2.

The block diagram of the optimal digital filter with approximation of APD on a rectangular lattice of indices is shown in Fig. 3.

This diagram shows: AT – analog signal path that includes the antenna amplifier, preselector, amplifier high frequency and the possible local oscillator and intermediate frequency amplifier in the case of a too high carrier frequency signal; ADC – analog-to-digital converter; Σ – adder with one inverse and one direct input; LFS – likelihood function shaper; SDL – shaper distribution in the lattice; Δt – delay element per quantization step to synchronize the operation of all elements of the scheme; BF APD – block of APD formation; GRS – generator of the reference signal based on the evaluation of the vector coordinates of the URES at the current step of the filter; JDS – joint density shaper; SNC – shaper of the normalizing constant; ILS – index lattice shaper; BCCME – block calculator the covariance matrix of the errors;

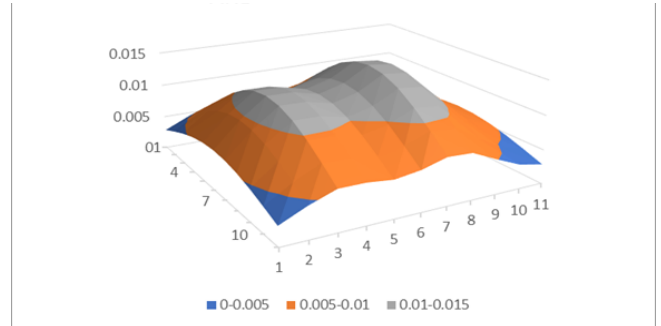


Fig. 4. The APD evolution. Initial filter operation mode.

AUCP – assessment unit of a continuous parameter; TD – a threshold device that is triggered when the errors in determining the coordinate vector of an acceptable level are reached; CU – crucial unit that issues coordinates URES the signal threshold of the device.

In the environment VisualStudio and using MSExcel spreadsheets, we performed a simulation of such a filter. The results of APD calculation for two coordinates on the plane are shown in Fig. 4 (initial filter operation mode), Fig. 5 (transient operation) and Fig. 6 (steady-state operation).

The dynamics of the information frequency resource of GST, obtained on the basis of APD processing, is presented in Fig. 7. Until the 10th cycle of the operation the URES did not include the transmitter. The value of the information frequency resource corresponds to the performance characteristics of the GST. At the 10th cycle of the filter operation the

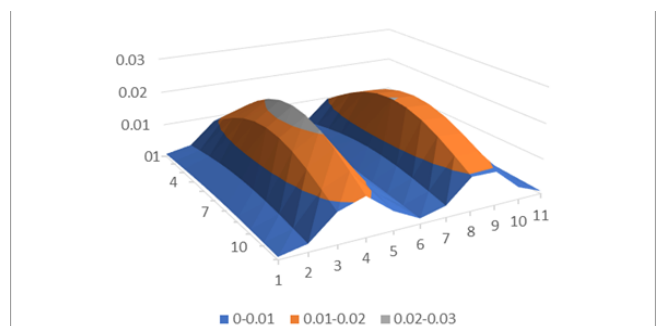


Fig. 5. The APD evolution. Transient operation.

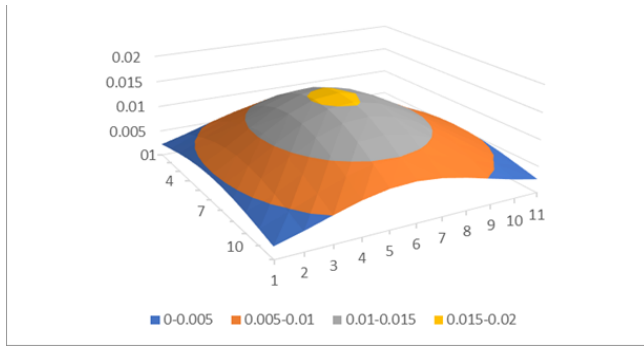


Fig. 6. The APD evolution. Steady-state operation.

activation of the transmitter URES passed and this event corresponded to the drop in the value of the information frequency resource. Further, up to the 52nd cycle of operation, the processing of the observed implementation of the input signal on the ECS was carried out. At the same time information frequency resource increased with increasing accuracy of estimation of the vector of coordinates of GST. Since the 52-th cycle the required accuracy of the vector coordinates URES was obtained and the shutdown of the transmitter URES occurred. The value of the information frequency resource returned to its original state.

The algorithms, obtained in the present work, designed for finding the information of the GST damage by function of the URES.

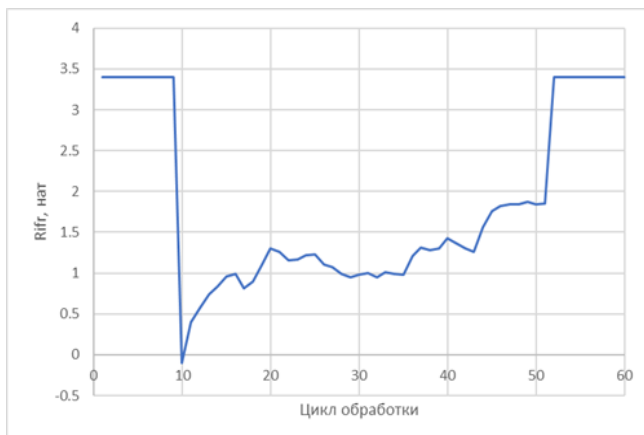


Fig. 7. Dynamics of information of the frequency resource.

6. CONCLUSION

Thus, the article considers the following provisions:

1. The phenomenological mathematical model of the CRPD is synthesized, comprising the GST, ECS, and URES, and defined the parameters needed for analysis and modeling of CRPD during the optimal estimation of the vector coordinates URES.

2. The partial differential decomposition is obtained by further transformation of the frequency tracking measurement equation. This decomposition allowed us to associate the unknown components of the vector of coordinates URES with the values of the measurements to allow for optimal estimation of the vector of coordinates with the use of optimal filtering algorithms.

3. The definition of information frequency resource based on differential entropy is formulated. The properties of IFR, defining a wide range of possibilities for its application, are described. IFR can be used as an indicator of the accuracy characteristics of GST. It can also be used as an indicator in international agreements on frequency sharing. Tables and graphs of information frequency resource dynamics can be used in the preparation of universal calendar plans and recommendations to eliminate unauthorized access to the frequency resource.

4. Solved the problem of estimating the vector of coordinates URES if you use the same earth test monitoring station with the use of APD approximation in the form of a point-mass on a rectangular lattice of indices.

5. The stages of the technological cycle of the information monitoring process of the frequency resource are given and the modeling of the optimal receiver is carried out. The obtained dynamic values of the

information of the frequency resource in different stages of operation of the GST.

ACKNOWLEDGMENTS

Work is made as part of national assignment for SRISA RAS (fundamental scientific research GP 14) on the topic No.0065-2019-0001 (AAAA-A19-119011790077-1).

REFERENCES

1. *Handbook on Spectrum Monitoring*. ITU, Switzerland, Geneva, 2011.
2. Chernyak VS. *Multiposition radiolocation*. Moscow, Radio i svyaz' Publ., 1993, 416 p.
3. Koets MA, Bentley RT. *Satellite Based Geolocation Using a Single Geosynchronous Satellite and an Inverse Doppler Technique*. SRI Publ., USA, S.A., 1999.
4. Reshetnikov VN, Savilkin S B, Sukhov AV. Monitoring chastotnogo resursa geostatsionarbykh sputnikov-retranslyatorov s ispolzovaniem entropii pokrytiya [Monitoring frequency resource of the geostationary transponders using entropy cover]. *Programmnye produkty i sistemy*, 2017, 1:119-123 (in Russ.).
5. Tikhonov VI. *Optimalny priem signalov* [Optimal signal reception]. Moscow, Radio i svyaz' Publ., 1983, 320 pp.
6. Tikhonov VI. *Nelineynoe preobrazovanie sluchaynykh protsessov* [Non-linear transformation of random processes]. Moscow, Radio i svyaz' Publ., 1986. 296 p.
7. Shannon K. *Raboty po teorii informatsii i kibernetike* [Works on information theory and cybernetics]. Moscow, Inlit Publ., 1963, 830 p.
8. Kolmogorov AN. *Teoriya informatsii i teoriya algoritmov* [Information theory and algorithm theory]. Moscow, Nauka Publ., 1987, 304 pp.
9. Korn G, Korn T. *Spravochnik po matematike* [Handbook of mathematics]. Moscow, Nauka Publ., 1977, 831 p.
10. Sage A, Mels J. *Teoriya otsenivaniya i ee primenenie v svyazi i upravlenii* [Evaluation theory and its application in communication and management]. Moscow, Svyaz' Publ., 1976, 496 p.
11. Loginov VP, Ustinov ND. Priblizhennyye algoritmy nelineynoy filtratsii [Approximate nonlinear filtering algorithms]. *Zarubezhnaya radioelektronika*, 1975. 3:3-28.
12. Sukhov AV, Zaitsev MA. *Modelno-algoritmicheskoe obespechenie infomatsionnykh sistem upravleniya* [Model-algorithmic support of control information systems: monograph]. Moscow, Witte Mos. Univ. Publ., 2016, 128 pp.
13. Bucy RS, Senne KD. Digital Synthesis of Nonlinear Filters. *Automatica*, 1971, 7:287-298.
14. Bucy RS. Bayes Theorem and digital Realisation for nonlinear Filters. *Journ. Am. Astronaut. Soc.*, 1969, 17:80-94.

DOI: 10.17725/rensit.2019.11.369

New additive technologies for forming complex bone structures for medical and biological applications

Vladimir N. Gorshenev

Emanuel Institute of Biochemical Physics of Russian Academy of Sciences, <http://ibcp.chph.ras.ru/>
Moscow 119334, Russian Federation

Vladimir V. Kolesov

Kotelnikov Institute of Radioengineering and Electronics of Russian Academy of Sciences, <http://cplire.ru/>
Moscow 125009, Russian Federation

Mayya Yu. Ziangirova, Larisa M. Krasnopolskaya

Gause Institute of New Antibiotics, <http://www.gause-inst.ru/>
Moscow 119021, Russian Federation

Alexander A. Prosvirin

Yevdokimov Moscow State University of Medicine and Dentistry, <http://www.msmsu.ru>
Moscow 127473, Russian Federation

Andrei T. Teleshev

Moscow Pedagogical State University, <http://mpgu.su>
Moscow 119001, Russian Federation

E-mail: gor@sky.chph.ras.ru, pchelka_mayya@mail.ru, kev@cplire.ru, lmkrasnopolska@gmail.com, prosvirin@mail.ru, teleshev@mail.ru

Received 30.09.2019, peer reviewed 14.10.2019, accepted 21.10.2019

Annotation. A synthesis of nanosized hydroxyapatite by the exchange reaction between diammonium phosphate and calcium nitrate under conditions of mechano-acoustic processing of the reaction mixture was developed. Methods are proposed for purifying hydroxyapatite from by-products. By dispersing raw materials of animal origin, a protein hydrosol was obtained in the medium of which hydroxyapatite was synthesized and a collagen-calcium-phosphate composite was obtained. Methods for the formation of porous collagen-calcium-phosphate composites, among which the effect of microwave radiation, are considered. It is shown that based on the developed biocompositions: calcium phosphate pastes, compositions from thermoplastic biodegradable polymers, non-woven fibrous materials, fabric-engineering constructions with an adjustable architecture can be made to solve various biomedical problems. The creation of three-dimensional structures capable of performing the functions of a particular natural tissue of the body, based on a combination of cells and scaffolds (three-dimensional structures, matrix, scaffold), as well as other factors affecting cell growth, their differentiation and organization of the extracellular matrix, is an important task of the tissue engineering.

Keywords: nanoscale hydroxyapatite, porous collagen-calcium-phosphate compounds, biodegradable polymers, non-woven fibrous materials, tissue engineering structures, 3D technologies

UDC 615.46

Acknowledgments: The work was carried out with the financial support of the Russian Federal Property Fund, project 18-29-23042.

For citation: Vladimir N. Gorshenev, Mayya Yu. Ziangirova, Vladimir V. Kolesov, Larisa M. Krasnopolskaya, Alexander A. Prosvirin, Andrey T. Teleshev. New additive technologies for forming complex bone structures for medical and biological applications. *RENSIT*, 2019, 11(3):369-390; DOI: 10.17725/rensit.2019.11.369.

CONTENTS

- 1. INTRODUCTION (370)**
- 2. SYNTHESIS OF CALCIUM PHOSPHATE COMPOUNDS TO COMBINE WITH THE COLLAGEN MATRIX (371)**
- 3. THE FORMATION OF COLLAGEN-CALCIUM-PHOSPHATE BIOCOMPOSITES (374)**
- 4. THE FORMATION OF POROUS MATERIALS BASED ON COLLAGEN-CALCIUM-PHOSPHATE COMPOSITIONS (375)**
- 5. PRODUCTION OF FABRIC ENGINEERING STRUCTURES (379)**
- 6. METHODS OF IMPLANTING POLYMER SAMPLES INTO A BONE DEFECT (383)**
- 7. PRODUCTION OF BONE SUBSTITUTE MATERIALS USING THE 3D PRINTING METHOD (384)**
- 8. CONCLUSION (387)**
- REFERENCES (387)**

1. INTRODUCTION

The problem of restoring the integrity of bones after their injuries and diseases is characterized by growing relevance and high socio-economic significance [1-3]. World clinical experience in the treatment of bone tissue pathology and replacement of bone defects constantly proves that the use of osteoplastic materials in reconstructive surgery is one of the decisive factors for achieving a positive result of the operation [4-7]. Tissue-engineering tasks for the development of complex designs of bone-substituting materials can be solved with the joint participation of multidisciplinary teams of physicians, biologists, chemists, physicists and engineers. Substitution of bone tissue defects with porous implants followed by restoration of living bone tissue of the body should be considered as a process of realization of genetic information [8-10].

To develop optimal conditions for the regeneration of damaged tissue, knowledge of the mechanisms of regulation of its growth and differentiation is necessary. Knowledge

about the process of osteogenesis, the processes of implant biodegradation in living systems, and the replacement of bone tissue defects contribute to the creation of new types of bone-replacing biomaterials when natural and synthetic polymers are mixed.

In modern implantology, it is fundamentally possible to distinguish several levels of technological developments in the manufacture of bioplastic bone materials [11]. The first donor level involves the use of donor tissues without their deep processing [12]. The second donor level is characterized by deep processing of donor tissue. An example is the manufacturing process of demineralized bone alloimplants, where the ratio of mineral and organic components is changed in bone tissue using decalcification with acid solutions. In such cases, the material acquires additional osteoinductive properties. In this case, bone demineralization can be superficial, partial or complete. Depending on the degree of decalcification, the material has different mechanical and plastic characteristics, which allows the surgeon to combine the material depending on the specific clinical situation [13].

The use of sterilization, viral inactivation using low-frequency ultrasound allowed to completely remove cellular elements, fat, bone marrow stroma, spongiosis [14]. The third level involves the creation of biocomposite materials containing both the main components of bone tissue and bioactive substances. Bioactive substances include growth factors, morphogenetic proteins and other components of the bone matrix, which play the role of activators and regulators of physiological tissue regeneration. Currently, the development of such biocomposite materials in Russia is becoming a priority [15, 16]. The fourth technological level, which has been actively developed recently, determines the

possibility of creating synthetic biocomposite materials based on modern technologies such as:

1. Stereolithographic copying of tissues [17].
2. Technologies for creating 3-dimensional implants [18, 19].
3. Liquid-distribution modeling [20].
4. Phase-changing creation of implants [21].

The combination of methods of the fourth technological level of bone engineering allows you to copy tissue objects with high accuracy and develop materials with clearly defined sizes, geometry and pore distribution, as well as fully reproduce the architectonics of the organ site and its internal channels in the implant being created.

When choosing the starting materials for forming biocomposites, collagen and hydroxyapatite are the most natural today, which in numerous animal experiments showed not only excellent biocompatibility, but also demonstrated their ability to stimulate bone formation and serve as a matrix for new bone tissue, depending on the composition, manufacturing method. However, when creating artificial collagen-apatite materials, the technological issues of regulating the porosity of the material, controlling the formation of its structure and mechanical strength remain far from solved. At that time, how exactly, these parameters are fundamentally important for the maximum manifestation of osteoconduction properties by the material during the reparative bone regeneration.

2. SYNTHESIS OF CALCIUM PHOSPHATE COMPOUNDS TO COMBINE WITH THE COLLAGEN MATRIX

A variety of biocompatible materials for clinical use as bone implants are being actively developed in world medical practice. At the same time, calcium phosphate compounds

with natural polymers and biocompatible, biodegradable synthetic polymers are the main components in the production of bone implants. Works in the world practice on the production of bone implants is carried out in the following areas:

- 1) synthesis of calcium phosphate compounds;
- 2) the combination of calcium phosphate compounds with natural and / or synthetic polymers;
- 3) the synthesis of calcium phosphate compounds in gellike media of natural and synthetic polymers.

All conventionally identified areas are aimed at creating biocomposites to replace bone defects.

The first area related to the synthesis of calcium-phosphate compounds during the production of bone implants, the development of nanotechnology for their realization is still an urgent task. This is due to the fact that the corresponding synthetic calcium phosphate compounds should induce and actively participate in biological reactions similar to those occurring in the process of osteogenesis. The synthesis of solid calcium-phosphate particles for medical applications is usually carried out by precipitation from solutions [22]: For example, from solutions of 1) calcium nitrate and ammonium hydrogen phosphate, 2) calcium chloride and sodium hydrogen phosphate, 3) calcium chloride and potassium hydrogen phosphate, 4) calcium acetate and potassium hydrogen phosphate. Thus, in the manufacture of ceramic biocomposites, calcium phosphate was obtained from calcium acetate and sodium hydrogen phosphate [23].

In [25, 26], to obtain biocomposites, calcium phosphate powders were used, having nanoparticles of various phase compositions and forms, such as lamellar 0.8–4.5 nm thick

and needle-like 5–10 nm in diameter, 40–50 nm long. It has been established that, depending on the synthesis conditions, phase composition, structural, morphological characteristics of calcium phosphate particles, its bioactivity can manifest itself in different ways. The possibility of modifying the surface of hydroxyapatite particles by radiation, chemical activation with the formation of radicals, and modification with chemical reagents and proteins has been established, which helps to strengthen the connection between the biocomposite and bone tissue.

This paper discusses the basics of energy-saving technology for the production of calcium phosphate using hydroxyapatite as an example by mechano-acoustic activation of reaction mixtures consisting of:

- 1) aqueous suspensions of calcium monophosphate and calcium hydroxide;
- 2) from aqueous solutions of diammonium phosphate, calcium nitrate tetrahydrate and ammonium hydroxide.

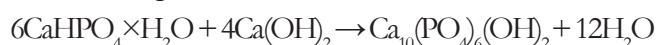
Mechano-acoustic activation, under conditions of self-heating of the reaction mixture, was carried out using the rotary-pulsation apparatus (RPA) "Delta-Rotor" (manufactured by "Aviatekhnik" Ltd.) [27], which allows the hydroxyapatite dispersion to be rapidly and completely formed in the aqueous medium.

The particle sizes of the dispersed phase were estimated using the dynamic light scattering method on a Zetasizer Nano ZS Zen 3600 Malvern instrument. The results of the distribution of the volume (mass) fraction of particles depending on their size indicate that in control syntheses, under standard laboratory conditions, the formation of rather large particles with an average hydrodynamic diameter of about 5.5 μm takes place. In contrast, mechano-acoustic

activation allows the formation of nanosized particles of hydroxyapatite having an average hydrodynamic diameter of about 20 nm.

2.1. SYNTHESIS OF "CONDENSATION" HYDROXYAPATITE

The synthesis of "condensation" hydroxyapatite (HAP-c) was carried out according to the reaction equation



Changes in the ratio of the mass of reagents to the mass of the reaction medium, in the synthesis of HAP-c condensation method, slightly affect the particle size of the resulting dispersed phase. However, it should be noted that the width of the particle size distribution is certainly smaller at a low partial concentration of HAP-c. The specific features of the synthesis of HAP-c obtained by the interaction of calcium monophosphate and calcium hydroxide include the difficulty of controlling the reaction. This is largely due to the purity of the reagents and the accuracy of taking samples of the starting reagents. Express control in this case was carried out by changing the pH of the reaction medium or by sampling with their subsequent instrumental analysis, for example, using IR spectroscopy.

Hydroxyapatite (HAP-c) has a pronounced crystalline structure, which is confirmed by electron microscopy. Micrographs (**Fig. 1**) show lamellar crystals with powder inclusions.

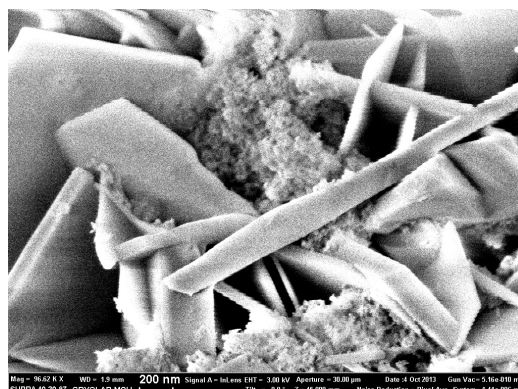
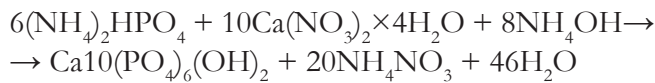


Fig. 1. Micrograph of particles (HAP-c). Scale-200 nm. Scanning electron microscope Neon 40 EsB-35-09.

**2.2. SYNTHESIS OF "ION-EXCHANGE"
 HYDROXYAPATITE**

The synthesis of hydroxyapatite by the ion exchange reaction (HAP-i) was carried out according to the reaction equation:



The particle sizes of the dispersed phase were estimated using the dynamic light scattering method. The results of the distribution of the volume (mass) fraction of particles depending on their size indicate that in the control synthesis (without using RPA), the formation of rather large particles with an average hydrodynamic diameter of about 5.5 μm takes place. In contrast, mechano-acoustic activation allows the formation of nanosized hydroxyapatite particles having an average hydrodynamic diameter of approximately 22 nm. The maPS fraction of such particles in the reaction medium is ≈75%. It should be noted that a decrease in the feed rate of the diammonium phosphate solution into the reactor and an increase in the rate of mixing of the reactants leads to an increase in dispersion. So, at a RPA rotor speed of 3100 rpm and a rate of introduction of a diammonium phosphate solution of 0.5 l / min into the reactor, a dispersion was obtained, characterized by particles having an average diameter of about 20 nm. The maPS fraction of such particles in the reaction medium is ≈90%.

The most energy-intensive part of the synthesis of HAP-i the exchange reaction is the purification of its sol from the by-product of ammonium nitrate. HAP-i nanoscale particles can only be separated from the liquid phase with great difficulty and freed from an admixture of ammonium nitrate. In this regard, the following options for obtaining pure HAP-i are implemented:

- 1) by decantation,
- 2) using centrifugation,

3) by heat treatment.

The second approach, in contrast to sedimentation in a gravitational field, allows you to increase the speed of the cleaning process. HAP-i cleaning by decantation is associated with high water consumption and cannot be considered effective. The interest is the heat treatment of the technical HAP-i, which was used in [28]. Indeed, we have shown that a HAP-i sample contaminated with ammonium nitrate can be successfully cleaned by heat treatment at 350°C for 30 minutes.

The data of elemental analysis, purified HAP-i confirm the complete absence of nitrogen-containing impurities in the heat-treated sample (standard- ammonium nitrate). An additional confirmation of the absence of ammonium nitrate in the purified HAP-i samples is the results of the calorimetric experiment. HAP-i obtained by the exchange reaction and subjected to heat treatment, passes into a xerogel having characteristic blue luminescence.

It should be noted that the crystalline phase is not dominant in the structure of purified HAP-i. This is observed both for the sample of its suspension, and for the sample - xerogel. This is indicated by the data of electron scanning microscopy.

Using the method of reference contact porometry to determine the weight of a sample treated with octane under vacuum, it was found that the porosity of the heat-treated HAP-i is about 75% with an average pore radius of $2.8 \cdot 10^3$ nm. HAP-i purified from impurities and dispersed in water, is prone to changes in its properties over time. These changes, in particular, are directed towards the enlargement of the particles of the dispersed phase. So, after holding the dispersion of purified HAP-i in an aqueous medium for 30 days, the average particle diameter increases to 44 nm. The change in time of the dispersion

of the HAP-i purified from byproducts of the reaction, may be due to: a change in the nature of the dispersion medium. In this case, the characteristic of the diffuse layer of counterions changes. This is indicated by the found drop in the zeta potential from +30 mV for the aqueous dispersion of the technical HAP-i and to a value of about +5 mV, characteristic of the dispersion of the purified product.

3. THE FORMATION OF COLLAGEN-CALCIUM-PHOSPHATE BIOCOMPOSITES

At the stage of production of biocomposites, calcium phosphate compounds are usually combined with both natural and artificial polymers, for example, collagen, gelatin, alginates, chitosan, polylactide, polyhydroethyl methacrylate, and others [29–33]. Of particular interest in polymeric materials is the possibility of obtaining hydrogels from them. Biocompatibility, cell adhesion, the ability to exist in the body without damaging neighboring cells are necessary criteria for the development of hydrogel biomaterials. Currently, in the manufacture of bone implants, interest is shown in technologies for combining natural and artificial polymers. This is due to the fact that such materials, by changing the properties of the biocomposite (sorption, diffusion, the ratio of hydrophobic and hydrophilic sites, etc.), make it possible to finely control the course of the basic processes of bone tissue restoration such as inflammation, dissolution, hydrolysis, enzymatic hydrolysis, and cellular biodegradation.

It has been established that after the introduction of a polymer-containing biocomposite into the animal organism, cells of various types group around it. At the first stage, loose connective tissue forms around the biocomposite, through which blood

vessels and nerve fibers pass. From the blood the cellular elements of connective tissue and fibroblast cells that produce collagen enter the forming tissue. At the same time for blood as one of the main connective tissues of the body, effective circulation in the volume of the biocomposite is necessary, which can be ensured by its porous structure.

In a simplified form, the regeneration process consists of the following stages:

- 1) in the area of a bone defect, a tissue clot from macrophages and fibroblasts is formed;
- 2) at the next stage, cells (osteoclasts) and cells (osteoblasts) are observed in the area of the defect;
- 3) as a result, the site is filled with fibrous tissue and bone tissue elements;
- 4) restoration of the periosteum, bone marrow and vascular system ultimately leads to the formation of new bone tissue.

In [34], it was noted that as a result of numerous experimental studies, high efficiency was established for the replacement of bone tissue defects and the activation of reparative osteogenesis of a biocomposite drug combining hydroxyapatite, collagen with the inclusion of antibiotics (Collapan). At the same time, the need to achieve a macropore value of the biocomposite of at least 300 μm is noted, which contributes to nutrition, cellular distribution on the surface of macropores and the formation of capillaries.

In this work, we developed the basics of energy-saving technology for producing collagen-calcium-phosphate biocomposites by combining hydroxyapatite and collagen under conditions of mechano-acoustic activation of reaction mixtures. In contrast to the known methods for combining calcium-phosphate particles of a solid phase with a polymer material, in the continuation of [35, 36],

MEDICAL PHYSICS

biocomposites were obtained by synthesizing calcium-phosphate compounds directly in a collagen matrix.

To obtain porous calcium phosphate biocomposites, pork skin (PS) used in the food industry was used as a source of organic binders [37]. It is known [38] that upon extraction of the skin of animals, a solution of protein fractions forming fibrils is obtained. The chains of fibrils are twisted in the form of an “electric cable”, and the side groups of all amino acid residues are on the outside of the molecule. Dispersion of PS was carried out in an aqueous medium to obtain a collagen sol. To obtain porous calcium-phosphate biocomposites, gelatin was also used- one of the best gel-forming agents of protein nature. Gelatin hydrosol as well as collagen with a concentration of 2% or more when cooled below 40°C forms stable gels. The mechanism of gelatin gel formation during the sol-gel transition is associated with the formation of a three-dimensional network structure due to hydrogen bonds. When a gelatin solution is cooled, randomly arranged helices of macromolecules change the conformation of polypeptide chains, forming a three-dimensional structure with a loss of fluidity. It was found that during the enzymatic treatment of collagen-containing raw materials, high molecular weight gelatins are formed, from which strong gels are formed.

As the initial collagen-containing raw material, we used PS, fat-free with hexane, subjected to cryogenization to a particle size of ≤5 mm and blanching at a temperature of 60° C. The synthesis of hydroxyapatite-collagen compositions was carried out in RPA during sequential loading of components according to the schemes: collagen-hydroxyapatite ratio, 6: 4 (HAP-C-1) and collagen-hydroxyapatite ratio, 4: 6 (HAP-C-2).

The immobilization of hydroxyapatite on the collagen matrix leads to the enlargement of the particles of the dispersed phase. So, unlike hydroxyapatite, formed in the absence of collagen having an average particle diameter of about 20 nm, particles of the HAP-C-1 composition have an average diameter of about 680 nm.

The IR spectrum of HAP-C-1 pulp has a strong absorption band of 1332 cm⁻¹, associated with the presence of ammonium nitrate in the impurity system. The composition of HAP-C-1 was purified from ammonium nitrate by sequential washing of the precipitate with distilled water. The multiple decantation leads to a HAP-C-1 composition, according to spectral data, excluding the presence of ammonium nitrate in the composition.

The purification of the HAP-C-2 composition from ammonium nitrate was carried out using the settling method with draining the liquid and sequential washing of the precipitate with distilled water. Multiple decantation leads to a HAP-C-2 composition, according to spectral data, excluding the presence of ammonium nitrate in the composition. The resulting collagen-hydroxyapatite compositions (HAP-C-1, HAP-C-2) were used to form porous medical materials.

4. THE FORMATION OF POROUS MATERIALS BASED ON COLLAGEN-CALCIUM-PHOSPHATE COMPOSITIONS.

Porous biomaterials are necessary for the effective interaction of implants with tissues in living systems. For all three-dimensional porous biomaterials (scaffolds) participating in the cell growth stage, it is important that their surface promotes adhesion, cell fixing and their migration

in the porous structure. New approaches developed in the work on the formation of porous biocomposites using the 3D printing technique and microwave radiation have allowed the formation of porous samples of biocomposites with different pore structures. The advantages of using porous materials for biomedical purposes based on natural and synthetic polymers are also associated with the ability to regulate the functional properties of the synthesized materials through the immobilization of enzymes, proteins, amino acids, and other natural substances [39].

The introduction into the defective areas of bone tissue of biocomposites, which include stem cells, can also be carried out using porous biocomposites.

When creating porous bone-substituting materials the biocompatible and biodegradable polymers are used, for which various methods of forming a porous structure are being developed. So, porous biocomposites are made using the following methods: 1) freeze drying; 2) microwave drying; 3) the use of devices with fibers (utility models); 4) the use of gas-releasing additives in the composition (porophores); 5) the formation of porous biocomposites in supercritical carbon dioxide; 6) the construction of porous biomaterials by 3D printing.

In the work some methods for the formation of porous collagen-calcium-phosphate composites were considered. The ability of the synthesized HAP and HAP-C to form plastic pasty compositions as a result of centrifugation and removal of excess water was used. Centrifugation was carried out on an "Allegro 64R, Beckman" centrifuge in the mode of 6000 rpm for 15-20 min at 10°C. After centrifugation, hydroxyapatite concentrates were placed in special forms for the manufacture of porous biocomposites. The

volumetric porous collagen calcium-phosphate biocomposites obtained by the developed methods of formation were used in models of orthopedics and traumatology to replace bone tissue defects in living systems [40].

4.1. THE FORMATION OF POROUS COLLAGEN-CALCIUM-PHOSPHATE BIOCOMPOSITES BY FREEZE DRYING

Samples of porous composites (**Fig. 2**) were formed by lyophilic drying of collagen-calcium-phosphate sols obtained according to the developed method. Additional cross linking was carried out with glutar aldehyde. Drying was carried out in a freeze dryer "Martin Christ Gamma 1-16 LSCplus" at a condenser temperature of -55°C.

After freeze drying, depending on the water content in the collagen component, porous samples with a density of 0.15-0.2 g/cm³ are obtained. Using the method of reference contact porometry [41] to determine the weight of samples processed under vacuum with an organic liquid-octane, it was determined that the bulk of the pores for the HAP-C-1 biocomposite are in sizes from 10 μm to 100 μm. In this case, pores of approximately 60 μm are dominant.

When comparing collagen-calcium-phosphate biocomposites with pure hydroxyapatite (without a binder organic component), it was found that the pore surface size depends on the ratio of the mineral and organic components of the

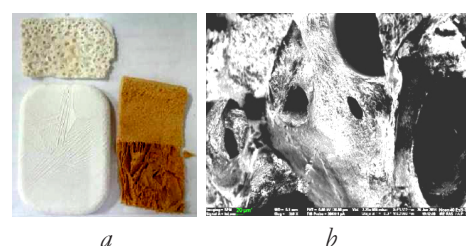


Fig. 2. Samples of collagen-calcium phosphate biocomposites after freeze drying (a), micrograph of pores of the biocomposite sample (b), scale - 20 μm.

composite and significantly decreases with an increase in the content of the organic component. So, the xerogel of pure HAP-2 is characterized by a pore area of about 616 m²/g, and for the collagen-calcium-phosphate composition this value decreases to 27 m²/g, which is due to the blocking of pores by the organic component.

4.2. THE FORMATION OF POROUS BIOCOMPOSITES BY GRANULATION AND FIBER FORMATION

The method of filling forms with granules or fiber is associated with percolation models. Between the granules and the fibers, physiological fluids flow that provide the conditions for the growth of cells. The production of granules and fibers in the work was carried out from flowing collagen-calcium-phosphate paste. When forming fibers, sodium alginate was additionally introduced into the composition. Extrusion of the mixture composition during the formation of fibers was carried out using a peristaltic pump in a solution of calcium chloride. The resulting granules and fiber were subsequently subjected to freeze-drying and a tissue-engineering structure using solutions of biodegradable polymers was assembled from them.

In Fig. 3 presents images of granules and fibers from which the tissue-engineering structure is assembled.

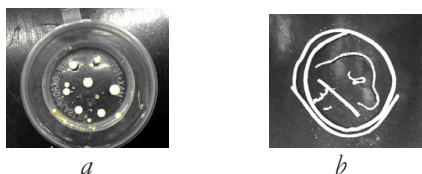


Fig. 3. Granules made by dispersing a suspension of HAP-C-2 in liquid paraffin (a), HAP-C-2 fibers formed in a solution of calcium chloride (b). The area is a 4x4 cm in the photo.

4.3. THE FORMATION OF POROUS BIOCOMPOSITES USING SPECIAL FORMS AND DEVICES

To form biocomposites with a large pore size of 100 to 300 μm, special forms and devices have been developed and manufactured [42]. The device (Fig. 4a) for the formation of a porous bone composite consists of a hollow cuvette (1) made with the possibility of filling with a biocomposite mass (2) and porosity-defining embedded fibers (3), which are fixed in through holes (4) made in the walls ditches. After filling with a biocomposite mass, drying and removing fibers, a composite is obtained with a given through porosity and a given fiber distribution. Fibers are selected from the group including textile, polymer, metal fibers, including biodegradable materials with a diameter of 100-500 microns.

A cuvette for filling with a biocomposite is made of polymethylmethacrylate, Teflon or metal if it is necessary to heat the binder component or to initiate the polymerization process. A cuvette for filling with a biocomposite mass can also be made in the form of a tube (Fig. 4b) from an elastic polymer, mainly rubber, and the insertion of embedded fibers (3) is carried out through the through holes in its walls formed by piercing with a needle and thread. The photos of the surface sections

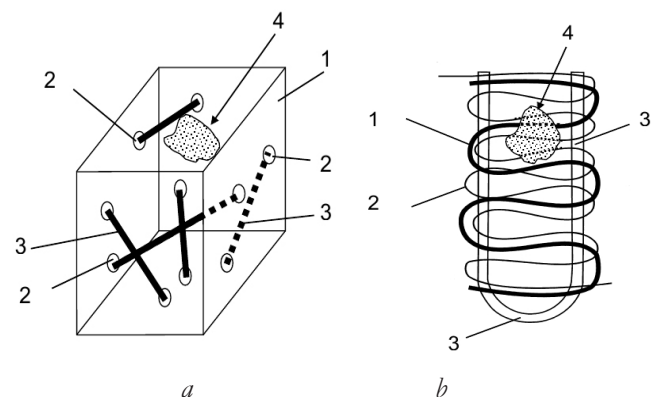


Fig. 4. Devices for the formation of biocomposites with through porosity.



Fig. 5. Sections of the surface of the composite with through pores.

of the collagen calcium phosphate composite with through pores are shown in **Fig. 5**.

Such methods can be used both for the manufacture of biocompositions from natural polymers, as well as mixed compositions from natural and synthetic polymers. Mixing aqueous pasty compositions with natural polymers and pasty synthetic polymers in organic solvents under the conditions of ultrasonic dispersion of mixtures made it possible to obtain pasty mixtures and extruding from the syringe to form biocomposites in the form of a lattice with a window of the order of 0.3-0.3 mm (**Fig. 6b**).

4.4. THE FORMATION OF POROUS BIOCOMPOSITES BY MICROWAVE HEATING

The use of microwave radiation to remove liquid phases from biocomposite compositions is promising especially in the conditions of formation of mixed compositions from natural and synthetic polymers. Biocomposites containing water, polar solvents, electrically conductive particles, when interacting with

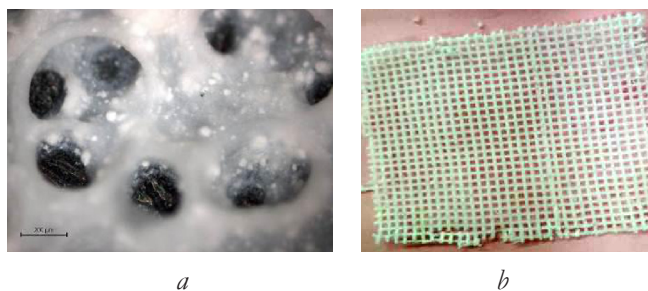


Fig. 6. a) Pores in the polylactide sample with hydroxyapatite particles were formed after combining the components and drying on a rotary evaporator; b) A sample from the composition of sodium alginate - HAP-2 in the form of a lattice, made in a special form.

microwave radiation (microwave range) are intensively heated. As a result, liquid substances moving into the gas phase are removed from the biocomposite and the porous structure of the material is formed [43].

The interaction of electromagnetic radiation (EMR) with samples of materials is characterized by reflection coefficients (R), absorption (Q), transmission (T). The values of R , Q , T are determined by the complex values of the dielectric and magnetic permeabilities of the samples of materials, the wavelength (λ) of the radiation and the thickness of the irradiated material (d). Model experiments with materials of various nature (intercalated graphites, fumed paper, liquids) showed that for effective interaction with electromagnetic radiation, a certain ratio of the specific volume resistance of the materials (ρ_v), the thickness of the material (layer d) and the location of the material on the dielectric substrate (with the value dielectric constant ϵ). The balance of all parts of the energy determines the heating conditions.

To remove the liquid phases from the collagen-hydroxyapatite composite, a microwave oven was used (frequency 2.45 GHz, power 800 W). The samples of biocomposites were made by applying a paste-like complex of the studied components on a dielectric Teflon substrate with followed by drying under the influence of radiation from a microwave oven.

It was found that the drying process in the mode of sequential heating of the collagen-hydroxyapatite composition for 15-20 seconds does not lead to strong heating of the samples and the development of destructive processes. Raman spectra (Raman spectra) of collagen-hydroxyapatite samples are lyophilically dried and dried under the influence of microwave radiation. The comparison of porometric parameters in the pore region of more than 10 μm of samples of biocomposites dried

freeze-dried and under the influence of microwave radiation also did not reveal obvious differences.

Microwave radiation was also used in the preparation of complex compositions including, in addition to collagen-hydroxyapatite, additional biodegradable polymers. In this case, an aqueous suspension of collagen-calcium phosphate under the influence of ultrasound with a frequency of 22 kHz and a generated emitter power of 100 W was mixed with a biodegradable polymer in an organic solvent. The formation of porous biocomposites was carried out by layer-by-layer deposition of compositions on a dielectric substrate and the removal of liquid components under the influence of microwave radiation. The amount of the polymer component M (g) required to ensure optimal film formation on the hydroxyapatite particles was estimated taking into account dry hydroxyapatite (m , g), specific surface area of hydroxyapatite powder (S cm²/g), polymer density, (ρ , g/cm³) and the thickness of the polymer layer on the surface of the powder particles (h , cm).

Noteworthy the biocomposite obtained on the basis of 2-hydroxyethyl methacrylate (HEMA) and HAP using microwave radiation. For this, HAP-2 paste with a water content of 12% in an amount of 19.8 g was mixed using a UZDN-1 low-frequency ultrasonic disperser (emitter frequency 15 kHz) with 5.1 g HEMA. The weight ratio of GEMA-HAP (in terms of dry HAP, 1:3.5). GEMA-HAP-2 paste was exposed to: drying by means of microwave radiation. When potassium persulfate is introduced into the paste, followed by microwave heating and drying, the polymerization process takes place and solid white organomineral compositions are formed.

As a result of studies, it was found that when additives are added to the composition of pasty compositions that affect the electrical

conductivity of the compositions, it is possible to control the rate of release of gaseous components, and thereby affect the porous structure of biomaterials. The introduction of fibrous additives can also significantly affect the distribution of the porous structure in the biomaterial.

The results of studies on the formation of a porous structure in samples of biopolymers have shown that the use of thermal and microwave (microwave) methods for removing the liquid phase is most effective for samples containing water. Therefore, the manufacture of porous biomaterials through the stage of creating aqueous emulsions from film-forming biocompatible polymers with calcium phosphate compounds is promising for the formation of porous biomaterials. It is established that a combination of thermal and microwave heating in a polymer matrix gives rise to a developed pore structure. During thermal heating, thermoplastic polymers become viscous, and the exit of gas-forming components from the liquid phase forms through pores in the material and large pores.

5. FABRICATION OF TISSUE ENGINEERING STRUCTURES.

For the manufacture of tissue-engineering structures, biocompositions from natural and synthetic polymers in the form of pastes, thermoplastic rods, and nonwoven fibrous materials were prepared. This approach made it possible to construct tissue-engineering structures with various combinations of the initial compositions, which are constituent structures and are themselves samples of materials for replacing bone tissue defects. Paste-like calcium phosphate compositions were prepared by mixing synthesized hydroxyapatite particles with suspensions of collagen, gelatin, sodium alginate and synthesizing hydroxyapatite particles directly in

polymer suspensions. Techniques for making pastes include the steps of synthesizing hydroxyapatite particles, ultrasonic dispersion, and the centrifugation step to obtain a paste-like consistency of the compositions.

Using indenter immersion methods under load in samples of calcium phosphate pastes, it was determined that the viscosity of the compositions is a characteristic of the plastic properties of pastes. Measurements of calcium phosphate paste samples were carried out according to the method of immersing an indenter in a sample under load. After application of the load, a creep process develops in the sample, associated with the development of irreversible deformation. The viscosity of the composition is 0.44 MPa. An increase in the concentration of hydroxyapatite particles led to an increase in the elastic properties of the composition (when the ratio of hydroxyapatite particles to HAP-C collagen was 6:4). When a 5% solution of glutaraldehyde is added to collagen-hydroxyapatite concentrate, and a 5-15% solution of calcium chloride is added to the composition of sodium alginate, the material samples acquire elastic properties and the strength of the samples increases due to the formation of crosslinks between polymer macromolecules.

The porous collagen samples of calcium phosphate compositions are made by filling pastes with molds and drying by freeze drying and microwave heating. As a result of drying the porous samples were obtained in the form of plates with a density of 0.15-0.2 g/cm³. Using the method of reference contact porometry, it was determined that the majority of the pores are in sizes from 10 μm to 100 μm. The porous samples in the form of plates are also made by mixing particles of hydroxyapatite with suspensions of sodium alginate.

After filling the forms of various designs with pastes and drying the porous samples

of various kinds were obtained. When mixing sodium alginate (Na alginate) and hydroxyapatite particles, in which a uniform, necessary consistency paste is formed (65% (2% Na alginate solution) and 35% hydroxyapatite powder (HAP). The resulting mixture (HAP and Na alginate) was carefully dispersed with using ultrasonic exposure by a low-frequency ultrasound generator with a frequency of 22 kHz for 5-10 minutes.

It has been found that it is possible to combine collagen calcium phosphate concentrates with solutions of synthetic polymers to produce pastes from a mixture of natural and synthetic polymers. A mixture of collagen calcium phosphate paste with a solution of polylactide (in a ratio of 1:1, by weight) was carried out under ultrasonic dispersion for 5 minutes. The formation of mixed plastic compositions from natural and synthetic polymers is a promising area of tissue engineering. Using various methods of forming a porous structure, tissue engineering structures of varying complexity can be manufactured for biomedical applications.

The results of comparative tests of the strength properties of biocomposites based on natural and synthetic polymers have shown that the combination of polymers of different nature leads to an increase in the strength properties of biocomposites and a change in the time of their biodegradation in living systems.

After saturated with water the samples acquire elastic properties. The highest strength (80 MPa) and the lowest tensile deformation (25%) have samples based on polyacrylamide gel (PAAG). Collagen based compositions have the highest tensile deformation (65%), but their strength (2 MPa) is low. With an increase in the thickness of the polymer layer of synthetic biodegradable polymers on the surface of a porous collagen of a calcium-phosphate

sample, strength characteristics increase, and the biodegradation time also changes.

Synthetic biodegradable polymers: polylactide- PLA (brand 4032D Nature Works LLC (LD, L)), poly-3-hydroxybutyrate - PHB obtained by microbiological synthesis (BIOMER, Germany) and polycaprolactone-PCL ("ADALIK" Ltd.), relate to a class of thermoplastic polymers and were used in the work to build tissue-engineering structures. To use thermoplastic polymers in 3D printing technologies, it is necessary to produce rods of a given thickness and strength. It follows from the experimental data that the polylactide sample has the highest strength, and the introduction of hydroxyapatite particles (20 mass%) into the synthetic polymer (PHB) leads to a decrease in strength characteristics.

Studies of the thermophysical and strength properties of thermoplastic biodegradable polymers are necessary for constructing tissue-engineering structures using 3D printing. Therefore, comparative studies of polymer samples, polymer blends, and composite material samples were carried out using the TGA, TMA, DMA, DSC methods.

The processes of heating and cooling during extrusion by the method of 3D printing affect the size of the fibers, the shape and size of the cells during the construction of cellular three-dimensional structures (Fig. 7). The results of measurements of the characteristics of polymer samples by the DSC method showed

that, in the heating-cooling mode, samples from PHB do not exhibit thermal stability compared to PLA. PHB is characterized by a change in crystalline phases with conversion to an amorphous state. The spreading of the thermoplastic material leads to an increase in the thickness of the samples in the manufacture of rods. A change in the thermal stability of PHB samples occurs when the polymer is mixed with hydroxyapatite particles.

The technological process for the manufacture of rods from thermoplastic polymers and their mixtures with natural polymers was carried out in two stages. At the first stage, using the IIRT-AM thermoplastics yield index meter, thermoplastics powders were poured into IIRT-AM, heated to the melting temperature, which was determined by the DSC method. After holding for 1 minute, the material was extruded from the chamber through a capillary with a diameter of 2.08 mm. The first stage was used to assess the feasibility of manufacturing polymer rods from new polymer combinations. The second stage was carried out in the manufacture of calibrated rods in sufficient quantities to work with a 3D printer. The production of polylactide-based rods was carried out by melt extrusion on an extrusion line manufactured by firm "Gottfert".

A mixture of polymers was obtained by mixing 7% solutions of PLA polymers with PHB in a ratio of 1:1 and drying. Using a melt extrusion method on an extrusion line, a bar of a given diameter (1.75 ± 0.05 mm) and length was manufactured.

At the IIRT-AM laboratory unit, rods were made from a mixture of PHB with particles of hydroxyapatite (HAP). The composition for the manufacture of the rod consisted of domestic polyhydroxybutyrate (PHB) obtained from the chloroform clarified biomass extract *Methylobacterium extorquens* G-10 (weight

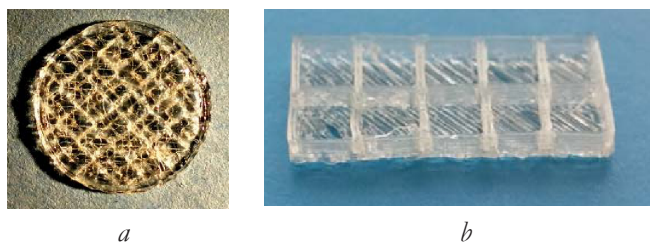


Fig. 7. Samples of tissue-engineering structures made of polylactide. a) the disk with cells from a polylactide bar, built according to 3D technology; b) the sample in the form of a pencil case, constructed of polylactide by 3D printing.

18 g), (Pushchino, Institute of Microbiology RAS) in the form of particles of size 0.5-2 mm and particles of hydroxyapatite in the form of a finely divided powder.

Another approach to the manufacture of the rod was to mix the polymer with hydroxyapatite particles. The manufacture of the rod from the PHB-HAP composition with a 20% mass fraction of hydroxyapatite particles was carried out after preliminary grinding of PHB particles in an IP-30 mill and mixing with HAP particles. The filler leads to a decrease in the fluidity of the polymer melt, and the forcing of the composite melt was carried out at a temperature of 180°C.

A new approach for mixing PHB with hydroxyapatite particles was to create an aqueous suspension of PHB by mechano-acoustic treatment of the suspension in RPA. Then, in the PHB suspension, the reaction of the formation of HAP particles was carried out according to the reaction between calcium monophosphate hydrate and calcium hydroxide (by analogy with the synthesis of collagen calcium phosphate compositions). The mechano-acoustic treatment of the PHB-HAP composition in water led to the formation of synthesis products in the form of a lower sediment layer, an upper layer in the form of foam and an intermediate layer of a suspension of nanoparticles. As a result of centrifugation of the precipitate, the product of the paste-like composition PHB / HAP was obtained. Using the TGA and DSC methods, it was found that the ratio of organic and inorganic components in the sediment is 80:20 wt.%, And the DSC dependence confirms the role of the influence of hydroxyapatite particles on the thermal stability of the composition.

In contrast to the synthetic polymers PLA, PHB, of which rods and extruded films were made at temperatures above 170°C, polycaprolactone (PCL) rods were produced

at extrusion temperatures over the extruder zones 60-80°C. A calibrated bar with a diameter of 1.7-1.8 mm was obtained on the extrusion line. The PCL melt flow rate, measured on an IIRT-AM device at 100°C, 2.16 kg was: 15 g/10 min; at 80°C - 7 g/10 min and at 60°C - 2.5 g/10 min. For maxillofacial surgery interest in polycaprolactone is due to the ability to produce samples of materials of specialized structures at temperatures of 60-80°C.

The results of the manufacture of thermoplastic rods for the 3D printing technique showed the need to develop polymer compositions with the necessary flow properties of polymer melts. Thus the process of constructing tissue-engineering structures is associated with the improvement of 3D printing technology. The development of a temperature controlled 3D printing technique, the use of UV, IR, and microwave radiation techniques when forming products of complex architecture by 3D printing can change the polymerization rate and form a porous structure in the samples.

The methods for the formation of porous polymer composites presented in this work allow the production of porous biocomposites with various architectures. The formation of mixed compositions from natural and synthetic polymers with inorganic and organic compounds allows to design a wide range of biomaterials of varying complexity. A new approach to the mixing of polymers of various nature is implemented under conditions of ultrasonic dispersion of solutions of biodegradable polymers in chloroform with colloidal aqueous suspensions and thermostimulated microwave heating.

Non-woven porous films were made by the method of electroforming of fibers (EFF) from solutions of biodegradable polymers (PHB, PLA, PCL).

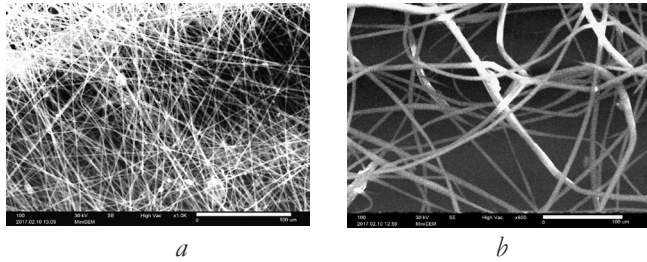


Fig. 8. Electron microscopy images of non-woven samples obtained by the method (EPI) from solutions of PHB a) and PLA b). Scale - 100 microns.

Fig. 8 shows electron microscopy images of nonwoven samples obtained by the EPI method from PHB and PLA solutions. The synthesis of nonwoven samples of materials from polymer solutions with inorganic and organic components was carried out under conditions of ultrasonic and mechanical-acoustic dispersion. The creation of multilayer samples of nonwoven materials with a different combination of layers and the construction of structures on samples of nonwoven materials using 3D printing made it possible to create porous structures with controlled porosity and bioresorption time.

The methods of formation of a porous structure in polymer composites developed in the work indicate the need to combine various methods to achieve a branched porous structure and the required pore sizes in biomaterials. The combination of samples of materials obtained by 3D printing and EPI is a promising direction in the manufacture of porous three-dimensional frame structures.

6. METHODS OF IMPLANTING POLYMER SAMPLES INTO A BONE DEFECT.

Studies of the effectiveness of calcium-phosphate biomaterials based on natural and synthetic polymers in traumatology and orthopedics were carried out using the method of implantation of samples into a skull bone defect in vivo. The implantation technique included: incision of the prepared skin up to

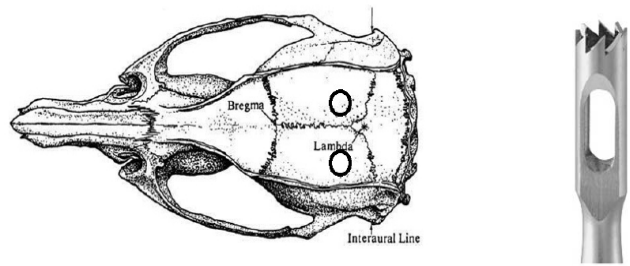


Fig. 9. Scheme for applying defects (3.5 mm) in the parietal bones of a rat with a round mill.

2 cm and atraumatic dilation of soft tissues to the parietal bones, then two holes were formed in the bones of the skull with a round cutter with a diameter of 3.5 mm (**Fig. 9**).

The defect was closed with a prepared collagen calcium phosphate sample (KHA matrix) in this model and the reactions at the border of the graft and bone tissue were studied. The graft mineralization process was also evaluated. For this purpose, computed tomography and histological preparations of the skull bones were used.

In the preparations of the experimental group on the 60th day the filling of the defect area with fibrous connective tissue of varying degrees of density was observed. The study of the toxicity of the KHA matrix was carried out on a fibroblast culture. The surface of the sample contributed to good spreading and fixation of cells. Attached fibroblasts on the material were alive. The staining with fluorescent nuclear probes (Hoechst 33342) after 48 hours after plating of cells on the material showed their complete survival. Moreover, among them cells in anaphase and metaphase state were revealed, which directly indicates cell growth on a sample of material.

The developed porous tissue-engineering construction- the KHA matrix, consisting of collagen and hydroxyapatite materials that are biologically natural for bone tissue, is close to the native bone in percentage. The production technology of such structures allows the

inclusion of drugs in its composition, depending on the specific clinical task. The structure and physicochemical properties of the developed bone implant provide it with high adhesive properties for fibroblast cells. This contributes to the activation of reparative processes in bone defects, without interfering with natural osteohistogenesis.

The use of the developed design with the inclusion of an antibiotic in it makes it possible to eliminate the purulent-destructive inflammatory process in the model of post-traumatic osteomyelitis with restoration of bone tissue. The developed methods for studying porous collagen-calcium-phosphate matrices were also used in the study of porous calcium-phosphate compositions based on other natural and synthetic polymers in the replacement of bone defects.

As a result of the synthesis of hydroxyapatite in a suspension of PHB, paste PHB/HAP with a 20% content of hydroxyapatite particles was obtained. Films 100-200 μm thick, rods for 3D printing, and a 2-layer fabric engineering design based on the porous non-woven material PHB obtained by EPI and paste - PHB/HAP were made from these compositions. The paste was applied to a nonwoven sample of PHB material and dried under the influence of microwave radiation. During subcutaneous implantation of the fabricated material samples, their biocompatibility and the absence of inflammatory reactions in the tissues were noted. The results obtained allowed us to proceed to the design of complex tissue-engineering structures by 3D printing in the form of volumetric cellular structures and filling their calcium with phosphate pastes. The method of 3D printing made porous cellular samples, it is planned to fill the cells with calcium phosphate pastes containing morphogenetic protein and other bioactive materials. Biomedical testing of samples of

biocomposites in living systems allows you to adjust the methods, composition and conditions for the manufacture of structures of complex architecture. The manufacture of biocomposites with the introduction of biological components from living organisms into them will stimulate the process of osteogenesis and restore the process of replacing a bone defect.

7. PRODUCTION OF BONE SUBSTITUTE MATERIALS USING THE 3D PRINTING METHOD.

The development of frame-type implants is currently an important area of tissue engineering. With this construction, a framework made of a thermoplastic polymer plays the role of mechanical support, and is filled with biomaterial that acts as an extracellular matrix.

The development of new methods and approaches for 3D printing of bone implants, which, after being introduced into the body, can be reconstructed into living bone tissue, for maxillofacial surgery and dentistry are the most popular and can be implemented in the first place. Jaw defects resulting from inflammatory and tumor processes, traumatic injuries, and tooth extraction make it difficult to rehabilitate patients and prosthetics.

Currently, biomaterials are used to replace jaw defects in the form of chips, blocks and gels, which, however, are not able to restore the shape and structure of lost bone. These limitations can be overcome with the help of new approaches to computer modeling and combined 3D printing methods, which allow creating bone implants close in structure and biological properties to living bone tissue.

As a layout, a 3D model of a bone with a defect was constructed using computed tomography data, using the example of the lower jaw. For this the ViSurgery program

was used. By software, a model of a bone implant was formed, repeating the contours of the defect and replenishing its volume with the formation of the internal structure of the implant in the form of a beam three-dimensional structure. **Fig. 10** shows the appearance of the 3D model of the lower jaw after it is divided into regular cells. The cortical (external) frame of the implant was printed using a polylactide rod. The formation of a spongy (internal) structure of the bone implant and jaw model was performed with hydroxyapatite paste.

The development of a lattice structure will allow us to split the 3D model of the implant into lattices (Fig. 10), which in turn repeat the individual implant geometry to restore the bone defect in the patient and allow the strength characteristics of the implant to be preserved after transplantation. At the same time, the space between the beams is communicated throughout the implant, which will not impede the growth of vessels deep into the implant and limit regeneration, simulating the natural structure of bone tissue.

The development of a 3D printer for combined printing with biocompatible polymers (polylactide, polyoxybutyrate, polyglycolide) by the method of layer-by-layer deposition (FFM) and pastes based on natural and synthetic components, the method of direct extrusion is an innovative and highly sought-after approach to solving the problem of timing and quality of bone restoration defects.

In the work, pastes based on hydroxyapatite and sodium alginate (HAP-AN) were used as biomaterials filling the framework of a thermoplastic polymer. HAP-AN paste was used in the preparation of compositions containing biopolymers with viscous-flowing properties and suitable for the construction of implants using the 3D printing method. The implants were constructed in layers. Various combinations of mixing the components of the compositions and the construction of product layers were used. At the same time, a new approach was implemented in the work, associated with the use of non-woven polymeric materials as a substrate for constructing a polymer skeleton. Non-woven polymeric materials obtained by electrofiber forming (EFF). Forming was carried out on a substrate of nonwoven polypropylene material using a 7% chloroform solution of polyhydroxybutyrate (PHB). The electrical conductivity of the solution was about $9 \mu\text{S}/\text{cm}$. The capillary diameter is 0.1 mm.

Electroforming of nonwoven fibrous materials from PHB was carried out with the aim of manufacturing

- substrates for further layering of calcium-phosphate compositions and construction of implant structures using a 3D printer;
- for electroforming non-woven fibrous materials with dosage forms.



Fig. 10. *The lattice structure of the lower jaw, modeled in the Inspire software package.*

So, on a non-woven material from PHB by 3D printing a polylactide (PLA) framework was constructed, which was then filled with a paste-like water composition HAP-AN. For the study of the behavior of biomaterials in living systems, samples of various architectures were made.

In **Fig. 11** shows PLA disks located on a PHB membrane constructed using 3D printing technology. The development of such structures from two polymers, one of which is of the membrane type, opens up new possibilities in the production of artificial bone substitute materials.

The samples of mesh (lattice) architecture seem to be the most promising for the replacement of bone defects, as it provides greater access to cells to three-dimensional porous structures during the formation of new tissue.

In the work, compositions were developed, including HAP and biodegradable polymers, suitable for the construction of implants using 3D printing technology. The combination of HAP with polymers was carried out under conditions of ultrasonic dispersion of mixtures using chloroform solutions of PHB, PLA, and aqueous suspensions of HAP. From compositions comprising HAP and biodegradable polymers, the corresponding fibrous non-woven materials were obtained by electroforming. The conditions of electrostatic forming of fibrous nonwoven materials do

not significantly affect the chemical nature of the starting biopolymers. This, in particular, is indicated by the results of IR spectroscopy. Spectra of reflection (not detecting significant differences among themselves) of PLA films obtained by pressing and electroforming.

Part of the polymer-containing compositions before doping was doped with the endoxan dosage form. The idea of creating fibrous non-woven materials with dosage forms is associated with the need to obtain implants with a prolonged ability to suppress bone tissue neoplasms.

Using 3D printing, samples from synthetic polymers were fabricated in a layer-by-layer manner on fabric-based non-woven samples from the corresponding polymers. On a nonwoven fibrous material obtained by the EFF method from solutions of biodegradable polymers, a tissue-engineering cellular structure with a predetermined pore size (100-500 μm) is formed by 3D printing, which is filled with calcium phosphate pastes containing natural polymers and necessary components. After assembly, the structure is dried by thermostimulated microwave heating.

To determine the changes in biocomposites that occur in living organisms over time, a series of samples were prepared based on biodegradable polymers and calcium phosphate pastes.

It was established by electronic, atomic force, and acoustic microscopy that polylactide wafers aged for 1-3 months in living organisms undergo changes. As a result of biodegradation, the average height of the microrelief decreases.

During histological examination of bone tissue samples containing a polymer three-dimensional structure, it was found that bridges and the outer membrane of the structure, around which the connective and bone tissue

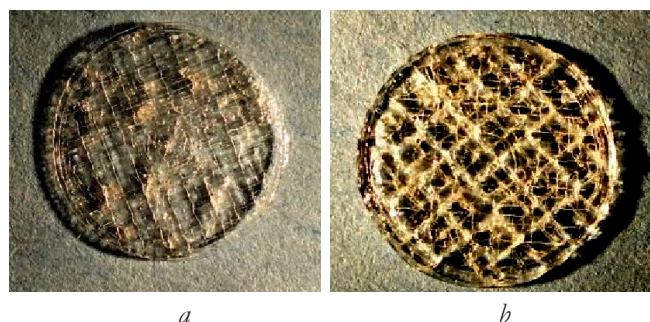


Fig. 11. The disks from PLA on the PHB (a, b), built using 3D technology.

of the regenerate are located, are clearly constructed among the bone regenerate.

Contact of bioimplant with bone tissue occurred without a layer of connective tissue. Regenerative type connective tissue with signs of focal osteogenesis was in contact with the bioimplant without visible cellular reactions characteristic of inflammation. Reticulofibrotic bone tissue rested on a bioimplant and spread along it. Osteoblast precursors evicted from immature connective tissue cells formed an osteoid in the immediate vicinity of the structure without significant signs of inhibition of reparative osteogenesis. A targeted study of the contact area of the connective tissue of the regenerative type and the material of the three-dimensional structure did not reveal a pronounced macrophage and inflammatory infiltration of it. The fibers of connective tissue penetrated into the gaps of the material, which indicates in favor of its hydrolytic dissolution.

A histological investigation of tissue samples containing a three-dimensional plastic structure created by the three-dimensional printing method revealed that the bioimplant from which the structure is produced has good supporting functions for connective, bone, and granulation tissue. The bioimplant does not cause severe inflammatory infiltration by lymphocytes, neutrophils and giant cells of foreign bodies. The bioimplant resorption probably occurs by hydrolysis, the metabolites released during this do not negatively affect reparative osteogenesis.

8. CONCLUSION

Thus, the synthesis of nanosized hydroxyapatite by the exchange reaction between diammonium phosphate and calcium nitrate under conditions of mechano-acoustic processing of the reaction mixture was developed. The methods for purifying hydroxyapatite from by-products are proposed. By dispersing raw materials of

animal origin, a protein hydrosol was obtained in the medium of which hydroxyapatite was synthesized and a collagen-calcium-phosphate composite was obtained. The methods of forming porous collagen-calcium-phosphate composites, including the action of microwave radiation, are considered.

It is shown that based on the developed biocompositions: calcium phosphate pastes, compositions from thermoplastic biodegradable polymers, non-woven fibrous materials, fabric-engineering constructions with an adjustable architecture can be made to solve various biomedical problems. The manufacture of biocomposites with the introduction of biological components from living organisms and drugs into their composition will stimulate the process of osteogenesis and restore the process of replacing a bone defect.

The creation of three-dimensional structures capable of performing the functions of a particular natural tissue of the body, based on a combination of cells and scaffolds (three-dimensional structures, matrix, framework), as well as other factors affecting cell growth, their differentiation and organization of the extracellular matrix, is an important task of the tissue engineering [44-46].

The work was carried out with the financial support of the Russian Federal Property Fund, project 18-29-23042.

REFERENCES

1. Joint European Commission/ETN nanomedicine: roadmaps in nanomedicine towards 2020. *Expert Report*, 2009, p. 33.
2. Popkov AV. Biosovmestimyye implantaty v travmatologii i ortopedii (obzor literatury). *Geniy ortopedii*, 2014, 3:94-99 (in Russ.).
3. Nekachalov VV. *Patologiya kostey i sustavov. Rukovodstvo*. SPb, Sotis Publ., 2000, 288 p.

4. Avdonin PV, Tkachuk VA. *Retseptory i vnutrikletochnyy kal'tsiy*. Moscow, Nauka Publ., 1994, 288 p.
5. Tkachuk VA. *Stvolovyye kletki i regenerativnaya meditsina*. Moscow, Lomonosov MSU Publ., 2014, 220 p.
6. Murayev AA, Dymnikov AB, Korotkova NL, Kobets KK, Ivanov SYU. Optimizatsiya parametra planirovaniya plasticheskikh operatsiy v chelyustno-litsevoy oblasti. *Sovremennyye tekhnologii v meditsine*, 2013, 5(3):57-62 (in Russ.).
7. Konyshchikov VA. *Stimulyatory i inhibitory rosta organov i tkaney zhivotnykh*. Moscow, Meditsina Publ., 1974, 191 p.
8. Tertsi M. *Genetika i zhivotnaya kletka*. Moscow, Mir Publ., 1977, 291 p.
9. Neyfakh AA, Lozovskaya YeR. *Geny i razvitiye organizma*. Moscow, Nauka Publ., 1984, 192 p.
10. Sveshnikov AA, Smotrova LA, Ovchinnikov YeN. Mekhanizmy demineralizatsii kostnoy tkani. *Geniy ortopedii*, 2005, 2:95-99 (in Russ.).
11. Lekishvili MV, Panasyuk AF. Novyye bioplasticheskiye materialy v rekonstruktivnoy khirurgii. *Vestnik RAMN*, 2008, 9:33-36 (in Russ.).
12. Salai M, Brosh T, Keller N, Perelman M, Dudkiewitz I. The effects of prolonged cryopreservation on the biomechanical properties of bone allografts: A microbiological, histological and mechanical study. *Cell and Tissue Banking*, 2000, 1(1):69-73.
13. Lekishvili MV. Tekhnologii izgotovleniya kostnogo plasticheskogo materiala dlya primeneniya v vosstanovitel'noy khirurgii: *Diss. dokt. med. nauk*. Moscow, 2005.
14. Volova LT, Kirilenko AG, Uvarovskiy BB. Sposob sterilizatsii liofilizirovannykh kostnykh transplantatov. *Patent RF:2156139*, 1999.
15. Shchepkina EA, Kruglyakov PV, Solomin LN at all. Transplantatsiya autologichnykh mezenkhimal'nykh stvolovykh kletok na demineralizovannom kostnom matritse pri plastike lozhnykh sustavov i kostnykh defektov. *Mater. III Vserossiyskogo simpoziuma s mezhdunarodnym uchastiyem «Aktual'nyye voprosy tkanevoy i kletochnoy transplantologii»*. Moscow, 2007, p. 113 (in Russ.).
16. Ershov YuA, Gorshenev VN, Kosenko NV. Sposob formirovaniya kostnogo implantata. *Patent RF:2206341*, 2002.
17. Ershov YuA, Gorshenev VN. Kollagen-gidroksiapatitovyye implantaty dlya ortopedii. *Materialy pervoy Vserossiyskoy konferentsii s uchastiyem RS. «Nanotekhnologii v onkologii-2008»*. Moscow, 2008, p. 127 (in Russ.).
18. Hull C. Method for production of three-dimensional objects by stereolithography. *US Patent: 4929402*, 1990.
19. Bredt JF, Sach E, Brancazio D, Cima M, Curodeau A, Fan T. Three dimensional printing system. *US Patent: 5807437*, 1998.
20. Landers R, Pfister A, Hubner U, John H, Schmelzeisen R, Mulhaupt R. Fabrication of soft tissue engineering scaffolds by means of rapid prototyping techniques. *J. Mater. Sci.*, 2002, 37(15):3107-3116.
21. Taboas JM, Maddox RD, Krebsbach PH, Hollister SJ. Indirect solid free form fabrication of local and global porous, biomimetic and composite 3D polymer-ceramic scaffolds. *Biomaterials*, 2003, 24(1):181-194.
22. Sachlos E, Czernuszka JT. Making tissue engineering scaffolds work. Review on the application of solid freeform fabrication technology to the production of tissue

- engineering scaffolds. **European Cells Materials**, 2003, 5:29-40.
23. Safronova TV, Shekhirev MA, Putlyayev VI, Tret'yakov YuD. Keramicheskiye materialy na osnove gidroksiapatita, sintezirovannogo iz rastvorov, podvergayutsya vozdeystviyu. *Neorganicheskiye materialy*, 2007, 43(8):1005-1014 (in Russ.).
24. Safronova TV, Kuznetsov AV, Putlyayev VI, Veresov AG, Ivanov VK. Keramika na osnove gidroksiapatita, sintezirovannogo iz atsetata kal'tsiya i gidrofosfata natriya. *Perspektivnyye materialy*, 2008, 6:96-99 (in Russ.).
25. Sinitsyna OV, Veresov AG, Kovalova YeS, Kolenko YuV, Putlyayev VI, Tret'yakov YuD. Polucheniye gidroksiapatita gidrolizom α -Ca₃(PO₄)₂. *Izvestiya Akademii nauk. Seriya khimicheskaya*. 2005, 1:78-85 (in Russ.).
26. Stevens MM. Biomaterials for bone tissue engineering. *Materials Today*, 2008, 11(5):18-25.
27. Sun JS, Tsuang YH, Liao CJ, Hang YS, Lin FH. The effect of sintered – dicalcium phosphate particale size on newbom wistar ratosteoblasts. *Artifinal Organs*, 1999, 23(4):331-338.
28. Kesel' BA, Fedorov AD, Gimushin IF, Volkov GA, Gataullin RSh, Voskoboynikov DV, Vesel'yev DA. Rotorno-pul'satsionnyy apparat (RPA). *Patent RF: 2166986*, 2006.
29. Kovaleva YeS, Filippo YaYu, Putlyayev VI, Tret'yakov YuD, Ivanov VK, Silkin NI, Galiullina LF, Rodionov AA, Mamin GV, Orlinskiy SB, Salakhov MKh. Biorezorbiruyemye poroshkovyye materialy na osnove Ca_{1-0,x}Nax(PO₄)_{6-x}(CO₃)_x(ON)₂. *Uchenye zapiski Kazanskogo universiteta. Seriya Estestvennyye nauki*, 2010, 152(1):79-98.
30. Saenger AT, Kuhs WF. *Golden Book of Phase Transitions*. Wroclaw, 2002, 1:1-123.
31. Nair LS, Laurencin CT. Polymers as Biomaterials for Tissue Engineering and Controlled Drug Delivery. *Adv. Biochem. Engin./Biotechnol.* 2006, 102:47-90.
32. Holland TA, Mikos AG. Biodegradable Polymeric Scaffolds. Improvements in Bone Tissue Engineering through Controlled Drug Delivery. *Adv. Biochem. Engin./Biotechnol.* 2006, 102:161-185.
33. Varghese S, Elisseeff JH. Hydrogels for Musculoskeletal Tissue Engineering. *Adv Polym Sci.*, 2006, 203:95-144.
34. Shtil'man MI. *Polimery mediko-biologicheskogo naznacheniya*. Moscow, Akademkniga Publ., 2006, 400 p.
35. Berchenko GN. Sinteticheskiye kal'tsiy-fosfatnyye materialy v travmatologii i ortopedii. *Sbornik rabot Vsesoyuznoy nauchno-prakticheskoy konferentsii. «Primeneniye iskusstvennykh kal'tsiyevykh fosfatnykh biomaterialov v travmatologii i ortopedii»*. Moscow, 2010, P. 3-5 (in Russ.).
36. Gorshenev VN, Teleshev AT, Yershov YuA, Kaziyev GZ, Kolesov VV, Sklyanchuk ED. Sposob polucheniya poristogo kostnogo biokompozita. *Patent RF: 2482880*, 2013.
37. Gorshenev VN, Yershov YuA, Teleshev AT, Sklyanchuk ED, Prosvirin AA, Grigor'yev SA. Gidroksiapatitovyye biokompozity meditsinskogo naznacheniya. *Meditsinskaya tekhnika*, 2014, 1:30-32 (in Russ.).
38. GOST 32244-2013 Subprodukty myasnyye obrabotannyye. Tekhnicheskiye usloviya. URL <http://docs.cntd.ru/document/1200107178>.
39. Neklyudov AD, Ivankin AN. *Kollagen: polucheniye, svoystva i primeneniye*. Moscow, GOU VPO MGUL Publ., 2007, 336 p.

40. Shtil'man MI. *Polimery mediko-biologicheskogo naznacheniya*. Moscow, Akademkniga Publ., 2006, 400 p.
41. Prosvirin AA, Sklyanchuk ED, Gur'yev VV, Gorshenev VN, Teleshev AT, Akatov VS, Fadeyeva IS, Fadeyev RS, Shushkevich AM. Fiziko-khimicheskiye svoystva i biosovmestimost' nanostrukturirovannogo poristogo kostnogo implantata. *Tekhnologii zhivnykh sistem*, 2013, 8:68-73 (in Russ.).
42. Vol'fkovich YuM, Sosenkin VE, Shkol'nikov YeI, Bagotskiy VS. Metod kontaktnoy etalonnoy porometrii. *Dokl. AN SSSR*, 1977, 232(3):603-606.
43. Gorshenev VN, Gorsheneva TD. Prispособleniye dlya formirovaniya kostnykh biokompozitov s otkrytoy poristost'yu. *Patent RF №143634*, 2014.
44. Gorshenev VN, Murayev AA, Teleshev AT, Ivanov SYu. Novyye additivnyye tekhnologii formirovaniya slozhnykh kostnykh struktur. *Materialy IV Mezhdistsiplinarnogo kongressa po zabolevaniyu organov golovy i shei*. Moscow, 2016, p. 80.
45. Tortelli F, Cancedda R. Three-dimensional cultures of osteogenic and chondrogenic cells: a-tissue engineering«approach to mimic bone and . cartilage in vitro. *Eur. Cell Mater.*, 2009, 17:1-14.
46. Devyatkov ND, Kislov VYa, Kolesov VV, Grachev VI. Diagnostics and correction of the functional state of the human organism with the "Charm"-diagnostic complex. *RENSIT*, 2018, 10(2):257-268, DOI: 10.17725/rensit.2018.10.257.